

UNIVERSITÀ DEGLI STUDI DI PISA

Facoltà di Ingegneria
Corso di Dottorato in Ingegneria Aerospaziale
XXII Ciclo

Tesi di Dottorato

**Low Thrust Trajectories
in Multi Body Regimes**



Tutore
Prof. Mariano ANDRENUCCI

Candidato
Pierpaolo PERGOLA

Direttore del Corso di Dottorato
Prof. Maria Vittoria SALVETTI

NOVEMBER 2010

A Maria



Abstract

More and more stringent and unique mission requirements motivate to exploring solutions, already in the preliminary mission analysis phase, going far beyond the classical chemical-Keplerian approach.

The present dissertation deals with the analysis and the design of highly non linear orbits arising both from the inclusion of different gravitational sources in the dynamical models, and from the use of electric system for primary propulsion purposes.

The equilibrium of different gravitational fields, on one hand, permits unique transfer solutions and operational orbits, on the other hand, the high thrust efficiency, characteristic of an electric device, reduces the propellant mass required to accomplish the transfer. Each of these models, and even better their combination, enables trajectories able to satisfy mission requirements not otherwise met, first of all to reduce the propellant mass fraction of a given mission.

The inclusion of trajectory arcs powered by an electric thruster, providing a low thrust for extended duration, makes essential the use of optimal control theory in order to govern the thrust law and thus design the required transfers so as to minimizing/maximizing specific indexes.

The goal is, firstly, to review the possible advantages and the main limits of dynamical models and, afterward, to define methodologies to preliminary design non-Keplerian missions both in interplanetary contexts and in the Earth-Moon system.

Special emphasis is given to the study of dynamical systems through which the main features of the Circular Restricted Three Body Model (the first one among the non-Keplerian models) can be identified, implemented and used. Purely ballistic solutions enabled by this model are first independently explored and after considered as target orbits for electric thrusting phases.

Electric powered arcs are used to link ballistic phases arising from the balancing of different gravitational influences. This concept is applied both for the exploration of planetary regions and for interplanetary transfer purposes. Together with low thrust missions to selenocentric orbits designed taking into account both the Earth and the Moon gravity, also transfer solutions toward periodic orbits moving in the Earth-Moon region are presented. These are designed considering electric thrusting arcs and ballistic segments exploring for free specific space regions.

In brief, theoretical models deriving from dynamical system theory and from optimal control theory are employed to design non conventional orbits in non linear astrodynamics models.

Sommario

Requisiti di missione sempre più stringenti e particolari spingono ad esplorare soluzioni, fin dalle fasi preliminari dell'analisi di missione, che vanno ben oltre il classico approccio impulsivo-Kepleriano.

Il presente lavoro tratta l'analisi ed il progetto di orbite altamente non lineari che emergono sia dall'inclusione di diverse fonti gravitazionali nel modello dinamico, sia dall'impiego di sistemi primari di propulsione elettrici.

Da un lato l'equilibrio di più campi gravitazionali consente soluzioni di trasferimento ed orbite operative uniche nel loro genere, dall'altro l'elevata efficienza propulsiva, tipica di un propulsore elettrico, riduce la massa di propellente necessaria per realizzare il trasferimento. Ognuno di questi due modelli, ed ancor meglio la loro combinazione, definisce traiettorie in grado di rispettare requisiti di missione non altrimenti soddisfabili, primo fra tutti quello di ridurre la massa di propellente richiesta per una specifica missione.

L'inclusione di fasi della traiettoria propulse da un sistema elettrico, che fornisce una bassa spinta per una durata prolungata, rende indispensabile la teoria del controllo ottimo per governare la legge di spinta e quindi realizzare il trasferimento minimizzando/massimizzando specifici indici.

L'obiettivo è, in primo luogo, quello di riesaminare i possibili vantaggi e limiti di questi modelli dinamici per poi definire metodologie per la progettazione preliminare di missioni non-Kepleriane sia in contesti interplanetari che nel sistema Terra-Luna.

Particolare enfasi viene data allo studio dei sistemi dinamici mediante il quale le principali caratteristiche del Modello Ristretto a Tre Corpi (il primo fra i modelli non-Kepleriani) possono essere identificate, implementate e quindi sfruttate. Le soluzioni balistiche che derivano da questo modello sono esplorate dapprima in maniera indipendente e successivamente considerate come orbite obiettivo per fasi propulse.

Archi propulsi elettricamente sono utilizzati per connettere fasi di volo balistico che nascono dal bilanciamento di diverse influenze gravitazionali. Tale concetto viene applicato sia per l'esplorazione di regioni planetarie che per trasferimenti interplanetari. Assieme a missioni a bassa spinta verso orbite selenocentriche progettate considerando sia l'attrazione gravitazionale della Terra che della Luna, sono presentate anche soluzioni per trasferimenti verso orbite periodiche che si muovono nel sistema Terra-Luna. Queste ultime sono costruite considerando archi di volo propulso e fasi balistiche che portano naturalmente ad esplorare specifiche regioni dello spazio.

In breve, strumenti derivanti dalla teoria dei sistemi dinamici e dalla teoria del controllo ottimo sono impiegati al fine di progettare missioni non convenzionali in modelli astrodinamici non lineari.

Acknowledgements

Facing this blank page that have to become this acknowledgement section, I worry that my thanks might result in a long trite list of names or in inadequate mentions of all those people who patiently worked on my side. Nevertheless I'm perfectly aware that I have to thank so many people if I'm at this stage.

Of course, the first one I will be always grateful is Prof. M. Andrenucci who gave me incommensurable chances of experiences, that helped me not just from a technical point of view and that is still first close to the person and than to the student.

A special thank is for Prof. M. Dellnitz, under whose supervision I had the opportunity to spend the long and extremely fruitful period in the Paderborn applied math department, and for A. Boutonnet and J. Schoenmaekers who gave me the chance to work on their side during my ESOC training. Last but not least, I wish to thank Prof. G. Mengali and A. Quarta for their very useful advices and suggestions.

Now I should start a long enumeration of friends, colleagues, mates and mentors among the guys of the Pisa university, of Alta, of the IFIM/PaSco group, of the Astronet project, of the ESOC mission analysis section, and so on. I'm sure that each of you knows how much helped me and how trivial any word on this page could result.

Finally, I wish to thank all of those people that make this period (also this one) not just work but fun, relax, experience, life in the complete sense of the word. I received and found so good fellow passenger that can not be just blind Chance.

My deepest thanks to all of you guys.

Contents

1	Introduction	1
1.1	Non-Keplerian Trajectories	1
1.2	Mission Analysis Trends	4
1.3	Goal and Outline	6
2	Dynamical Models	7
2.1	The N -body Problem	8
2.2	The Restricted Three Body Problem	14
2.2.1	Synodic, Non Dimensional Reference System	17
2.2.2	Equations of Motion	19
2.2.3	The Integral of the Motion	23
2.2.4	Libration Points	26
2.2.5	Equilibrium Regions	31
2.3	Restricted Four Bodies Models	37
2.4	Dynamical System Elements	40
3	CR3BP Model Investigation and Exploitation	47
3.1	Periodic Orbits	48
3.1.1	Periodic Orbits around Libration Points	48
3.1.2	Global Periodic Orbits	52
3.1.3	Stability of Periodic Orbits	57
3.2	Manifolds	63
3.2.1	Manifold Globalization Procedure	64
3.2.2	Normal Forms to Compute Invariant Manifolds Near and Far the Libration Points	67
3.3	Homoclinic Orbits	76
3.4	Heteroclinic Orbits	77
3.5	Transit Orbits	79

3.6	Poincaré Sections	81
3.7	Resonances	84
3.8	Chaos and Lyapunov Exponents	90
4	Optimal Control	96
4.1	The Optimal Control Problem	96
4.1.1	Direct Methods	97
4.1.2	Indirect Methods	100
4.1.3	Global Methods	106
4.2	Low Thrust	107
4.3	Two Body Application: Low Thrust Earth-Mars Transfers	108
4.4	Three Body Application: Low Thrust Heteroclinic Transfers . . .	113
4.5	Considerations	118
5	Low Energy, Low Thrust Deep Space Missions	120
5.1	Low Thrust Transition between one dimensional Manifolds . . .	120
5.1.1	The Moon Tour	124
5.1.2	Earth-Uranus Transfer	125
5.2	Low Thrust Halo to Halo Interplanetary Transfers	127
5.2.1	Design Strategy	129
5.2.2	Earth-Mars: A Study Case	133
6	Novel Mission Scenarios in the Earth-Moon System	142
6.1	Low Thrust Transfer to a Manifold Chain	143
6.1.1	GTO to Manifold Chain Transfer	145
6.2	Optimal Earth-Moon CR3BP Low Thrust Trajectories	148
6.2.1	Thrust-Coast-Thrust Approach	150
6.2.2	Earth-Moon Transfer Examples	153
6.3	Low Thrust Transfer To Backflip Orbits	157
6.3.1	Transfer Design	161
6.3.2	Results	166
7	Conclusions	171
A	Parameter Values	173
	Bibliography	175
	List of Figures	186
	List of Tables	191

Chapter 1

Introduction

The trajectory design is a constitutive part of each space mission and it is one of the basic aspects since the preliminary mission planning phase. The fulfillment of all the mission targets results only by an adequate mission analysis and design, usually aimed at saving as much spacecraft resources as possible to accomplish the required path. The mission goals and the probe performance are the main mission analysis driving factors. The trajectory provides several fundamental parameters (e.g. propellant mass fraction, transfer time, radiation absorption dose, illumination conditions and so on) required for the complete system design. This results in an iterative process where the mission analysis plays a fundamental role, in depth it is constrained and constrains the scientific payload and the overall mission architecture.

1.1 Non-Keplerian Trajectories

The modern space mission concepts are becoming more and more ambitious. Mission requirements, costs, duration, payload constraints and so on, evolve requiring trajectories more challenging and complex.

This can be faced by “violating” the two body assumptions and going beyond classical models for a clever exploitation of the dynamical environment ruling the motion of the spacecraft. Taking into account, beside the main gravity force source, all the forces acting on the spacecraft, results in highly non linear dynamics. Although the nature of the perturbing accelerations can be extremely various, additional gravitational influences and small magnitude propulsion forces are sufficiently powerful and useful to design unconventional missions. An adequate exploitation of one of these two forces, or, even better of their combination, can result in innovative trajectories able to satisfy specific mission concepts, e.g. extremely low propellant usage,

specific illumination conditions or unique space locations.

From a propulsion point of view, space trajectories can be basically divided into three main classes. The first one are ballistic trajectories, where the on board propulsion subsystem does not play any role and only the natural dynamical environment drives the probe. Then there are high thrust trajectories, where the spacecraft propulsion subsystem is able to give an almost instantaneous impulse (much shorter than the mission duration) and much stronger than the local gravity force. This impulse is usually provided by means of a chemical thruster while, before and after, only the natural dynamics act on the probe. Thirdly, also the so called *Low Thrust Trajectories* have to be considered, where the propulsion subsystem acts for times of the same order of the whole mission duration providing an acceleration with a magnitude comparable with the local gravity. In this last case it is clear that the path of the probe is defined not just by the natural dynamics, but also by the active control given by the low thrust engine. Due to the current power generation performance, these small accelerations are typically provided by electric thrusters.

Historically, high thrust missions have been widely used; they represent the origin of the space exploration. Recently, however, low thrust missions are becoming more popular as they demand mass consumptions smaller than chemical thrusters to obtain the same total mission impulse. Nevertheless they usually require longer transfer times and need to be carefully designed already in the preliminary mission phase.

In the design of such trajectories the optimization plays a fundamental role, as it has to satisfy the mission requirements and it has to provide a criterion to choose a specific path among all the possible choices, the one minimizing or maximizing specific performance indexes. Such as the transfer time, usually longer when a low thrust strategy is adopted, or the propellant mass, usually higher when a chemical thruster is considered. The propellant mass is directly related to the specific characteristics of the thruster employed and it influences the whole spacecraft mass, especially at launch.

On the other side, the gravity is the main force always acting on the probe, independently of its on-board propulsion capabilities. All bodies act at the same time on each point of the space by means of their gravity field that obeys (as the Newton universal gravitation law states) to the inverse-square law. This determines the orbits of any natural body and, from a mission analyst's point of view, the main forces acting on the probe.

The historical approach of classical celestial mechanics is to study the motion of a body subject to just one gravity field at a time. The closest and/or more massive body is the responsible of the gravity field and the re-

sulting equations of motion can be integrated in closed form. This is the *Keplerian model* that still remains the main choice for classical preliminary mission analysis. However, in this way all the other gravity effects have to be compensated, as they represent deviations from the nominal path. Moreover with this approach only conic orbits (resulting from the Keplerian model) can be designed and many of the advantages of the real dynamical environment can not be identified nor exploited. The actual main limit is that the Keplerian model is not suitable for the design of trajectories characterized by extended arcs where two or more gravitational accelerations balance.

The next natural step is to consider not just one attractor, but at least a couple of them. This can be done by taking into account a center body and a gravitational perturbation, or considering simultaneously two massive attractors. In this way, also when applying several simplifications (leading to the so called *Circular Restricted Three Body Problem*) the resulting equations of motion can not be integrated anymore. Dynamical system theory can be exploited to describe many features that result very useful both for transfer purposes and for nominal operational orbits. Just as an example, closed orbits around massless points can be found in this case; something completely impossible with the Keplerian approach.

One step further, with increasing complexity, is to consider in the circular restricted three body model another attractor acting as gravitational perturbation, this is the idea of the *Four Body Models* (e.g. BiCircular Model).

It is worth nothing that also the application of the classic *Patched Conic Approach* is a preliminary step toward the inclusion of more than one gravity field. In fact, the changing of the main body at a given point, is just a way to consider more than a single attractor during the mission (although not at the same time) and this is very useful to design close passages with massive bodies.

There are, however, several other influences acting with significant magnitude on specific orbits; these are effects like Sun radiation pressure, bodies oblateness, drag and so on. All of these, although crucial for real mission applications, can be neglected in the preliminary mission analysis phase. This applies unless the specific application is heavily affected by one of these perturbations; for instance the atmospheric drag can not be neglected for a low Earth orbit, not even in preliminary analyses. However, these cases are not investigated in the present work, while special emphasis is given to the consequences of gravitational perturbations.

For instance, in these sophisticated frameworks it is possible to highlight methods to gain energy without any use of the on-board propulsion resources. The so called *Resonant* configurations arise, where the spacecraft and the

perturber mean motion are coupled. These are very useful as can be used to “steal” a bit of the energy of the perturbing body for extended times and properly modify the orbit when the spacecraft is still far from the origin of perturbation, i.e. from a planet/moon. On the other hand, when the probe and the perturber are much closer than the probe and the main attractor, this “energy-stealing” process is modeled by the classical swing-by concept and thus by means of the patched conic approach.

These innovative approaches take advantages of the nonlinearities arising by considering a N -body dynamics. The idea is to exploit such dynamics, including their chaotic aspects, to design missions neither conceivable with the classical celestial mechanics methods or transfers less expensive (with respect to a given performance parameter) than the standard ones. These so called *Low Energy Trajectories* require, typically, a total velocity change for the whole mission smaller than a two body (like Homann or Patched Conics) approach. This is the basic reason motivating the exploitation of multi body regimes, as the combined influences of more gravity forces can reduce the spacecraft on-board resources to be allocated to accomplish a given task.

All in all, the classic mission analysis approach employs a Keplerian model with impulsive transfers and it is still a natural benchmark for each space mission. Nevertheless more complete dynamics, like Three (or more) Body Models, possibly coupled with electric thrusting arcs, give rise to completely new mission analysis concepts, *Non-Keplerian Trajectories*, that can be explored in order to improve specific mission aspects.

This innovative approach has in the low thrust propulsion scheme its technological innovation and in the more bodies models a better exploitation of the natural forces acting on the probe. This combination is often referred as *Low Energy - Low Thrust* missions.

1.2 Mission Analysis Trends

Already in the seventies the space exploration began to employ innovative concepts based on non-Keplerian models with approaches able to satisfy novel mission requirements^[1]. The goal of this section is not to give a complete list of all the non classical missions, but to give an idea of the trend in the mission analysis from the seventies on.

The first real application involving a non-Keplerian orbit dates back to the late seventies. The mission ISEE-3 was sent to a periodic orbit around a Sun-Earth libration point to investigate about the interaction of the solar wind and the Earth magnetosphere^[1]. This point is an equilibrium point between the Sun and Earth gravity approximately located $1.5e6$ km far from the Earth. Many others missions were planned and flew towards libration

point orbits, like the WIND^[2] or WMAP and others are in operation or under investigation like SOHO, JWST, GAIA and LISA Pathfinder^{[1][3]}. The unique positions of these libration points are particularly appealing; they are quite far from the physical perturbations of a massive body (e.g. tides or drag), have quasi constant Earth distance for communications and can easily satisfy requirements of constant Sun illumination/shielding^[3].

Nevertheless, only in 1990 there was the first transfer designed considering non-Keplerian models. The idea of Sun perturbed trajectories and weak capture was used to rescue the Japanese mission HITEN that reached successfully the Moon^[4]. More sophisticated methods, borrowed from the dynamical field theory, were lately used to carefully design other non conventional missions^[5], like the GENESIS, designed to reach a periodic orbit around a Sun-Earth libration point to collect samples of solar winds and bring them back on Earth^[6]. The whole path was completed with less than 100 m/s of deterministic chemical impulse since ballistic trajectories, enabled by the balancing of Sun and Earth gravity fields, were exploited^[6].

Although in the beginning the electric thrusters were used only for station-keeping and small maneuvers, many missions equipped with an electric device as main propulsion system were successfully launched. The first interplanetary probe powered by an electric device was the NASA Deep-Space 1^[7], launched in 1998. This probe exploited an ion thruster to reach the asteroid Braille and subsequently the comet Borrelly. After this mission, many others low thrust equipped missions were planned and launched, like the asteroid sample return mission Hayabusa or the ongoing DAWN towards the main asteroid belt^[7]. Of course, beside these, there are also missions equipped (or foreseen to be) with electric thruster for drag compensation, control systems or fine pointing, like GOCE, GAIA or LISA^{[3][8]}.

Finally, also the combination of these two innovative mission approaches has been employed in the SMART-1 mission^[7], a small mission for advanced research in technology that reached the Moon in 2006 using an electric Hall effect thruster and Moon resonances^[8]. Moreover, the same combination is still under investigation for the Bepi Colombo mission, an interplanetary mission towards Mercury. Its trajectory is conceived by employing low thrust arcs in combination with several gravity assists and a final ballistic capture at the Mercury arrival^{[3][8]}.

Thus, more and more missions were and are planned by directly considering completely non-Keplerian approaches. This gives an idea of the current approaches to non conventional mission analysis and design; nevertheless, the classical Keplerian model coupled with chemical impulses remains a valuable working option.

1.3 Goal and Outline

The goal of the present work is to combine the low energy and the low thrust concept. This is done by exploring the relevant features of the underlying dynamical models together with control theory elements before to address several specific applications. A theoretical understanding is mandatory before considering particular mission applications that represent test cases of the capabilities of these non canonical mission analysis schemes.

The applications presented make use, depending on the case, of more than one gravity fields and/or low thrust propulsion strategies. Several applications are presented, both restricted to planet-moon systems, and in the interplanetary framework. These applications must be intended as design methodologies for non-Keplerian missions in initial mission design phases. Thus, the main outcome of the present work is to provide design schemes for low thrust transfers in dynamical regimes ruled by more than one body.

As said, when a low thrust scheme is involved, the optimization of the thrust law becomes a fundamental part of the trajectory design, so these applications have to be intended as optimal solutions, at least locally. Actually, the main aim is to design feasible solutions in complicated dynamical models and this means that the resulting transfers do not represent the absolute minima for a specific problem. They are, instead, feasible solutions minimizing, into a suitable neighborhood of solutions, a specific performance index.

Employing dynamical system theory, the main features of the restricted three body model are deviated and computed before to be used in practical mission design concepts. The work is not supposed to give detailed theoretically explanations, but an overview of the main theoretical tools required to model such a kind of trajectories.

In the second Chapter the dynamics of the circular restricted three body model are derived from the general N -body model and are analyzed. In the Chapter three several useful characteristics of this model are derived from theoretical analyses and framed in mission analysis contexts. In the fourth Chapter elements of the control theory are given and applied to two/three body basic examples. In the Chapter five two applications of non-Keplerian mission analysis are presented in a planetary-moon realm and for an interplanetary transfer, while in the sixth Chapter low thrust missions in the Earth-Moon circular restricted three body system are proposed.

Chapter 2

Dynamical Models

In the beginning of space exploration, chaos used to be considered as an undesirable side effect in the design of any space mission. This happened because the extreme sensitivity to any change in the initial conditions makes hard to predict the trajectory flowing and imposes strict requirements on the mission control. However, it was soon realized^{[9][10]} that it is possible to take advantage from chaotic behaviors to design a space path. This results in low energy trajectories, usually requiring long orbital arcs to patch together extremely carefully. They involve many parameters to tune and are difficult to model with the classical celestial mechanics approaches. Thus, the discovery of the chance to control the chaos opened a wide range of possibilities and new approaches in the celestial mechanics. All of these non-Keplerian approaches are enabled by models far beyond the classical two body model. The circular restricted three body model is the fundamental more-body setting enabling a wide set of non conventional orbits and providing a theoretical background to understand them.

In this chapter a survey of the dynamical models used through the whole work is given. The basic characteristics of the N -body model are outlined together with its main limitations for an analytical approach. Thus, the three body model, in its full version and with the introduction of the restricted hypothesis is introduced. For this model the equations of motion, the stationary points and the constant of the motion are derived in constructive ways. Finally, also an overview of the complex dynamics arising in the model is presented in order to use this theoretical background in the following chapters.

The general definition of the N -body model, its features and its specification to the case of three masses follows^{[11][12]}. The fundamental reference for the circular restricted three body model is^[13], furthermore the derivations

presented follow also^{[14][15]}. For the dynamical system section the reader can refer to^[16].

2.1 The N -body Problem

The Newton inverse square law is the foundation of each model to study the motion of a body in space. The main force always acting in any point of the space is the gravity; it is always attractive, directly proportional to the bodies masses and inversely to the square of their distance.

Let us consider N bodies moving in the Euclidean space \mathbb{R}^3 only under the influence of their mutual gravitational interaction. Combining the Newton's second law and the universal gravitation law, the *Newtonian Formulation* of the problem reads^[11]:

$$m_i \ddot{\mathbf{q}}_i = -Gm_i \sum_{\substack{j=1 \\ j \neq i}}^N \frac{m_j}{\|\mathbf{q}_i - \mathbf{q}_j\|^3} (\mathbf{q}_i - \mathbf{q}_j) \quad (2.1)$$

where G is the universal gravitation constant, \mathbf{q}_i the position vector of the mass m_i and the dots are the derivatives with respect to time, which is the independent variable.

The gravity is a conservative force, so also the equivalent potential formulation of the N -body problem can be given by defining the negative gravitational potential U (also called the self potential), depending only on the product of the masses and their mutual distance^[12]:

$$m_i \ddot{\mathbf{q}}_i = -\frac{\partial U}{\partial \mathbf{q}_i} \quad \text{where} \quad U = \sum_{\substack{j=1 \\ j \neq i}}^N \frac{Gm_i m_j}{\|\mathbf{q}_i - \mathbf{q}_j\|} \quad (2.2)$$

Eq. (2.1) represents a set of $6n$ equations of the first order ($3n$ of the second order) and rules the motion of each of the N bodies under the gravitational influence of the other $N-1$ bodies. The sum of this relation should be extended to all the bodies in the universe making a rigorous analysis impossible.

Defining $\mathbf{q} = \{\mathbf{q}_1, \mathbf{q}_2, \dots, \mathbf{q}_N\} \in \mathbb{R}^{3n}$, the set of generalized positions, and $M = \text{diag}(3 \times m_1, \dots, 3 \times m_N)$, the vectorial form of Eq. (2.2) reads:

$$M\ddot{\mathbf{q}} + \nabla U(\|\mathbf{q}\|) = 0 \quad (2.3)$$

A particularly convenient expression of any mechanical problem is the *Hamiltonian Formulation*^[11], also used later on for the circular restricted three body problem (cfr. Sec. 2.2.2). Since the Newton equations involve

the second derivative of positions with respect to time, it is possible to define the first derivatives as new variables to reduce the order of the system. These are the velocities or, equivalently in the Hamiltonian formulation, the *conjugate momenta*: $\vec{\mathbf{p}}_i = m_i \dot{\vec{\mathbf{q}}}_i$. Defining $\mathbf{p} = \{\vec{\mathbf{p}}_1, \vec{\mathbf{p}}_2, \dots, \vec{\mathbf{p}}_N\} \in \mathbb{R}^{3n}$, the vectorial form of the relation giving the momenta with respect to the positions derivatives is: $\mathbf{p} = M\dot{\mathbf{q}}$ ^[12].

What makes this formulation extremely convenient is that the equations of motion take a very easy form, independent of the specific dynamical system under consideration. These are the so called *canonical equations*:

$$\begin{aligned} \dot{\mathbf{q}} &= H_p \\ \dot{\mathbf{p}} &= -H_q \end{aligned} \Rightarrow \dot{\mathbf{z}} = J \nabla_z H = \begin{pmatrix} \mathbf{0} & \mathbf{I} \\ -\mathbf{I} & \mathbf{0} \end{pmatrix} \nabla_z H \quad (2.4)$$

where the subscripts identify the derivatives, ∇ the gradient operator, $\mathbf{z} = [\mathbf{q}, \mathbf{p}]$ and J is a $4n \times 4n$ square block matrix, the *Symplectic Matrix*¹, with \mathbf{I} the unity matrix and $\mathbf{0}$ the null matrix.

Here H is the *Hamiltonian* and it is an equivalent of the total energy of the system given by the combination of the kinetic and potential energy:

$$H = \sum_{i=1}^N \frac{\|\vec{\mathbf{p}}_i\|^2}{2m_i} - U = \frac{1}{2} \mathbf{p}^T M^{-1} \mathbf{p} - U \quad (2.5)$$

Specifying the canonical equations for the N -body problem^[12]:

$$\begin{aligned} \dot{\mathbf{q}} &= M^{-1} \mathbf{p} \Rightarrow \dot{\vec{\mathbf{q}}}_i = \frac{\partial H}{\partial \vec{\mathbf{p}}_i} = \frac{\vec{\mathbf{q}}_i}{m_i}; \\ \dot{\mathbf{p}} &= U_q \Rightarrow \dot{\vec{\mathbf{p}}}_i = -\frac{\partial H}{\partial \vec{\mathbf{q}}_i} = -\sum_{\substack{j=1 \\ j \neq i}}^N \frac{m_i m_j (\vec{\mathbf{q}}_j - \vec{\mathbf{q}}_i)}{\|\vec{\mathbf{q}}_i - \vec{\mathbf{q}}_j\|^3}; \end{aligned} \quad (2.6)$$

It is worth nothing that the potential U is a continuous function and, in particular, it is Lipschitz continuous; this allows the application of the Cauchy theorem that assures the existence and uniqueness of the solution.

In both formulations, the N -body problem results in a system of $6n$ first order equations, so a complete set of $6n-1$ time independent integrals, i.e. quantities conserved during a generic trajectory, plus a time dependent one would be required in order to solve the problem^[12].

In any mechanical conservative system the total energy of the system (or, equivalently, the Hamiltonian) is always an integral of the motion^[11]. To

¹A Symplectic Matrix M is a non singular square $2n \times 2n$ matrix satisfying the relation: $M^T \Lambda M = \Lambda$. Where the superscript T indicates the transpose and $\Lambda = \begin{bmatrix} 0 & I_n \\ -I_n & 0 \end{bmatrix}$ is a skew symmetric matrix with I_n $n \times n$ identity matrix.

check the invariance of the Hamiltonian it is sufficient to verify the vanishing of its time derivative:

$$\frac{dH}{dt} = \frac{dH}{d\mathbf{q}} \dot{\mathbf{q}} + \frac{dH}{d\mathbf{p}} \dot{\mathbf{p}} = \frac{dH}{d\mathbf{q}} \frac{dH}{d\mathbf{p}} + \frac{dH}{d\mathbf{p}} \left(-\frac{dH}{d\mathbf{q}} \right) = 0 \quad (2.7)$$

Setting $\vec{\mathbf{Y}}_N = m_1 \vec{\mathbf{q}}_1 + \dots + m_N \vec{\mathbf{q}}_N$, that is the center of mass of the system, and $\vec{\mathbf{L}} = \vec{\mathbf{p}}_1 + \dots + \vec{\mathbf{p}}_N$ the *total linear momentum*, the application of the canonical equations Eq. (2.6) lads to:

$$\dot{\vec{\mathbf{Y}}}_N = \vec{\mathbf{L}}, \quad \dot{\vec{\mathbf{L}}} = 0, \quad \ddot{\vec{\mathbf{Y}}}_N = 0 \quad (2.8)$$

so $\vec{\mathbf{Y}}_N = \vec{\mathbf{L}}_0 t + \vec{\mathbf{Y}}_N(t=0)$ and $\vec{\mathbf{L}} = \vec{\mathbf{L}}_0$ are time invariant constants of motion; as vectorial relations they constitute six integrals of motion. The conservation of the linear momentum provides the conservation of the motion of the center of mass, specifying the uniform motion of this point.

Defining now $\vec{\mathbf{O}} = \sum_1^N \vec{\mathbf{q}}_i \wedge \vec{\mathbf{p}}_i$ the *total angular momentum* and computing its time derivative, it results in:

$$\dot{\vec{\mathbf{O}}} = \sum_1^N \dot{\vec{\mathbf{q}}}_i \wedge \vec{\mathbf{p}}_i + \sum_1^N \vec{\mathbf{q}}_i \wedge \dot{\vec{\mathbf{p}}}_i = 0 \quad (2.9)$$

where Eq. (2.6) have been exploited. This means that the angular momentum represents other three scalar integrals of motion.

Thus, besides the Hamiltonian, also the total angular and linear momenta are integrals of motion. Since these are vector quantities, they result respectively in three and six linear independent constants of motion^[11]. These ten integrals are independent, i.e. they form a system in involution (the Poisson brackets² between two of them are zero). Moreover the Bruns-Poincaré theorem^[17] states that do not exist any other first integrals linearly independent of these.

These ten first integrals are sufficient to completely specify the motion of a *Two Body Model* (or Keplerian Model), studying the motion of a body subject to only one gravitational influence at a time³. This holds as, given an autonomous canonical system with n degrees of freedom endowed with n

²Considering two functions in \mathbb{R}^{2n} , $F(p, q), G(p, q)$ the *Poisson Brackets* between them are defined as:

$$\{F, G\} = \sum_{j=1}^n \left(\frac{\partial F}{\partial q_j} \frac{\partial G}{\partial p_j} - \frac{\partial F}{\partial p_j} \frac{\partial G}{\partial q_j} \right)$$

It is a bilinear map defined on a smooth differential manifold. This operator is linear, skew symmetric and satisfies the Jacobi identity and the Leibnitz rule.

³This model was introduced already in the 1600 by J. Kepler in his works *Astronomia nova* and *Harmonices Mundi* where the three Kepler's laws are also stated.

first integrals in involution, the Liouville theorem^[16] assures the integrability of such a system (and offers a way to compute the solution)^[18].

In fact, considering Eq. (2.1) restricted to $N = 2$, it follows that twelve constants of motion are required to solve the problem. Considering these ten first integrals of motion, there remain only two constants to completely determine the motion^[19]. This approach results in a completely integrable model, composed by Keplerian orbits given by conic sections and the two remaining integration constants reduce to the trajectory and the time integral^[11].

Let us write down the equations of motion for a two body model in cartesian coordinates:

$$m_1 \ddot{\mathbf{q}}_1 = -\nabla U(\rho); \quad m_2 \ddot{\mathbf{q}}_2 = -\nabla U(\rho) \quad (2.10)$$

where $\rho = |\vec{\rho}| = |\mathbf{q}_2 - \mathbf{q}_1|$ is the distance between the two masses (i.e. the position of m_2 with respect to m_1) and U is the self potential introduced in Eq. (2.2). Introducing a transformation of coordinates such that $\vec{\mathbf{Y}}_2$, the system center of mass, is given by $\vec{\mathbf{Y}}_2 = (m_1 \mathbf{q}_1 + m_2 \mathbf{q}_2)/(m_1 + m_2)$; the equations of motion reduce to:

$$\ddot{\mathbf{Y}}_2 = 0; \quad \tilde{\mu} \dot{\vec{\rho}} = -\nabla U(\rho) \quad \text{with} \quad \tilde{\mu} = \frac{m_1 m_2}{m_1 + m_2} \quad (2.11)$$

From these equations it is straightforward to conclude that:

- the center of mass moves of rectilinear uniform motion;
- the motion of m_1 with respect to m_2 is exactly the same we would observe if m_1 is fixed and it exerts on a massless m_2 a force of potential $\overline{U}(\rho) = G(m_1 + m_2)/\rho$.

None of the two masses is privileged in this model and the choice of $\vec{\rho}$ is based on the idea to study the motion of one of the two masses from an observer posed on the other one^[11]. To refer the motion of both masses to the center of mass it is sufficient to perform just a translation and it results, beside a scale factor, in the same motion observed by a system of reference posed on one of the two masses.

This is the explicit representation of the integrals of motion for the two body model resulting in the two integration constants, determined by the initial conditions, required to solve the problem by quadratures^[12].

The next logical step after the Keplerian approach is the inclusion of another body. Including another gravity source would involve the sum in Eq. (2.1) up to three, so the first integrals required would be eighteen. Nevertheless the ten first integrals discussed for the general N -body problem

do not depend on the number of bodies involved^[17]. This means that, already dealing with three attractors, there are eight missed constants of motion.

This is sufficient to state that the resulting *Full Three Body Problem* is not integrable; i.e. the solution (the shape of the trajectory) can not be obtained by means of explicit integration operations^[17].

Of course, the initial position and velocity conditions provide all the information required to obtain a *single* solution of the problem. This is assured again by the Cauchy theorem, since the Newtonian mechanic is deterministic. Thus, the initial conditions allow the computation of the motion of a specific path, but they do not provide enough information for general solutions.

Although the general problem of the three bodies presents these theoretical limits, there are some particular initial configurations that allow the determination of general solutions.

A given configuration $\vec{\mathbf{r}}_c = [\vec{\mathbf{q}}_1, \vec{\mathbf{q}}_2, \vec{\mathbf{q}}_3]^T$ is defined a *central configuration* if it collapses homotetically (orientation preserving) on its center of mass when the three masses are released at rest^[20]. It is the best situation that can be present in a dynamical system without any fix point (like the N -body problem) as these are configurations changing only by symmetries.

This situation is equivalent to the existence of a constant $\varphi < 0$ such that: $\varphi m_i \vec{\mathbf{q}}_i = \sum_j m_j m_i / \|\vec{\mathbf{q}}_j - \vec{\mathbf{q}}_i\|^3 (\vec{\mathbf{q}}_j - \vec{\mathbf{q}}_i)$ for $i, j = 1, 2, 3$ and $i \neq j$ (to avoid collisions resulting in singularities). In other words, in this case there exist solutions where the acceleration is proportional to the positions: $\ddot{\vec{\mathbf{q}}}_i = \varphi \vec{\mathbf{q}}_i$. Since the acceleration can be expressed by means of the derivatives of the self potential U (Eq. (2.2)), it follows that $M^{-1} \partial U / \partial \mathbf{q} = \varphi \mathbf{q}$.

Defining $I = M^{-1} \sum_{i < j} m_i m_j \|\vec{\rho}_{ij}\|^2 = \mathbf{q}^T M \mathbf{q}$ as the *moment of inertia* of the whole system, with algebraic manipulations^[20] and considering that U is a homogeneous potential of degree -1, it is possible to define a central configuration by:

$$\frac{\partial U}{\partial \mathbf{q}} + \varphi \frac{\partial I}{\partial \mathbf{q}} = 0 \quad \Rightarrow \quad \sum_j m_j \left(\frac{1}{\rho_{ij}^3} + \frac{\varphi}{M} \right) \vec{\rho}_{ij} = 0 \quad (2.12)$$

where $\vec{\rho}_{ij} = \vec{\mathbf{q}}_j - \vec{\mathbf{q}}_i$ and $\rho_{ij} = \|\vec{\rho}_{ij}\|$ (indeed a generalization of ρ introduced in Eq. (2.10)).

In this formulation φ behaves like a sort of Lagrange multiplier, in fact the equality 2.12 is an extremum for the potential U under the condition that $\sum_j m_j \vec{\rho}_{ij} / M = \text{const}$ ^[21]. Thus, a central configuration is a critical point of the potential constrained on surfaces of constant moment of inertia (these can also be reduced to unit spheres).

For non-collinear configurations, the vectors $\vec{\mathbf{q}}_j$ and $\vec{\mathbf{q}}_i$ are linearly independent and so the coefficient of the sum in Eq. (2.12) has to vanish. This

results in a solution where the three masses lie at the vertices of an equilateral triangle (Lagrange, 1772)^[22]. Thus, the three masses form at each instant a rigid equilateral triangle rotating with constant angular velocity within its circumscribing circle.

On the other hand, it is possible to have the vector $\vec{\rho}_{ij}$ equal to zero, this is the case when the three masses are moving along a straight line (Euler, 1767)^[23]. This solution is a special situation since it does not correspond to an extremum of the potential, but the additional constraint that the three masses move on the same line has to be imposed.

Central configurations change by similarities and each body moves, according to Keplerian motion, on a specific conic with the same eccentricity of all the other bodies paths. In this situation, when $e = 1$ the orbits are parabolic and the motion is homotetic (the masses move along straight lines towards/from the center of mass), while, for $e = 0$ the motion is along circles and the configurations change only by isometries (the masses move on three circles that can be all scaled by the same factor).

Variational methods give an additional general solution in the special case that the three masses are equal and move in the same plane. This solution foresees the three bodies chasing one each other along an eight-shaped curve^[21]. This solution explores a combination of the two previous solutions, as at some time instants the three bodies are aligned or one of them sits at the midpoint of the segment defined by the other two^[19].

Central configurations arise also in the general N -body problem and, imposing additional constraints on the path followed by the masses (e.g. planarity, symmetry, similarity and so on), it is also possible to identify particular general solutions for the 4/5-body problems^[24].

However, what we are interested in is often the motion of something much smaller than the bodies causing the gravity fields. We are talking about spacecraft, asteroids, or even planets if compared with stars. Bodies of this kind can be considered massless from a gravitational point of view, i.e. their gravity (directly proportional to their mass) is too weak to influence the motion of bodies many orders of magnitude more massive.

This leads to the *restricted assumption*, where the problem is reduced to the study of a “massless” body moving under the gravitational influence of other $N-1$ bodies^[22]. It is easy to see that for an arbitrary value of N also the restricted N -body problem can not be analytically integrated (although it is again numerically integrable), while when $N = 2$ the problem reduces to the Keplerian problem^[19].

It is worth noting that the application of the restricted hypothesis to the two body model affects only the mass-dependent constant of the potential

term $(\bar{U}(\rho))$ that changes from $m_1 + m_2$ to only m_1 (assuming $m_1 \gg m_2$).

2.2 The Restricted Three Body Problem

Restricting the general Eq. (2.1) to the situation $N = 3$, we are dealing with the well known full three body model.

Let us specify the equations of motion of the N -body problem to the case of three masses (each identified by a subscript number) in an inertial Euclidean reference frame, where the position vectors are represented by $\vec{\mathbf{R}}_i = [X_i, Y_i, Z_i]^T$ and R_{i-j} is the norm of the distance between the bodies i and j :

$$\begin{aligned}\ddot{\vec{\mathbf{R}}}_1 &= -Gm_2 \frac{(\vec{\mathbf{R}}_1 - \vec{\mathbf{R}}_2)}{R_{2-1}^3} - Gm_3 \frac{(\vec{\mathbf{R}}_1 - \vec{\mathbf{R}}_3)}{R_{3-1}^3}; \\ \ddot{\vec{\mathbf{R}}}_2 &= -Gm_1 \frac{(\vec{\mathbf{R}}_2 - \vec{\mathbf{R}}_1)}{R_{1-2}^3} - Gm_3 \frac{(\vec{\mathbf{R}}_2 - \vec{\mathbf{R}}_3)}{R_{3-2}^3}; \\ \ddot{\vec{\mathbf{R}}}_3 &= -Gm_1 \frac{(\vec{\mathbf{R}}_3 - \vec{\mathbf{R}}_1)}{R_{1-3}^3} - Gm_2 \frac{(\vec{\mathbf{R}}_3 - \vec{\mathbf{R}}_2)}{R_{2-3}^3};\end{aligned}\tag{2.13}$$

To apply the restricted hypothesis, the moving mass m_3 has to be much smaller than the other two, the *primaries* m_1 and m_2 : $m_3 \ll (m_1, m_2)$ ^[13]. Moreover, also the two primaries have different masses, although both much larger than the test particle. This hypothesis ($m_3 = 0$) causes the last term on the right hand side in the first two equations to vanish, resulting in the decoupling of the motion of the two primaries^[13].

This model is intended to study the behavior of a test particle moving in the gravity field of a very massive body, m_1 , but perturbed by another attractor, m_2 , that is not the main attractor but an additional gravitational perturbation. This means that we are considering a situation where: $m_1 > m_2 \gg m_3$.

The decoupling of the motion of the primaries is the natural result of the restricted hypothesis, since in this way the motion of the two massive bodies obeys to the Keplerian model and it is completely predictable. What we are interested in is the last equation of Eq. (2.13) describing the motion of the massless body under the gravitational fields of the two primaries. This equation houses in itself the essence of the *Restricted Three Body Model*^[13].

As it is, the last vectorial equation in Eq. (2.13) is time dependent as the distances of m_3 from the primaries are function of the time^[11]: $\vec{\mathbf{R}}_1 = \vec{\mathbf{R}}_1(t)$ and $\vec{\mathbf{R}}_2 = \vec{\mathbf{R}}_2(t)$.

Given a couple of rotating objects, it is always convenient to study the motion in a reference frame rotating with the two objects so that these appear

at rest. Of course, this is straightforward only when the primaries are moving in circular orbits, as in this case the angular velocity is constant. Otherwise (like in the Elliptic Restricted Three Body Problem) the rotating frame have to be pulsating, i.e. with an angular velocity variable as function of the radius along an ellipse (this makes the resulting model non-autonomous even in a rotating frame).

For this reason the easiest assumption, among all the possible conic paths the two primaries have to follow, is that these bodies are moving along circular orbits around their common center of mass. The resulting model is the *Circular Restricted Three Body Model* (CR3BP), also known in its planar version, assuming the three bodies moving in the same plane (PCR3BP)^[13].

The first obvious question is if such a problem is integrable. The natural approach, following the already mentioned Liouville theorem on integrable systems, is to search for first integrals of the problem^[17]. To briefly follow this approach a short excursion into the integrability of a dynamical system is mandatory (cfr. also Sec. 2.4).

A dynamical (Hamiltonian) system results *Liouville Integrable* (or *Completely Integrable*) on the domain $B \subset \mathbb{R}^{2n}$ if there exists a canonical diffeomorphism $\omega : B \rightarrow D \times \mathbb{T}^n$, where $D \subset \mathbb{R}^n$ and \mathbb{T}^n is a n -dimensional torus, such that the transformed Hamiltonian $\tilde{H} = H \circ \omega^{-1}$ does not depend on the Angles: $\tilde{H}(I, \Theta) = K(I)$ ^[25]. Here K is a generic function $K : D \rightarrow \mathbb{R}$ and (I, Θ) are the *Action-Angle variables* (cfr. also Sec. 3.2.2). Thus, the system is integrable if it can be transformed into a new canonical coordinates⁴ system where it depends only upon the new momenta, I ^[18].

If these new momenta are everywhere independent and the energy surfaces compact, it is possible to choose the conjugate variables of the momenta (like \mathbf{p} is the conjugate of \mathbf{q}), Θ , as periodic in the range $[0, 2\pi]$ ^[25]. These are the Action-Angle variables. Considering these variables, the dynamical system can be written as:

$$\begin{aligned} \dot{I} &= 0 \quad \Rightarrow \quad I = \text{const} \\ \dot{\Theta} &= \frac{\partial H}{\partial I} = \Omega(I) \end{aligned} \tag{2.14}$$

In other words, if a system can be posed in Action-Angle variables it is integrable (in the Arnol'd sense)^[25]. This means that an integrable Hamiltonian system in Action-Angle variables depends only on the Actions: $H(\Theta, I) = H_0(I)$. For any integrable system the motion takes place on n -dimensional

⁴A Canonical Transformation is a change of coordinates that preserves the Hamiltonian form of the dynamical equations, although it might not preserve the Hamiltonian. Actually it preserves the Poisson brackets.

tori with $I = \text{const}$, and the orbits wind around these tori with frequencies $\Omega(I)$ depending on the specific torus. When the frequency is not resonant, i.e. does not exist any integer vector m such that $m \cdot \Omega = 0, \Omega \neq 0$, then the motion is dense on the torus. In this situation, in fact, the trajectories wind on the torus without repeat the same track^[16].

A *quasi-integrable* Hamiltonian system^[26] is a system with Hamiltonian in the form: $H(\Theta, I) = H_0(I) + \varepsilon H_1(\Theta, I) + \dots$. Where ε is the small perturbative parameter and H_1 is again a Hamiltonian depending periodically on the Angles. The CR3BP can be stated as a quasi-integrable system^[26], where the perturbation is due to the smaller primary that perturbs an exactly Keplerian motion due to the larger one⁵ (cfr. Sec. 3.2.2).

To investigate about the integrability of a quasi-integrable system, the idea is to search for a sequence of canonical transformations close to the identity that makes also H_1 independent of the Angles, at least up to a given order in ε ^[25]. In this way, at the second ε order, the new Hamiltonian would read: $H(\Theta, I) = H_0(I) + \varepsilon \tilde{H}_1(I) + \varepsilon^2 \tilde{H}_2(\Theta, I) + \dots$ with \tilde{H}_1 of the order of the unit, usually given by the average of H_1 over the Angles. When this operation is successful up to a given ε order, the part of the new Hamiltonian depending only on the Actions is the integrable approximation of the dynamics up to that ε order^[27].

In principle this approach can be iterated up to any ε order; however, Poincaré proved^[27] that if H_0 is not degenerate ($\det \partial^2 H_0(I) / \partial I^2 \neq 0$) and H_1 can be expanded in Fourier series with a finite number of vanishing coefficients, then the Hamiltonian system is not integrable^[26]. This actually means that, in general, the convergence radius of the series shrinks down for increasing ε order.

This is due to the fact that H_1 can be posed as function of the only Actions only if the $\Omega(I)$ are non-resonant. The resonance, or near resonance, conditions reflect in the occurrence of denominators, in the series coefficients, that are proportional to the resonance conditions. This means that can arise (and accumulate during the series development) denominators that become closer and closer to zero as the frequencies tend to be rational dependent. This is the well known problem of small denominators that creates topologically distinct regions of the motion^{[15][25]}.

The non convergence of the Fourier series is the case of the CR3BP that results non integrable, neither in its planar version. In the sense that does not exist any other first integral functionally independent of the Hamilto-

⁵This is not true for the degenerate case when m_2 is negligible. This is the Keplerian situation and the model is an integrable Hamiltonian system since the Hamiltonian turns out to be dependent only on one Action.

nian. So, also for this relatively simple model, it is not possible neither solve the equations of motion nor completely describe the general behavior of the solutions.

However it has to be mentioned that Sundmann^[28], in the early nineties, proved that actually exists a solution of the restricted three body problem exploiting a uniformly converging infinite series of powers of $t^{1/3}$. The solution holds in the whole plane, once singularities are removed through the regularization process, since the radius of convergence is affected by the distance to the nearest singularity. This result is not in contradiction with what Poincaré stated since it uses not “Weierstrass-kind series” (the ones normally used in celestial mechanics), but extremely slowly converging series^[28]. To have a sufficient accuracy with this method a number of coefficient of the order 10^{800000} must be used making this approach, outstanding from a theoretical point of view, useless in any practical application^[13].

2.2.1 Synodic, Non Dimensional Reference System

Thus, the motion of the massless body is studied in a rotating frame where m_1 and m_2 appear at rest. This rotating (*synodic*)^[13] frame is centered in the center of mass of the two primaries that lie along the x -axis and is rotating with constant angular velocity around the z -axis of the system, parallel to the angular momentum vector of the two primaries.

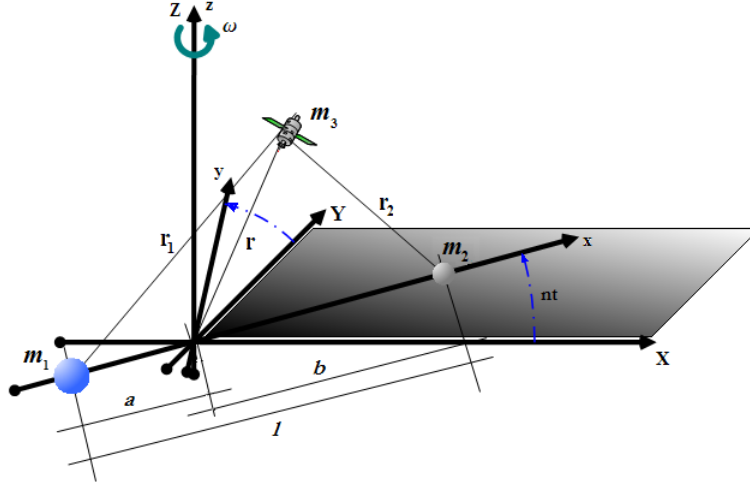


Figure 2.1: Inertial and synodic barycentric frames.

In this reference system, in order to have a circular motion for the primaries around the common center of mass, there have to be a balancing

between gravitational and centrifugal forces. The centrifugal forces depend on the distances of the primaries from the center of mass, while the gravity is function of the product of the two masses and the total distance between them. Using the Gauss formulation for the gravitational law⁶ and naming the distances according to Fig. 2.1:

$$k^2 \frac{m_1 m_2}{l^2} = m_2 a n^2 = m_1 b n^2 \rightarrow \begin{cases} k^2 m_1 = a n^2 l \\ k^2 m_2 = b n^2 l \\ k^2 (m_1 + m_2) = n^2 l^3 \end{cases} \quad (2.15)$$

where $k = \sqrt{G}$ (when G is expressed in proper units) is the gaussian gravity constant and n is the orbital mean motion.

A suitable set of units can be chosen in order to simplify the problem in this reference frame^[13]. Defining a proper system of units, the angular velocity of the primaries ω (or, equivalently n) and consequently the one of the reference frame, can be chosen unitary. Such a system of units is defined by:

- the distance between the primaries as Unit of Distance [$DU = d_{m_1-m_2}$];
- the sum of the primaries masses as Unit of Mass [$MU = m_1 + m_2$];
- the angular velocity of the primaries equal to one. This results in a Unit of Time [TU] such that the period of revolution around the center of mass is 2π .

This means that $\omega = 1$, $n = 1$ and $G = 1$ (or, equivalently $k = 1$). Accordingly, from Eq. (2.15), also the positions of the primaries along the x -axis result defined in inverse proportion to their masses (in MU): $a = m_1$ and $b = m_2$.

Since the sum of the masses is unitary, the *mass parameter* of the system is simply defined as the non dimensional mass of the small primary^[13]:

$$\mu = \frac{m_2}{m_1 + m_2} \quad (2.16)$$

This gives $m_2 = \mu$, the mass of the small primary in non dimensional units and, analogously, $m_1 = 1 - \mu$ from the definition of MU. The value of μ ranges from 0, if the small primary can be neglected and resulting the two body model, to 1/2 if the two masses are equal.

⁶It was introduced by Gauss in his work *Theoria motus corporum coelestium in sectionibus conicis solem ambientum* in the 1800 where he developed the methods of the Least Squares to predict the orbits of Ceres using three complete observations of G. Piazzi.

This parameter is sufficient to univocally characterize a CR3BP model using the equivalence between masses and positions given by: $a = \mu$ and $b = 1 - \mu$. Only the convention about the location of the small primary along the positive or negative x -axis direction has to be added. If not differently stated, m_2 is assumed to lie on the positive side of the x -axis in this work, like in Fig. 2.2.

2.2.2 Equations of Motion

The aim is to study the motion of m_3 in the CR3BP rotating system, so the equations of motion have to be derived in such a frame where the coordinates are identified by $\vec{\mathbf{r}} = [x, y, z]^T$ and the dotted are the corresponding non dimensional time derivatives.

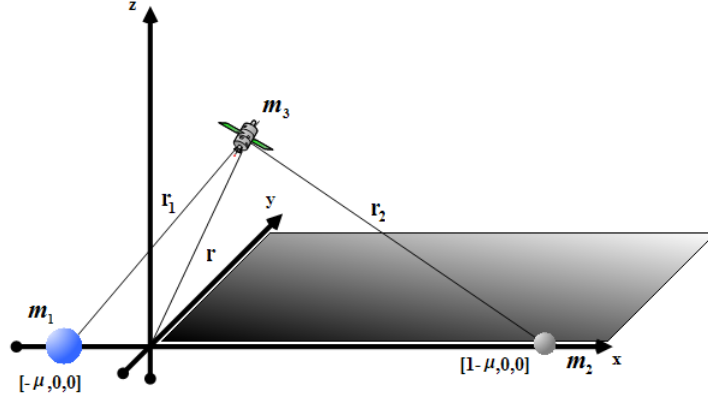


Figure 2.2: CR3BP synodic barycentric reference frame.

The rotation of the reference system introduces in the equations of motion two terms of apparent forces: the centrifugal and the Coriolis one. In rotating coordinates, the third of Eq. (2.13) reads^[13]:

$$\frac{d^2 \vec{\mathbf{r}}}{dt^2} + \underbrace{2\omega \wedge \frac{d\vec{\mathbf{r}}}{dt}}_{\text{Coriolis Force}} + \underbrace{\omega \wedge (\omega \wedge \vec{\mathbf{r}})}_{\text{Centrifugal Force}} + Gm_1 \frac{\vec{\mathbf{r}} - \vec{\mathbf{r}}_1}{\|\vec{\mathbf{r}} - \vec{\mathbf{r}}_1\|^3} + Gm_2 \frac{\vec{\mathbf{r}} - \vec{\mathbf{r}}_2}{\|\vec{\mathbf{r}} - \vec{\mathbf{r}}_2\|^3} = 0 \quad (2.17)$$

here $\vec{\mathbf{r}}$ denotes the distance of the infinitesimal mass, or of the primaries if with subscript, relative to the center of the rotating frame.

With the convention chosen for the units and for the frame, the two primaries are located in: $\vec{\mathbf{r}}_1 = [-a, 0, 0]^T = [-\mu, 0, 0]^T$ and $\vec{\mathbf{r}}_2 = [b, 0, 0]^T = [1 - \mu, 0, 0]^T$, see Fig. 2.2.

The distances of m_3 from the two primaries are, indeed^[13]:

$$\begin{aligned} r_1^2 &= (x + \mu)^2 + y^2 + z^2 \\ r_2^2 &= [x - (1 - \mu)]^2 + y^2 + z^2 \end{aligned} \quad (2.18)$$

Replacing these distances, and all the quantities in non dimensional units, in Eq. (2.17), it reads by components:

$$\begin{aligned} \ddot{x} - 2\dot{y} - x &= -(1 - \mu) \frac{x - x_1}{r_1^3} - \mu \frac{x - x_2}{r_2^3} \\ \ddot{y} + 2\dot{x} - y &= -(1 - \mu) \frac{y}{r_1^3} - \mu \frac{y}{r_2^3} \\ \ddot{z} &= -(1 - \mu) \frac{z}{r_1^3} - \mu \frac{z}{r_2^3} \end{aligned} \quad (2.19)$$

It is worth nothing that the last equation does not present any trace of the rotation of the frame, since the z -axis is also the spin axis. This results in the decoupling of the out-of-plane motion.

The synodic frame preserves also the potential nature of the gravity law. So, the equations of motion can still be expressed by means of a potential function^[13]. Indeed, the gravity potential, Eq. (2.2), has to be slightly modified to include also the centrifugal force:

$$\Omega(x, y, z) = -\frac{1}{2} (x^2 + y^2) - \frac{(1 - \mu)}{r_1} - \frac{\mu}{r_2} - \frac{1}{2} \mu (1 - \mu) \quad (2.20)$$

Here the first term results from the centrifugal force, the second and the third ones are the effect of the gravitational potentials of m_1 and m_2 and the last one is just a constant offset^[29]. Thus, the right hand side of the system (2.2.2) can be replaced by the derivatives of this potential with respect to the proper coordinate.

The plot of this potential function, also called the *Effective Potential* or the *Modified Potential* is represented in Fig. 2.3 where the two “wells” are due to the two primaries and extend in direct relation with their masses.

This system allows only the energy integral, given by the sum of kinetic and potential energy. However, due to the rotation of the reference system, also a centrifugal part is taken into account, resulting in the energy integral in the rotating frame:

$$E(x, y, z, \dot{x}, \dot{y}, \dot{z}) = \frac{1}{2} (\dot{x}^2 + \dot{y}^2 + \dot{z}^2) + \Omega(x, y, z) \quad (2.21)$$

It is extremely interesting to observe, and is also used later on to describe special orbits enabled by this model, that these equations show also some symmetries^[13]:

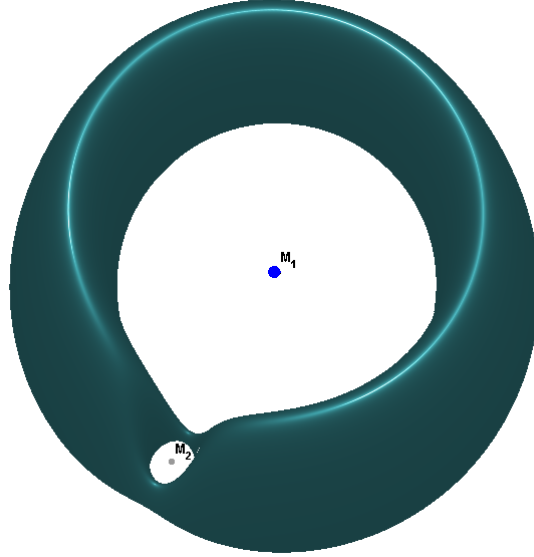


Figure 2.3: Effective Potential for the Earth-Moon system.

- with respect to the x - y plane: $[x(t), y(t), z(t)] \rightarrow [x(t), y(t), -z(t)]$;
- with respect to the x - z plane and negative times: $[x(t), y(t), z(t)] \rightarrow [x(-t), -y(-t), z(-t)]$;
- replacing μ with $1-\mu$: $[x(t), y(t), z(t), \mu] \rightarrow [-x(t), -y(t), z(t), 1-\mu]$.

So far, we derived the equations of motion of the CR3BP by means of a series of assumptions, changes of coordinates and units from the N -body problem. There are, however, at least another couple of approaches that is worth to underline.

Lagrangian Approach

The motion of a point under a given force field from one point to another has to maintain stationary the *Lagrangian* of the system. This statement is expressed by the well known *Euler-Lagrange Equations*, that for a generic Lagrangian L and generic generalized coordinates \vec{q}_i read^[13]:

$$\frac{d}{dt} \frac{\partial L}{\partial \dot{\vec{q}}_i} = \frac{\partial L}{\partial \vec{q}_i} \quad i = 1, 2, \dots, n \quad (2.22)$$

The Lagrangian is just another expression of the energy of the system given by the difference between kinetic and potential energy. The expression

of these two quantities in an inertial frame is^[14]:

$$\mathfrak{L}(\vec{\mathbf{R}}, \dot{\vec{\mathbf{R}}}) = \underbrace{\frac{1}{2} (\dot{X}^2 + \dot{Y}^2 + \dot{Z}^2)}_{\text{Kinetic term}} + \underbrace{\frac{1-\mu}{R_1} + \frac{\mu}{R_2} + \frac{1}{2}\mu(1-\mu)}_{\text{Potential term}} \quad (2.23)$$

with $R_1^2 = [X + \mu \cos t]^2 + [Y + \mu \sin t]^2 + Z^2$ and $R_2^2 = [X - (1-\mu) \cos t]^2 + [Y - (1-\mu) \sin t]^2 + Z^2$ the distances of m_3 from the two moving primaries.

Since the Euler-Lagrange Equations are invariant under coordinate transformations, it is possible to replace the expression of \mathfrak{L} in rotating coordinate by means of the transformation^[14]:

$$\begin{pmatrix} X \\ Y \\ Z \end{pmatrix} = A_t \cdot \begin{pmatrix} x \\ y \\ z \end{pmatrix}; \quad \begin{pmatrix} \dot{X} \\ \dot{Y} \\ \dot{Z} \end{pmatrix} = A_t \cdot \begin{pmatrix} \dot{x} - y \\ \dot{y} + x \\ \dot{z} \end{pmatrix} \quad (2.24)$$

where A_t is the time dependent transformation matrix representing the rotation around the z -axis, given by:

$$A_t = \begin{pmatrix} \cos t & -\sin t & 0 \\ \sin t & \cos t & 0 \\ 0 & 0 & 1 \end{pmatrix} \quad (2.25)$$

Applying this transformation, the Lagrangian takes the form:

$$L(\vec{\mathbf{r}}, \dot{\vec{\mathbf{r}}}) = \underbrace{\frac{1}{2} [(\dot{x} - y)^2 + (\dot{y} + x)^2 + \dot{z}^2]}_{\text{Kinetic term}} + \underbrace{\frac{1-\mu}{r_1} + \frac{\mu}{r_2} + \frac{1}{2}\mu(1-\mu)}_{\text{Potential term}} \quad (2.26)$$

where the time dependent distances between m_3 and the two primaries in Eq. (2.23) are replaced by the time independent distances of Eq. (2.18).

Specifying the Euler-Lagrange equations, Eq. (2.22), with this expression of the Lagrangian, Eq. (2.26), it is possible to write down the equations of motion in compact form as:

$$\begin{aligned} \ddot{x} - 2\dot{y} &= -\Omega_x \\ \ddot{y} + 2\dot{x} &= -\Omega_y \\ \ddot{z} &= -\Omega_z \end{aligned} \quad (2.27)$$

where the subscripts indicate derivatives and the potential, including both a centrifugal and a potential part, is the same of Eq. (2.20), the Effective Potential. The expression obtained for the equations of motion is exactly the same of the system (2.2.2), demonstrating the equivalence of the two approaches.

Hamiltonian Approach

Another equivalent and powerful way to derive the equations of motion for the CR3BP is following the same Hamiltonian approach like for the N -body problem^[12] (cfr. Sec. 2.1).

The partial derivatives of the Lagrangian with respect to the derivatives of the generalized positions (\vec{q}_i) are the conjugate momenta \vec{p}_i of the test particle. This is the *Legendre Transformation*^[16] expressed by: $\vec{p}_i = \partial L / \partial \dot{\vec{q}}_i$. Whenever known the Lagrangian of the problem, by means of this transformation, the Hamiltonian can be obtained by: $H(\vec{q}_i, \vec{p}_i) = \sum_{i=1}^3 \vec{p}_i \dot{\vec{q}}_i - L(\vec{q}_i, \vec{p}_i)$.

Restricting to the motion of m_3 , the generalized coordinates are, in this case, the position coordinates in the rotating frame: $\vec{q}_3 = \vec{r} = [x, y, z]^T$, while the conjugate momenta play the role of the velocities of the massless body: $\vec{p}_3 = \vec{p}_3(\vec{r}, \dot{\vec{r}})$.

Thus, the Hamiltonian (that represents, like L , just another expressions of the total energy) for the moving body can be expressed as:

$$H(\vec{q}_3, \vec{p}_3) = \frac{1}{2} \left[(p_x + y)^2 + (p_y - x)^2 + p_z^2 \right] + \Omega(x, y, z) \quad (2.28)$$

Once the expression of the Hamiltonian is known, the canonical equations (Eq. (2.6)) give the equations of motion by means of simple derivatives:

$$\begin{aligned} \dot{x} &= \frac{\partial H}{\partial p_x} = p_x + y & \dot{p}_x &= -\frac{\partial H}{\partial x} = p_y - x - \Omega_x \\ \dot{y} &= \frac{\partial H}{\partial p_y} = p_y - x & \dot{p}_y &= -\frac{\partial H}{\partial y} = -p_x - y - \Omega_y \\ \dot{z} &= \frac{\partial H}{\partial p_z} = p_z & \dot{p}_z &= -\frac{\partial H}{\partial z} = -\Omega_z \end{aligned} \quad (2.29)$$

All the three approaches are equivalent and lead to autonomous equations of motion in the rotating frame defining equivalent six dimensional phase spaces.

2.2.3 The Integral of the Motion

The total energy is an integral of the motion for any newtonian system, and also the Lagrangian and the Hamiltonian are integrals of motion for the relevant formulation. The invariance of the Hamiltonian can be easily checked by means of its time derivative, Eq. (2.7). Let us compute now the following time derivative:

$$\frac{1}{2} \frac{d}{dt} (\dot{x}^2 + \dot{y}^2 + \dot{z}^2) = \dot{x} (2\dot{y} - \Omega_x) + \dot{y} (-2\dot{x} - \Omega_y) + \dot{z} (-\Omega_z) = \frac{d}{dt} (-\Omega) \quad (2.30)$$

This means that defining J , the so called *Jacobi Integral*, as the sum of $(\dot{x}^2 + \dot{y}^2 + \dot{z}^2)$ and 2Ω , it is possible to obtain a quantity conserved along the motion^[13]. This is the definition of first integral, but it can not be a new integral of the CR3BP as only the total energy is allowed (cfr. Sec. 2.2). There exists, in fact, a relation between J and E (equivalently H in the proper coordinates), Eq. (2.21), given by:

$$J(x, y, z, \dot{x}, \dot{y}, \dot{z}) = -2\Omega(x, y, z) - (\dot{x}^2 + \dot{y}^2 + \dot{z}^2) = -2E \quad (2.31)$$

A very interesting conclusion about the motion of the test particle can be drawn by the relation 2.31. The first term depends only on the position of m_3 relative to the two primaries, while the second part only on the velocity of this massless body. Since the motion of a body is allowed only where its kinetic energy is positive, the regions where $-2\Omega - J < 0$ are forbidden regions. The value of J depends on the initial conditions (zero subscript) that determine both a specific energy value and zones where the motion can take place^[13]. The boundaries of these forbidden regions, the *Hill Regions*, are given by the equality $J(x_0, y_0, z_0, \dot{x}_0, \dot{y}_0, \dot{z}_0) = -2\Omega(x, y, z)$ defining *zero velocity surfaces*. The projections of these curves in the two dimensional position space are the so called *zero velocity curves*. In Fig. 2.4 these curves are represented for the Earth-Moon mass parameter ($\mu = 0.0121506683$) for increasing J values.

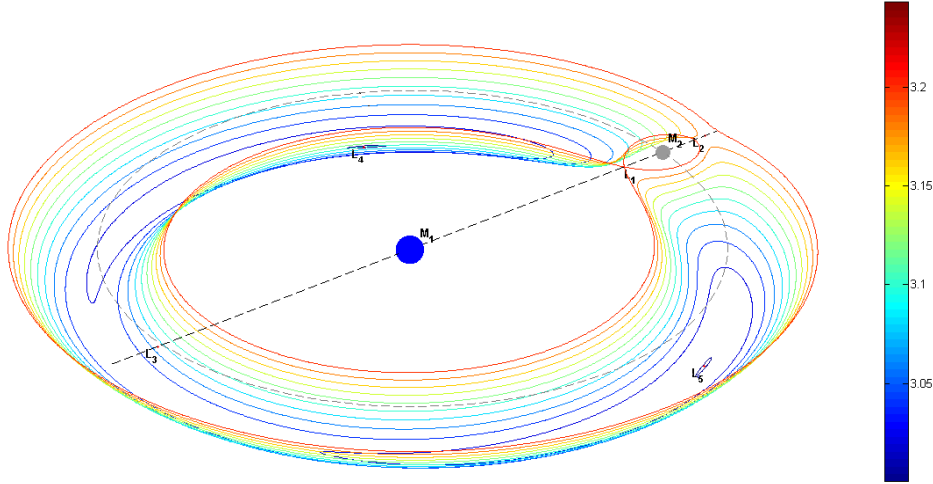


Figure 2.4: Zero velocity curves for increasing energy values for the Earth-Moon system.

The specific value of J actually sticks a specific height on the graph of the Effective Potential, so the zero velocity curves are level sets (isolines)

of this potential function, i.e. slices of the plot of Fig. 2.3. These surfaces represent a sort of barriers through which solutions with a specific value of the Jacobian constant can not pass. This defines also regions, closed or not depending on the initial energy, where the motion is confined.

All the initial conditions are constrained to evolve in the six dimensional phase space, on the five dimensional hypersurface defined by the invariance of the Jacobi integral. This *Manifold* (general term to identify any surface of arbitrary dimensions), embedded in a six dimensional space is defined by:

$$M(\mu, J) = \{[x, y, z, \dot{x}, \dot{y}, \dot{z}] \in \mathbb{R}^6 | J(x, y, z, \dot{x}, \dot{y}, \dot{z}) = J(x_0, y_0, z_0, \dot{x}_0, \dot{y}_0, \dot{z}_0)\} \quad (2.32)$$

where the zero subscript denotes again the initial state.

For the planar case the Jacobi constant define a three dimensional surface embedded in a four dimensional space where the motion is constrained to evolve.

A very important feature of the planar problem that the spatial CR3BP does not have, is the possibility to reduce the flow to a two dimensional map. This can be done by setting a surface of section with a fix coordinate. This coordinate and the three dimensional energy surface reduce the phase space to be two dimensional. Each iteration of the flow from the section to itself produces a first return map completely characterizing the flow. This method has been introduced by Poincaré^[30] to qualitatively study the behavior of a dynamical system and the corresponding sections are often called *Poincaré Sections* (cfr. Sec. 3.3-3.6).

The Jacobi constant, beside its role to identify regions of feasible motion, can be also used to derive a relationship between the osculating orbital parameter of an object before and after a gravitational encounter with a massive one. This results in the *Tisserand Parameter* that has been successfully employed to re-identify comets whose orbits have been heavily deflected by a planet⁷.

Since for $\mu = 0$ the CR3BP reduces to the classical two body model (cfr. Sec. 2.2.1) the phase space is divided by the value of the Keplerian energy, $E_k = -1/(2a)$. When this energy is negative the orbits are bounded

⁷This parameter was introduced by F. F. Tisserand in his work *Traité de mécanique céleste* (1889-1896). It is a re-interpretation of the Jacobi integral that relates the classical orbital parameter before and after a gravitational encounter. It reads:

$$a^{-1} + 2\sqrt{a(1-e^2)}\rho^{-3}\cos(i) = \text{const}$$

where a, e, i are the semi-major axis, eccentricity and inclination and ρ the distance between the primaries. It holds far from the encounter (before and after) and represents an expression to relate the pericenter and the period before and after a gravitational encounter. Thus, it also offers a useful tool to design sequences of gravity assists.

(circular or elliptic), while for zero or positive values the motion is unbounded (parabolic or hyperbolic)^[14]. The initial conditions fix the specific energy value, and the set of all of these energy surfaces *foliate* (like onion layers) the whole phase space, as this is a completely integrable model (cfr. Sec. 2.4).

2.2.4 Libration Points

As for any dynamical system, the left hand side of the equations of motion vanishes only in the stationary (equilibrium) points of the system; i.e. locations where a body placed at rest remains indefinitely.

Form Eq. (2.27), the accelerations are zero when the partial derivatives of the effective potential vanish. This means that the points where the slope of Ω (Fig. 2.3) is horizontal are rest points of the vector field.

In the CR3BP the accelerations vanish in five points^[13], as can be seen in Fig.2.3. Three are collinear with the two primaries and the other two forming an equilateral triangle with them. These *Libration Points* (or *Lagrangian Points* although Euler discovered the first three of them^[23]) are named with $\mathcal{L}_1, \mathcal{L}_2, \mathcal{L}_3$ for the three *collinear* and $\mathcal{L}_4, \mathcal{L}_5$ for the two *equilateral*.

Regardless the planar or spatial version of the model, the equilibrium points are always located in the x - y plane, like in Fig. 2.5.

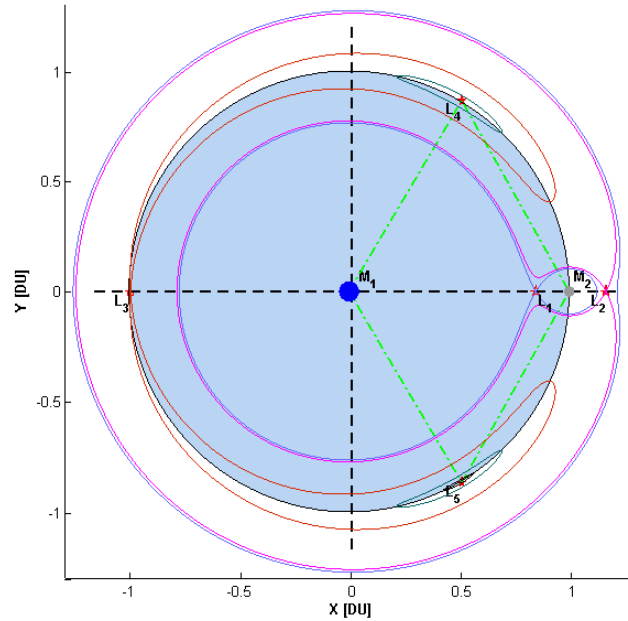


Figure 2.5: Earth-Moon libration point positions in the synodic frame with the zero velocity curves associated to their energy values.

Computing the energies corresponding to these five points from Eq. (2.31), it is possible to see that for all the values of μ , unless $\mu = 0$ where the five energies are equal, $E_{\mathcal{L}_1} < E_{\mathcal{L}_2} < E_{\mathcal{L}_3} < E_{\mathcal{L}_4} = E_{\mathcal{L}_5} = -1.5$, or equivalently, in terms of Jacobi constant, $J_{\mathcal{L}_1} > J_{\mathcal{L}_2} > J_{\mathcal{L}_3} > J_{\mathcal{L}_4} = J_{\mathcal{L}_5} = 3$.

Also the location along the x -axis of the equilibrium points changes with μ as presented in Fig. 2.6. This happens since changing μ means to change the ratio of the two masses and consequently also the locations where the two gravitational influences balance. The black vertical line represents the mass parameter value of the Earth-Moon system, one of the highest μ for a real meaningful system.

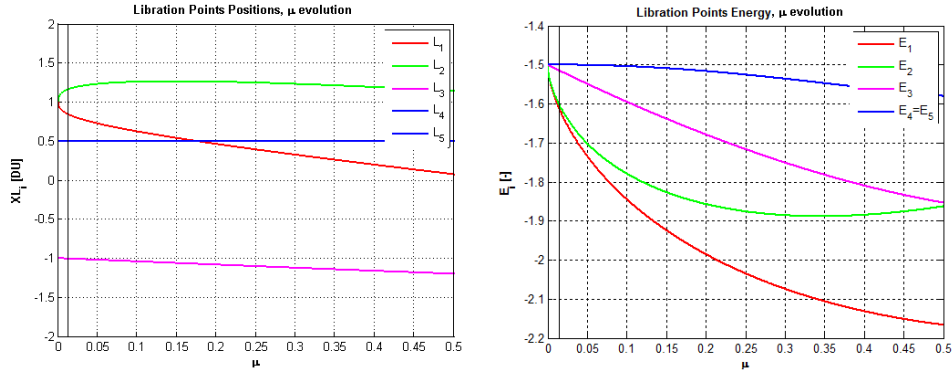


Figure 2.6: Dependence on μ of the x coordinate of the libration points (left) and their energy (right).

Moreover, observing the trend of the zero velocities curves for increasing energy values, it is easy to see the “gate-like” behavior^[14] of the equilibrium points (see also Fig. 2.5 where the zero velocity curves are plotted for the first three libration points energies, and for an energy close to the one of the equilateral points).

With reference to Fig. 2.7, the regions where the motion is allowed (white zones) evolve according to the energy value and this evolution passes through the equilibrium points.

Starting from a situation where orbits around the two primaries can not be connected (upper left plot) and increasing the energy value, indeed, up to $E_{\mathcal{L}_1}$, the closed regions (*Realms*) around m_1 and m_2 connect (upper right plot). Thus a body in orbit around one of the primaries can pass orbiting the other one. Increasing again the energy value also the gate associated to \mathcal{L}_2 opens (lower left plot) and the moving body can now move also in the outer space, far from the primaries. For further increasing values, the gate

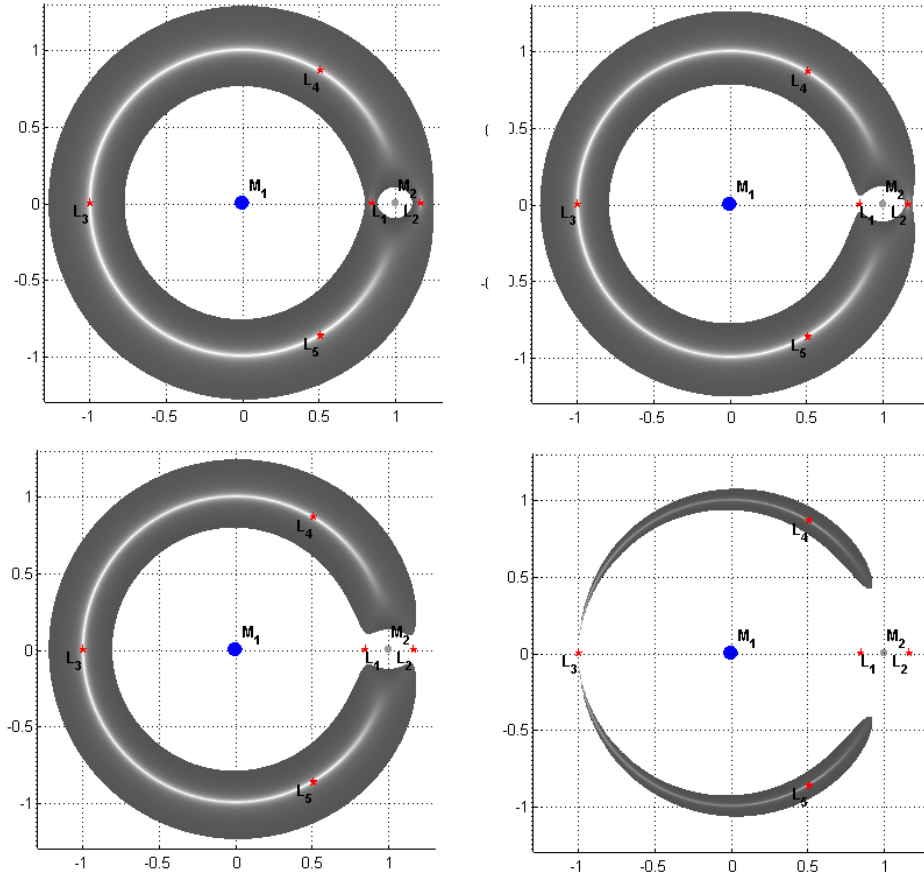


Figure 2.7: Regions allowed for the motion (white) for increasing energy values (from the upper left corner) for the Earth-Moon system.

corresponding to \mathcal{L}_3 (lower right plot) opens, making m_3 free to jump directly from the outer realm to the m_1 realm without passing through the m_2 realm. For even higher energy values, only a narrow region around the equilateral points is forbidden and afterwards, for very high energies, the whole space is allowed for the motion. This results from the fact that \mathcal{L}_4 and \mathcal{L}_5 are the maximum points of the Effective Potential.

Obviously, the most interesting case, from a mission design point of view, is when $J_{\mathcal{L}_2} > J > J_{\mathcal{L}_3}$ because this is the minimum energy configuration allowing the passage among all the three realms. However, if only a transfer between the two primaries is sought, $J_{\mathcal{L}_1} > J > J_{\mathcal{L}_2}$ is sufficient.

These points are stationary solutions in the rotating frame, so there has to

be a balancing between gravitational and centrifugal forces. Thus these points must lie where these two forces equal. The centrifugal force is linear with the distance from the origin of the reference frame, while the gravity changes by means of a parabolic law with the distances from the two primaries, see Fig. 2.8. The intersections of these curves give the location of the equilibria.

Fig. 2.8 holds for the three collinear equilibrium points and it is clear that these points are alternatively placed between the two primaries; the other two are out from the x -axis at equal distances from the two primaries. To exactly locate the collinear points, it is easy to start imposing $y = 0$ in the expression of Ω and check where its first derivative vanishes, since to have stationarity $\ddot{\mathbf{r}} = \ddot{\mathbf{r}} = 0$ has to be satisfied^[14]:

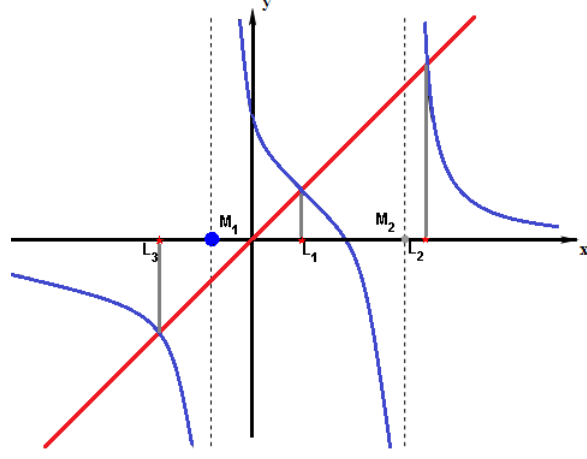


Figure 2.8: Intersection points between the centrifugal (red) and gravitational (blue) force to locate the collinear equilibria.

$$\Omega(x, 0) = -\frac{1}{2}x^2 - \frac{(1-\mu)}{||x+\mu||} - \frac{\mu}{||x-1+\mu||} \Rightarrow$$

$$\frac{d}{dx}\Omega(x, 0) = \delta^5 \mp (3-\mu)\delta^4 + (3-2\mu)\delta^3 - \mu\delta^2 \pm 2\mu\delta - \mu = 0 \quad (2.33)$$

where $\delta = x + 1 - \mu$ is the distance from the small primary (m_2). The second one of Eq. (2.2.4) results in a fifth order equation with three real solutions which are the locations of the collinear points. From the analysis of the signs of the terms of Eq. (2.2.4), it is possible to derive, in another way, that the three real solutions must be located in the intervals $]-\infty, -\mu[$, $]-\mu, 1-\mu[$, $]1-\mu, \infty[$, i.e. spaced out by the primaries.

Numerical solutions have to be sought for the quintic equation, although series expansions are available as function of the Hill radius^[31] ($R_h = (\mu/3)^{1/3}$) which gives a first order approximation of the locations of \mathcal{L}_1 and \mathcal{L}_2 ^[13] (cfr. App. A).

To locate the equilateral points, instead, it is sufficient to compute the derivative Ω_y , equating this to zero and replace the expression in the $\Omega_x = 0$:

$$\frac{d}{dy}\Omega(x, y) = 1 - \frac{1-\mu}{r_1^3} - \frac{\mu}{r_2^3} = 0 \Rightarrow \frac{d}{dx}\Omega(x, y) = \frac{1}{r_1^3} - \frac{1}{r_2^3} = 0 \quad (2.34)$$

In this way $\Omega_x = 0$ implies: $r_1 = r_2$. Replacing this last relation again in $\Omega_y = 0$ results in $r_1 = r_2 = 1$. This means that the two equilibrium points must be located in the intersection of two unitary circumferences centered in the primaries. The points satisfying this relation form an equilateral triangle with the two primaries: $x = -\mu + 1/2$, $y = \pm\sqrt{3}/2$ ^[11].

The derivative of Ω with respect to z is zero if and only if $z = 0$ which assures that the equilibrium points are always in the x - y plane.

To investigate about the stability of the equilibrium points, the sign of the second derivative of the Effective Potential has to be studied. $d^2\Omega(x, 0)/dx^2$ results always concave, demonstrating that the collinear points are unstable for all the values of the mass parameter; this implies a saddle component in the linearized phase space around those points (see Sec. 2.2.5). The same conclusion can be drawn intuitively observing a section of the effective potential, Fig. 2.9, where the “diverging” directions are given by the shape of the potential function^[14].

On the other side, the equilateral points are stable until the mass parameter reaches a critical value^[13] $\mu_{Routh} \simeq 0.0385208965$, also called *Routh critical mass parameter*. Afterwards they destabilize, i.e. for the critical Routh mass parameter they change their linear stability^[32].

The existence of $\mathcal{L}_4/\mathcal{L}_5$ has a special meaning in the Sun-Jupiter system, as there are two set of bodies located in these points. The set anticipating by 60 deg the Jupiter position is named *Greeks*, while the set following *Trojans*. Jupiter orbit is not exactly circular ($ecc_J \approx 0.05$), the actual motion is affected by many perturbations and these bodies might have been captured (with suitable initial conditions), so the actual motion is a slow libration around the exact equilibrium point in tadpole or horseshoe orbits (due to stable nature of \mathcal{L}_4 and \mathcal{L}_5). Trojan-kind bodies have been also found near the equilateral points of Mars, Neptune and Saturn moons. For the Earth-Moon system in these locations only an overabundance of dust (Kordylewski cloud) is present.

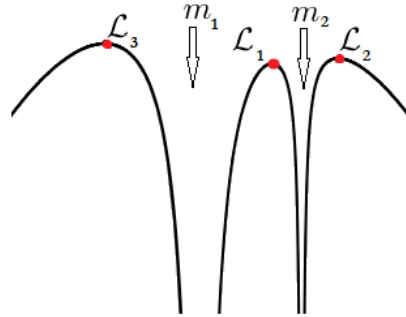


Figure 2.9: $y = 0$ section of the Effective Potential, it shows the concavity of this function in the three collinear equilibrium points.

It is worth noting that the unstable component of \mathcal{L}_3 is much smaller than the one associated with the other two collinear points (since the perturber is much far away) and the natural outcome is that the dynamics leading to/off this point is quite mild^[33].

It is possible to show that there are no new equilibrium points neither in elliptic problem^[13] nor in the Hill problem^[31], a local approximation of the motion near the small primary (see also App. A).

2.2.5 Equilibrium Regions

To study the phase portrait in the neighborhood of a libration point, the first approach is to investigate the linear behavior of the flow. It has been already demonstrated (cfr. Sec. 2.2.4) that the collinear points are unstable, while the triangular ones are stable up to a critical μ value, much larger than any physical meaningful system.

Let us move the origin of the reference frame into the generic $\mathcal{L}_i = [x_0, 0, 0]^T$ collinear equilibrium point and Taylor expand the equations of motion (generically g) up to the first order: $g(x_0 + \delta x) = g(x_0) + \partial g(x)/\partial x|_{x=x_0} \delta x + O(\delta x^2)$. The resulting system of linear differential equations can be written as^[34]:

$$\begin{aligned}\ddot{x} - 2\dot{y} - ax &= 0 \\ \ddot{y} + 2\dot{x} + by &= 0 \\ \ddot{z} + cz &= 0\end{aligned}\tag{2.35}$$

where $a = 1 + 2c$, $b = c - 1$ and $c = \mu/(1 - \mu - x_0)^3 + (1 - \mu)/(\mu + x_0)^3$. In this linearized approach the energy and the Hamiltonian take the forms^[14]:

$$\begin{aligned}E_l &= \frac{1}{2} (\dot{x}^2 + \dot{y}^2 + \dot{z}^2 - ax^2 + by^2 + cz^2) \\ H_l &= \frac{1}{2} [(p_x + y)^2 + (p_y - x)^2 + p_z^2 - ax^2 + by^2 + cz^2]\end{aligned}\tag{2.36}$$

As everything is referred to the libration point, surfaces with $E_l = H_l = 0$ are energy surfaces passing through the equilibria.

Like for the non linear equations of motion, the out-of-plane motion is decoupled from the in-plane one. The last equation of system (2.35) represents a harmonic oscillator and can be analytically solved to define the out-of-plane eigenvalues (or, equivalently, eigenfrequencies): $\lambda_{5,6} = \pm i\omega_z = \pm i\sqrt{c}$.

The x and y components of the in-plane motion are still coupled, but in the linear approximation also these ones can be analytically solved^[13]. To solve this linear system, it is required to write it down in matrix form and compute the characteristic equation $p(\lambda)$. This is a bi-quadratic relation

with four solutions (λ_i with $i = 1, \dots, 4$) that are the eigenvalues of the linear problem. This means:

$$p(\lambda) = \lambda^4 + (2 - c)\lambda^2 + (1 + c - 2c^2) \Rightarrow \begin{aligned} \lambda_{1,2} &= \pm \sqrt{-\beta_1 + \sqrt{\beta_1^2 + \beta_2^2}} \in \mathbb{R} \\ \lambda_{3,4} &= \pm i \sqrt{\beta_1 + \sqrt{\beta_1^2 + \beta_2^2}} \in \mathbb{Z} \end{aligned} \quad (2.37)$$

where $\beta_1 = 2 - c/2$, $\beta_2 = \sqrt{(2c+1)(c-1)}$ and the first subscript is intended to be the positive root. Since, for the instability, it is sufficient that at least one of the eigenvalues has a positive real part (time diverging forward in time), this leads to the same conclusion that the collinear libration points are unstable^{[13][14]}.

Moreover, exploiting in this linear approach the behavior of the eigenvectors, the whole phase space can be characterized around a collinear libration point^[35]. Indeed the general solution of the linear system (2.35) can be expressed as:

$$\begin{aligned} x(t) &= A_1 e^{\lambda t} + A_2 e^{-\lambda t} + A_3 \cos \omega t + A_4 \sin \omega t \\ &= A_1 e^{\lambda t} + A_2 e^{-\lambda t} + A_x \cos(\omega t + \varphi) \\ y(t) &= -k_1 A_1 e^{\lambda t} + k_1 A_2 e^{-\lambda t} - k_2 A_3 \sin \omega t + k_2 A_4 \cos \omega t \\ &= -k_1 A_1 e^{\lambda t} + k_1 A_2 e^{-\lambda t} - k_2 A_x \sin(\omega t + \varphi) \\ z(t) &= A_5 \cos \nu t + A_6 \sin \nu t \\ &= A_z \cos(\nu t + \psi) \end{aligned} \quad (2.38)$$

where $\lambda = \lambda_1$, $\omega = \lambda_3$, $\nu = \lambda_5$, $A_i (i = 1, \dots, 6)$ are arbitrary constants (actually amplitudes related to the initial conditions) and the two constants are $k_1 = (2c+1 - \lambda_1^2)/2\lambda_1$ and $k_2 = (2c+1 + \lambda_3^2)/2\lambda_3$. The second equalities in the system (2.38) are only a rewriting of the oscillatory parts in terms of planar (A_x, φ) and orthogonal (A_z, ψ) amplitudes and phases.

It is easy to see that, if the aim is to find only periodic solutions, the amplitudes related to the exponential terms have to be taken equal to zero. This results in a set of $[x(t), y(t), z(t)]^T$ harmonic functions depending only on amplitudes and phases^[34]. On the other hand, the component associated with A_1 is the unstable one, as it leads far from the equilibrium point exponentially fast, and the one associated with A_2 is the stable one.

As the out-of-plane motion is still decoupled, to have an exactly three dimensional periodic solution the eigenfrequencies ω and ν should be equal, otherwise quasi-periodic motion results. This is not the general case, so to find such a kind of solutions non linear terms must be involved in order to use their contribution to obtain this eigenfrequencies matching.

In brief, Eq. (2.38) underlines the typical behavior in a neighborhood of a collinear libration point^[35]. It is given by the combination of two periodic motions, one outside the x - y plane and the other one living in this plane, together with an aperiodic component exponentially diverging forward and backward in time^[34]. This is expressed by the product *center* \times *center* \times *saddle*.

Of course, a clever selection of the initial conditions leads to select only some constants, A_i , and results in specific periodic or aperiodic motions. This is the core idea exploited to generate specific kinds of motion (Sec. 3.1-3.2).

To understand the phase space around the collinear libration points from a topological point of view, it is interesting to approach the problem by means of another change of coordinates. Let us define a new reference frame centered into the generic collinear libration point with the eigenvalues as axes^[34]. The linearized canonical equations of motion take a very easy form:

$$\begin{aligned} \dot{q}_1 &= \lambda q_1 & \dot{p}_1 &= -\lambda p_1 \\ \dot{q}_2 &= \omega p_2 & \dot{p}_2 &= -\omega q_2 \\ \dot{q}_3 &= \nu p_3 & \dot{p}_3 &= -\nu q_3 \end{aligned} \quad (2.39)$$

Such a system is again analytically solvable and the same centers and saddle behaviors can be identified. The general solutions of Eq. (2.39) are:

$$\begin{aligned} q_1(t) &= q_1^0 e^{\lambda t} \\ p_1(t) &= p_1^0 e^{-\lambda t} \\ q_2(t) + ip_2(t) &= (q_2^0 + ip_2^0) e^{-i\omega t} \\ q_3(t) + ip_3(t) &= (q_3^0 + ip_3^0) e^{-i\nu t} \end{aligned} \quad (2.40)$$

where 0 refers to the initial conditions. The decoupled q_1, p_1 equations represent the exponential motion, while the complex conjugate variables q_2, p_2 and q_3, p_3 are the periodic in-plane and out-of-plane harmonic oscillators, with eigenfrequencies ω and ν .

In this reference system the first integral, Eq. (2.36), takes the form:

$$E_l = \lambda q_1 p_1 + \frac{\omega}{2} (q_2^2 + p_2^2) + \frac{\nu}{2} (q_3^2 + p_3^2) \quad (2.41)$$

and it must remain constant ($E_l = \varepsilon > 0$) during the motion. Moreover, in this linear version, also the single elements involved in the definition of E_l are locally constant quantities⁸.

The already mentioned *center* \times *center* \times *saddle* behavior is topologically understandable looking separately at the p_i - q_i planes, like in Fig. 2.10.

⁸Let us consider an autonomous Hamiltonian system with three degrees of freedom

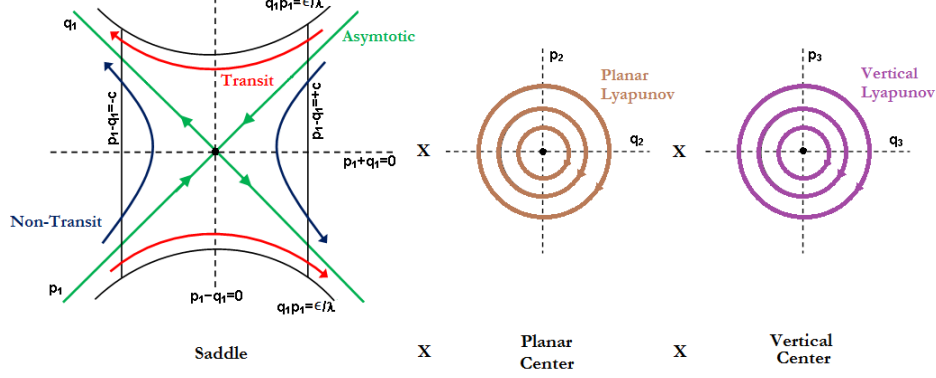


Figure 2.10: *center x center x saddle* behavior of the flow in the neighborhood of a collinear equilibrium point.

To define the region of validity of the linear approximation, an *Equilibrium Region* have to be defined around the generic collinear lagrangian point^[34] such that the particle can not move more than a constant $c > 0$ far away from the center point. In the eigenvectors referred frame this results in $|p_1 - q_1| < c$, as the center components define bounded orbits (circles in the proper plane) like in Fig. 2.10. The boundaries of the Equilibrium Region are defined by the outermost hyperbola (depending on the energy value ϵ): $q_1 p_1 = \epsilon/\lambda$, given by the saddle directions, while the two other sides are given by the segments $p_1 - q_1 = \pm c$, the maximum distance allowed to bound this region^[35].

Thus, this Equilibrium Region is homeomorphic to the product of a four dimensional spherical surface, resulting from the linear energy conservation Eq. (2.41), and an interval, i.e.^[14]:

$$\frac{\lambda}{4}(p_1 + q_1)^2 + \frac{\omega}{2}(p_2^2 + q_2^2) + \frac{\nu}{2}(p_3^2 + q_3^2) = \epsilon + \frac{\lambda}{4}(p_1 - q_1)^2 \quad \text{x} \quad |p_1 - q_1| \leq c \quad (2.42)$$

Each point in the q_1 - p_1 plane corresponds to a circle of given radius in the other planes (actually a three dimensional spherical surface in the Equilibrium Region given by $\omega/2 (q_2^2 + p_2^2) + \nu/2 (q_3^2 + p_3^2) = \epsilon - \lambda q_1 p_1$).

where there exists a non-degenerate equilibrium point with a hyperbolic component. The linearized equations read like Eq. (2.40) and are obtained considering only the second order terms in H . The *Moser Theorem*^[14] states that, beside H , these equations admit also the product of the saddle components $p_1 q_1$ and the square of the norm of the center ones $|z_{2/3}|^2 = p_{2/3}^2 + q_{2/3}^2$ as integrals of motion. The non linear equations admit analogous *local* integrals, i.e. there exist power series beginning with $p_1 q_1$ and $p_{2/3}^2 + q_{2/3}^2$ converging in some neighborhood of the equilibrium point. A special case is the Conley formulation where the center variables are complex^[35].

Since $p_1 q_1$ is a local integral of the motion in this region (element of Eq. (2.41) and cfr. also Sec. 3.2.2), the motion in this plane describes hyperbolic paths: $p_1 q_1 = \text{const}$. If such a constant is positive the branches are able to move from a distance c on one side of the origin to the same distance on the other side^[35]. It is clear, since now, that these are the only kinds of orbits able to cross the Equilibrium Region. If this constant is less than zero the branches start and end on the same side of the equilibrium point^[14], so they can not cross the region, see Fig. 2.10.

The center point of the q_1 - p_1 plane represents completely harmonic solutions, this corresponds to the situation $\omega/2 (q_2^2 + p_2^2) + \nu/2 (q_3^2 + p_3^2) = \epsilon$ which is homeomorphic to a three dimensional spherical surface of periodic and quasi-periodic (bounded) orbits. The saddle component is zero and it is the case when $A_1 = A_2 = 0$ in Eq. (2.38), in this situation three scenarios are possible^[35].

If $A_x \neq 0$ and $A_z = 0$ the point is the center also of the q_3 - p_3 plane and the motion is confined to be periodic in the q_2 - p_2 plane. These are the well know *Planar Lyapunov Orbits*^[13].

The other possible situation is when $A_x = 0$ and $A_z \neq 0$, with this condition the resulting motion is periodic only in the vertical plane resulting in the *Vertical Lyapunov Orbits*^[36] (figure-eight-shaped).

This is summarized in the well know *Lyapunov's Centre Theorem*^[36] stating that each center in any Hamiltonian system gives rise to a family of periodic solutions with periods tending to the eigenfrequencies of the planar and vertical center (ω, ν) when approaching to the equilibrium point.

Moreover, if at the same time $A_x \neq 0$ and $A_z \neq 0$ the resulting motion is the combination of two harmonic oscillators. The general situation is when ω/ν is irrational, in this case the motion is quasi-periodic, giving rise to the so called *Lissajous Orbits*. A special situation is when the two frequencies are equal; in this case the motion is exactly periodic both in the planar and in the vertical plane. The resulting *Halo Orbits*^[37] are generated when the amplitudes are large enough to allow the non linear terms to produce equal eigenfrequencies.

A completely different situation arises isolating the saddle part; i.e. choosing the initial conditions such that $A_x = A_z = 0$ ^[38]. In this case the motion takes place only in the q_1 - p_1 plane. The *Unstable Manifold* W^u results from $A_1 \neq 0$ and $A_2 = 0$ where the solution is moving far from the center point, while the *Stable Manifold* W^s , when $A_2 \neq 0$ and $A_1 = 0$, points towards the

periodic motion^[38]. These behaviors result from $q_1 p_1 = 0$ so:

$$\begin{aligned} \frac{\nu}{2} (q_2^2 + p_2^2) + \frac{\omega}{2} (q_3^2 + p_3^2) &= \epsilon, & q_1 &= 0 & \text{Stable Manifold} \\ \frac{\nu}{2} (q_2^2 + p_2^2) + \frac{\omega}{2} (q_3^2 + p_3^2) &= \epsilon, & p_1 &= 0 & \text{Unstable Manifold} \end{aligned} \quad (2.43)$$

Thus, each manifold is composed by two branches, a positive and a negative one, depending on the sign of the non zero saddle component, i.e. $W_+^u, q_1 > 0$, $W_-^u, q_1 < 0$, $W_+^s, p_1 > 0$, $W_-^s, p_1 < 0$. The branches defined by the minus subscript flow from left to right in the q_1 - p_1 plane, while the ones with the plus subscript flow from right to left, by convention^[14]. It is worth noting that the manifolds correspond topologically to four cylinders asymptotic to the periodic solution.

Solutions with $q_1 p_1 = \text{const} > 0$ are situations where the cylinders cross the boundary of the two-sphere in the same semi-sphere^[34]. This means that it is possible to have orbits transiting from one region to another of the phase space. This is again the “gate-like” behavior of the collinear equilibrium points reflecting in these *Transit Orbits* through the Equilibrium Region^[38]. This situation is the same resulting from $A_1 A_2 < 0$ in Eq. (2.38).

The last category of solutions is composed by those with $A_1 A_2 > 0$, i.e. $q_1 p_1 = \text{const} < 0$. In this case the orbits can not cross the boundaries of the Equilibrium Region and are trapped in the region where they came from. In this case orbits born around one of the two primaries or in the exterior region can not switch their realm of motion. These are *Non-Transit Orbits*^[38].

In summary, the motion results from the combination of two kinds of dynamic. The center parts generating periodic solutions and the saddle one giving rise to hyperbolic orbits, see Fig. 2.11. There are two kinds of asymptotic orbits tending towards and winding off from the periodic solutions. These orbits lie on tube-like structures, the manifolds, that are asymptotic solutions acting as separatrices between two completely different kinds of motion, both for the planar and the spatial version of the model^[39]. Orbits inside the manifolds are transit orbits, able to cross the Equilibrium Region and move from one realm to another; orbits living outside these structures are confined into one realm, see Fig. 2.11. It is important to observe that the transit orbits have to jump from the interior of the stable to the interior of the unstable manifold; from the stable to the unstable linear subspaces.

From the center components of the solutions (2.40) it is possible to see that, considering $q_i + \iota p_i$ with $i = 2, 3$ a complex number, the change in the argument is proportional to the time required for the mapping to go from the domain to the range, and it is possible to show that this time tends to infinity as the orbit approaches to the manifolds^[14]. This means that orbits

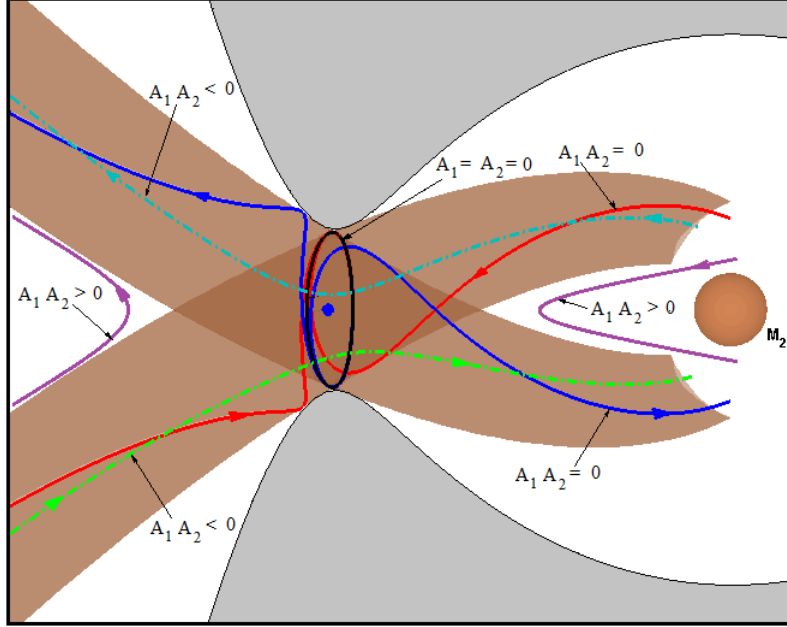


Figure 2.11: Schematic representation of the flow in the Equilibrium Region.

close to the manifolds tend to follow their same dynamics in terms of time and passing/non-passing behavior.

Let us conclude stressing that the whole analysis is based on behavior of the linear subspaces and to actually compute these families the complete CR3BP equations must be propagated.

2.3 Restricted Four Bodies Models

The patched conic approach is the classical way to approximate the motion into a N -body model. This is done by splitting the motion of a massless body into pieces and considering only one attractor at a time. This chain of two body models is patched on surfaces (the Spheres of Influence, similar to the Hill radius^[31]) identified by the order of one gravity acceleration with respect to the other. This model does not represent the real dynamics when the approaching to this “discontinuity” takes place with very low relative velocity. In this case, the moving body spends long times into a region where none of the two gravitational accelerations is dominating.

The CR3BP results enough accurate to study the motion in the space nearby a planet perturbed by its moon (e.g. Earth-Moon), or in the solar system considering only the Sun and Jupiter (99.9% of the whole solar

system mass) or the Sun and another relevant planet. Nevertheless, for a body moving further far away from the planet-moon distance or in regions where additional perturbations drastically change the dynamical regimes, it does not provide an adequate description of the motion. It is clear that the motion of a body orbiting around Earth-Moon \mathcal{L}_2 can not be modeled without taking into account the Sun; any interplanetary path toward the outer planets suffers, at least, from the Jupiter/Saturn gravitational perturbations.

A sort of *Restricted Four Body Model* can be outlined to model the motion of a massless body in the gravity fields of other three massive attractors. A possible approach is the so called *Bi-Circular Model* (BCM)^[14]. In this model the spacecraft motion is studied as in the CR3BP but also the perturbation of an additional attractor, moving in circular motion around the center of mass of the other two primaries, is considered. The motion of the three massive bodies takes place in the same plane.

It is worth noting that this model is non-coherent^[39], i.e. the three primaries does not obey to the Newton gravity law, as the motion of the additional perturber is forced to be circular around the other two, although this can be a quite realistic approximation in many situations.

Furthermore, the presence of an additional attractor sweeps away all the useful features of the CR3BP. Libration points, Jacobi integral, manifolds and Lyapunov/Halo orbits do not exist anymore. The absence of a first integral and of equilibrium points (impossible in non autonomous Hamiltonian systems, like the BCM) changes drastically also the space portrait.

Similarly to the CR3BP, in the BCM the motion is studied in a synodic non dimensional frame in which two of the primaries appear at rest. This frame is depicted on the left of Fig. 2.12^[14].

Differently from the CR3BP the mass parameter μ of the smaller primary is no more sufficient to describe the entire system, also the mass of the perturbing body (m_p) is required. Moreover, the resulting equations of motion are non-autonomous, due to the presence of the additional revolving perturber, also in the synodic frame^[39].

Nevertheless, the equations of motion can be still written with the partial derivatives of a sort of modified effective potential (Ω_4) on the right hand side:

$$\begin{aligned}\ddot{x} - 2\dot{y} &= \partial\Omega_4/\partial x \\ \ddot{y} + 2\dot{x} &= \partial\Omega_4/\partial y \\ \ddot{z} &= \partial\Omega_4/\partial z\end{aligned}\tag{2.44}$$

This modified effective potential (like the one in Eq. (2.20)) takes into account the gravitational attraction of the two main primaries, the centrifugal

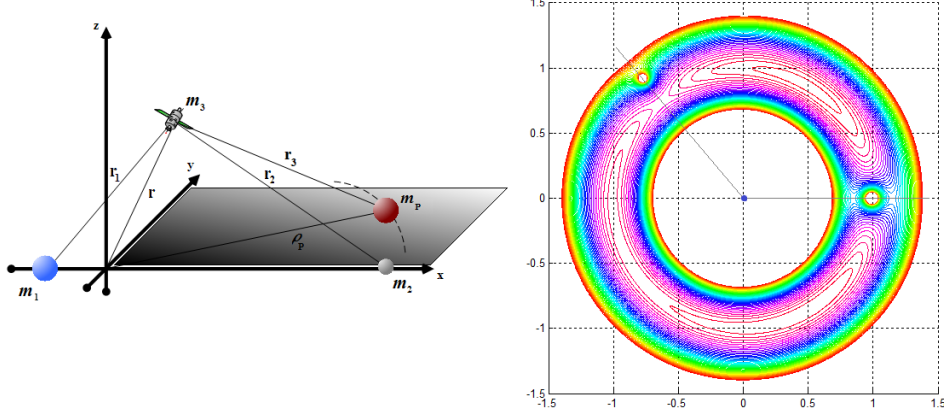


Figure 2.12: Left: the BCM reference frame. Right: Modified Effective Potential slices for a representative system where $\mu = 1e-2$, $\mu_p = 5e-3$ placed at 135 deg and $\rho_p = 1.2$ DU.

acceleration due to the rotating frame, and the time-dependent gravitational attraction of the perturbing body. It reads^[14]:

$$\Omega_4 = \underbrace{\frac{1}{2}(x^2 + y^2) + \frac{1-\mu}{r_1} + \frac{\mu}{r_2} + \frac{1}{2}\mu(1-\mu)}_{\Omega_{CR3BP}} + \underbrace{\frac{\mu_p}{r_3} - \frac{\mu_p}{\rho_p^2}(x \cos \Theta_p + y \sin \Theta_p)}_{\text{Additional Perturbation}} \quad (2.45)$$

where $\mu_p = m_p/(m_1 + m_2)$, the relative distances are given by Eq. (2.18) and $r_3 = \sqrt{(x - x_p)^2 + (y - y_p)^2 + z^2}$.

The subscript p denotes the quantities related to the additional perturber and the distances of the moving particle with respect to this body are given by: $x_p = \rho_p \cos \Theta_p$, $y_p = \rho_p \sin \Theta_p$ with ρ_p the distance of m_p from the center of mass of m_1 and m_2 .

Accordingly, the main difference of this system with respect to the CR3BP is the time dependence of the effective potentials^[39], i.e. $\Omega_4 = \Omega_4(x, y, z, \Theta_p) \Rightarrow \Omega_4 = \Omega_4(t)$. In the right plot of Fig. 2.44 slices of a snapshot of Ω_4 at a given time instant are represented, the geometry of these sort of zero velocity curves varies in time since the small “hole” due to m_p moves.

The time dependence is introduced by the angular position of m_p in the reference frame rotating with the other two primaries: $\Theta_p = \Theta_p(t=0) + \Delta\omega t$, with $\Delta\omega$ the apparent angular velocity of m_p in the system rotating with m_1

and m_2 .

This is a more general model from which the classical CR3BP can be derived, just by setting μ_p equal to zero; moreover, if also μ is zero again the two body model is obtained.

Another possible approach to model the motion under three gravity fields is to consider two bodies moving in circular orbits around a central, more massive mass. This results in the so called *Concentric Circular Model* which is again non-coherent and non-autonomous^[40].

2.4 Dynamical System Elements

As shown, the motion in the CR3BP can not be analytically predicted, but exploiting the linear approximation (actually using this as initial guess for numerical procedures) it is possible to define a set of useful special orbits. Nevertheless this model remains a chaotic model, where each small change in the initial conditions results in completely different paths.

Let us conclude this chapter underling, from a mathematical point of view, the deep reasons generating regular and chaotic behaviors in the CR3BP. These ideas are exploited in Sec. 3.1-3.2 to compute periodic orbits, manifolds and later on transfer trajectories. The CR3BP represents a complex dynamical system exhibiting different kinds of behaviors due to the presence of a small perturbation to an integrable system and to the presence of equilibria of different nature.

Instead of addressing the classical CR3BP, the main feature of any dynamical system of this kind can be found in an easier example, the *Standard Map* (Chirikov-Taylor map)^[41]. It is actually a discretization that transforms the time continuous pendulum model into a time discrete map. It results in a combination of elementary functions that shows a complex dynamics with chaotic phenomena. The dynamics of the Standard Map is ruled by^[42]:

$$\begin{aligned} x_{k+1} &= x_k - h^2 \sin x_k + y_k \\ y_{k+1} &= y_k - h^2 \sin x_k \end{aligned} \quad \Rightarrow \quad \varsigma \mapsto \chi(\varsigma), \quad \varsigma = (x_k, y_k) \quad (2.46)$$

where h is the time step used for the discretization and the application of the Standard Map is represented, in general, by χ . It is interesting to stress since now that if $h = 0$ the system corresponds to a simple rotation on the unitary annulus^[41]. That is a conservative discrete dynamical system (the determinant of its Jacobian is +1) with 2π periodicity both in x and y .

Independently from the h value, the system presents two fix points ς_j^0 , i.e. points such that $\chi(\varsigma_j^0) = \varsigma_j^0$. These two points are $\varsigma_1^0 = (0, 0)$ and $\varsigma_2^0 = (\pi, 0)$. The Jacobian matrix in ς_1^0 has, for $h < 2$ two complex eigenvalues with unitary modulus; it is an *elliptic equilibrium point*.

On the other hand, in ς_2^0 the eigenvalues of the Jacobian are real and, as the determinant is unitary, one is larger and the other smaller than 1; it is a *hyperbolic equilibrium point*. This means that the application χ is stable in ς_1^0 and unstable in ς_2^0 .

In Fig. 2.13 a hyperbolic point of the ς_2^0 kind is represented together with the stable and unstable manifolds emanating from it, W^s and W^u . These manifolds are tangent to the local stable and unstable eigen-spaces, E^s and E^u so that a linear combination of these spans the whole linear (tangent) space in the fix point.

In other words, a hyperbolic equilibrium point has a saddle component, while an elliptic one has not^[41]. The dynamics near these fix points are the same described in Sec. 2.2.4-2.2.5, where the equilateral libration points are elliptic points and the collinear ones are hyperbolic.

Iterating the Standard Map, Eq. (2.46), for many initial conditions and assuming a fix value of h , completely different behaviors around the two equilibrium points result (the same approach is used considering the CR3BP model in Sec. 3.6).

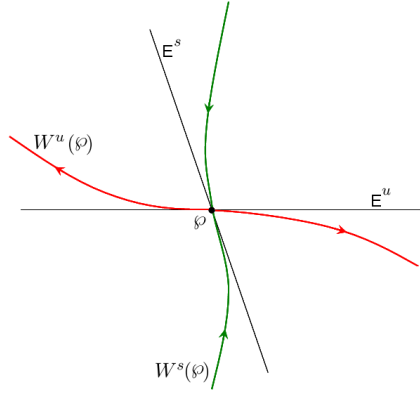


Figure 2.13: Stable and Unstable manifolds emanating from a hyperbolic equilibrium point.

Near the hyperbolic fixed point the orbits seem to fill a chaotic region, i.e. any specific pattern in the iterations of the map is absent. Although a unique definition of *chaos* does not exist, it can be visualized here as an aperiodic long-time behavior arising in a deterministic dynamical system (like the Standard Map) that exhibits a sensitive dependence on initial conditions^[18].

On the other side, initial conditions near the elliptic equilibrium point seem to arrange on *Moser invariant curves*, i.e. curves such that the iterates of the map shift just their location changing the angular location remaining on these closed lines. In this case a sort of “ordered regions” appears in the map iterations. Moreover, also closed curves with periods larger than one appear. These curves are closed lines filled alternatively for different iterations of the map and are arranged around higher order periodic points (e.g. $(0, \pi)$). For increasing values of h , the measure of these ordered curves decreases and the measure of the chaotic region increases (see also later on).

These different behaviors are depicted in the phase portraits of the Standard Map in Fig. 2.14. In the picture four values of the “perturbation” h are used, the above mentioned behaviors can be appreciated better for the intermediate values.

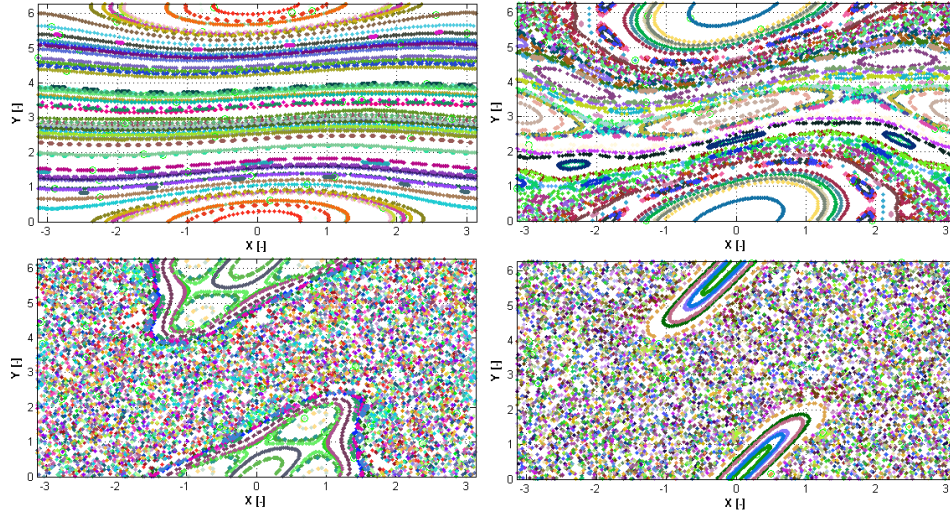


Figure 2.14: Phase portraits of the Standard Map for $h = 0.5, 1.0, 1.5, 2.0$ from the upper left corner.

In a dynamical system, a *separatrix* is a phase curve that separates the phase space into two distinct regions. For the Standard Map, the separatrices occur at the angular momentum where the oscillations give way to rotations^[41]. Actually a separatrix is an invariant manifold of the hyperbolic point. Within the separatrix the motion is oscillatory, whereas the outside corresponds to motions with the pendulum continuously turning through circles^[18] (this is exactly the behavior described for the tube-like structure in Sec. 2.2.5).

Let ς^0 be a hyperbolic fixed point for the application $\chi : \mathbb{R}^2 \rightarrow \mathbb{R}^2$ and A the matrix of the linearized system in ς^0 . Hence there exist a regular and injective curve $\gamma : \mathbb{R} \rightarrow \mathbb{R}^2$ such that^[16]:

- $\gamma(0) = \varsigma^0$;
- the speed $\gamma'(0)$ is an eigenvector of A with eigenvalue λ ;
- the image of the curve is an *invariant set*, i.e. $\chi(\gamma(s)) = \gamma(s_1)$ where $s_1 = s_1(s)$ a continuous function;

- $\lim_{k \rightarrow \pm\infty} \chi^k(\gamma(s)) = \varsigma^0$.

If the eigenvalue of A , λ , is larger than one and the limit tends to $-\infty$, the separatrix is an *unstable separatrix*. Otherwise, if the eigenvalue of A is smaller than one and the limit tends to $+\infty$, the separatrix is a *stable separatrix*.

To define the behavior of the separatrices at infinity, it is possible to approximate a piece of these by means of the linearized subspaces in the hyperbolic equilibrium. As the separatrix is tangent to the linear subspace in ς^0 , the real eigenvalues, $\lambda^{s/u}$ of the Jacobian evaluated in the hyperbolic point, corresponding to the eigenvectors $\mathbf{v}_{s/u}$ (where s is the stable one and u the unstable), give the approximate stable or unstable direction of the separatrix. Choosing a $\varepsilon > 0$ small, a point $\varsigma^{s/u} = \varsigma^0 + \varepsilon \mathbf{v}_{s/u}$ does not belong to the separatrix, but it is ε -close to it^[25]. Thus its (linear) image will be also ε -close to the separatrix in the form $\chi(\varsigma^{s/u}) = \varsigma^0 + \lambda^{s/u} \varepsilon \mathbf{v}_{s/u} + o(\varepsilon)$. So, the segment joining these two points is an approximation of the true separatrix^[18]. The approach can be reiterated for a sufficient number of iterations to obtain an approximation of the whole separatrix. This linear mapping is exploited in Sec. 3.2.1 to produce numerically the manifolds introduced in Sec. 2.2.5

Since the separatrices are injective curves these can not intersect themselves, otherwise the uniqueness existence theorem (Cauchy-Lipschitz theorem) would not held anymore. Nevertheless, it is possible for a separatrix to intersect the other one. In this case the intersection point belongs, at the same time, to the stable and unstable subspaces of the linearized system around a hyperbolic equilibrium. These are the well known *Homoclinic Points*^[30]. A homoclinic point is doubly asymptotic as it tends toward the same ς^0 both forward and backward in time (cfr. Sec. 3.3). Moreover, if the two separatrices are linearly independent in the homoclinic point, i.e. their combination can span the whole linear subspace in that point, the intersection is *transversal*^[29]. All the iterates of a homoclinic point are homoclinic and they constitute an *homoclinic orbit*, and if the first homoclinic point is transversal the whole homoclinic orbit is transversal.

On the other hand, a phase curve connecting two different hyperbolic fix point is an *heteroclinic orbit* (cfr. Sec. 3.4).

Thus, two separatrices or meet in a hyperbolic fix point or connect the stable and unstable manifolds of two different hyperbolic fix points.

If \wp is the homoclinic point and \wp' is ahead of \wp along the stable manifold and \wp'' along the unstable one, the mapping of these two points, $\chi(\wp')$ and $\chi(\wp'')$ must be ahead of the mapping of the homoclinic point $\chi(\wp)$ ^[30], like depicted in Fig. 2.15. This can happen only if the manifolds loop back and

cross again the other one in a new homoclinic point. It is equivalent to the consideration that the homoclinic point belongs to both separatrices, and its image as well. This is schematic represented in the left side of Fig. 2.15.

Thus, once the two separatrices cross they will fold to get another cross. This process takes place indefinitely and, if the first intersection is transversal, also the others are^[25].

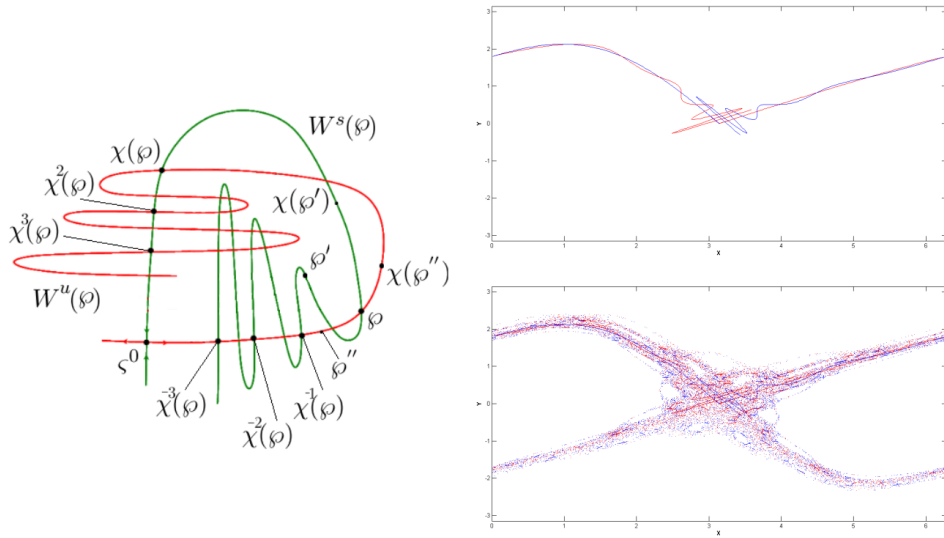


Figure 2.15: Left: schematic representation of the homoclinic tangle. Right: homoclinic tangle of the saddle point of the Standard Map after few (up) and 15 iterations (down).

Moreover, as the map is area preserving^[41] (the determinant of the linearized system is unitary) and the distance between the iterates decreases, the curves must extend further before to get the intersection with the other one. In this way the loops become longer and thinner, with the homoclinic points closer and closer. This forms a sort of network of curves that intersect infinitely many times in a small disk around the homoclinic point^[30]. This phenomenon is referred as the *homoclinic tangle* and it represents the dynamical origin of the chaos. To give an idea of the complex situation described, in the right hand side of Fig. 2.15 the global interweave of the hyperbolic fix point of the Standard Map is represented. The figure has been produced with a time step of 1 and a perturbation of $1e-10$. In the upper right plot only the first eight intersections of the separatrices are represented, while in the lower right plot the whole tangle after 15 iterations is shown. The center

point of the plots is the homoclinic point⁹.

So far we discussed the behavior of the Standard Map (intended as representative application of a generic Hamiltonian system^[41] subject to a small perturbation) considering a fix, not too high, value of the parameter h in Eq. (2.46).

In 1954 Kolmogorov^[43] laid the basis of the general theory of perturbed dynamical systems filling the gap left by Poincaré about quasi-integrable Hamiltonian system^[25]. The core question to answer was if the foliation of the phase space represented by the invariant tori (like the role of E_k ins Sec. 2.2.3) was destroyed by a small perturbation of the dynamical system. The Poincaré's answer was positive for rational tori (where the eigenfrequencies ratio has rational value). Thus, in a perturbed Hamiltonian system all the rational invariant tori vanish and just a finite number of periodic solutions survives. Many years later it was proven^[43] also the fate of the irrational tori.

This laid the foundations of the so called Kolmogorov-Arnol'd-Moser (*KAM*) theory dealing with small perturbations of completely integrable Hamiltonian dynamical systems^{[16][26]}.

As observed in Sec. 2.2, a quasi-integrable system can be posed as: $H(\Theta, I) = H_0(I) + \varepsilon H_1(\Theta, I) + \dots$ and the relevant canonical equations (in place of Eq. (2.14)) governing its dynamics are:

$$\begin{aligned} \dot{I} &= -\varepsilon \frac{\partial H_1}{\partial \Theta}(\Theta, I) \\ \dot{\Theta} &= \omega I + \varepsilon \frac{\partial H_1}{\partial I}(\Theta, I) \quad \omega := \frac{\partial H_0}{\partial I}(I) \end{aligned} \quad (2.47)$$

ω is often referred as the *frequency map*. If $\varepsilon = 0$, the Actions I , slow variables, are constants, whereas the Angles Θ , fast variables, move linearly on the tori $I = \text{const}$ and the resulting motion is quasi-periodic.

The main result of the KAM theory is that, for a perturbation ε which is analytic and small, most of the invariant tori are not destroyed by the perturbation, but are just deformed^[26]. Thus, the motion of the quasi-integrable, non-degenerate (cfr. Sec. 2.2) system is quasi periodic and fill everywhere densely a deformed torus. This holds only for those KAM tori with a sufficient non rationality of their eigenfrequencies. This last condition is known as the *Diophantine Condition*. Considering a generic $\gamma > 0$ the set of the

⁹This has been discovered by Poincaré that depicted in his mind this phenomenon without any computer and without trying to trace the homoclinic tangle on a paper. In this sense he discovered the chaos using the CR3BP as dynamical system. The chaotic phenomena originating from this behavior are quite conventional in any conservative non integrable dynamical system.

γ -diophantine frequencies is given by^[18]:

$$\Omega_\gamma = \{\tilde{\omega} \in \Omega : |k \cdot \tilde{\omega}| \geq \frac{\gamma}{||k||_\infty^n} \forall k \in \mathbb{Z}^n\} \quad (2.48)$$

Thus, only the tori with frequencies belonging to Ω_γ survive.

In the example of the Standard Map the parameter h^2 plays the role of perturbative parameter. Thus if it is zero the phase space is completely foliated by invariant tori (Fig. 2.14 would be a collection of horizontal lines), while for increasing values of h some stability regions, represented by the KAM tori, take place around the fixed elliptic points and their size decreases for increasing perturbation values until the whole space is covered by the chaotic sea^[16]. This trend is represented in Fig. 2.14.

Summarizing, the case of the Standard Map is an area-preserving application of the unitary annulus to itself. The unperturbed map, restricted to a given circle ($I = \text{const}$), results in a standard rotation with rotation angle depending on the specific torus (consequence of the non degeneracy condition). For the non resonant cases the images of the points on a given circle fill densely the circle. Otherwise, for resonant cases, the images are periodic and the tori are not completely filled. These last tori do not survive to the introduction of a small perturbation.

Finally, concerning the stability of a perturbed Hamiltonian system (thus, the one of the CR3BP), the most outstanding result is represented by the *Nekhoroshev Theorem*^[18]. It provides an exponential estimate of the time stability of a quasi-integrable non-degenerate Hamiltonian system. Actually it states that the confinement of the Action variables holds for times proportional to the inverse of the non-integrability parameter ($T \sim 1/\varepsilon$). As usually ε is very small, this leads to the concept of the “Nekhoroshev stability regime”, that is a regime of chaotic orbits but with stable motion over very long times. This approach has been successfully applied to several bodies of the asteroid main belt.

Chapter 3

CR3BP Model Investigation and Exploitation

After centuries of theoretical analysis, the circular restricted three body model was actually considered a valuable alternative to design specific space paths, as it allows many unique orbits to be defined. The deep exploitation of this model is still object of research and many trajectories designed in this framework were based only on heavy numerical computations. One of the first missions, instead, designed by considering a “manifold approach” and thus exporting the theoretical CR3BP characteristics to the real space environment, was the Genesis^{[6][44]}. It was sent to a periodic orbit around the Sun-Earth \mathcal{L}_1 (nominal operational orbit neither conceivable with another model) flowing along its stable manifold. Moreover, the solar wind samples here collected were brought back on Earth by means of the unstable manifold of this orbit exploiting also a heteroclinic connection to obtain a day-light reentry.

In general, the current direction in the mission analysis is to search for convenient trajectories enabled by a specific model considering a dynamical system approach^[45]; this results in first guess transfers to be refined in full force models.

In this Chapter, periodic orbits enabled by the CR3BP are derived by means of analytic guesses, numerical schemes and continuation procedures. Ballistic trajectories, moving towards/from equilibrium points and connections of these, are computed in order to be used later on as mission analysis options. Indicators of the chaotic regime existent in the CR3BP are presented and applied. The resonance idea is introduced and used to observe resonance transitions as well as to obtain exact resonant orbits.

For the computation of Halo orbits and manifolds, the derivation in^{[14][1]} is followed. Here also the basics of the homoclinic/heteroclinic connections can be found. A global analysis of the periodic orbits and relevant stability

considerations can be found in^{[46][42]}. For the Poincaré sections, the analysis of their domain and the resonance transitions the reader can refer to^{[47][48]}.

3.1 Periodic Orbits

The motion of a particle in a given dynamical system is defined periodic if its position and velocity repeats after a given time interval^{[46][49]}.

To generate a periodic solution in the framework of the CR3BP, the standard approach is to produce high order non-linear analytical approximations to be used as initial conditions in numerical schemes^[15].

3.1.1 Periodic Orbits around Libration Points

As explained in Sec. 2.2.5, the periodic orbits around a collinear libration point can be divided into planar/vertical Lyapunov (if only one periodic motion is taken into account)^[36], Lissajous orbits (when the in-plane and the out-of-plane eigenfrequencies are different)^[42] and Halo orbits (when the two eigenfrequencies match)^[37]. Following this subdivision, it is clear that the Lissajous are quasi-periodic orbits, while all the other types are exactly periodic solutions.

The Lissajous orbits have four degrees of freedom represented by the planar and vertical amplitudes (related to initial conditions) and the two initial phases^[42], i.e. A_x , A_z , φ and ψ in Eq. (2.38) together with $A_1 = A_2 = 0$. These orbits are bounded by the invariant KAM tori around the libration points. Their analytic initial guess is still given, at the first order, by the integration of the linearized equations, Eq. (2.38), and at higher orders by methods like the ones described in this section for the Halo orbits. Their numerical construction, instead, is quite challenging due to the non periodicity of these solutions. The numerical approach aims firstly at the identification of target positions at given time instants. Afterwards the position continuity among those points is satisfied with velocities discontinuities that are subsequently reduced by means of an iterative process.

However, it is worth stressing that the four dimensional center manifold around a collinear equilibria (cfr. Sec. 2.2.5) is occupied, for an energy value enabling the existence of Halo orbits, by quasi-periodic orbits of two different families: the Lissajous family around the vertical Lyapunov orbits (always present) and the *Quasi-Halo Orbits* around the Halo orbits (that appear with the inherent Halo). These quasi-periodic orbits reside on invariant tori (cfr. Sec. 2.4) about the corresponding periodic orbit^[50].

In this work Lissajous/quasi-Halo orbits are never used as target orbits; thus, let us focus on exactly periodic solutions to describe how these can be implemented analytically and numerically. The method is outlined for

the three dimensional Halo orbits; the extension to the Lyapunov case is straightforward.

Halo orbits appear when the non linear terms allow $\nu = \omega$ (cfr. Eq. (2.39))^[51]. The solutions of the linear equations of motion can be written, restricting to the periodic component, for this situation. Following a Lagrangian approach, L can be expanded in series of Legendre polynomials and the recursive relationships of these polynomials can be exploited to produce high order analytic approximations of the motion. In this way third order approximations for the Halo orbits are available from Richardson^[51].

Another way to generate periodic solutions employees the Lindstedt-Poincaré method^{[52][25]}. In this case, the idea is to find a parameter altered by the perturbation and expand the dependent variable and this parameter in power of the perturbation. The gravitational potential is expanded in power series and frequency corrections are introduced in order to get rid of the secular (unbounded) terms. This approach is more precise and allows the derivation of all kind of invariant objects^[42].

The approach used in this work refines the initial guess of periodic solutions obtained by a “Richardson approach”^[53] by means of a *Differential Correction Procedure*. This is essentially a Newton method using the analytic expansion as initial seed and taking into account the real dynamical field^[54].

The main proprieties exploited to compute the periodic solutions are their symmetries, like outlined in Sec. 2.2.2. If, at a given time instant, the state of the system is such that the velocity is perpendicular to the radius vector, the corresponding configuration is a so called *Mirror Configuration*. If at two separate epochs two mirror configurations occur, the resulting orbit is periodic^[49]. This assures that two mirror configurations are sufficient for the existence of a periodic solution. Thus, imposing to reach another mirror configuration starting from a given one is a condition to compute a periodic orbit.

In the CR3BP there exist two kinds of symmetries: *A symmetry* if the corresponding solution is symmetric with respect to an axis (m_3 crosses the x -axis with perpendicular velocity) and *P symmetry* if it is symmetric with respect to a plane (when the crossing is through a plane with perpendicular velocity). Moreover, there exist also *doubly-symmetric Solutions* given by the combination of *A* and *P* symmetries^[55].

The intersection of a Halo orbit with the x - y plane is a mirror configuration of the *P* kind since these solutions are symmetric with respect to the x - y and x - z planes. The *P-symmetry* with the x - y plane is exploited to compute the periodic solutions, while the symmetry with respect to the x - z plane defines the *Northern* family, Halo orbits with a maximum excursion of

the z -amplitude in the positive z semi-axis, and the *Southern* family, with maximum z excursion below that plane.

A mirror configuration is identified by an initial state in the form: $\vec{x}_0 = \{x_0, 0, z_0, 0, v_0, 0\}$. If after a semi-period ($T_{1/2}$ with T the orbital period) the state of the flow is of the kind $\vec{x}_t = \{x^*, 0, z^*, 0, v^*, 0\}$, another mirror configuration is found and the Halo orbit is computed^[55].

The Newton method computes iteratively the corrections to the orbital period and to the initial conditions so that the required final state is obtained. The differential correction scheme works as a first order expansion of the flow that, propagated from the analytic approximation, at the next intersection with the x - z plane results, in general, in the form: $\Phi(\vec{x}_0, T_{1/2}) = \{\tilde{x}, 0, \tilde{z}, \tilde{u}, \tilde{v}, \tilde{w}\}$. Denoting $\Phi(\vec{x}_0, t)$ the trajectory of the system with $\vec{x}(t_0) = \vec{x}_0$, i.e. $\Phi(\vec{x}, t) : \vec{x}_0 \mapsto \vec{x}(t)$ that is the *flow map* of the dynamical system¹. Thus, the aim is to find the corrections $\Delta = \{\Delta x, 0, \Delta z, 0, \Delta v, 0\}$ and Δt such that $\Phi(\vec{x}_0 + \Delta, T_{1/2} + \Delta t) = \vec{x}_t$. This can be done by means of a first order Taylor expansion:

$$\Phi(\vec{x}_0 + \Delta, T_{1/2} + \Delta t) = \Phi(\vec{x}_0, T_{1/2}) + \left[\frac{\partial \Phi(\vec{x}_0, T_{1/2})}{\partial \vec{x}} \right] \cdot \Delta + \frac{\partial \Phi(\vec{x}_0, T_{1/2})}{\partial t} \cdot \Delta t \quad (3.1)$$

The unknowns of this equation are the components of Δ and Δt . The matrix $\Omega(\vec{x}, t) = \partial \Phi / \partial \vec{x}$ is the so called *State Transition Matrix*. It is worth nothing that this matrix Ω , evaluated after one period of the periodic orbit, is called the *Monodromy Matrix* M (cfr. Sec. 3.1.3). The Eq. (3.1) can be written by components as:

$$M \{\Delta x, 0, \Delta z, 0, \Delta v, 0\}^T + \mathbf{f}(\Phi) \Delta t = \{x^*, 0, z^*, 0, v^*, 0\}^T - \{\tilde{x}, 0, \tilde{z}, \tilde{u}, \tilde{v}, \tilde{w}\}^T \quad (3.2)$$

where $\mathbf{f}(\Phi) = \partial \Phi / \partial t$. This results in three equations (the non trivial ones) in four unknowns: $\Delta x, \Delta z, \Delta v$ and Δt .

This indeterminacy is a consequence of the presence of a family of solutions where the specific Halo orbit is embedded in. In any Hamiltonian system the periodic solutions present as a family and a parameter (resulting in a specific energy value) has to be chosen in order to extract a specific solution from this family².

¹The flow map satisfies the equations of motion ($\dot{\vec{x}} = f(\vec{x})$):

$$d\Phi(\vec{x}_0, t)/dt = f(\Phi(\vec{x}_0, t)), \quad \Phi(\vec{x}_0, t_0) = \vec{x}_0$$

²In general, around a fixed point of a Hamiltonian system, with eigenvalues in the form $\pm \omega i$ and under suitable non-resonance conditions for the remaining eigenvalues λ_i ,

Setting $\Delta z = 0$ the procedure establishes an iterative technique to correct the initial analytic guess with a new condition: $\vec{x}_0^{new} = \vec{x}_0^{old} + \Delta$ until the mirror condition is reached after half-period.

This differential correction procedure requires the propagation of time derivatives of the monodromy matrix (with initial conditions $M(t=0) = \mathbf{I}$) together with the equations of motion. This results in $36 + 6$ equations for the Halo orbits and $16 + 4$ for the planar Lyapunov ones.

This holds as the state transition matrix, hence of the monodromy matrix, solves the initial values problem defined as: $\dot{\Omega}(\vec{x}, t) = Df(\vec{x}) \Omega(\vec{x}, t)$ with $\Omega(\vec{x}, t_0) = \mathbf{I}_n$, where $Df(\vec{x})$ is the Jacobian of the generic dynamical system $\dot{\vec{x}} = f(\vec{x})$ and \mathbf{I}_n is the $n \times n$ identity matrix. As $Df(\vec{x})$ is time dependent, it can not be solved analytically so that it usually requires the numerical propagation of the additional n^2 equations representing the elements of $\Omega(\vec{x}, t)$.

The Richardson seed and the numerically corrected orbits are presented for a set of Southern Halos (left) and planar Lyapunov orbits (right) around \mathcal{L}_1 in the Sun-Earth system in Fig. 3.1.

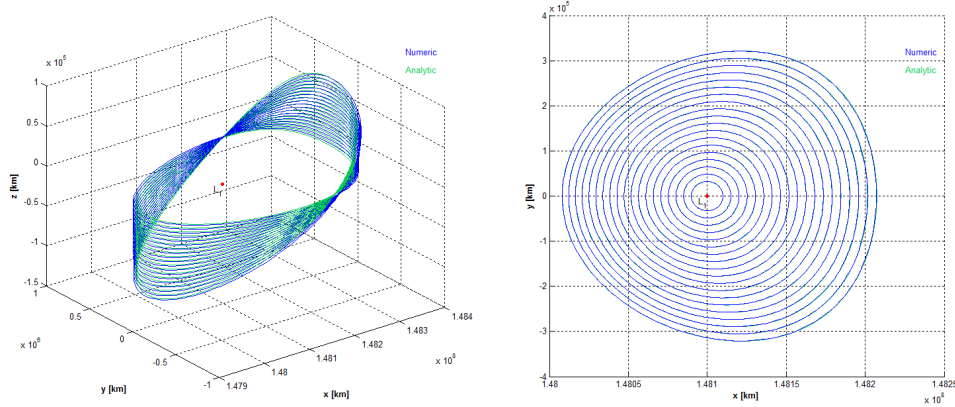


Figure 3.1: Analytical seed (green) and numerical differential correction (blue) of southern Halos (left) and planar Lyapunov orbits (right) around \mathcal{L}_1 in the Sun-Earth system.

The Halo orbits span a z -amplitude of $[1e4:5000:1e5]$ km with a Jacobi constant in the range $[3.0008314, 3.0008342]$. On the other side, the Lyapunov orbits presented have the same range $[1e4:5000:1e5]$ km as x -amplitude and they span a J of $[3.000885, 3.0009008]$. It is also possible to observe from Fig. 3.1 that, in this energy range and for this μ value, the analytic initial

there exist a one-parametric family of periodic orbits emanating from the equilibrium with limiting period $2\pi/\omega$. This is the *Lyapunov's Centre Theorem*^[36] (cfr. also Sec. 2.2.5).

guess resulting for the planar case is much better than the one for the three dimensional solutions. Indeed it is almost impossible to distinguish between the analytic and numeric Lyapunov orbits.

To compute the planar Lyapunov family, the corresponding condition to solve the indeterminacy of the system, Eq. (3.2), is to set $\Delta x = 0$ and solve for the two remaining unknowns. In this case the symmetry with respect to the x -axis is exploited and any size of orbit can be computed up to Earth collisions, see Fig. 3.2.

It is worth underlining that the non linear terms play a growing role for increasing amplitudes and the corresponding orbits are much more distorted as can be observed looking at the whole family of \mathcal{L}_1 - \mathcal{L}_2 Halo and planar Lyapunov orbits shown in Fig. 3.2 for the Earth-Moon system.

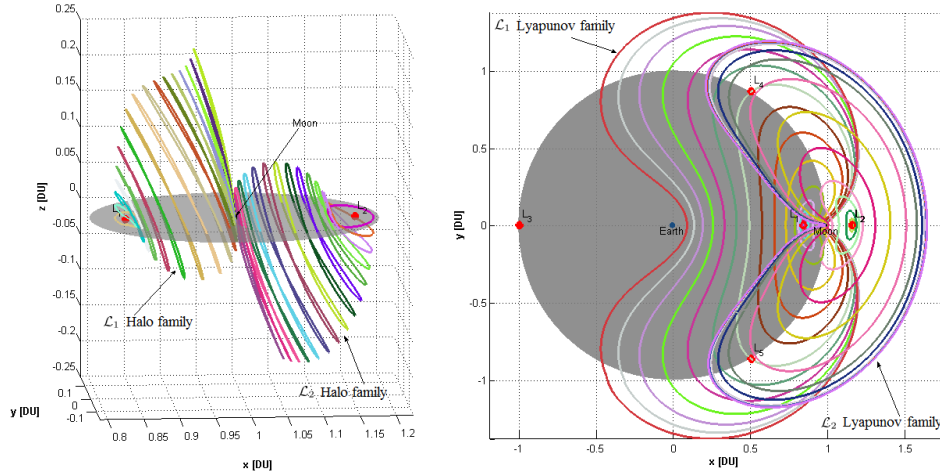


Figure 3.2: Northern \mathcal{L}_1 /Southern \mathcal{L}_2 Halo (left) and \mathcal{L}_1 / \mathcal{L}_2 Lyapunov families (right) in the Earth-Moon system.

Finally, the Richardson approximation can also be derived for the vertical Lyapunov orbits related to the situation $\omega = 0$ in Eq. (2.38). In this case, only the vertical amplitude parameterizes these orbits that (as the planar one for the Lyapunovs) represent a subset of the Lissajous orbits with $A_x = 0$. These, or more commonly close Lissajous, are very useful to have a good polar coverage of the small primary or for telescope missions that can move beyond the primaries plane where most of the dust is concentrate.

3.1.2 Global Periodic Orbits

Beside the periodic solutions close to the collinear libration points analyzed so far, the CR3BP gives rise to a whole set of periodic orbits in the phase

space. These can be identified by means of *Continuation Procedures* starting from the basic sets of periodic solutions (i.e. the planar and vertical families) emanating from the libration points and increasing a parameter of the system. In this way have been computed the Earth-Moon Halo and Lyapunov families presented in Fig. 3.2.

The main idea of this procedure is to compute the set of solution of: $F(x) = 0$, $F : \mathbb{R}^{n+1} \rightarrow \mathbb{R}^n$. These are under-determined systems (one more unknown than equations) and, away from the singularities, the set of solutions is a nD manifold embedded in a $(n + 1)$ -dimensional space.

Let us suppose to have a solution (tilde state) of this kind of problem with a dependence on a parameter that we wish to vary: $F(\tilde{x}) = 0$; $\tilde{x} = (\tilde{y}, \tilde{\lambda})$, $F : \mathbb{R}^n \times \mathbb{R} \rightarrow \mathbb{R}^n$, $y \in \mathbb{R}^n$, $\lambda \in \mathbb{R}$.

The idea is to slightly perturb this parameter in order to obtain a new solution of the system. Of course, a variation of $\tilde{\lambda}$ gives a new point that is not solution of the problem, but it is close to, so several *predictor-corrector methods* can be used to approach such a problem. The general scheme is to use the previously known point as initial guess for a zero finding method (e.g. Newton method) in order to define the new solution. This results in a continuation curve that gives the evolution of the zeros of the system F with respect to a variation of the parameter λ ^[56].

Usually, the variation of the parameter gives a new point which is not solution of the original problem, but it is close to it in the form $F(\tilde{y}, \tilde{\lambda} + \delta\tilde{\lambda})$. The classical approach is to use a sort of Newton method for the augmented problem^[57]:

$$\begin{aligned} F(y, \lambda) &= 0 \\ \lambda - (\tilde{\lambda} + \delta\tilde{\lambda}) &= 0 \end{aligned} \tag{3.3}$$

Each zero finding procedure requires an initial guess within the basin of attraction of the zero to converge. Thus, if the continuation curve presents a sudden fold, the previous initial guess of the parameter can be very poor and outside the basin of attraction, so there are no guarantees that the zero finding procedure converges.

Moreover, when a small variation of the continuation parameter causes a sudden qualitative change of the behavior of the system a *bifurcation point* occur^[18]. In this situation a new branch of solutions arises and the two solution curves have to be continued independently^[55]. A bifurcation is a situation where a very small change in the continuation parameter of a dynamical system suddenly generates completely different solutions, both topologically and qualitative. The bifurcation is a sort of separation of the behaviors of the dynamical system in different parts and it is often related to the chaos

onset^[58].

Therefore, the main limit of this classic *Natural Continuation Method* is that it does not take into account the actual shape of the continuation curve so it may fail in a fold of this curve. Furthermore, it requires a continuation parameter explicitly present in the equations of motion, and this is not the case for the CR3BP.

The *Pseudo Arc-length Method*^[58] is a natural improvement of the previous method where the new value of the continuation parameter is determined by the geometry of the curve by means of an approximation of its arc-length. The resulting problem can be stated as^[57]:

$$\begin{aligned} F(x_1) &= 0 \\ (x_1 - x_0)^T \dot{x}_0 &= \delta s \end{aligned} \quad (3.4)$$

Where \dot{x}_0 is the unit tangent to the continuation curve in the point x_0 and δs is the step size adapted along the curve (to assure the convergence of the Newton method) and approximating the arc-length along the curve^[59].

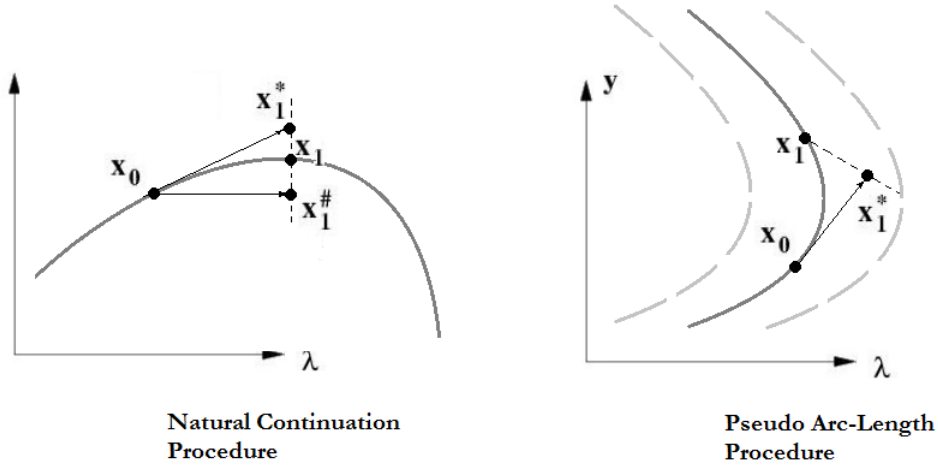


Figure 3.3: Schematic ideas of the Natural Continuation procedure (left) and of the Pseudo Arc-length one (right).

The CR3BP equations of motion, Eq. (2.2.2), do not present any natural parameter to perform the continuation procedure, so they have to be re-written to introduce an *unfolding term* to allow the parametrization of the family of periodic solutions^[60]. The continuation is performed on this unfolding parameter that breaks the symmetry of the solutions and must be zero (within the numerical precision) when a periodic solution is found.

Moreover, the application of the Pseudo Arc-length method to detect periodic solutions in the CR3BP requires first of all the computation of one periodic orbit of the planar and vertical Lyapunov family that are the two basic families of periodic solutions emanating from the libration points^[57].

The approach here implemented consists of the continuation of a planar and a vertical Lyapunov orbit around each libration point and store each bifurcation point found. Afterwards these bifurcation points are further continued and the new set of bifurcation points found are stored to reiterate the process. The procedure ends when the family which is going to be computed is identified as already stored or an impact with one of the primaries occurs. This procedure has been implemented using the software AUTO^[61].

A complete diagram of the initial conditions in the position space, giving rise to a generic periodic orbit in the Earth-Moon CR3BP is represented in Fig. 3.4. All the emanating bifurcations curves are presented in the real position space (left) and in a schematic version (right). The white balls are the bifurcation points and each family is computed until it crashes with one of the primaries, it grows to infinity or it bifurcates into another family. These results show a good agreement with^[59].

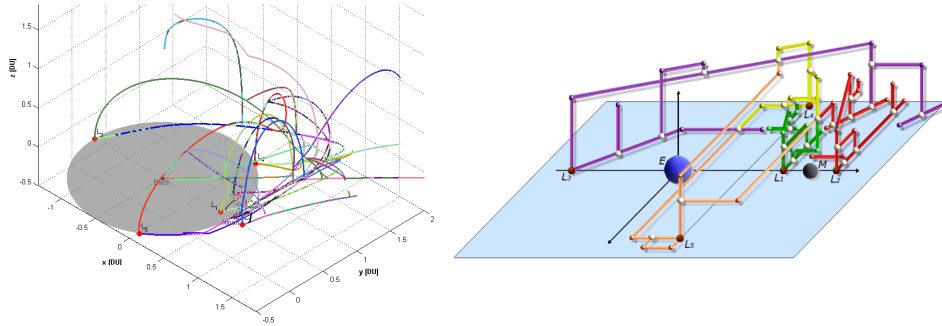


Figure 3.4: Real (left) and schematic (right) bifurcation diagram for the Earth-Moon CR3BP. Each curve is a continuation curve of periodic orbits emanating from one of the five equilibria.

As representative families computed with this approach, the \mathcal{L}_3 Halo orbits and the \mathcal{L}_4 - \mathcal{L}_5 vertical orbits are presented in Fig. 3.5 and 3.6. The \mathcal{L}_3 Halos arise again from a bifurcation of the \mathcal{L}_3 planar Lyapunov family, like for the \mathcal{L}_1 and \mathcal{L}_2 inherent Halos. They end with Earth impacts and can reach approximately two times the Earth-Moon distance as out-of-plane amplitude. Their period can vary in the range $[4.7, 6.3]$ TU with a Jacobi constant in $[2.5, 4.5]$.

On the other hand, vertical orbits of the triangular points can transit from

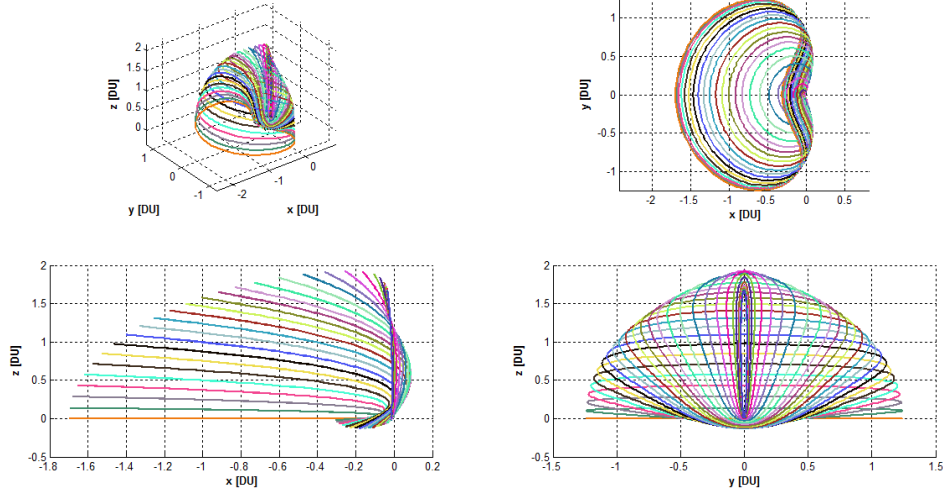


Figure 3.5: Family of \mathcal{L}_3 Halo orbits in the Earth-Moon system.

one to the other elliptic equilibrium point. These constitute by themselves two of the basic families emanating from the triangular libration points and are symmetric with respect to the x - y plane. Thus, they can reach approximately the Earth-Moon distance above and below the Moon orbital plane. They have a Jacobi constant in the range $[-0.9, 3]$ and a quite narrow period variation around 6.3 TU.

In general, the most important bifurcation phenomenon in the CR3BP is the one generating the Halo orbits. As said, these arise from a bifurcation of the planar Lyapunov family when the amplitudes are large enough to allow non linear terms to produce equal eigenfrequencies (cfr. Sec. 2.2.5). In this situation, around a single Halo, also the relevant invariant torus filled by quasi-Halo appears. In Fig. 3.2 also the last Lyapunov orbits, generating the Halo families, are represented.

In the global bifurcation diagram of Fig. 3.4 there are some general aspects to stress. The \mathcal{L}_1 Halo family, differently from the other Halo families, does not crash on one primary but it is linked to the vertical family of $\mathcal{L}_4 - \mathcal{L}_5$ ^[59]. Furthermore, there is a continuous and direct transition among the vertical Lyapunov orbits of $\mathcal{L}_3 - \mathcal{L}_4 - \mathcal{L}_5$. Finally, there are periodic orbits passing twice in the Moon vicinity. These kinds of solutions are quite attractive from a mission analysis point of view and are considered for the application presented in Sec. 6.3.

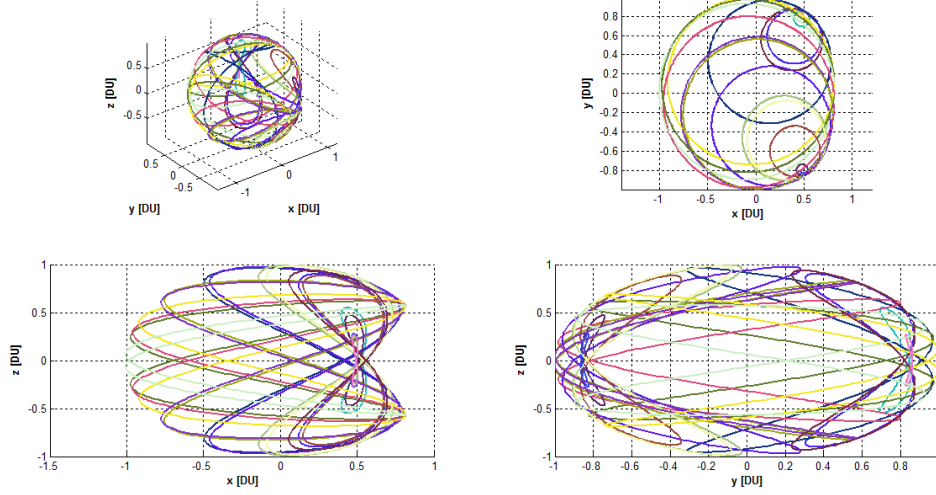


Figure 3.6: Family of \mathcal{L}_4 - \mathcal{L}_5 vertical orbits in the Earth-Moon system.

3.1.3 Stability of Periodic Orbits

Bearing in mind that a detailed analysis of the stability conditions is beyond the scope of this work, let us conclude this exploration of periodic solutions in the CR3BP with few comments about their stability.

Let us consider a reference trajectory $\vec{x}(t) = \Phi(\vec{x}_0, t)$ (cfr. Sec. 3.1.1) and a trajectory starting slightly away from this one. It has perturbed initial conditions in the form $\vec{x}_0 + \delta\vec{x}_0$ and thus its time evolution reads: $\delta\vec{x}(t) = \Phi(\vec{x}_0 + \delta\vec{x}_0, t) - \Phi(\vec{x}_0, t)$. Measuring the displacement at a given time \bar{t} and expanding it at the first order in Taylor series, it reads: $\delta\vec{x}(\bar{t}) = \partial\Phi(\vec{x}_0, \bar{t})/\partial\vec{x}_0 \delta\vec{x}_0 + O(\delta^2\vec{x}_0)$. The matrix $\partial\Phi(\vec{x}_0, \bar{t})/\partial\vec{x}_0$ satisfying this relation is the state transition matrix introduced in Sec. 3.1. Replacing \bar{t} with the period T of a periodic solution, the monodromy matrix is obtained and the evolution of a small perturbation in the nearby of a periodic solution is approximated at the first order. This is particularly important as, according to Poincaré^[30], in a chaotic system are the periodic solutions that organize the phase space as they constitute the “bones” of each organized structure.

A general dynamical system with T -periodic coefficients is defined by: $\dot{\vec{x}} = A\vec{x}$ with $A(t+T) = A(t)$. In this case, the set of all solutions can be expressed as the product of a T -periodic matrix and a solution matrix with constant coefficients³. This is the core of the Floquet theory^[62] that

³The Floquet Theorem^[62] states that the state transition matrix ($\Omega(t)$) can be expressed as: $\Omega(t) = P(t)e^{Qt}$ where $P(t)$ is T -periodic and Q is a constant matrix that has as eigenval-

gives the solution of a linear differential system with periodic coefficients as linear combination, with non constant coefficients, of exponentials of the *characteristic multipliers*, λ . These characteristic multipliers are actually the eigenvalues of the monodromy matrix (cfr. Sec. 3.1.1) after one period T ^[62] and are given by $\lambda = e^{\alpha T}$, with α the *characteristic exponents*. This means that these exponents rule the stability of the solution that is given by the study of the behavior of the periodic solutions at the end of one period or, equivalently, after an iteration of the Poincaré map (of which the characteristic exponents are eigenvalues as well) from a section plane to itself.

Thus, to study the linear stability of a periodic orbit, it is sufficient to study the multipliers at the end of one period. As a periodic orbit represents a fix point on a suitable Poincaré section transverse to the flow, its stability can be analyzed directly on the surface of section linearizing the first return map around the fix point corresponding to this periodic solution. In the (P)CR3BP the section is (2)4-dimensional and the linearized map is a (2x2)4x4 symplectic matrix (cfr. Sec. 2.1). Thus, it has eigenvalues of the form η and $1/\eta$; the *stability index* is defined as $s = \eta + 1/\eta$ ^[42].

Furthermore, for a periodic orbit in a Hamiltonian system there is a unitary eigenvalue with algebraic multiplicity of two (the second one arising from the symplectic behavior of the map) corresponding to the periodic motion (the so called *non-degenerate eigenvalues*).

Thus, two stability indices can be defined in the three dimensional problem (4 conjugate eigenvalues left beside the two unitary ones). If $s_1 < 2, s_2 < 2$ and both are real, the corresponding periodic orbit is linearly stable. One of these is the measure of the in-plane stability, while the other one of the vertical stability^[42].

There are many kinds of bifurcations (cfr. Sec. 3.1.2) determined by the motion (resulting from the continuation of a system parameter) of the Floquet multipliers in the complex plane^[18]. For a continuous dynamical system the crossing of the unit circle of these multipliers is index of a change in the stability of the family of solutions. Floquet multipliers larger than one represent instability while ones smaller represent stability^[62]. Since these are always in conjugate pairs and two are unitary, a given periodic orbit in the CR3BP can be stable or linearly unstable of order one or two.

In general, a bifurcation occurs when a single real, or a pair of complex conjugate multipliers passes through the unitary circle in the complex plane^[18]. The point and the direction of the cross determine the specific bifurcation kind. A bifurcation can change the stability of the solution in three

ues the characteristic exponents of the periodic orbit over one orbital period. Furthermore, $\Omega(kt) = M^k$ where M is the monodromy matrix, $M = \Omega(T)$.

basic ways^[63], see Fig. 3.7:

- a pair of multipliers moves along the unit circle, collide at $+1$ ($s_i = +2$) on the real axis and continue moving along the real axis. It is a *Tangent Bifurcation* (also called *Saddle-Node*, since there is a saddle and a node annihilating each other) that leads to a change in the stability of the solution with creation (*Pitchfork Bifurcation*) or not (*Cyclic-Fold Bifurcation*) of a new family of solutions. Particularly important are the Pitchfork bifurcations, these are associated with the stability change of a symmetric solution whereas the new solutions break this symmetry. There are two types of pitchfork bifurcations, *supercritical* and *subcritical*. The first one loses stability by emanating a pair of stable asymmetric orbits and the subcritical form loses stability by absorbing a pair of unstable asymmetric orbits^[46];
- a pair of multipliers moves along the unit circle, collide at -1 ($s_i = -2$) on the real axis and continue to move along the real axis. It is a *Period Doubling Bifurcation* and the new family has twice the period of the original one. Again, there are two kinds of period-doubling bifurcations, the supercritical and the subcritical. The supercritical type loses stability by emanating a stable period-doubled orbit whereas the subcritical one loses stability by absorbing an unstable period-doubled orbit^[46]. This is one of the classical routes leading a regular system to a chaotic behavior through a period doubling cascade that, for increasing energy, loses any kind of periodicity of the solution;
- two pairs of complex conjugates eigenvalues collide on the unit circle off from the real axis and continue moving in the complex plane. This is a so called *Secondary Hopf Bifurcation*. In general this situation leads to a new family of invariant tori around the original periodic solution.

There are several others bifurcation phenomena^[63] that usually generate a new family without changing the order of linear instability of the original family but resulting in different qualitative behaviors. In particular, the situation of two eigenvalues crossing the imaginary axis on the complex plane, the *Hopf Bifurcation*. Also the situation when they collide on the real axis (out from the unit circle) and then move in the complex plane, the so called *Modified Secondary Hopf Bifurcation*, does not change the linear instability of the orbit^[46]. Finally, a *transcritical bifurcation* is a particular local bifurcation, characterized by the passage of an eigenvalue through the imaginary axis. In this case the stability of a stable and an unstable fix points (periodic orbits) is exchanged, but no new families are generated.

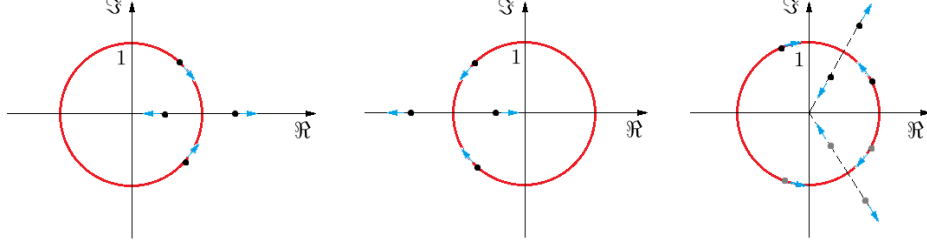


Figure 3.7: From left to right schematic representation of: Tangent, Period Doubling and Secondary Hopf Bifurcation.

As representative cases of these bifurcations, let us follow the evolution in the complex plane of a generic periodic orbit, in Fig. 3.8, of the Earth-Moon CR3BP.

The energy range of this kind of orbits is quite small (the Hill regions are closed also in \mathcal{L}_1) and it has been found, together with many others, by means of a grid search^[64] of P-symmetric (Sec. 3.1.1) initial conditions. For each of these initial states the differential correction scheme described in Sec. 3.1.1 has been applied and, for procedures converging in less than 25 iterations, the resulting orbit considered as an initial seed to continue. The test periodic orbit of Fig. 3.8 has initial conditions (in non dimensional units): $[1.3677, 0, 0.0500, 0, -0.5664, 0]$. This is a doubly symmetric periodic orbit presenting three mirror configurations, two P symmetries and one A symmetry^[46].

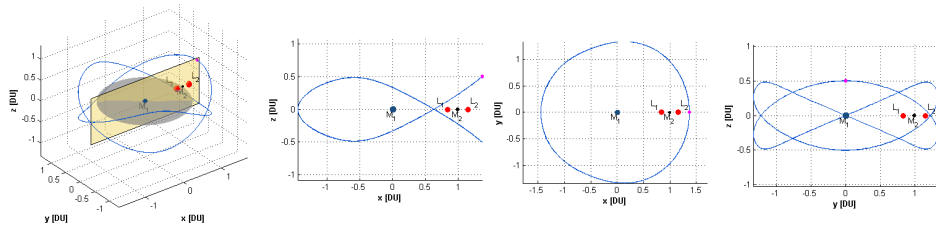


Figure 3.8: Views of a P-symmetric, 1-linearly unstable periodic orbit in the Earth-Moon system.

In this case, quite far from the two primaries, a local natural continuation procedure has been carried out on the out-of-plane initial amplitude, exploiting at each step the previous, lower inclined, initial conditions. A step

of 0.003 DU has been used to change the out-of-plane amplitude, for 700 orbits centered around the nominal seed. The family range has approximately 36 days of period and spans a Jacobi constant range [3.09, 3.43].

This particular family exhibits a remarkable pitchfork bifurcation for $J \approx 3.16$, see Fig. 3.9. At this energy two eigenvalues collide in +1 along the real axis and start moving long it. Thus, the stability index presents a new branch and the family gains an order one linear instability. Beside the two unitary ones, the other two eigenvalues not involved in the bifurcation keep on moving along the unit circle, i.e. the other stability index remains constant. The continued family together with the motion of the Floquet multipliers and the stability indexes evolution is shown in Fig. 3.9.

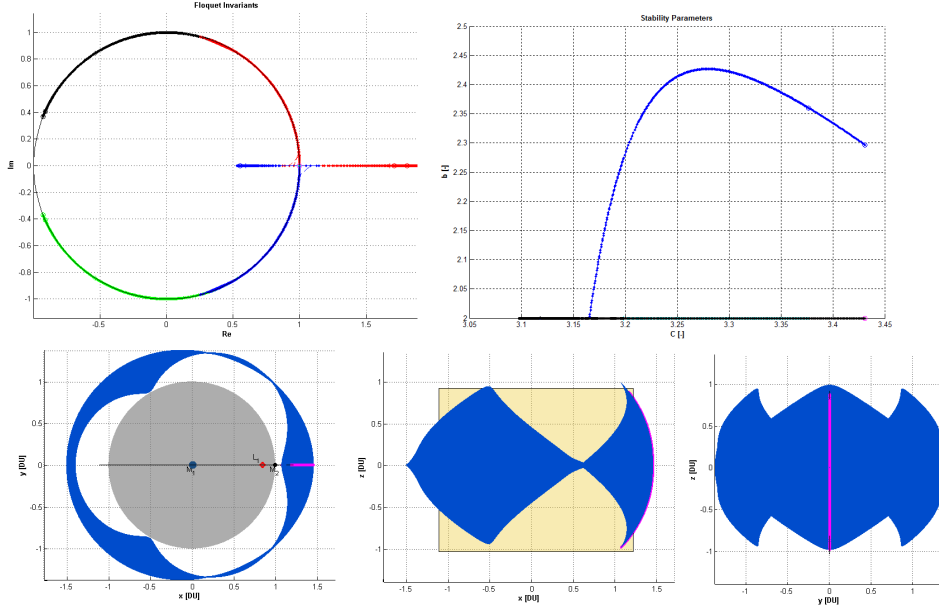


Figure 3.9: Form the seed of Fig. 3.8: in the upper left corner the motion of the characteristic multipliers for different energies; in the upper right corner the evolution of the stability indexes and in the lower row three views of the continued branch of the periodic family.

A different behavior presents, instead, the orbit depicted in Fig. 3.10. This orbit, obtained with the same method described above, presents two P symmetries and moves again quite far from the two primaries. The eigenvalues of this orbit are all real, two larger than one and two smaller. This solution has initial conditions of $[-2.0605, 0, 0.300, 1.3664, 0]$, $J = 3.441$ and period of ≈ 21.6 days.

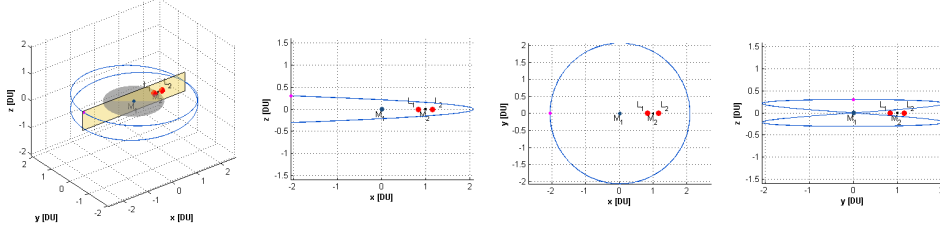


Figure 3.10: Views of a P-symmetric, 2-linearly unstable periodic orbit in the Earth-Moon system.

The same brute-force continuation procedure has been carried out considering this as the initial seed for 1300 orbits centered around this solution. The period remains approximately the one of the original seed, while the Jacobi constant changes in $[3.38, 5.29]$. In this case there are two stability indexes larger than one for low values of the Jacobi constant. However, increasing the energy, there are a couple of eigenvalues keep on moving along the real axis and consequently one stability index growing in time. On the other hand, there is a couple of eigenvalues colliding in $+1$ and start moving along the unit circle. This is represented by a second stability index that decreases in time until it assumes magnitude $+2$. Thus, the family gains one order of linear stability. These two indexes, together with the motion of the characteristic multipliers (and close up of the regions of interest) are shown in Fig. 3.11

As shown, bifurcation phenomena with possible corresponding change in linear stability of the periodic solution can also be recognized by the two critical values (± 2) of the stability indexes^[42]. For $s_i = +2$ ($\lambda = 1$) the resulting periodic orbit has the same period of the set of periodic solutions the new branch bifurcates from. On the other hand if $s = -2$ ($\lambda = -1$), the new periodic orbit has a period double of the original orbit. Between these two critical values there exist other possible bifurcation situations where the period of the new branch is a multiple period of the emanating one.

If $s_i > 2, s_i \in \mathbb{R}$ (hyperbolic case), there is a stable/unstable manifold of the periodic orbit tangent to the λ_i direction^[42]. This is the case of the collinear points and is exploited to generate the inherent manifolds (Sec. 3.2).

If $s_i < 2, s_i \in \mathbb{R}$ (elliptic case), it means that $\lambda_i = \cos \rho + i \sin \rho$ that represents a one dimensional family of periodic solutions. These are invariant under linearization of the flow (first order mapping given by M) around the fix point and ρ is their rotation number. Rational values of ρ correspond to bifurcations of families of periodic orbits. For $\rho = 0$ and $\rho = 2\pi$, the stability

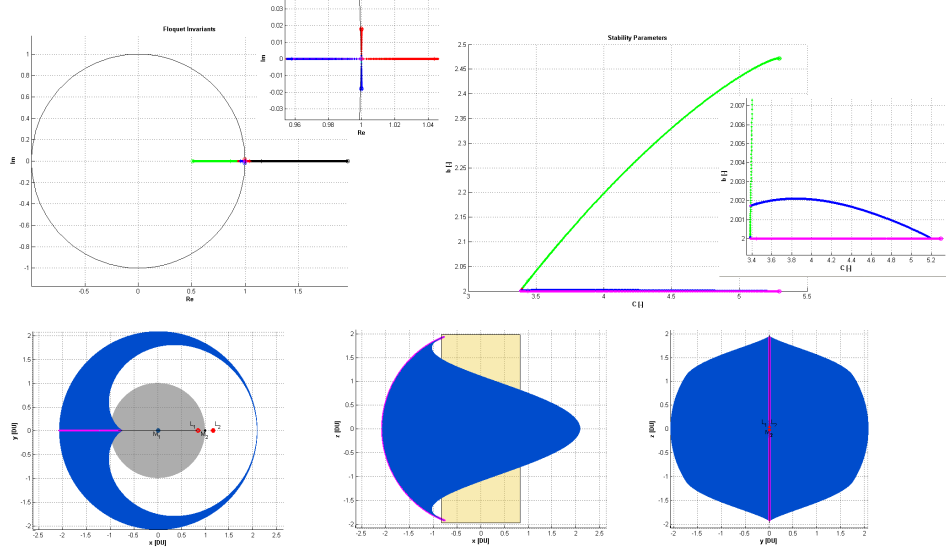


Figure 3.11: Form the seed of Fig. 3.10: in the upper left corner the motion of the characteristic multipliers for different energies; in the upper right corner the evolution of the stability indexes and in the lower row three views of the continued branch of the periodic family.

index assumes the two critical values (parabolic case)^[42].

The first crossing of $s = 2$ for the planar Lyapunov family is the pitchfork bifurcation giving rise to the Halo orbits (cfr. Sec. 2.2.5). For any Lyapunov orbit before the critical bifurcation point, there is one unstable eigenvalue, a stable one and four center eigenvalues. Two of these are unitary and the other two lies on the unit circle. Approaching to the critical amplitude (i.e. energy), the two eigenvalues on the unit circle move towards one and at $s = +2$ there are four unitary eigenvalues. Afterward there are other two eigenvalues moving along the real axis so that the resulting Halo family and the original Lyapunov, after this bifurcation, are 2-linearly unstable^[65].

3.2 Manifolds

The qualitative study of any dynamical system is based on the detection of invariant objects such that a given orbit evolves in time constrained to belong to one of those^[30]. The *Invariant Manifolds* belong to this class of objects and are a powerful tool, both to study the behavior of a dynamical system and to preliminary design purposes^[1]. The most important application of the invariant manifold theory to the mission design is the exploitation of the

saddle component associated with the three collinear points, in particular with \mathcal{L}_1 and \mathcal{L}_2 ^[14]. The \mathcal{L}_3 dynamics is quite slow and its location quite far to represent a valuable mission analysis option, however also some approaches to reach this point, in the Sun-Earth CR3BP have been developed^[33].

There exists a stable and an unstable manifold winding, respectively, on or off, for positive times, the periodic solution as well as from an unstable equilibrium point since in both cases a (very large) saddle component exists.

3.2.1 Manifold Globalization Procedure

Let us start with the computation of the invariant manifolds associated with the equilibrium point^[1]. With this aim it is sufficient to perturb the initial state from the equilibrium position along the hyperbolic directions. This *Manifold Globalization Procedure* requires the propagation, under the full CR3BP equations, of initial conditions on the saddle component of the flow around an unstable equilibrium point^[66].

These directions are given by the eigenvectors associated with the real eigenvalues of the matrix of the linear system (Eq. (2.35)), \vec{u}_s/\vec{u}_u . An equilibrium position is shifted on one of these by means of the application of a small perturbation. This perturbation is applied along the positive and negative directions and the corresponding initial state is propagated forward/backward in time to compute the unstable/stable manifold. This means that: $\vec{x}_0^{W_{\mathcal{L}_i}^s} = \vec{x}_e \pm d\vec{u}_s$ has to be backward integrated to compute the stable manifold, while $\vec{x}_0^{W_{\mathcal{L}_i}^u} = \vec{x}_e \pm d\vec{u}_u$ gives, by forward integration, the unstable manifold associated with the generic collinear point \vec{x}_e . The double sign for each situation gives the positive and negative branch and $d > 0$ is the small perturbation.

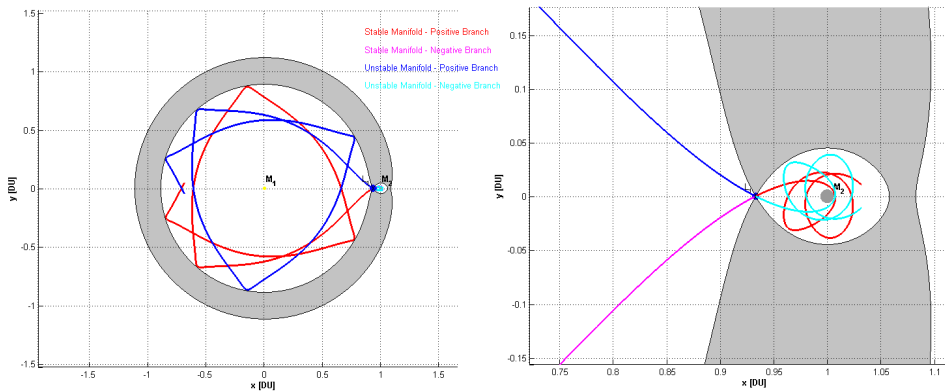


Figure 3.12: One dimensional manifolds of \mathcal{L}_1 in the Sun-Jupiter system.

Considering the Sun-Jupiter system ($\mu = 9.5369e-4$), the two branches of these one dimensional stable and unstable manifolds of \mathcal{L}_1 and \mathcal{L}_2 are depicted in Fig. 3.12 and 3.13.

This approach results in invariant “lines”, actually one dimensional manifolds, associated with a generic unstable point. It is interesting to observe that the one dimensional manifolds of \mathcal{L}_2 , as well as the two dimensional ones of a periodic orbit around this point, after performing several revolutions in the m_2 realm are able to move into the m_1 realm. This holds as the energy level assures that the \mathcal{L}_1 gate is already open (cfr. Sec. 2.2.4) and the CR3BP dynamics lead $W_{\mathcal{L}_2}^{s/u}$ to pass very close to \mathcal{L}_1 experiencing its unstable dynamics.

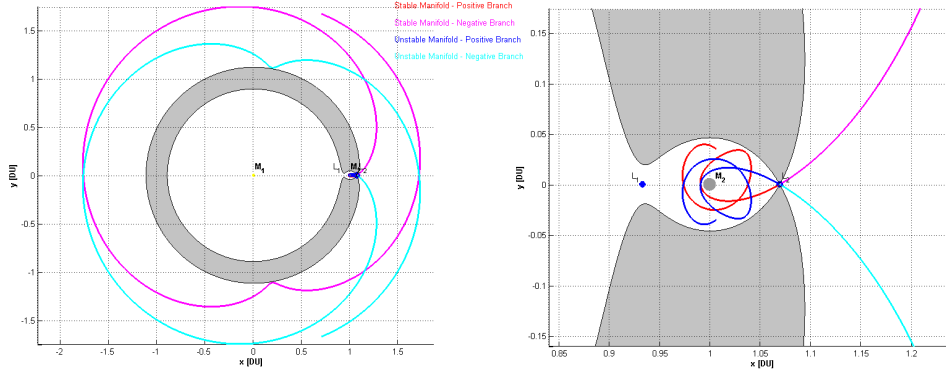


Figure 3.13: One dimensional manifolds of \mathcal{L}_2 in the Sun-Jupiter system.

One of the most representative applications of the CR3BP to a real system comes out from the observation of orbit of the comet P/Oterma^[6]. This comet experiences a transition from a $2:3$ Jupiter resonant orbit to a $3:2$ resonance. This transition brings the comet from the outside to the inside of the Jupiter orbit and the crossing follows exactly the chain resulting from the linking of \mathcal{L}_1 and \mathcal{L}_2 one dimensional manifolds of the Sun-Jupiter system^[67].

A manifold associated with a periodic solution is a hyper-surface made out of a collection of orbits. These are the asymptotic orbits dividing passing and non-passing trajectories through the Equilibrium Region (cfr. Sec. 2.2.5). This is obvious for the planar problem (due to the three dimensional constraint introduced by the Jacobi constant) and has been demonstrated^[66] also for the spatial version, where the manifolds under consideration are associated with Halo orbits.

The computation of the manifolds pertinent to a periodic orbit follows a similar approach like the computation of the one dimensional manifolds.

Initial conditions on the saddle component of the flow around a periodic orbit have to be identified. The main difference is that the matrix of coefficients is replaced by a linear approximation of the flow^{[1][14]}. This linear mapping is again represented by the monodromy matrix introduced in Sec. 3.1.1: $\vec{x} \rightarrow \vec{x}_0 + M(\vec{x} - \vec{x}_0)$.

Thus, once M associated to a periodic solution has been obtained, the manifolds are given by the propagation of a small perturbation, $d > 0$, along the directions of the stable/unstable Floquet multipliers, i.e. the eigenvectors of M , \vec{v}_s/u , after one period. The initial conditions are given by: $\vec{x}_0^{W_{p.o.}^s} = \vec{x}_0 \pm d\vec{v}_s$ for the backward propagation to compute the stable manifold and $\vec{x}_0^{W_{p.o.}^u} = \vec{x}_0 \pm d\vec{v}_u$ forward propagating for the unstable manifold. Here \vec{x}_0 is any initial condition lying on the center part of the flow in the neighborhood of an unstable equilibrium point, e.g. a point of a Lyapunov/Halo orbit. The whole invariant manifolds are given by the envelope of the paths obtained by this procedure repeated for all the values of \vec{x}_0 .

In Fig. 3.14 and 3.15 the two branches, one in the inner/outer realms and the other one in the m_2 realm are represented for two Lyapunov orbits with the same energy ($J = 3.0331$) around \mathcal{L}_1 and \mathcal{L}_2 in the Sun-Jupiter system.

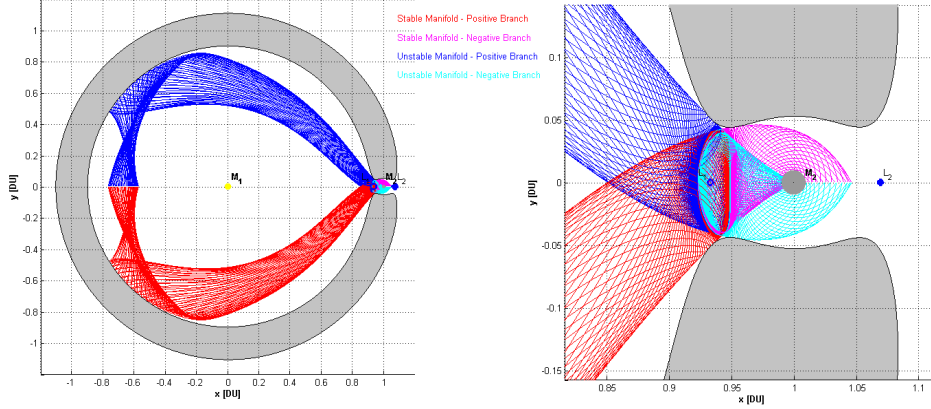


Figure 3.14: Two dimensional manifolds of \mathcal{L}_1 with $J = 3.0331$, for the Sun-Jupiter system in the inner and in the Jupiter realm.

The value of d has to be small in order to introduce an error not larger than the linear approximation validity, but not so small to not fall in the asymptotic behavior of the manifold; this depends on the mass parameter of the specific system.

Due to the complex nature of non-Keplerian motions, the underlying dynamical systems can be only partially treated by means of theoretical tech-

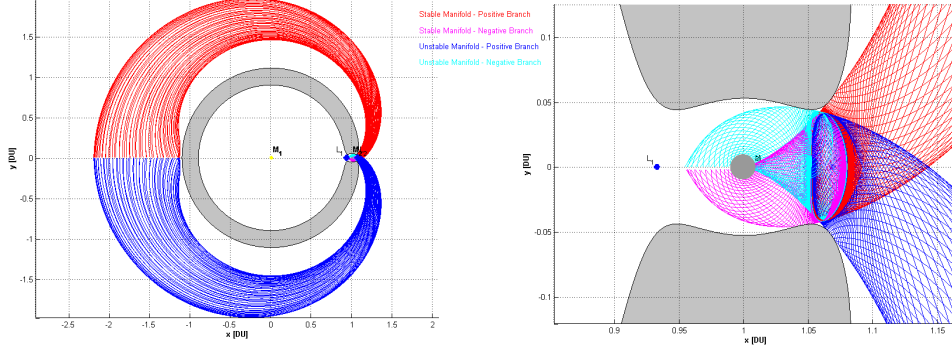


Figure 3.15: Two dimensional manifolds of \mathcal{L}_2 with $J = 3.0331$, for the Sun-Jupiter system in the outer and in the Jupiter realm.

niques. Thus, several numerical approaches have been developed to exploit the structures enabled by these models. Beside the manifold globalization procedure here implemented, the *set oriented approach* deserves to be mentioned^[68]. In this method the invariant manifolds, that are actually invariant sets of the CR3BP, are computed by means multilevel subdivision procedures. The phase space is divided into boxes and many short term propagations are performed in order to identify the boxes belonging to the invariant object and the ones to discharge. This approach is particularly useful to detect intersections among manifolds, especially in high dimensions, and has been applied also to non conventional interplanetary trajectories^[69]. Similar approaches can also be used to extract statistical information and for optimization purposes.

3.2.2 Normal Forms to Compute Invariant Manifolds Near and Far the Libration Points

Another approach for the computation of the invariant manifold is based on a more mathematical technique. The idea is to compute a higher order approximation of the flow^[70] and restricting to the hyperbolic directions. This can be done by approaching the CR3BP as a perturbed version of the Kepler problem.

The procedure here outlined tends to apply several transformations to the PCR3BP Hamiltonian to produce an approximate expression analytically integrable in two domains: near and far from a libration point^[71]. The planar version of the problem is used and the first libration point is considered.

Let us recall the Hamiltonian formulation of the problem, Eq. (2.28),

that for the PCR3BP can be written in a m_1 centered frame as:

$$H_0(\vec{\mathbf{R}}, \dot{\vec{\mathbf{R}}}, t, T) := T + \frac{|\dot{\vec{\mathbf{R}}}|^2}{2m} - mm_1 \frac{1}{|\vec{\mathbf{R}}^{(2)}|} + mm_2(\vec{\mathbf{R}} \cdot \vec{\mathbf{R}}_2(t)) - mm_2 \frac{1}{|\vec{\mathbf{R}} - \vec{\mathbf{R}}_2(t)|} \quad (3.5)$$

where $\vec{\mathbf{R}}_2(t)$ is the time dependent position of the smaller primary and T the time conjugate variable. This is defined with respect to the symplectic form⁴ $d\vec{\mathbf{R}} \wedge d\dot{\vec{\mathbf{R}}} + dt \wedge dT$ (small and capital letters are intended as conjugate variables and \wedge is the cross product) and with $m > 0$ free parameter. This parameter is actually related to the perturbative parameter and in this form the perturbation theory can be applied. In a perturbative formulation the motion of the massless body m_3 is determined by the main gravity field of m_1 , but perturbed by another gravitational attraction due to m_2 . so the perturbation intensity is proportional to the small primary mass. This is, indeed, also the reason why a given CR3BP system is defined only by means of the small primary mass, the mass parameter introduced in Sec. 2.2.1.

The perturbative parameter can be rephrased as: $\varepsilon := mm_2 = m(1 - m_2) = m(1 - M)$ and m chosen as $m = M^{-2/3}$. However, in this way it is not clear the magnitude of the parameter ε , which has to be much smaller than the large mass determining the main gravity field. With this aim, let us introduce: $M = 1 - \delta^3$ that makes clear that the perturbation δ is much smaller than the mass M . The relations between these two parameters are:

$$\begin{aligned} \varepsilon &= M^{-2/3}(1 - M) = (1 - \delta^3)^{-2/3}\delta^3 \\ \delta(\varepsilon) &= \sqrt[3]{\varepsilon} - \frac{2}{9}\sqrt[3]{\varepsilon^4} + O(\sqrt[3]{\varepsilon^7}) \end{aligned} \quad (3.6)$$

where the second one can be obtained by inverting the first one and expanding $\delta(\varepsilon)$.

Now the aim is to perform several manipulations to transform the Hamiltonian in a suitable form for the subsequent normalization procedure. For this purpose Delaunay-Poincaré Variables are introduced^[26].

To apply the Delaunay coordinates, two preliminary steps are required. The Hamiltonian has to be re-written in polar coordinates $((r, \tilde{\varphi}), (R, \tilde{\Phi}))$ and then made time independent. This is the equivalent of the change of reference

⁴A symplectic form is a 2-form (a map taking 2-dim vectors and returning a number) which is closed on a smooth manifold M and non-degenerate. A 2-form between $u, v \in \mathbb{R}^2$ is the determinant of $[u_1 \ v_1, u_2 \ v_2]$, i.e. the area defined by the two vectors. It is a skew-symmetric, non-degenerate bilinear form and a vectorial space endowed with this is a symplectic vectorial space. All the canonical transformations are defined on such a kind of spaces.

system from the inertial to the rotating one. The resulting Hamiltonian reads:

$$H_{\text{spc}}(R, r, \Phi, \varphi) := \frac{R^2}{2m} + \frac{\Phi^2}{2mr^2} - \frac{mM}{r} - \Phi + \varepsilon r \cos \varphi - \varepsilon \frac{1}{\sqrt{r^2 + 1 - 2r \cos \varphi}} \quad (3.7)$$

So far all the transformations are symplectic and it is already possible to identify the perturbative contributes. The last two terms are ε proportional, so they have to be small everywhere to consider the gravity of m_2 a perturbation. However, the rightmost term blows up when the angular variable $\varphi = 0$ and $r = 1$. This is the situation when the test particle collides with the small primary; when m_3 is too close to m_2 the dynamics can not be considered as determined by m_1 and perturbed by m_2 and the described perturbative approach can not be applied.

Originally developed for the two body problem (which results completely integrable in this form), the Delaunay variables^[17] are applied to the CR3BP to transform the system into a quasi-integrable system (cfr. Sec. 2.4).

This means that there exists a canonical transformation such that: $\Psi_D : (L, \ell, G, g) \rightarrow (R, r, \Phi, \varphi)$ is *implicitly*^[16] defined by the *generating function* $S(L, G, r, \varphi)$ ⁵.

The resulting Hamiltonian takes the form of a nearly integrable system:

$$H_D(L, \ell, G, g) := \underbrace{-\frac{1}{2L^2} - G}_{\text{IntegrablePart}} + \underbrace{\varepsilon r \cos \varphi - \varepsilon \frac{1}{\sqrt{r^2 + 1 - 2r \cos \varphi}}}_{\text{PerturbativePart}}, \quad (3.8)$$

The Delaunay coordinates are actually Action-Angle variables (cfr. Sec. 2.2). Thus, the problem must be stated in these variables to investigate about its integrability (cfr. Sec. 2.1 and 2.4). A Hamiltonian depending only on the Action variables is exactly integrable since they remain constant through the motion and only the relative Angles vary filling the tori^[26]. L, G are Actions, while ℓ, g are the Angles variables. The Delaunay variables are implicitly defined, i.e $r = r(L, \ell, G)$ and $\varphi = g + v$ with $v = v(L, \ell, G)$ the *true anomaly*. These abstract variables have a physical meaning and can be related to the classical orbital parameters^[13]:

⁵A generating function is a sort of passage between two sets of canonical variables. In general a transformation $g : (p, q) \rightarrow (P, Q)$ is canonical if $PdQ - pdq = dS$ for a suitable generating function S . There exist four basic kinds of generating functions involving a mixture of “old” and “new” variables. The Delaunay’s one reads:

$$S(L, G, r, \varphi) = \int \sqrt{-\frac{m^4 M^2}{L^2} + \frac{2m^2 M}{r} - \frac{G}{r^2}} dr + G\varphi$$

- $L = m\sqrt{Ma}$, it is related to the semi-major axis a ;
- $\ell = u - e \sin u$, it is the mean anomaly satisfying the Kepler equation;
- $G = \sqrt{(1 - e^2)L}$, $|G|$ is the module of the angular momentum;
- g is the argument of pericenter.

The integrable part of Eq. (3.8) is composed by two terms. The first one is the Keplerian Hamiltonian, it is analytically integrable and also *degenerate* since it depends only on one Action although there are two of such variables. The second term of the integrable part results from the rotation of the system of reference^[26].

The Hamiltonian obtained at this step, Eq. (3.8), suffers from a singularity which appears for zero eccentricity ($e = \sqrt{1 - G^2/L^2}$); the Poincaré variables are introduced to remove this lack. This is done by means of the two step canonical transformation:

$$\begin{aligned} \Psi_{P_t} : \left((\Lambda, \Gamma), (\lambda, h) \right) &\rightarrow \left((L, G), (\ell, g) \right) \Rightarrow \begin{cases} \Lambda = L, & \Gamma = L - G \\ \lambda = \ell + g, & h = -g \end{cases} \\ \Psi_{P_{aa}} : \left((\Lambda, \eta), (\lambda, \xi) \right) &\rightarrow \left((\Lambda, \Gamma), (\lambda, h) \right) \Rightarrow \begin{cases} \sqrt{2\Gamma} \cos h = \eta \\ \sqrt{2\Gamma} \sin h = \xi. \end{cases} \end{aligned} \quad (3.9)$$

such that $\Gamma = (\eta^2 + \xi^2)/2$. The first transformation is just a translation and the second one is symplectic preserving the 2-form $d\Gamma \wedge dh = d\eta \wedge d\xi$.

Combining all the transformations introduced $\Psi_{DP} : ((\Lambda, \eta), (\lambda, \xi)) \rightarrow (\vec{\mathbf{R}}, \vec{\dot{\mathbf{R}}})$ the Hamiltonian takes the nearly integrable form:

$$H^{DP} = -\frac{1}{2\Lambda^2} - \Lambda + \frac{\eta^2 + \xi^2}{2} + \varepsilon P(\Lambda, \eta, \lambda, \xi; \varepsilon) \quad (3.10)$$

where the first two terms represent again the integrable part. The perturbative term, is a quite complicate expression composed by two parts:

$$\begin{aligned} \varepsilon P &:= P_1 + P_2 \\ P_1 &= \delta^3(1 - \delta^3)^{-1/3} \Lambda^2 \left[\cos(\lambda + G_0) - \frac{\eta}{\sqrt{\Lambda}} F_1 + \right. \\ &\quad \left. - \frac{\xi}{\sqrt{\Lambda}} F_1 \left(\sin(\lambda + G_0) \frac{\eta}{\sqrt{\Lambda}} F_1 + \cos(\lambda + G_0) \frac{\xi}{\sqrt{\Lambda}} F_1 \right) F_2 \right] \end{aligned}$$

$$\begin{aligned}
P_2 = & -\delta^3(1-\delta^3)^{-2/3} \left\{ 1 + (1-\delta^3)^{2/3} \Lambda^4 \left[1 - 2 \cos(\lambda + G_0) \frac{\eta}{\sqrt{\Lambda}} F_1 + \right. \right. \\
& 2 \sin(\lambda + G_0) \frac{\xi}{\sqrt{\Lambda}} F_1 + \cos^2(\lambda + G_0) \frac{\eta^2}{\Lambda} F_1^2 + \sin^2(\lambda + G_0) \frac{\xi^2}{\Lambda} F_1^2 + \\
& \left. - 2 \cos(\lambda + G_0) \sin(\lambda + G_0) \frac{\eta \xi}{\Lambda} F_1^2 \right] - 2(1-\delta^3)^{1/3} \Lambda^2 \left[\cos(\lambda + G_0) + \right. \\
& \left. - \frac{\eta}{\sqrt{\Lambda}} F_1 - \frac{\xi}{\Lambda} F_1^2 \left(\sin(\lambda + G_0) \eta + \cos(\lambda + G_0) \xi \right) F_2 \right] \Big\}^{-1/2} \quad (3.11)
\end{aligned}$$

The first one, P_1 , is of order δ^3 everywhere so it is bounded independently on the specific region of the phase space, while the second part, P_2 , is bounded only far away from the singularity. There are regions where P_2 blows up to infinity and thus it does not represent anymore a perturbative term and the perturbative theory can not be applied. This is the consequence of the singularity already stressed in Eq. (3.7) and it highlights the necessity to define a region of validity for the current approach.

The first libration point, \mathcal{L}_1 , is an equilibrium point of the original Hamiltonian, so it has to be an equilibrium point also for the transformed one. Its coordinates in these new variables are:

$$\begin{aligned}
\Lambda_{\mathcal{L}_1} = L_{\mathcal{L}_1} = 1 - \frac{2}{\sqrt[3]{3}}\delta + \frac{37}{6\sqrt[3]{3^2}}\delta^2 - \frac{175}{27}\delta^3 + O(\delta^4), \quad \lambda_{\mathcal{L}_1} = 0, \quad \xi_{\mathcal{L}_1} = 0, \\
\eta_{\mathcal{L}_1} = -\sqrt{2(L_{\mathcal{L}_1} - G_{\mathcal{L}_1})} = -\sqrt[3]{3^2}\delta + \frac{7}{\sqrt[3]{3^2}}\delta^2 - \frac{355}{72}\delta^3 + O(\delta^4) \quad (3.12)
\end{aligned}$$

Normal forms are a standard tool in Hamiltonian mechanics used to study the dynamics in a neighborhood of invariant objects, like equilibrium points, periodic orbits or invariant tori^[70]. From a theoretical point of view, they provide nonlinear approximations of the dynamics in a neighborhood of the invariant object. From a more practical point of view, they can be used as a computational method to obtain very accurate approximations of the flow by taking the normal form up to a suitable finite order^[72]. This is the classical approach and it is applied to the CR3BP considering the Hamiltonian in Delaunay-Poincaré variables, Eq. (3.10), and \mathcal{L}_1 .

To perform the normalization procedure around \mathcal{L}_1 the Hamiltonian has to be re-written by considering that the variables are centered in the libration point and are δ -close to it:

$$\begin{aligned}
\Lambda = \Lambda_{\mathcal{L}_1} + \delta \hat{\Lambda} = 1 + (\Lambda_1 + \hat{\Lambda})\delta + \Lambda_2 \delta^2 + O(\delta^3), \quad \lambda = \lambda_{\mathcal{L}_1} + \delta \hat{\lambda} = \delta \hat{\lambda}, \\
\eta = \eta_{\mathcal{L}_1} + \delta \hat{\eta} = (\eta_1 + \hat{\eta})\delta + \eta_2 \delta^2 + O(\delta^3), \quad \xi = \xi_{\mathcal{L}_1} + \delta \hat{\xi} = \delta \hat{\xi} \quad (3.13)
\end{aligned}$$

The resulting Hamiltonian expanded in δ , reads:

$$H^{\mathcal{L}_1}(\hat{\Lambda}, \hat{\eta}, \hat{\lambda}, \hat{\xi}; \delta) = \bar{C} - \frac{27}{2}\hat{\Lambda}^2 + \frac{3}{2}\hat{\lambda}^2 - \frac{5}{2}\hat{\eta}^2 + \frac{13}{2}\hat{\xi}^2 + 12\hat{\Lambda}\hat{\eta} + 6\hat{\lambda}\hat{\xi} + \delta P(\hat{\Lambda}, \hat{\eta}, \hat{\lambda}, \hat{\xi}; \delta) \quad (3.14)$$

with \bar{C} generic constant defined by initial conditions (non influential as are the derivatives of H involved in the canonical equations). At this point the first step is to put the quadratic terms of H (the ones resulting in the linear approximation) in a suitable form. With this aim, the following lemmas hold^[71]:

- There exists a linear canonical change of coordinates that puts the unperturbed quadratic part of $H^{\mathcal{L}_1}$ in diagonal form, i.e. exists: $\Phi_0 : (\tilde{p}, \tilde{q}, \tilde{z}, \tilde{\bar{z}}) \rightarrow (\hat{\Lambda}, \hat{\eta}, \hat{\lambda}, \hat{\xi})$, such that:

$$H^*(\tilde{p}, \tilde{q}, \tilde{z}, \tilde{\bar{z}}) := H^{\mathcal{L}_1} \circ \Phi_0 = \lambda_0 pq + \omega_0 z \bar{z} + \delta P(p, q, z, \bar{z}; \delta) \quad (3.15)$$

- Fix an integer $j_0 > 0$ and let H_2^* be the quadratic part of H^* . Then for δ small enough there exists a canonical transformation δ -close to the identity: $\Phi_\delta : (p, q, z, \bar{z}) \rightarrow (\tilde{p}, \tilde{q}, \tilde{z}, \tilde{\bar{z}})$, such that:

$$H_2^* \circ \Phi_\delta = h_2(p, q, z, \bar{z}) = \lambda(\delta) pq + \omega(\delta) z \bar{z} \quad (3.16)$$

where $\lambda(\delta) = \sum_{j=0}^{j_0} \lambda_j \delta^j$, $\omega(\delta) = \sum_{j=0}^{j_0} \omega_j \delta^j$.

These lemmas perform the diagonalization of the quadratic part of the Hamiltonian for all orders in δ , i.e. they put the second order part in the form $h_2 = \lambda(\delta) pq + \omega(\delta) z \bar{z}$, where for $\delta = 0$ the unperturbed coefficients are intended^[70]. These unperturbed coefficients are the 0-order approximations in the perturbative parameter and are the same eigenvalues introduced, for the spatial case, in the linear energy expression of Eq. (2.41). These series are the ones stated by the Moser Theorem (cfr. Sec. 2.2.5) beginning with quadratic terms of the center and saddle components.

The Hamiltonian is now in the form: $H =: H^* \circ \Phi_\delta = h_2 + H_3 + H_4 + \dots$, where H_k , $k \geq 3$ is a polynomial of degree k in (p, q, z, \bar{z}) . The aim is now to cancel out as many terms as possible for increasing order of the polynomial H_k ^{[71][73]}.

The approach is outlined for the cubic terms that have the structure: $H_3 = \sum_{m+n+a+\bar{a}=3} H_{m,n,a,\bar{a}}(\delta) p^m q^n z^a \bar{z}^{\bar{a}}$. To erase terms, a generating function \mathcal{X} of known structure (third order in this case, \mathcal{X}_3), but unknown coefficients is introduced with the aim to detect the coefficients such that the resulting combination $H \circ X_{\mathcal{X}_3}^1$ cancels out as many terms as possible. $X_{\mathcal{X}_3}^1$ is the flow at time one of \mathcal{X}_3 that is nothing else than a Hamiltonian^[18].

This approach works since the Liouville theorem states that the flow of a Hamiltonian system is volume preserving at each time^[16].

The mathematical approach to this transformation is to use the *Lie Series*^[74] and iteratively solve for the unknown coefficients of the function $\mathcal{X}_3 = \sum_{m+n+a+\bar{a}=3} \mathcal{X}_{m,n,a,\bar{a}}(\delta) p^m q^n z^a \bar{z}^{\bar{a}}$. The *Lie Series* is an approximation of the composition between H and \mathcal{X}_3 as sum of coefficients $L_{\mathcal{X}_3}^j$ of increasing order in j . These coefficients can be obtained by combining the third order part of the Hamiltonian with the generating function by means of the *Poisson Brackets* (cfr. Sec. 2.1): $\{F, G\} := \partial_p G \partial_q F - \partial_q G \partial_p F + i(\partial_z G \partial_{\bar{z}} F - \partial_{\bar{z}} G \partial_z F)$ preserving, in this case, the symplectic structure: $idz \wedge d\bar{z} + dp \wedge dq$.

In equations:

$$\begin{aligned} H^{[1]} &:= H \circ X_{\mathcal{X}_3}^1 = \sum_{j=0}^{\infty} \frac{L_{\mathcal{X}_3}^j}{j!} = H + \{H, \mathcal{X}_3\} + \frac{1}{2} \{\{H, \mathcal{X}_3\}, \mathcal{X}_3\} + \dots \\ &= h_2 + [H_3 + \{h_2, \mathcal{X}_3\}] + [H_4 + \{H_3, \mathcal{X}_3\} + \frac{1}{2} \{\{h_2, \mathcal{X}_3\}, \mathcal{X}_3\}] + \dots \\ &=: h_2 + H_3^{[1]} + H_4^{[1]} + \dots \end{aligned}$$

Thus, the goal is to have \mathcal{X}_3 such that:

$$\begin{aligned} H_3 + \{h_2, \mathcal{X}_3\} &= 0 \quad \Rightarrow \\ \sum_{m+n+a+\bar{a}=3} \{H_{m,n,a,\bar{a}} + [\lambda(m-n) + i\omega(a-\bar{a})] \mathcal{X}_{m,n,a,\bar{a}}\} p^m q^n z^a \bar{z}^{\bar{a}} &= 0 \end{aligned} \quad (3.17)$$

This equation is known as the *Homological Equation* that has to be solved for the coefficients $\mathcal{X}_{m,n,a,\bar{a}}$. It is obvious that this equation can be solved only if it is invertible, so when the coefficient of the unknown is different from zero:

$$\chi_{m,n,a,\bar{a}} := \begin{cases} \frac{-H_{m,n,a,\bar{a}}}{\lambda(\delta)(m-n) + i\omega(\delta)(a-\bar{a})} & \text{if } m \neq n \text{ or } a \neq \bar{a} \\ 0 & \text{if } m = n \text{ and } a = \bar{a} \end{cases} \quad (3.18)$$

In this specific case, of course, the second situation is never possible as $m+n+a+\bar{a}=3$ and this is true for all the odd order polynomials of the Hamiltonian. However if the k -order terms are of even order, the terms with $m=n$ and $a=\bar{a}$ of order k must be kept. This results in a Hamiltonian of the form $H = h_2 + h_4 + h_6 + h_8 + \dots$ where $h_k = \sum_{2m+2a=k} h_{m,m,a,a} (pq)^m (z\bar{z})^a$.

In this way pq and $z\bar{z}$ are integrals of motion for the truncated Hamiltonian and the stable manifold takes the form $[p_0, 0, 0, 0]$, while the unstable manifold can be written as $[0, q_0, 0, 0]$. It has to be stressed that the variables (p, q, z, \bar{z}) are different from the original (p, q, z, \bar{z}) since they result from

the application of all these canonical transformations to the original set of variables.

These two new first integrals are not linearly independent of the linearized energy integral, Eq. (2.36); in particular these are its two part (the saddle and the center one) in the planar version of the model.

So far we worked δ -close to \mathcal{L}_1 to obtain an analytic approximation of the invariant manifolds up to an arbitrary order, this is comparable with some other works^{[73][50]}. The aim now is to define an approximation of the dynamics in a not yet investigated region, i.e. to put the Hamiltonian in a suitable normal form in a region far from \mathcal{L}_1 ^[71]. The same Lie Series approach is used and, similarly, the goal is to define a set of canonical transformations accomplishing the task.

To work far from the equilibrium point, let us recall the Hamiltonian in Delaunay-Poincaré variables, Eq. (3.10), and apply the symplectic transformation: $\sqrt{2}z = \eta + i\xi$, $\sqrt{2}\bar{z} = \eta - i\xi$, often referred as the *complexification* of H . The Hamiltonian now reads:

$$H^{(0)} := h^{(0)}(\Lambda, z\bar{z}) + \varepsilon P(\Lambda, \lambda, z, \bar{z}; \varepsilon), \quad h^{(0)}(\Lambda, z\bar{z}) := -\frac{1}{2\Lambda^2} - \Lambda + z\bar{z} \quad (3.19)$$

This complexification is introduced in order to allow the estimation of the perturbation. In particular, analyzing the order of each perturbative contribution in Eq. (3.11), it turns out that the perturbation is bounded into the domain^[71]:

$$\mathcal{D} := \{(\Lambda, \lambda, z, \bar{z}) \text{ s.t. } 0 < |1 - \Lambda| < \mu, \quad |z|, |\bar{z}| \leq \mu, \quad \bar{\lambda} < \lambda < 2\pi - \bar{\lambda}\} \quad (3.20)$$

where $\mu > 0$ small and $\varepsilon \ll \mu$. This means that inside \mathcal{D} a perturbative approach can be applied.

The main differences of this normal form with respect to the previous one is that this is a partial normal form, only in z, \bar{z} . This is a transformation that is local in z, \bar{z} with Λ close to 1. This choice makes possible to keep the variable λ of order 1 in $[\bar{\lambda}, 2\pi - \bar{\lambda}]$, namely to have an analytic approximation of the Hamiltonian in a suitable region far from equilibria. A drawback of this method is that the homological equation is no more an algebraic equation, but it becomes an Ordinary Differential Equation.

It is like to normalize the Hamiltonian only in the Actions allowing the Angles to remain large. In that way it is possible to move away from the libration point with the normalization procedure. This process requires the normalization only in a couple of conjugated variables.

The perturbation coefficients P can be expanded in the variables and

considering that this is analytic also in ε :

$$P = \sum_{j \geq 0} \varepsilon^j P^{(j)}(\Lambda, \lambda, z, \bar{z}), \quad P^{(j)}(\Lambda, \lambda, z, \bar{z}) = \sum_{a, \bar{a} \geq 0} P_{a, \bar{a}}^{(j)}(\Lambda, \lambda) z^a \bar{z}^{\bar{a}} \quad (3.21)$$

The generating function with unknown coefficients we are searching for has exactly the same structure as Eq. (3.21), but $P^{(j)}$ is replaced by $\chi^{(j)}$ and $P_{a, \bar{a}}^{(j)}$ by $\chi_{a, \bar{a}}^{(0)}$.

Considering again the flow at time one of the Hamiltonian $\varepsilon \chi^{(0)}$, $X_{\varepsilon \chi^{(0)}}^1$, the Lie Series method, at the 0-step, reads:

$$H^{(1)} := H^{(0)} \circ X_{\varepsilon \chi^{(0)}}^1 = h^{(0)} + \varepsilon [P^{(0)} + \{h^{(0)}, \chi^{(0)}\}] + O(\varepsilon^2) \quad (3.22)$$

To simplify the terms in the square brackets, namely the first order terms in ε , we reduce again to the homological equation in the form:

$$[\dots] = \sum_{a, \bar{a} \geq 0} \left[P_{a, \bar{a}}^{(0)}(\Lambda, \lambda) + i(a - \bar{a}) \chi_{a, \bar{a}}^{(0)}(\Lambda, \lambda) - \left(\frac{1}{\Lambda^3} - 1 \right) \partial_\lambda \chi_{a, \bar{a}}^{(0)}(\Lambda, \lambda) \right] z^a \bar{z}^{\bar{a}} \quad (3.23)$$

This equation has to be solved for the unknown coefficients $\chi_{a, \bar{a}}^{(0)}$, i.e.:

$$\begin{cases} P_{a, \bar{a}}^{(0)}(\Lambda, \lambda) + i(a - \bar{a}) \chi_{a, \bar{a}}^{(0)}(\Lambda, \lambda) - \left(\frac{1}{\Lambda^3} - 1 \right) \partial_\lambda \chi_{a, \bar{a}}^{(0)}(\Lambda, \lambda) = 0 & a \neq \bar{a} \\ \chi_{a, a}^{(0)}(\Lambda, \lambda) = 0 & a = \bar{a} \end{cases} \quad (3.24)$$

The only difficulty in solving this ODE is the degeneration close to $\Lambda = 1$ ^[71]. The canonical transformation is given by the flow at time one of the Hamiltonian $\chi^{(0)}$. It is analytic in a suitable complex neighborhood of the domain \mathcal{D} .

Applying $\chi^{(0)}$ the Hamiltonian takes the form:

$$H^{(1)} = H^{(0)} \circ X_{\varepsilon \chi^{(0)}}^1 = f_0(\Lambda) + z\bar{z} + \varepsilon g_1(\Lambda, \lambda, z\bar{z}) + O(\varepsilon^2) \quad f_0(\Lambda) := -\frac{1}{2\Lambda^2} - \Lambda \quad (3.25)$$

Like before, by means of this approach we gain that $z\bar{z}$ is an integral of the motion for the truncated Hamiltonian. Thus, also in this case, it is possible to obtain two first integrals independent in involution and this is sufficient to state (and compute in the outlined way) that the system is locally integrable (cfr. Sec. 2.1).

Both approaches have been implemented^[71] and the relevant coefficients detected up to order 15 for the normal form near the \mathcal{L}_1 libration point and up to order 5 for the one far away. The main numerical issue to take care is that the application of the Lie method quickly generates thousands of quite

complicated coefficients^[73] thus time consuming to compute and to store. The numerical way adopted is based on the *Lie-Deprit triangle*^[75].

All in all, the approach proposed presents two approximations, by means of truncated series, that can be analytically integrated to define the behavior of the flow near and far the equilibrium points of the PCR3BP and, in particular, it gives analytic expressions of the stable/unstable manifolds.

3.3 Homoclinic Orbits

Intersecting the images of the manifolds on a proper Poincaré section, it is possible to construct orbits winding to and off from the same periodic orbit (as well as from two different ones, cfr. Sec. 3.4). These are the so called *Homoclinic Orbits* that are double asymptotic to the same periodic (unstable) orbit (cfr. Sec. 2.4).

It has been proven that there exist homoclinic orbits in the interior and exterior realm and that the formers flow in counterclockwise sense while the others in clockwise direction^{[38][34]}. Analytical proofs exist only for transversal symmetric homoclinic orbits at the first intersection of stable and unstable manifold in the inner realm^[29], while in the exterior realm and for more encounter points there are only numerical explorations confirming the existence of these orbits^[14]. Moreover these orbits result to be transversal and, since these are given by the intersection of the stable and unstable manifold of the same periodic solution, this implies that also the stable and unstable manifold intersect transversally (cfr. Sec. 2.4)⁶.

Let us consider the Sun-Jupiter system and a periodic orbit around \mathcal{L}_1 with an Jacobi constant of 3.0380. Once the relevant Lyapunov orbit has been computed, it is possible to globalize the inherent manifold with the procedure outlined in Sec. 3.2.1. Considering a section located on the x -axis in the inner realm, it is possible to store the image of the stable and unstable manifold on that section, therefore build their Poincaré section. A point lying in the intersection of these images is a point that move towards the periodic solution for positive times (on the stable manifold) and also for negative times (on the unstable manifold)^[14]. This is the same concept introduced for the homoclinic points in Sec. 2.4.

A symmetric homoclinic connection in the inner realm is presented in Fig. 3.16 where the initial conditions are represented by the bold circle on the Poincaré section plane. Keep on integrating and considering not just the first intersection but the n^{th} with the section plane, it possible built homoclinic orbits performing more than a single loop in the inner realm.

⁶A given intersection is called transversal if at that point the tangent subspaces of the stable/unstable manifold span the complete tangent subspace at the point.

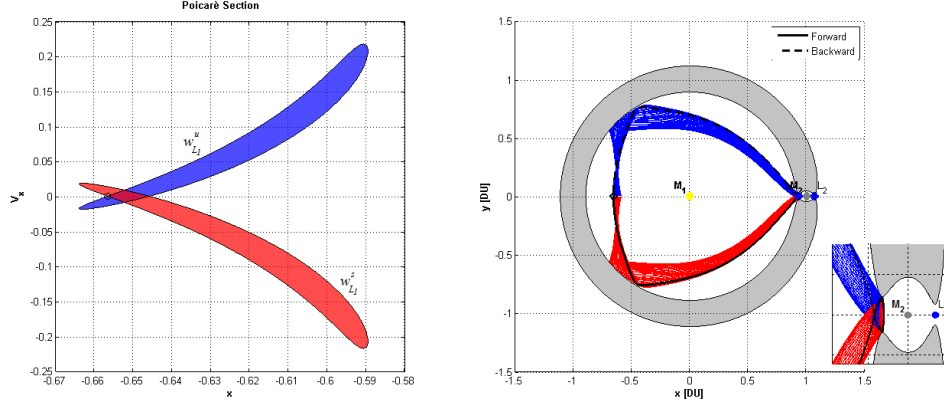


Figure 3.16: \mathcal{L}_1 Homoclinic connection for the Sun-Jupiter system in the inner realm; on the left on the Poincaré section plane and on the right in the position space.

It has been proven that the set of μ for which there are symmetric homoclinic orbits (with a generic number of cuts) is discrete^[29].

A similar approach can be also used to build homoclinic connections in the m_2 realm. In this case the branches of the manifolds to consider are the negative ones, i.e. the parts flowing towards m_2 . Again, the intersections with a section located on the x -axis, provide initial conditions winding to and off from the same periodic orbit. In Fig. 3.17 the two symmetric homoclinic connections resulting from the first cut of the stable and unstable manifold of a Lyapunov orbit around Sun-Jupiter \mathcal{L}_1 are shown.

The two initial conditions are again indicated with the bold circles in the leftmost plot and the one with the smaller x results in the homoclinic orbit experiencing the closer Jupiter passage.

All the initial conditions for symmetric homoclinic orbits are on the $v_x = 0$ axis.

3.4 Heteroclinic Orbits

Let us consider now the same methodology of the previous section to design ballistic solutions moving to and off from two different periodic orbits for positive and negative times; the *Heteroclinic Orbits*. This means defining an orbit that is on the stable manifold of a periodic (unstable) orbit and on the stable one of another periodic solution^[76].

In this case not just a single periodic orbit is required and the stable and unstable manifolds have to be generated both for a \mathcal{L}_1 Lyapunov orbit

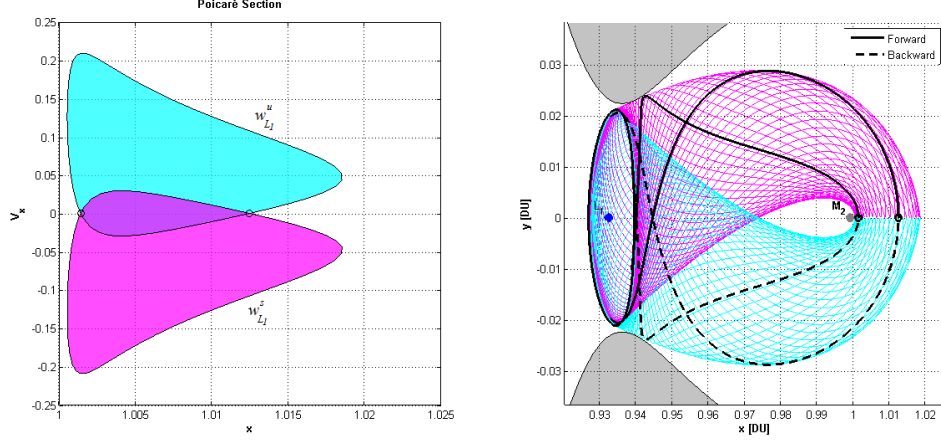


Figure 3.17: \mathcal{L}_1 Homoclinic connections for the Sun-Jupiter system in the Jupiter realm; on the left on the Poincaré section plane and on the right in the position space.

and for a \mathcal{L}_2 one. Locating a section along the y -axis, in the negative semi-plane at $x = 1 - \mu$, the image of the stable manifold of a periodic orbit can be stored together with the one of the unstable manifold of the other orbit. In this situation the intersection between these two images results in a solution moving for free between the two Lyapunov orbits. The selected plane maximizes the number of intersections of the manifolds for values of μ and J producing manifolds performing a limited number of revolutions around m_2 before escaping^[14].

Considering again the Sun-Jupiter system and $J = 3.03569$, the first image of the stable manifold of the relevant \mathcal{L}_1 Lyapunov does not intersect the one of the unstable manifold of the \mathcal{L}_2 Lyapunov. Thus, to design a heteroclinic connection with this value of μ and J , the second cut of the manifolds has to be computed. In Fig. 3.18 the first and second images of the \mathcal{L}_1 -stable and \mathcal{L}_2 -unstable manifolds are plotted together with the resulting symmetric heteroclinic connection. It is worth nothing that in this case the energy associated with the two periodic solutions, corresponding to the manifolds energy, has to be the same in order to consider the intersection of both branches on the same section as an initial condition to propagate forward and backward.

Also these heteroclinic connections are transversal, since again the intersection between manifolds is transversal; this is confirmed only by means of numerical explorations, although also tangential situations can appear^[39].

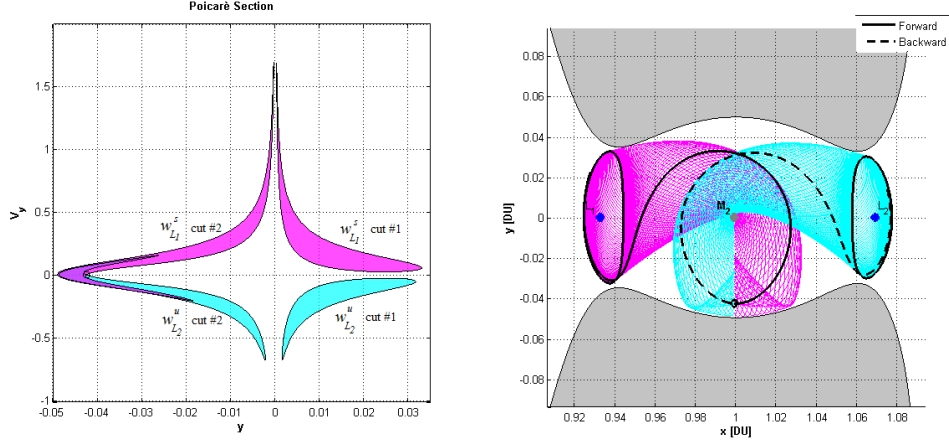


Figure 3.18: \mathcal{L}_1 - \mathcal{L}_2 Heteroclinic connection for the Sun-Jupiter system in the Jupiter realm; on the left on the Poincaré section plane and on the right in the position space.

Moreover, the sum of the cuts of both manifolds must be an even positive integer number and the number of revolutions around m_2 is one half of the sum of the cuts minus one^[71]. Since for the case of Fig. 3.18 the second intersection of the manifolds with the section plane is required, the resulting heteroclinic orbit performs one full revolution around the small primary. Keep on intersecting, heteroclinic orbits performing more revolutions around m_2 can be designed. It has to be pointed out, however, that the shape of the images of the manifolds become more and more complex and, due to the chaotic behavior of the model, there is a maximum number of cuts resulting in initial conditions enough accurate to propagate backward and forward to obtain homoclinic or heteroclinic connections (this increasing sensitivity is also observed designing the target ballistic trajectory in Sec. 6.1).

Due to the symmetry of the problem a reverse heteroclinic connection, going from a Lyapunov \mathcal{L}_1 orbit to a Lyapunov \mathcal{L}_2 orbit, is just the reflection of the trajectory of Fig. 3.18 with respect to the x -axis. Considering together these two heteroclinic connections result in a symmetric *heteroclinic cycle* moving back and forth between the two periodic solutions.

3.5 Transit Orbits

Once the existence of a generic homoclinic and heteroclinic connection has been, at least numerically, proven, it is possible to combine these two dynamics to obtain a *homoclinic-heteroclinic cycle*. This is a net of ballistic

connections between \mathcal{L}_1 and \mathcal{L}_2 passing through the three realms. To design such a net, the same energy value has to be assumed for the homoclinic and heteroclinic connections.

Besides the motion on the surface of these manifolds also the motion into their interior gives useful hints about the dynamics in the CR3BP. As observed in Sec. 2.2.5, an orbit flowing inside these tubes is able to transit from one realm to another, so an initial condition lying in the intersection of two manifolds inherits the dynamics of both. With these considerations, it is possible to design orbits with prescribed itineraries^{[14][40]}.

Let us assume again the planar case and an energy level assuring that the motion among the three realms is possible. The only kind of orbits able to transit through the m_2 realm are the ones into the intersection of the \mathcal{L}_2 -unstable and \mathcal{L}_1 -stable manifold for exterior to interior transitions and in the opposite way for interior to exterior transitions. Considering the Sun-Jupiter system and $J = 3.0331$, the stable and unstable manifolds of \mathcal{L}_1 and \mathcal{L}_2 intersect on a Poincaré section located at $x = 1 - \mu$ at the first cut (differently from the example of Fig. 3.18). This means that there exist heteroclinic connections performing no revolutions around Jupiter and the points in the intersection region are the only ones passing through the Jupiter realm for this energy value and this mass parameter. Fig. 3.19 presents the intersection of \mathcal{L}_2 -stable and \mathcal{L}_1 -unstable manifolds on the section plane and a couple of initial conditions resulting in a 0-loop heteroclinic connection and in a transit orbit. In particular, this passing orbit is able to flow from the inner realm to the Jupiter one and finally into the outer realm.

Such a kind of orbits are also “robust” in the sense that initial conditions near the assigned one follow the same path as these are expected to lie also into the intersection region.

This analysis outlines global structures to exploit to design orbits with prescribed interior- m_2 -exterior sequences just considering two dimensional maps. The manifold intersections can involve more than one cut and the intersection area has to be mapped forward up to the next intersection with the interior of the manifold satisfying the prescribed passage. This is a classical problem of *symbolic dynamics*^[29].

Finally, it is interesting to observe that several CR3BP can be coupled together and the manifold structures for each system computed. The intersection in the phase space of these nets defines a sort of “dynamical channels” where a massless body can move for free from one system to another.

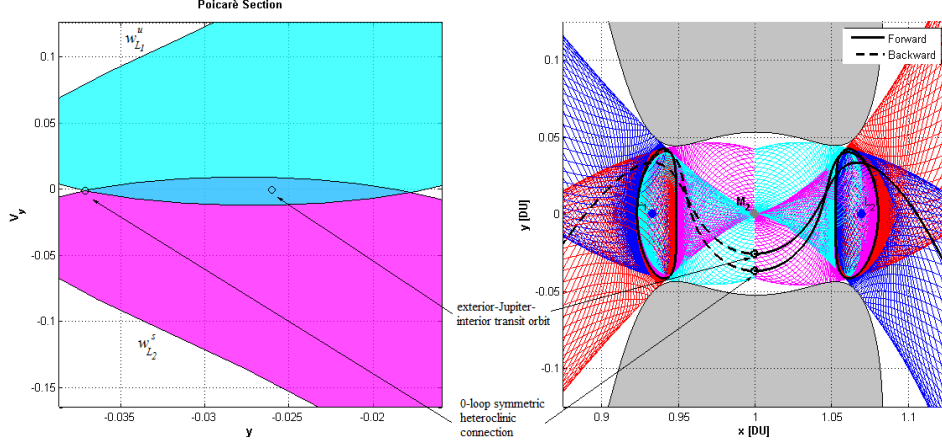


Figure 3.19: \mathcal{L}_1 - \mathcal{L}_2 transit orbit and Heteroclinic connection for the Sun-Jupiter system in the Jupiter realm; on the left on the Poincaré section plane and on the right in the position space.

3.6 Poincaré Sections

The phase space can reveal very important features of any dynamical system that are often hardly identifiable by looking at orbits in the position space. A powerful tool to disclose the structures of the phase space is the use of hyper-planes that intersect transversally the flow. For the PCR3BP these Poincaré sections (cfr. Sec. 2.2.3 and 3.3-3.5) are essential tools for a global study of the orbits where this can be done by means of two dimensional maps.

In the planar problem, the Jacobi integral identifies a three dimensional manifold in the four dimensional phase space where the motion has to take place^[48]. This manifold is the low dimensional version of Eq. (2.32):

$$M(\mu, C) = \{(x, y, \dot{x}, \dot{y}) \in \mathbb{R}^4 \mid J(x, y, \dot{x}, \dot{y}) - J(x_0, y_0, \dot{x}_0, \dot{y}_0) = 0\} \quad (3.26)$$

Let us consider now the intersection with a fix suitable plane placed in the phase space of the kind:

$$\gamma = \{(x, y, \dot{x}, \dot{y}) \in \mathbb{R}^4 \mid y = 0, \dot{y} > 0\} \quad (3.27)$$

This is a plane with a fix y component that is intersected transversally by the flow, i.e. the local linear subspaces of the flow are not tangent to the plane.

The domain of the intersection between the energy manifold and the plane γ can be analytically defined by considering that $J^{-1}(J|_0) \cap \gamma = \{x, \dot{x} \in$

$\mathbb{R}^2 | F(x, \dot{x}) > 0\}$ results in a square root, representing the velocity associated with the coordinate fixed by the plane location, that can not be negative^[47]. This means that:

$$\dot{y} = F(x, \dot{x}) = \sqrt{x^2 + \frac{2(1-\mu)}{|x+\mu|} + \frac{2\mu}{|x+\mu-1|} + \mu(1-\mu) - \dot{x}^2 - J|_0} \quad (3.28)$$

where $J|_0 = J(x_0, y_0, \dot{x}_0, \dot{y}_0)$ is the value of the Jacobi constant fixed by the initial conditions. The positiveness of the square root results in an inequality involving the coordinate not fixed and the relative velocity: $\dot{x} < \phi(x, J|_0)$.

Summarizing, one coordinate is fixed by the location of the section, one is obtainable by the energy integral and the other two lie in one plane within the region delimited by the validity of Eq. (3.28). All the intersections of the flow with such a plane have to lie within this domain. It is worth stressing that this domain depends on the energy level $J|_0$, therefore for increasing energy values it is possible to define the evolution of these regions. For the Earth-Moon system, a three dimensional representation of a Poincaré section placed in $y = 0$ is showed in Fig. 3.20. Here also the evolution of its sections for increasing Jacobi constant values is plotted. Again the gate-like behavior of the libration points is recognizable.

Moreover, the representation of the flow on this hyperplane makes also possible to visualize the region where the Keplerian energy of the moving body referred to the small primary is negative^[47]. In this subset both the invariant tori, composed by the periodic orbits surrounding the small primary, and what is referred as the *Weak Stability Boundary* (WSB)^{[77][78]} lie.

The WSB is defined as a boundary set between the stable and unstable motion relative to the small primary in the phase space. The concept of stability is here intended as a given (fixed a-priori) number of closed orbits performed around m_2 before leaving its realm. This concept was heuristically introduced in the beginning of the nineties^[4] and subsequently related to dynamical system theory. In particular, by means of numerical explorations, it was suggested that the WSB is bounded by the stable manifolds of periodic orbits, with the same energy level, around the two collinear libration points near m_2 ^[78].

To obtain a specific Poincaré section, it is possible to iterate a set of initial conditions, starting from the section plane and store the relevant components of the state when the flow intersects transversally again that plane. These sections have to be produced numerically to understand the behavior of the global orbit structure.

Let us consider 1000 initial conditions in the Earth-Moon PCR3BP to integrate forward for 500 time units (≈ 2300 days). A Poincaré section is

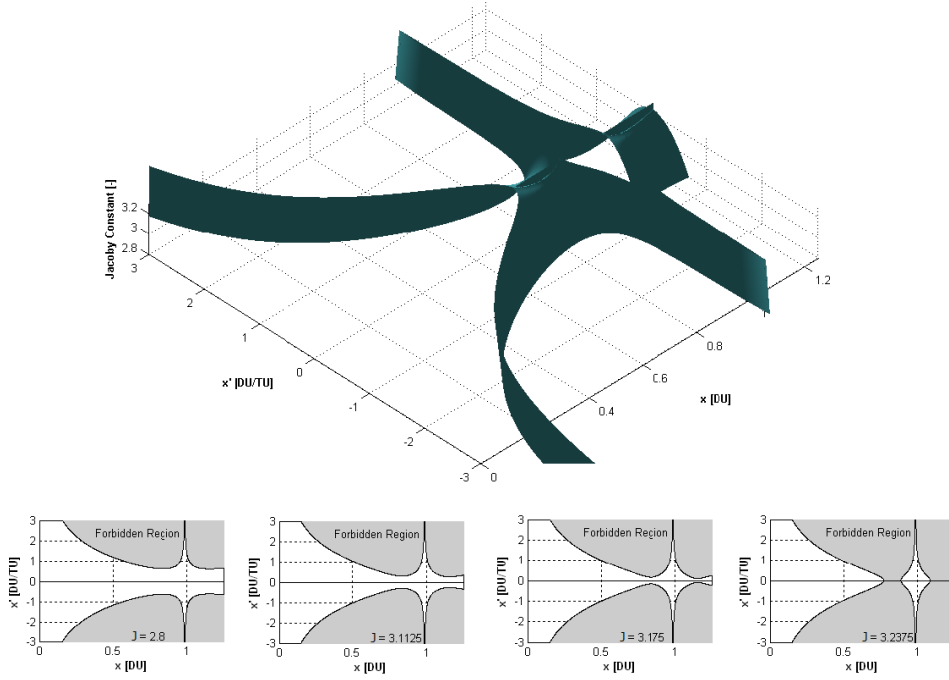


Figure 3.20: Energy evolution of the $y = 0$ Poincaré sections domain. In a three dimensional view and with slices for four energy values.

constructed on the plane $y = 0$ placed in the Earth realm on the Moon side with $J = 3.160$. This value corresponds to an energy slightly higher than $E_{\mathcal{L}_2}$ so that the motion among all the three realms is allowed.

The phase space portrait represented in Fig. 3.21 highlights a set of completely different behaviors.

An exactly periodic orbit is represented by a point in this section. These points are surrounded by regions where the orbits are quasi-periodic and their images lie on closed curves^[25] (cfr. Sec. 2.4). These form resonance islands where the eigenfrequencies of the orbit are somehow coupled with the ones of the model. Since the CR3BP is a perturbed Hamiltonian system (resulting, in proper coordinates a quasi-integrable model, cfr. Sec. 2.1 and 3.2.2), these persisting invariant structures are the well known KAM tori^[25]. For these objects the eigenvalues ratio is enough irrational (actually diophantine, cfr. Sec. 2.4) to allow them to survive when a small perturbation is applied to an integrable Hamiltonian system.

The region nearby the Moon is filled with these tori resulting in closed orbits around it. The resonance islands are located in the Earth realm and

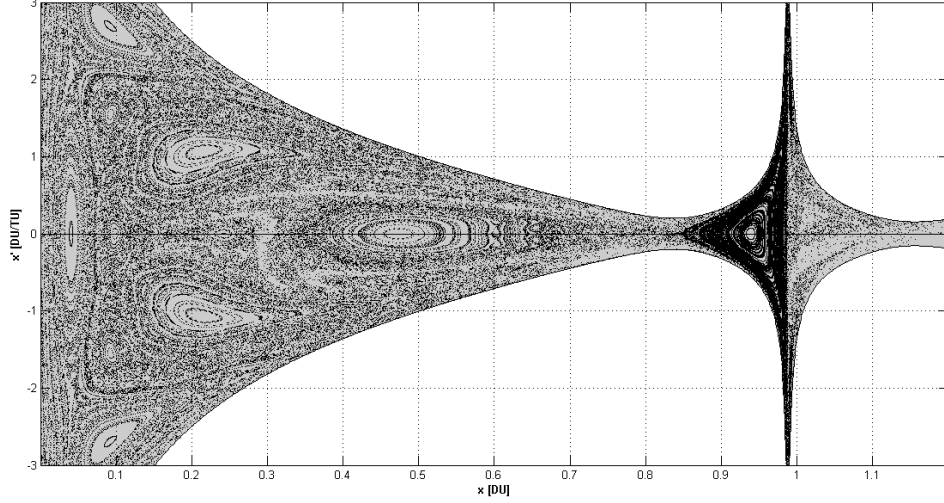


Figure 3.21: Earth-Moon Poincaré section on the $y = 0$ plane with $J = 3.160$.

represent orbits repeating indefinitely the same path. Finally, these resonances, of different orders, are surrounded by chaotic orbits represented by a sea of random points, revealing the chaotic nature of the CR3BP.

3.7 Resonances

In order to complete this exploration of the model, let us carry out a brief analysis on the resonances in the context of the PCR3BP.

There are several kinds of resonances. These can be grouped in orbit-orbit resonances, involving relations between the motion of the centers of mass of two bodies, and spin-orbit resonances, where the motion around the center of mass of one body is coupled with the gravitational perturbation exerted by another attractor. The orbit-orbit resonances can be secular, involving precession phenomena, and of mean motion where the periods of two bodies are coupled^[49]. The most famous mean motion resonance in the solar system is the *Great Inequality* involving Jupiter and Saturn. Only mean motion resonances are analyzed in this section.

Mean motion resonances result from the interaction in regular time intervals between celestial bodies where these periodic perturbations have cumulative effects during the motion. On the other hand, if these gravitational perturbations would be out of phase their effect would cancel out without change the orbital motion of one of the bodies.

For the CR3BP, in the case $\mu = 0$ (cfr. Sec. 2.2.3), the reference frame is still rotating with unitary angular velocity ($\omega = 1$) and centered in m_1 . If the initial Keplerian energy of the massless body is negative it revolves in ellipses with mean angular velocity $\bar{\omega} = 2\pi/T$, where T is the ellipse period. When the ratio $\bar{\omega}/\omega$ is rational the motion of m_3 is resonant with a hypothetical small primary m_2 . Nevertheless, when this ratio is irrational the motion is quasi-periodic, even studied in the rotating frame.

The fundamental resonance condition is the commensurability between the orbital periods (T) of two generic bodies (1 and 2); their ratio can be expressed as the ratio of two small integers: $pT_1 = qT_2$ ^[47].

Resonance Hopping

In the CR3BP framework, the resonance condition is transformed in a relation between the period of the moving body m_3 (no subscript), $T = 2\pi a^{3/2}/\sqrt{1-\mu}$, and the period of m_2 , $T_2 = 2\pi$. This results in a condition that the semi-major axis a of the moving body m_3 has to satisfy to represent a resonant orbit^[48].

Another fundamental relation, in the planar model, is derived by taking into account that the m_2 gravitational influence is maximized when the moving body lies on its apogee. In this situation also the velocity of m_3 is the lowest one and this can result in temporary captures caused by m_2 . So, there is an initial value of the longitude of periapsis ω assuring that after p revolutions, m_3 lies at the apogee of its m_1 centered orbit in conjunction with m_2 .

Assuming, without losing in generality, that the moving body starts on the perigee of the orbit, the previous considerations result in^[48]:

$$a = \left(\frac{q}{p}\right)^{2/3} (1-\mu)^{1/3}, \quad \omega_0 = \pi \left(1 - \frac{q}{p}\right), \quad \nu_0 = 0 \quad (3.29)$$

Where the classical two body relations are considered for the definition of the orbital period requiring the transformation of the phase space coordinates from the synodic barycentric frame into the inertial one centered in m_1 .

Since the natural way to identify a resonance condition is to observe the behavior of the semi-major axis, in order to better understand this phenomenon also in the CR3BP, a map translating positions and velocities into a set of classical orbital elements is required^[48]: $(x, y, \dot{x}, \dot{y}) \rightarrow (a, e, \omega, \nu)$ with e the eccentricity and ν the true anomaly. The explicit representation of this map reads^[47]:

$$\begin{aligned}
x &= r \cos(\omega + \nu) - \mu & \dot{x} &= \dot{r} \cos(\omega + \nu) - r\dot{\nu} \sin(\omega + \nu) + \dot{\omega} r \sin(\omega + \nu) \\
y &= r \sin(\omega + \nu) & \dot{y} &= \dot{r} \sin(\omega + \nu) + r\dot{\nu} \cos(\omega + \nu) + \dot{\omega} r \cos(\omega + \nu)
\end{aligned}
\tag{3.30}$$

with $r = a(1 - e^2)/(1 + e \cos \nu)$, $\dot{\nu} = (a(1 - e^2)(1 - \mu))^{1/2}/r^2$ and $\dot{r} = (ae(1 - e^2)\dot{\nu} \sin \nu)/(1 + e \cos \nu)^2$.

The inverse of this map can be applied to the previous Poincaré section represented in Fig. 3.21 and the semi-major axis (constant) corresponding to the nominal resonance conditions superimposed. Fig. 3.22 shows the map in semi-major axis vs longitude of periapsis.

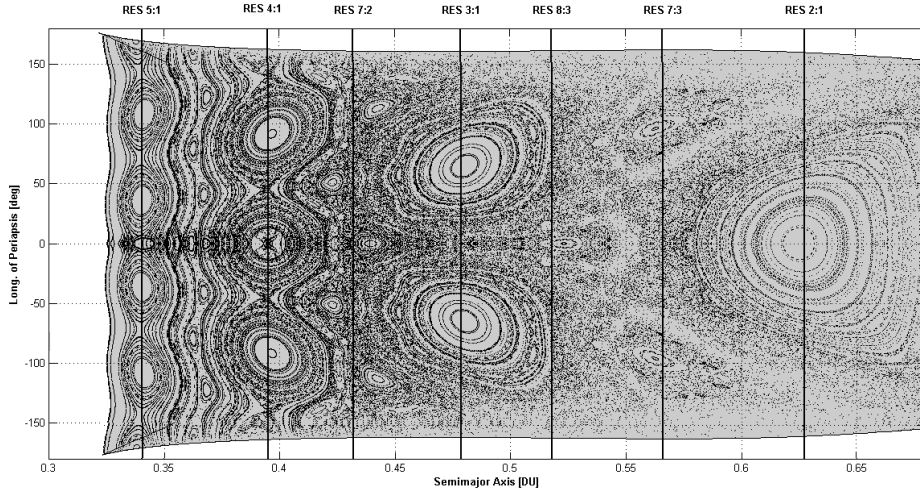


Figure 3.22: Semi-major axis vs longitude of periapsis map of the Poincaré section presented in Fig. 3.21. Also the nominal resonant semi-major axes are overlapped.

It is clear that the regular islands in the phase space are located exactly where the resonances take place. The size of the ordered regions is an indicator of the size of the inherent KAM torus. The probability to get trapped into one of these resonances, on the other way the effort to get out, increases for increasing size of these resonance islands. Also the resonance order can be revealed by the number of centers of these ordered regions.

Considering again the map $(x, y, \dot{x}, \dot{y}) \rightarrow (a, e, \omega, \nu)$, Eq. (3.30), and the ideal resonance condition of Eq. (3.29), it is clear that each initial condition in this new set of variables has only one free parameter: the eccentricity e .

Thus, only this value is required to parameterize each initial condition for a resonant orbit.

Varying this value it is possible to identify specific orbits temporarily captured or in close passage with m_2 . These can be considered as initial conditions to propagate in order to obtain an encounter with m_2 when its gravity perturbation is high and the particle velocity is small and thus possibly resulting in (temporary) captures in the m_2 WSB. After this encounter, however, the m_1 gravity can become again dominating pushing the body to escape from the m_2 realm.

Let us restrict to the Earth-Moon system and numerically propagating initial conditions given by Eq. (3.29) considering a $2:1$ resonance with eccentricity varying from 0 to 0.95 with step of 0.01. The resulting trend of the selenocentric distance and of the Jacobi constant evolution is plotted for changing eccentricity in Fig. 3.23. It is important to point out that changing the initial eccentricity results in the change of the energy of the orbit, i.e. $J = J(e)$, depicted on the right of Fig. 3.23.

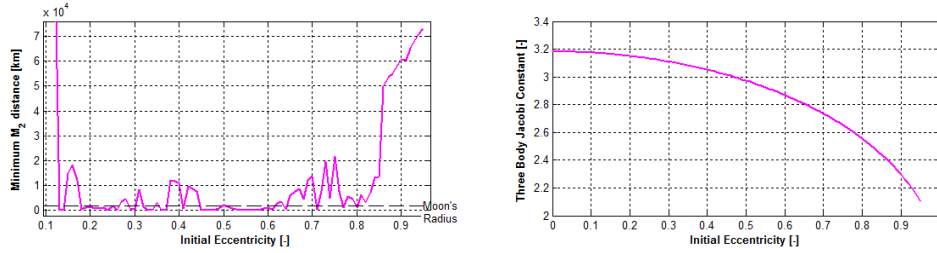


Figure 3.23: Minimum Moon distance and Jacobi constant for varying eccentricity for the $2:1$ resonance in the Earth-Moon system.

From the trend of the minimum Moon distance with respect to the eccentricity (on the left of Fig. 3.23), it is possible to select initial conditions highly perturbed by the Moon, but performing completely different paths. In particular a couple of behaviors can be highlighted; a “soft” resonance transition with some time spent around the Moon and a sudden variation of the resonance status.

The first kind of behavior can be obtained by considering $e = 0.1762$, corresponding to a not-too-close Moon passage. This specific value results in a path temporarily captured by the Moon. The time-varying specific mechanical energy is less than zero for a while (≈ 20 days) and, afterward, the trajectory is shifted close to a $3:1$ resonance, value non a-priori identifiable, see Fig. 3.24.

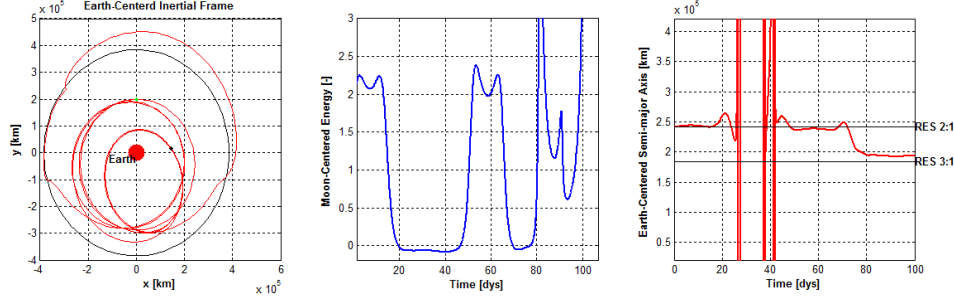


Figure 3.24: 2:1 resonance hopping with temporary Moon capture for $e = 0.1762$ in the Earth-Moon system.

This phenomenon is referred as *weak capture* in the Moon WSB^[48] and, in general, to obtain this kind of solutions, the initial eccentricity has to be quite small. As we are working with a chaotic model, a small change in the eccentricity reflects in significant differences in the circumlunar phase and, in particular, it allows the Moon impact to be avoided. Of course, a small maneuver during the temporary capture can stabilize the selenocentric orbit.

Again from the analysis of Fig. 3.23, a sudden resonance hopping from the original 2:1 resonance can be obtained by considering an initial condition with $e = 0.505$ resulting in a very close (but not impact) Moon passage, see Fig. 3.25. Thus, an orbit starting close to the 2:1 resonance is, at the first Moon encounter, suddenly shifted to another resonances, firstly 1:3 and afterward 1:4. Of course, the magnitude of the jump results from the periselenium distance and can be controlled, again, by means of the eccentricity. The values used for Fig. 3.25 has been chosen by considering the small non-impact peak around $e = 0.5$ in Fig. 3.23.

Finally, it is also worth stressing that the resonant conditions given in Eq. (3.29) are exact only if the mass parameter is zero, while they represent just approximations in the CR3BP. This is clear observing the oscillations around the nominal resonant semi-major axes in the evolution of the osculating semi-major axes in Fig. 3.24 and 3.25 (rightmost plots).

Exact Resonances

As outlined in the previous section, Eq. (3.29) do not provide exact resonance relations in the CR3BP. The aim of this section is to refine these resonance conditions in order to define actual resonant orbits not experiencing any resonance shifting, also in the CR3BP. To compute exact resonances in the PCR3BP a numerical scheme has been implemented to identify the actual resonance conditions starting from the nominal approximations.

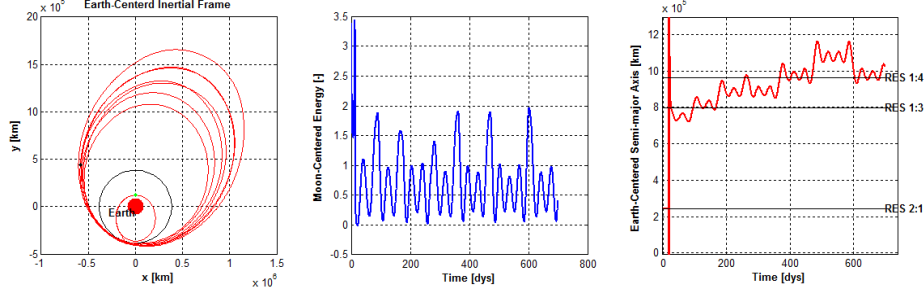


Figure 3.25: 2:1 resonance hopping to external resonances for $e = 0.505$ in the Earth-Moon system.

The fundamental problem is to consider the relations derived by a classical two body approach, still valid when another attractor is taken into account. The Keplerian orbital period is not the real one for an orbit in the CR3BP. This means that the classical resonance definition can not be used as it is based on the two body orbital periods of the moving body and of another attractor (T_1, T_2).

Thus, the goal is to determine the new orbital period and, from this, the semi-major axis which assures resonance conditions. The idea is to consider an orbit as resonant if it is in the same relative conditions with respect to the main attractor at the end of p periods.

A Nelder-Mead simplex scheme^[79] has been used to implement a zero finding procedure to correct the two body approximation on the semi-major axis in order to obtain an orbit ending in its initial position in the phase space. This means that, as the synodic frame is considered, the moving body is in the same conditions with respect to m_2 after the p periods.

The main limit of this approach is that it results valid just in a range of the possible resonances. When the semi-major axis is too small, the m_2 gravity is not really significant so the $\mu = 0$ approximation is still valid and no numerical corrections are required (the corrected semi-major axis turns out to be the guessed one). On the other side, in resonances involving too large values of the semi-major axis, the m_2 gravity is too strong and the chaotic regime prevents the convergence of the numerical method. As practical explanation of this range, this method works in the Earth-Moon system from a 4:1 resonance ($a \approx 1.5e5$ km) up to 7:5-4:3 resonances, depending on the initial eccentricity guess.

As an example, the 5:2 resonance is presented in Fig. 3.26, where the semi-major axis has been correct from $a = 207835$ km to $a = 208150$ km.

In the same figure the two body resonance (nominal a) in the rotating and inertial frame is shown in the first two plots from the upper left corner. The third plot shows the evolution of the nominal a (constant) and the one corrected into the CR3BP. In the fourth and fifth plots, the exact resonance in the Earth-Moon CR3BP in the rotating and inertial frame is presented. Finally, in the lower right corner also the two body energy value is presented; it has the same trend of the semi-major axis as it has a linear dependence on this.

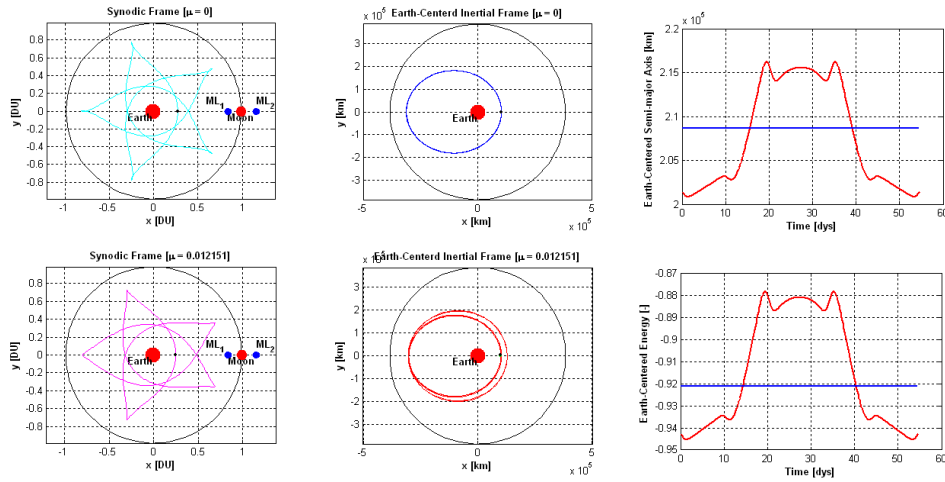


Figure 3.26: 5:2 Exact Resonance in the synodic (first column) and in the inertial (second column) frame for the Earth-Moon system. Also the trends of the semi-major axis (upper right corner) and of the energy (lower right corner) is shown.

Let us conclude this analysis stressing that these exactly resonant orbits do not experience the resonance hopping observed in the Sec. 3.7, but they repeat indefinitely the same path. To avoid to fall into the Moon WSB or in close Moon passages the computations have been done by assuming a generic initial longitude of periapsis different from the value of Eq. (3.29).

3.8 Chaos and Lyapunov Exponents

One of the fundamental tools to study the behavior of a dynamical system in its chaotic regime are the *Lyapunov Exponents*. These are used to measure how fast nearby trajectories are converging or diverging in time; this is a characterization of the global behavior of a dynamical system. A chaotic regime is represented by a positive value of the Lyapunov Exponent that results in

exponentially fast time diverging nearby trajectories; it is an indication of the stochastic component of the model^[80].

The idea is to study the evolution of a small difference $\delta\vec{x}$ between two nearby solutions. This can be done by exploiting the exponential solution of a system of first order differential equations. Thus, given a generic dynamical system, $\dot{\vec{x}} = f(\vec{x}, t)$, we are interested in studying its linearized version (the variational equations, cfr. Sec. 3.1.1): $\delta\dot{\vec{x}} = \Omega(t, t_0)\delta\vec{x}(t_0)$, where $\Omega(t, t_0)$ is again the state transition matrix. Since this matrix is a linear operator representing the evolution of a small perturbation, the Lyapunov Exponent (Λ) can be expressed as^[81]:

$$\Lambda = \lim_{n\Delta t \rightarrow \infty} \frac{1}{n\Delta t} \ln ||\Omega(n\Delta t + t_0, t_0)|| \quad (3.31)$$

The operator norm, in the \mathbb{R}^4 Euclidian space, can be defined as the maximum eigenvalue of the norm of a linear operator^[80], as the operator norm gives the maximum stretching of the perturbation under the action of the linear operator (in this case the state transition matrix). Thus, defining $\Xi = \sqrt{\Omega(n\Delta t + t_0, t_0)\Omega^T(n\Delta t + t_0, t_0)}$, χ its eigenvalues, and stopping the computation after n time steps (instead of taking the limit), Eq. (3.31) can be locally approximated by:

$$\lambda = \frac{1}{n\Delta t} \ln(\text{Max}[\chi \Xi]) \quad (3.32)$$

These are the so called *Local Lyapunov Exponents* (LLE) and qualify the effects that an external force has on the orbit in a given time interval. This approach provides an easily computable value that gives qualitatively how the stability varies along an orbit^[80].

Periodic Orbits around \mathcal{L}_1 and \mathcal{L}_2

One of the easiest applications of this concept is to compute the value of the Local Lyapunov Exponent along a periodic orbit around a libration point^[81]. Let us suppose to have two Halo orbits around \mathcal{L}_1 and \mathcal{L}_2 in the Earth-Moon system and to compute the value of λ after a time period of one day. The magnitude of the LLE indicates the effect that a perturbation exerts over one day. First of all a Halo orbit around $\mathcal{L}_1/\mathcal{L}_2$ has to be computed. This can be done with the procedure sketched in Sec. 3.1.1 considering, arbitrarily, a vertical amplitude of 300 km.

A periodic orbit around \mathcal{L}_2 presents only one peak in the Moon closest point, see Fig. 3.27. Of course, the lower value of the LLE can not be zero since the CR3BP remains a chaotic model. The direction of arrows in Fig. 3.27 does not have any physical meaning, while their length represents the scaled value of the LLE.

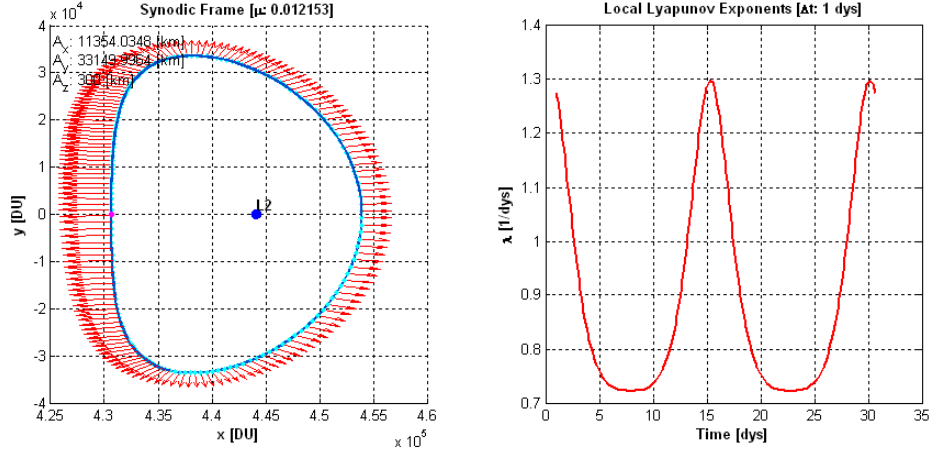


Figure 3.27: Local Lyapunov Exponent for an Earth-Moon \mathcal{L}_2 Halo orbit; on the left the magnitude of the LLE along the orbit and on the right its time behavior.

A periodic orbit around \mathcal{L}_1 is, instead, more interesting as it is located between Earth and Moon so it suffers from both influences, with maxima in different locations. This results in the two peaks of Fig. 3.28. The higher one is due to the Earth, while the lower one to the Moon and both are located in the points of the Halo closer to the relative primary.

Changing the A_z amplitude for both Halos does not result in a remarkable changing neither of the trend of the LLE nor of their values. This holds unless the periodic orbit becomes so distorted to pass extremely close to one primary; in this degenerate case only one and very high peak is present.

Of course, changing the time interval after which the LLE are computed changes their value (the perturbation acts for a longer period), but the shape of the evolution remains the same as well as the number of peaks and their meaning. The general trend observed is a diminution of the height of these peaks for increasing times; i.e. the difference between peaks and valleys in Fig. 3.27 and 3.28 becomes smaller. Both the peaks due to the Earth and to the Moon decrease, however, with a Δt of the order of half period, the peaks due to the Moon are no more detected. For decreasing time intervals the magnitude of the LLE increases and the width of the peaks reduces around the closer Halo-primary point.

In brief, this analysis shows that there are points along the Halo orbits (or any other periodic orbits around \mathcal{L}_i) where the gravitational perturbation of one of the primary is higher, so the orbit is more sensible to any other

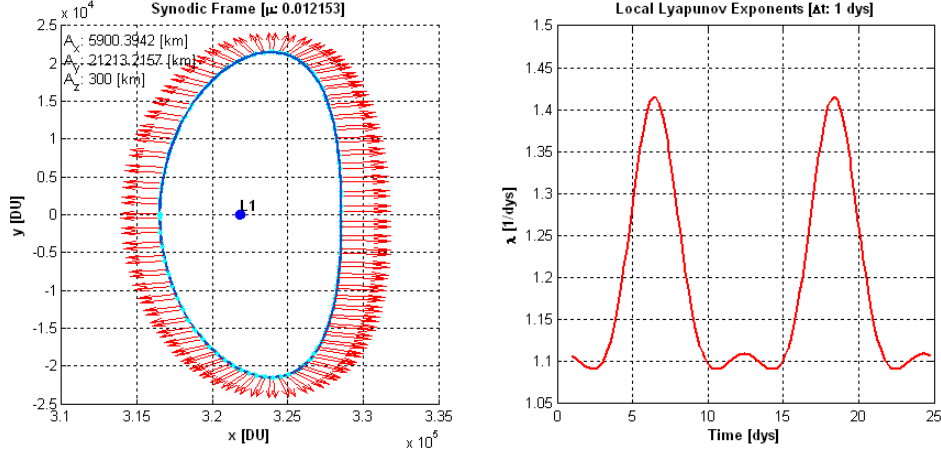


Figure 3.28: Local Lyapunov Exponent for an Earth-Moon \mathcal{L}_1 Halo orbit; on the left the magnitude of the LLE along the orbit and on the right its time behavior.

perturbation. For instance these could be the right points to apply an impulse for station keeping maneuver or where the navigation uncertainties have to be reduced^[81].

Form a practical point of view, it is well known that maneuvers on Halo and Lissajous orbits are more effective when they take place near the line connecting the two primaries^[81].

It is worth stressing that the CR3BP is still the dynamical model, therefore no other forces, besides the two primaries, are considered. Taking into account a full ephemeris model would result in a completely different trend of the LLE, nevertheless their higher values still reveal the more “sensible” points of an orbit^[44].

Small Primary’s Realm

Another worth application of the same concept is the characterization of the phase space around m_2 . Let us restrict again to the Earth-Moon PCR3BP with the idea to define a grid of initial conditions around the Moon and compute the value of the LLE of each point after a given time span.

It is expected that the points more perturbed, so with higher values of the LLE are more unstable, so these can be captured/ejected more easily by means of the combination of the gravitational forces. Locally, in the m_2 realm, any initial condition can be expressed by means of the correspondent condition on an osculating ellipse around the Moon. Considering only posi-

tive velocities, i.e. osculating retrograde motions around the Moon, for the departing osculating ellipses, the initial conditions in the classical PCR3BP reference frame can be expressed as^[78]:

$$\begin{aligned} x &= 1 - \mu + r_2 \cos \theta & \dot{x} &= r_2 \sin \theta - v_2 \sin \theta \\ y &= r_2 \sin \theta & \dot{y} &= -r_2 \cos \theta + v_2 \cos \theta \end{aligned} \quad (3.33)$$

where $r_2 = a(1 - e)$ is the pericenter distance from the small primary and $v_2 = \sqrt{\mu(1 + e)/r_2}$ is the pericenter velocity.

Fixing an eccentricity value and defining a grid on the initial semi-major axis (a) and the departing angle (θ , measured counterclockwise from the positive x -axis), it is possible to associate the LLE to each point around m_2 by means of Eq. (3.32).

In Fig. 3.29 the LLE values are presented for a grid with zero eccentricity and computed after a time interval of 5 days. The stable points are represented by the valleys, while the higher the peaks the more unstable the relevant initial conditions are. The reference frame is centered in the small primary.

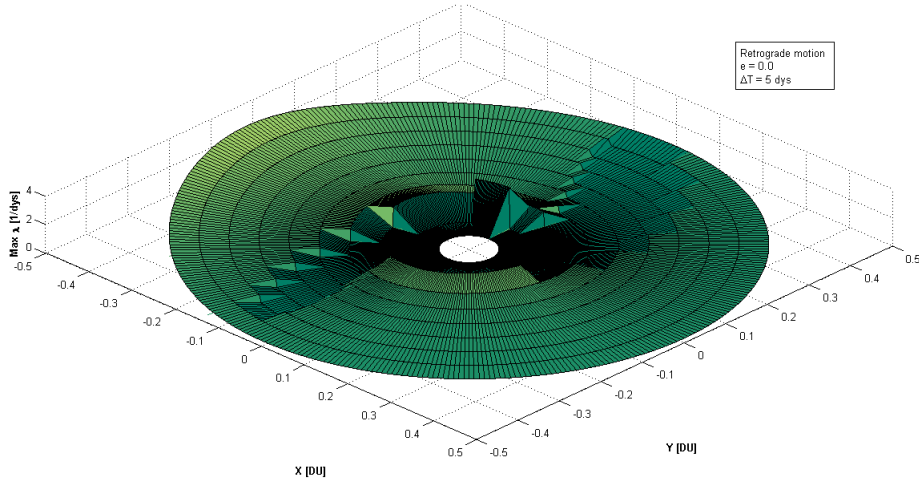


Figure 3.29: Moon realm characterization by means of the LLE for $e = 0$.

Considering the same approach, an interesting comparison can be done with results obtained for a quite high eccentricity values. In Fig. 3.30 the characterization of the m_2 realm associated with an initial eccentricity of 0.70 is presented. It is worth nothing that although the general shape of the stable region looks similar, the magnitude of the LLE is much different. In

particular it increases for increasing eccentricity as the aposelenium moves far from Moon and thus it can be easily perturbed by Earth.

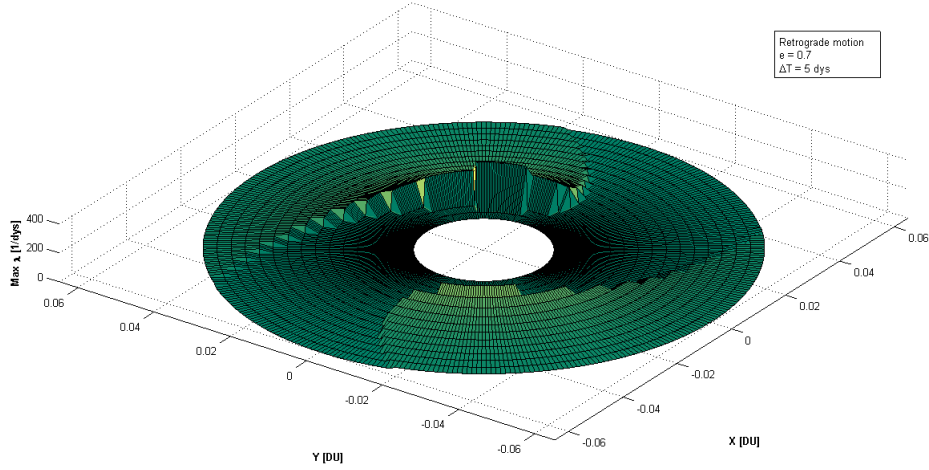


Figure 3.30: Moon realm characterization by means of the LLE for $e = 0.70$.

In the a - θ representation it comes out that the LLE are higher, for a given a , when the angle is 180 deg, and this is clear as in this situation the initial condition lies along the x -axis on the side of the larger primary. Moreover, the height of the peaks increases for increasing a values. Nevertheless, there are regions with very low LLE values also when the magnitude of a is relatively large, these regions are very close to the Moon and are composed by points trapped into the invariant tori.

The approach presented closely follows the definition of Weak Stability Boundary, where the aim is to define the boundary between the m_2 escaping trajectories and the ones captured into the KAM invariant tori.

The representation by means of LLE of this region has the advantage that no “stability concept” has to be introduced and the number of revolutions does not have to be a-priori defined, but only the time after which the LLE has to be computed remains arbitrary. Nevertheless also this approach represents an algorithmic characterization of this region of the phase space.

Chapter 4

Optimal Control

Some of the most useful tools, already in the initial mission analysis phases, derive from optimal control theory. It permits to choose a specific path among multiple possibilities, and it reflects the optimality concept sought in the specific mission. For instance, dealing with human space missions it is extremely important to reduce the transfer time as much as possible, while for a cargo mission would be useful to limit the propellant mass so that a larger part of the total mass can be allocated for the equipments. A selection criteria is fundamental especially in the preliminary mission analysis where the number of free parameters is quite high and a criterion to pick out a specific trajectory has to be defined.

In the Chapter the basics of optimal control theory are presented for low thrust mission analysis. Also applications involving two/three-body dynamics are presented in order to show how the optimization schemes work. The approaches here presented are also the basics of the applications proposed in the following chapters.

The general definition of the direct and indirect optimization schemes follows^{[82][83]} and^[84] is the fundamental reference for the electric propulsion. The results of the indirect method in the two body cases can be compared with^{[85][86]} while the hybrid scheme refers to^{[87][88]}.

4.1 The Optimal Control Problem

Let us assume to have a generic dynamical system whose equations depend, beside on the states also on a control (\vec{u}): $\dot{\vec{x}} = f(\vec{x}, \vec{u}, t)$ with $t > 0$, $\vec{u} \in U \subset \mathbb{R}^n$, $f : \mathbb{R}^n \times U \rightarrow \mathbb{R}^n$. In this situation the state of the system ($\vec{x}(t)$) depends instantaneously on the value of $\vec{u}(t)$.

The goal of an optimal control problem is to define the time law of a

control so that a given scalar performance index (J) is minimized/maximized. This is a typical formulation for a continuous system and usually there is a set of initial (subscript 0), final (subscript f) and path constraints that the resulting optimal trajectory has to satisfy. The performance index is composed, in general, by a term depending on the final state and another one depending on the state and the control along the path^[89]. The mathematical formulation of the problem is:

$$\begin{aligned}
 \text{Minimize } J &= \phi(\vec{\mathbf{x}}_f, t_f) + \int_{t_0}^{t_f} L(\vec{\mathbf{x}}, \vec{\mathbf{u}}, t) dt \\
 \dot{\vec{\mathbf{x}}} &= f(\vec{\mathbf{x}}, \vec{\mathbf{u}}, t) \\
 \mathbf{g}(\vec{\mathbf{x}}, \vec{\mathbf{u}}, t) &\geq 0 \\
 \Psi_0(\vec{\mathbf{x}}_0, t_0) &\geq 0 \\
 \Psi_f(\vec{\mathbf{x}}_f, t_f) &\geq 0
 \end{aligned} \tag{4.1}$$

The performance index expressed in the form of Eq. (4.1) is called in the *Bolza Form*, where J is composed of the *Mayer Term* (the first one) and of the *Lagrange Term* (the second one), involving the integral along the path of the Lagrangian of the problem, L . This last term becomes a sum in case of discrete dynamical systems, moreover only one of these terms can be zero. J can be also expressed only by means of the Mayer or of the Lagrange term. The three formulations are theoretically equivalent; it is sufficient to expand the state vector with another variable (and relevant differential equation) representing the evolution of the term neglected in the definition of J .

A typical constraint for low thrust missions to be satisfied along the path (g) is that the control has a limited operative range, e.g. $0 \leq \|\vec{\mathbf{u}}(t)\| \leq \vec{\mathbf{u}}_{MAX}$.

Seldom this problem can be solved analytically and usually a numerical scheme has to be considered to obtain the solution. There are two main methods, *Direct* and *Indirect*.

4.1.1 Direct Methods

As the name suggests, these methods solve directly for the unknowns control variables. The approach does not require nothing more than the equations of motion, boundary conditions and constraints, but it is necessary to resort to efficient solvers of non linear and constrained algebraic equations with many variables and many constraints. This is the reason why they require more computational power and grew up with the modern computers in the late seventies^[83].

The problem is transformed, by means of a *transcription* procedure, into a *constrained nonlinear programming problem* (NLP) and the time law $\vec{\mathbf{u}}(t)$ is approximated by a discrete time evolution of the control^[82]. Basically, the

transcription procedure is a discretization of the problem that results in an approximation of the original continuous problem. This leads to a sort of sub-optimal solution, but usually the error introduced by the discretization process is much smaller than the error introduced by the model.

The basic idea is to define a grid of time intervals and evaluate both the state and the constraints only at the knots of this discrete problem^[83]. Direct methods can be divided into *Direct Shooting* and *Direct Collocation* methods, depending on the presence of an explicit numerical integration of the states.

Direct Shooting methods born originally to solve the Two Point Boundary Value Problem (TPBVP). They require the numerical integration of the trajectory and the control is evaluated in order to “hit the target”. The target is, in this case, the error between the obtained state at the knots and the required one. $\vec{u}(t)$ is computed only in the mesh points and then interpolated among these; also the path constraints are discretized and satisfied only in the mesh points. The optimization parameters are the initial state and the control vector evaluated in the mesh points. An improvement of this method is the so called multiple shooting, that introduces intermediate points among the knots of the mesh where the integration is re-started. Otherwise the trajectory can be started from both sides of the interval and also the error at an intermediate match point considered; these are the shooting to a fitting point methods.

In Direct Collocation methods, $\vec{u}(t)$ is intrinsically continuous, but approximated using a piecewise continuous polynomial between two consecutive mesh points. These polynomials have to satisfy (collocate) the dynamics between the knots. Thus, the control parameters are the values of the state and of the control in the grid points^[82]. In this case at each knot there is both a right and a left control value since discontinuities are allowed in the points between the polynomial approximations of the state. Each integration step is actually a segment on which the values of the state and of the control have to be determined. One of the most used approximations is based on the Hermite polynomials and the Simpson rule to approximate the integral. Also the trapezium rule is widely used. These methods are faster than the previous ones and have a larger convergence radius, as the number of parameters and constraints increases. They are also numerically robust, although the computational effort increases for increasing transcription accuracy, i.e. with the increasing of the number of control parameters.

On the left of Fig. 4.1 a schematic view of a direct shooting phase, with a single state and a single control, is represented. The initial condition of the state remains an optimization parameter and the control is discretized into n mesh points, resulting in a vector of optimization parameters. On the right

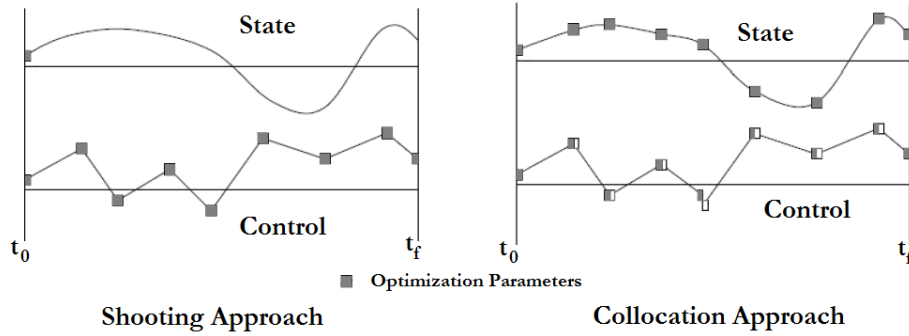


Figure 4.1: Schematic view of the single shooting method (right) and of the direct collocation method (left) for a system with a single state and a single control.

side of Fig. 4.1, a scheme of the direct collocation method is shown with a single discretized state and control. In general the state is continuous, while right and left control values are considered (empty and filled rectangles) for the control. The control continuity can be imposed by means of additional constraints.

Summarizing:

- in a shooting approach there is an explicit integration of the dynamical equations that eliminates the state variables using algebraic conditions. Controls are parameterized and collocated while states are propagated;
- in a transcription approach the state of the system is a variable and this represents a sort of implicit integration of the equations of motion. It is required that the states satisfy the constraints resulting from the integration. Both control and state are parameterized.

An initial guess is required in both approaches, although an important property of direct methods is their numerical robustness, so the “quality” of the initial set of control variables is not so crucial for the convergence of the method.

After the transcription procedure, the optimal control problem is transformed into a NLP, not involving anymore the dynamics of the original problem. A set of nonlinear algebraic constraints (c) has to be solved over a set of unknown variables together with an objective function to maximize/minimize $(F)^{[83][82]}$. Also boundaries on the domain where the extremum has to be

found can be present ($\vec{\mathbf{x}} \in [\vec{\mathbf{x}}_L, \vec{\mathbf{x}}_U]$). Thus, the problem is stated as:

$$\begin{aligned} & \text{Minimize } F(\vec{\mathbf{x}}) \quad f : \mathbb{R}^n \rightarrow \mathbb{R} \\ & \mathbf{c}_L \leq \mathbf{c}(\vec{\mathbf{x}}) \leq \mathbf{c}_U \\ & \vec{\mathbf{x}}_L \leq \vec{\mathbf{x}} \leq \vec{\mathbf{x}}_U \end{aligned} \tag{4.2}$$

where, in general, $\vec{\mathbf{x}} \in \mathbb{R}^n$ and $\mathbf{c}(\vec{\mathbf{x}}) \in \mathbb{R}^m$ with $m \leq n$. The set of constraints can be divided into the ones that are strictly satisfied, $\mathbf{c}_i(\vec{\mathbf{x}}) > 0$ that are *inactive* and the ones that define the bounds of the constraints, $\mathbf{c}_i(\vec{\mathbf{x}}) = 0$, that are actually the *active* ones. Therefore, once the active set of constraints is known, it is possible to get rid of the inactive set and simplify the problem by considering only equality constraints.

The necessary conditions to solve this problem come out from the Lagrange theory of constrained maxima. In particular, the Lagrangian of the problem is defined as: $L(\vec{\mathbf{x}}, \vec{\boldsymbol{\lambda}}) = f(\vec{\mathbf{x}}) - \vec{\boldsymbol{\lambda}}^T \mathbf{c}(\vec{\mathbf{x}})$, that is a scalar function of n variables and m multipliers $\vec{\boldsymbol{\lambda}}$. The necessary conditions a point has to satisfy to be the constrained optimum are that it is a stationary point of the Lagrangian with respect to all of its dependencies.

This results in a non linear system that can be solved by means of a Newton iteration scheme to compute the correction $(\Delta\vec{\mathbf{x}}, \Delta\vec{\boldsymbol{\lambda}})$ to apply to an initial guess to move one step toward a stationary solution, i.e. it gives the searching directions. In matrix form this means^[89]:

$$\begin{bmatrix} \mathbf{H}_L & -\mathbf{G}^T \\ \mathbf{G} & 0 \end{bmatrix} \begin{Bmatrix} \Delta\vec{\mathbf{x}} \\ \Delta\vec{\boldsymbol{\lambda}} \end{Bmatrix} = \begin{Bmatrix} -\mathbf{g} \\ -\mathbf{c} \end{Bmatrix} \tag{4.3}$$

where $\mathbf{g} = \nabla_x F$ is the gradient of the objective function $F(\vec{\mathbf{x}})$, \mathbf{G} is the Jacobian of the equality constraint vector $\mathbf{c}(\vec{\mathbf{x}}) = 0$ and $\mathbf{H}_L = \nabla_x^2 F - \sum_{i=1}^m \lambda_i \nabla_x^2 c_i$ is the Hessian of the Lagrangian in x .

The linear system of Eq. (4.3) is referred as the Karush-Kuhn-Tucker system and gives the necessary conditions to solve a NLP^{[89][90]}.

It is worth nothing that this is equivalent to minimize the quadratic form $1/2 (\Delta\vec{\mathbf{x}}^T \mathbf{H}_L \Delta\vec{\mathbf{x}}) + \mathbf{g}^T \Delta\vec{\mathbf{x}}$ subject to the linear constraints $\mathbf{G} \Delta\vec{\mathbf{x}} = -\mathbf{c}$. This approach is often referred as *Quadratic Programming* (QP) problem, also in its Sequential version (*Sequential Quadratic Programming*, SQP)^[91].

4.1.2 Indirect Methods

Indirect methods aim to solve the optimal control problem by considering the variation of an augmented performance index including the equations of motion and the constraints over the states and the controls. These methods are based on the *Calculus of Variations*, begun in the '600 with Newton, and on the *Pontryagin's Minimum Principle*, stated in the sixties^[92].

Indirect methods require a deep mathematical understanding of the specific problem and often slightly variations in the dynamics or in the constraints result in a completely different optimal solution.

The Lagrange constrained minimum theory allows the computation of the minimum (maximum) of a specific function, $f(\vec{\gamma})$, subject to some constraints, $\mathbf{g}(\vec{\gamma})$, defining an augmented function, $F(\vec{\gamma})$, that includes both by means of some coefficients $\vec{\nu}$, the *Lagrange Multipliers*: $F(\vec{\gamma}) = f(\vec{\gamma}) + \vec{\nu}^T \mathbf{g}(\vec{\gamma})$.

A stationary point of F corresponds to a stationary point of f , so from $\partial F / \partial \vec{\gamma} = 0$ it is possible to compute $\vec{\gamma}$ to replace in $\mathbf{g}(\vec{\gamma})$. This leads to the equations for the Lagrange multipliers that can be solved (seldom analytically) and replaced into f to obtain the maximum of the function or into $\partial F / \partial \vec{\gamma}$ to have the value of $\vec{\gamma}$ that maximizes f .

In our case the goal is to define the optimal value of the control ($\vec{\mathbf{u}}^*$) that maximizes the objective function J satisfying the constraints of the problem (cfr. Eq. (4.1)). This results in the optimal trajectory, $\vec{\mathbf{x}}^*$, depending on $\vec{\mathbf{u}}^*$. To apply the Lagrange constrained minimum theory, the augmented functional \hat{J} , to be minimized, has to be defined. Referring to the problem stated in Eq. (4.1) it reads:

$$\hat{J} = \phi(\vec{\mathbf{x}}(t_f), t_f) + \vec{\nu}^T \cdot \Psi(\vec{\mathbf{x}}(t_f), t_f) + \int_{t_0}^{t_f} \left\{ L(\vec{\mathbf{x}}, \vec{\mathbf{u}}, t) + \vec{\lambda}^T \cdot [\vec{f}(\vec{\mathbf{x}}, \vec{\mathbf{u}}, t) - \dot{\vec{\mathbf{x}}}] \right\} dt \quad (4.4)$$

where the Lagrange multipliers are different for the discrete final constraints, $\vec{\nu}$, and for the continuous ones, $\vec{\lambda}$, the *costate* or *adjoint* variables.

Eq. (4.4) can be integrated by parts obtaining^[83]:

$$\hat{J} = \Phi + \vec{\lambda}^T(t_f) \cdot \vec{\mathbf{x}}_f + \vec{\lambda}^T(t_0) \cdot \vec{\mathbf{x}}_0 + \int_{t_0}^{t_f} \left[H_x + \dot{\vec{\lambda}}^T \cdot \vec{\mathbf{x}}(t) \right] dt \quad (4.5)$$

where $\Phi = \phi + \vec{\nu}^T \cdot \Psi$ is a function taking into account the Mayer term augmented with the final constraints. Depending on the explicit dependence of the Mayer term on the final time, it is possible to classify *Open Time Problems* ($\phi(\vec{\mathbf{x}}_f)$) and *Fix Time Problems* ($\phi(\vec{\mathbf{x}}_f, t_f)$). Moreover, in Eq. (4.5), H is again the Hamiltonian of the problem:

$$H = L(\vec{\mathbf{x}}, \vec{\mathbf{u}}, t) + \vec{\lambda}^T \cdot \vec{f}(\vec{\mathbf{x}}, \vec{\mathbf{u}}, t) \Rightarrow H = H(\vec{\mathbf{x}}, \vec{\mathbf{u}}, \vec{\lambda}, t) \quad (4.6)$$

It is interesting to observe that this definition is strictly related to the definition of the functional J and contains both terms only in the Bolza formulation.

The basic idea of the calculus of variations is to study the consequences on the functional of an infinitesimal variation of the control. With this end, let us consider a $\delta \vec{u}$ and its effects on $\delta \vec{x}$ and $\delta \hat{J}$. This last one can be expressed as^[83]:

$$\delta \hat{J} = \left[\left(\Phi_x - \vec{\lambda}^T \right) \cdot \delta \vec{x} \right]_{t_f} + \left[\vec{\lambda}^T \cdot \delta \vec{x} \right]_{t_0} + \dot{\Phi} dt_f + \int_{t_0}^{t_f} \left[\left(H_x + \dot{\vec{\lambda}}^T \right) \cdot \delta \vec{x} + H_u \cdot \delta \vec{u} \right] dt \quad (4.7)$$

where $\dot{\Phi} = (\partial \Phi / \partial t)_{t=t_f} + \Phi_x \cdot \dot{\vec{x}}$ is the total derivative of Φ at the final time.

In order to avoid that a variation of the control results also in a variation of the state, it is possible to choose the Lagrange multipliers such that the coefficients of $\delta \vec{x}(t)$ and $\delta \vec{x}(t_f)$ vanish. This results in the well known *Euler-Lagrange equations* that define the time evolutions of the costate:

$$\begin{aligned} \dot{\vec{\lambda}}^T &= -H_x \equiv -L_x - \vec{\lambda}^T \cdot f_x \\ \vec{\lambda}^T(t_f) &= \Phi_x(t_f) = \phi_x(t_f) + \vec{\nu}^T \cdot \Psi_x(t_f) \end{aligned} \quad (4.8)$$

Now, the system of differential equations is expanded in order to propagate simultaneously both the equations of motion and the costate evolution, $\dot{\vec{\lambda}}^T = -H_x$.

Usually the initial state of the problem is fixed so its variation is zero, i.e. it is not required to constrain the initial state of the multipliers. The final state, instead, can be free or fixed.

The optimality conditions come out from the stationarity of the augmented functional, i.e. $\delta \hat{J} = 0$. For an arbitrary value of $\delta \vec{u}$ and δt_f in Eq. (4.7); this is possible only if the following first order *necessary* conditions are satisfied:

$$\begin{aligned} H_u &= 0 = L_u + \vec{\lambda}^T \cdot f_u \\ \dot{\Phi} &= 0 \end{aligned} \quad (4.9)$$

The first one of Eq. (4.9) is the condition to impose on the Hamiltonian to satisfy the optimum conditions, while the second one is a condition that makes sense only for open time problems (otherwise it reduces to the banal identity $0 = 0$)^[90]. It is referred as the *transversality condition* representing the final time boundary conditions for the costate^[91].

Moreover, the first order condition represented by $H_u = 0$ assures only the stationarity of the Hamiltonian so second order conditions are required to assure that this is a minimum/maximum point. This requires the computation of second order derivatives of the augmented functional with respect to the

control, For minimization problems this results in the well known *Legendre-Clebsh* conditions^[90]: $\partial^2 H / \partial \vec{u}^2 > 0$. Here > 0 denotes a positive definite matrix and the sign has to be inverted if the aim is to solve a maximization problem.

The first one of Eq. (4.8), together with the Legendre-Clebsh conditions, is a particular application of the Pontryagin's minimum principles stating, in general, that the optimal control law \vec{u}^* can be written as^[92]:

$$\vec{u}^* = \arg \min_{\vec{u} \in U} H(\vec{x}, \vec{u}, \vec{\lambda}, t) \quad (4.10)$$

This means that the optimal control vector must instantaneously minimize H ; it is a sort of constrained minimization at each time instant. In another way, the optimal solution lies in the hyperplane where the first derivative of H is zero, the second one is positive and \vec{u} is in its domain^[91].

It is worth nothing that actually the principle involves only the part of the Hamiltonian that depends on the control, the remaining part has simply zero derivatives.

For fix time problems the infinitesimal variation of the functional becomes:

$$\delta \hat{J} = \left[\vec{\lambda}^T \cdot \delta \vec{x} \right]_{t=t_0} + \int_{t_0}^{t_f} [H_u \cdot \delta \vec{u}] dt \quad (4.11)$$

H_u is the impulsive response for J ; i.e. keeping $\vec{x}(t_0)$ constant and evolving the dynamics, an unitary impulse in $\delta \vec{u}$ at t_1 produces $\delta \hat{J} = H_u(t_1)$. Moreover, at the initial time $\vec{\lambda}^T(t_0) = \hat{J}_x(t_0)$, i.e. the multipliers value at the initial time is the gradient of J with respect to \vec{x}_{t_0} .

In open time problems (typical application to find minimum time transfers) the final state is itself objective of optimization. This results in an additional condition to impose on H . It is like to solve many fix time problems and choose the one satisfying also the transversality condition on the Hamiltonian, i.e. also the condition $\dot{\Phi} = 0$ (cfr. Eq. (4.9)) has to be considered^[91]. It reduces to:

$$\begin{aligned} \dot{\Phi} = \left(\frac{\partial \Phi}{\partial t} + \frac{\partial \Phi}{\partial \vec{x}} \cdot \dot{\vec{x}} \right)_{t=t_f} &= \Phi_{t_f} + \vec{\lambda}^T(t_f) \cdot f = \Phi_{t_f} + H = 0 \Rightarrow \\ \left[\frac{\partial \phi}{\partial t} + \vec{\nu}^T \cdot \frac{\partial \Psi_f}{\partial t} + H \right]_{t=t_f} &= 0 \end{aligned} \quad (4.12)$$

Usually for an open time problem $J = \phi(\vec{x}(t_f), t_f) = t_f$ and $\Psi_{t_f} = 0$ and consequently the transversality condition takes the very easy form: $1 + H(t_f) = 0$. Therefore, in this case, the time interval satisfying the final transversality condition on the Hamiltonian has to be found.

The second one of Eq. (4.8) gives the value of the costate at the final time. Bearing in mind that it has always to be avoided to over-constrain the problem, the minimum number of λ_i have to be fixed on t_f and the states let free at the final time simply require that $\lambda_{x_i}|_{t=t_f} = 0$, with λ_{x_i} a generic multiplier associated with the state x_i . For fix time problems, generally, the performance index to be minimized is the mass consumption $J = m_{prop}$ that results in $\lambda_m|_{t=t_f} = -1$. On the other hand, for an open time problem, where $J = t_f$, $\lambda_m|_{t=t_f} = 0$, where λ_m is the costate of the mass. In both cases the optimal control problem results in a Mayer formulation that is also computationally advantageous.

Usually the constraints $\vec{\nu}$ are not imposed directly as they are automatically satisfied by the costate at the final time, if non special boundaries are imposed; i.e. $\vec{\lambda}(t_f) = \vec{\nu}$.

In practice, indirect methods reduce the optimal control problem to the problem:

$$\begin{aligned}
 \dot{\vec{x}} &= f(\vec{x}, \vec{u}, t) \\
 \dot{\vec{\lambda}}^T &= -H_x \equiv -L_x - \vec{\lambda}^T \cdot f_x \\
 H_u &\equiv L_u + \vec{\lambda}^T f_u = 0 \\
 \Psi_0(\vec{x}_0, t_0) &= 0 \\
 \Psi_f(\vec{x}_f, t_f) &= 0 \\
 \vec{\lambda}^T(t_f) &= \phi_x(t_f) + \vec{\nu}^T \cdot \Psi_x(t_f)
 \end{aligned} \tag{4.13}$$

That is a two point boundary value problem that requires the identification of the initial values of the Lagrange multipliers such that the dynamics of the system, the Euler-Lagrange equations, the optimal conditions, the final conditions and the transversality conditions are satisfied.

It is worth nothing that a TPBVP time independent admits a first integral that turns out to be again the Hamiltonian.^[91]

The solution of a TPBVP requires again to apply numerical techniques to modify the initial guesses for the unknowns initial costate. Usually a shooting approach is used; i.e. the initial guess is propagated in order to have an “error” to minimize. In its basic version it involves a reduced number of variables but it is very sensitive with respect to the accuracy of the initial guess. Exactly like observed in Sec. 4.1.1, it is possible to improve it by considering a multiple shooting approach or shooting to a fitting point. Both methods increase the numerical stability of the problem and reduce the sensibility with respect to the initial guess.

Thus, the major problem to solve this resulting TPBVP is to supply an initial guess of the unknowns. This has to be enough accurate to lie already in

the region of the optimum and such that the solution does not diverge. The adjoint variables do not have any specific physical meaning and the system is quite sensitive with respect to any small variation of their values.

Bearing in mind that the idea is to use these methods in low thrust paths, at least a couple of remarks are mandatory.

If the control is scalar and the Hamiltonian is linear with the control, the optimum time law is described by an instantaneous jump of the control between the two extremes of its domain. This situation is usually referred as *bang-bang strategy* and it applies to the case of a switch variable controlling if an electric thruster is operating or not.

In particular, considering a condition like: $\dot{\vec{x}} = F \vec{x}(t) + G \vec{u}(t)$, the Hamiltonian takes the form: $H = \vec{\lambda}^T \cdot [F \vec{x}(t) + G \vec{u}(t)]$. Assuming now that $\vec{u} = u$ is a scalar with values in a given domain $u \in [u_L, u_U]$, it follows that u has to assume the lowest value allowed when the coefficient deriving from $\partial H / \partial u$ is lower than zero and the highest one when this coefficient is positive; i.e $H(u) = \text{coeff } u \Rightarrow \text{coeff } u^* \leq \text{coeff } u$. This is the bang-bang strategy defined by:

$$u^* = \begin{cases} u_L, & \text{if } S > 0 \\ u_U, & \text{if } S \leq 0 \end{cases}$$

The function ruling the switch, $S = \vec{\lambda}^T \cdot G$, is called the *switch function* and the conditions have to be inverted if the performance index is maximized.

The adjoint velocity vector deserves special attention. $\vec{\lambda}_{\vec{v}}$ is the so called *primer vector*^[93] and in case of *chemical* transfers it has been proven that four necessary conditions have to be verified for the optimality of the solution. The primer and its derivatives have to be continuous everywhere, any impulse must be supplied along the primer, its modulus is one during any ballistic arc and the time derivative of the primer has to be zero when a chemical impulse is applied.

For the electric transfer case, the primer plays again a very important role as it turns out that, during the powered arcs, the thrust has to be aligned with it. This results as the thrust direction $\hat{\mathbf{a}}$ appears in the velocity derivatives that are coupled, in the Hamiltonian, with the primer. It results in the scalar product $\hat{\mathbf{a}} \cdot \vec{\lambda}_{\vec{v}}$ that has to be minimum in the optimal conditions and this happens when the thrust direction is along the primer and opposite to it: $\hat{\mathbf{a}} = -\vec{\lambda}_{\vec{v}}$. Minimizing the performance index the thrust direction must be opposite to the primer, while it has to be exactly along the primer for maximization problems.

4.1.3 Global Methods

Both direct and indirect approaches are suitable for the identification of local minima. However, the optimization of low thrust trajectories (as well as many other optimization problems) presents many local minima. Thus, for the identification of the global minimum some global optimization approaches have to be considered.

Usually these are stochastic methods presenting a very large convergence region and are widely used in early steps of the optimization process. These methods are often used to obtain an initial guess to supply to a local direct or indirect optimizer. The more common methods are the so called *evolutionary methods* that are based on the evolution of a population of possible solutions and a sort of selection of the best individuals^[94].

The *Genetic Algorithms* (GA) are a typical example of such methods and are the ones used in this work (cfr. Sec. 5.2). Although a detailed explanation is beyond the scope of the present dissertation, the main ideas are briefly recalled in this section.

These methods are actually based on the natural selection concept. An initial random population of individuals is defined within the range of the admissible controls and it is evolved. This means that for each individual a fitness function (basically a merit value) is defined in order to drive the better individuals to survive. The optimum is given by the combination of parameters that makes a specific individual the one with the best fitness value.

From a given generation, the next one is obtained by considering the mechanisms of the biological evolution^[94]. For instance, a single individual can change by means of *mutations*, where a random part of a specific individual is changed randomly in order to obtain a new individual that can result better or worse of the original one. Two individuals can give a new one using *coupling* and *selection* mechanisms; “parents individuals” are merged in order to get “children” with associated new fitness values. There are several other operators that can work,^[94] the most relevant are: the *crossing over*, where the best part of the heritage of two parents is merged together; the *elitism*, where the better individuals pass directly to the next generation without any selection criteria; the *migration*, where a part of the population evolves separately. Moreover there are many other related approaches based on evolutionary methods, like Ant Colony, Differential Evolution or Particle Swarm, to name just a few of them.

It is worth nothing that these are heuristic methods and, although there are several numerical confirmations of their ability to find good solutions of complex problems, there are few theoretical results about their convergence.

One of the most critical points in GA optimization is to define a stop condition. This can be the maximum number of generations, the maximum number of evaluation of the fitness function or similar. In this work, the maximum number of generations without any improvement in the best individuals (stall generations) has been used.

4.2 Low Thrust

While a classical chemical burn is an impulse acting on a time scale much shorter than the one of the whole mission, a low thrust engine acts on extended arcs for a time of the same order of the mission duration. Low thrust transfers are characterized by increased transfer times, but reduced propellant mass consumption if compared with the chemical ones.

Without go into detailed explanations of the physical mechanisms involved in an electric thruster, it is sufficient to think the electric thrust as the acceleration of a propellant mass by means of electric heating or electromagnetic forces. The mechanisms can be of electrothermal, electromagnetic or electrostatic nature^[84].

The main feature of an electric thruster is the high velocity of the exhaust gas, v_e . This is related to a characteristic parameter of the thruster, its *specific impulse* I_{sp} , by means of a scale factor. This factor is conventionally chosen as the Earth gravity acceleration at sea level: $v_e = I_{sp} g_0$. The specific impulse for an electric thruster is usually one order of magnitude higher than the one of a chemical thruster; approximately in the range $I_{sp} \in [1000, 7000] \text{ s}$ ^[84]. The power to thrust ratio of these electric devices is quite high so, with the current satellite onboard power capabilities, these thrusters can provide quite low thrusts (thus the correspondence between electric thrust and low thrust), roughly in the range $[1e-4, 5e-1] \text{ N}$. The thrust T can be modeled by means of the specific impulse and the available power through a thrust efficiency η_T ^[84], see Eq. (4.14).

The inclusion of a low thrust device results in an additional perturbative term on the right hand side of the equations of motion. The acceleration a_T due to the thruster acts at each time step with a magnitude given by the thrust over the instantaneous mass ratio. Moreover, the mass consumption \dot{m} is determined only by the thruster by means of its thrust and its specific impulse. This represents an additional differential equation to integrate at each time step during the thruster working phases. In equations:

$$T = \frac{2 \eta_T P}{I_{sp} g_0} \quad \dot{m} = -\frac{T}{I_{sp} g_0} \quad a_T = \frac{T}{m_0 - \dot{m} t} \quad (4.14)$$

where $g_0 = 9.81 \text{ m/s}^2$ is the Earth gravity acceleration used as non di-

mensionalizing factor and the last equation is valid for a continuous operating thruster.

A reference value considered as the cost of a specific mission is the Δv that represents the velocity change that could be obtained in a rectilinear uniform path with the same propellant amount required to accomplish a specific mission/manoeuvre considering the same thruster. This can be obtained by means of the *Tsiolkovsky formula* (or *Rocket Equation*)¹, Eq. (4.15), which is basically an application of the second Newton law to a body subject to thrust^[95]. Inverting this equation also the final mass and the propellant mass consumption can be defined as function of the Δv :

$$\Delta v = I_{sp} g_0 \log \frac{m_0}{m_f} \Rightarrow \frac{m_f}{m_0} = e^{-\Delta v / I_{sp} g_0}, \quad \frac{m_{\text{prop}}}{m_0} = [1 - e^{-\Delta v / I_{sp} g_0}] \quad (4.15)$$

The propellant mass consumption of an electric device is much smaller than the one of a chemical thruster, but not of one order of magnitude. On the other hand its specific impulse is one order of magnitude larger and thus the resulting Δv for an electric mission is usually higher than the one of a chemical mission. This reflects the fact that an electric device has to accelerate also the propellant it will use later on, limiting its efficiency. This effect is known as *Gravity Losses*^[95]. In other words, an electric thruster is able to produce high total impulse missions with limited mass consumptions, in particular with mass consumptions smaller than a chemical thruster.

Moreover, as already outlined, the inclusion of the low thrust propulsion requires, already in the preliminary mission analysis phase, some kind of optimization because the thrust magnitude and direction are unknowns and continuously varying along arcs of the path.

4.3 Two Body Application: Low Thrust Earth-Mars Transfers

As a basic application of the indirect method described in Sec. 4.1.2, let us consider an Earth-Mars interplanetary transfer. Only the heliocentric part of the transfer is addressed and zero escape and arrival hyperbolic excesses are considered ($C_3 = 0$).

A polar reference frame $\vec{x} = [r, \theta, u, v]$ is used and the initial and final positions are fixed on two circular orbits with radii equal to the average semi-major axes of the two planets (1 and 1.523 AU). The standard planar

¹Developed by K. Tsiolkovsky in his pioneering work *The Exploration of Cosmic Space by Means of Reaction Devices* published in 1903. In the early 20th Tsiolkovsky theorized several aspects of space flight, of which he is considered the father, of the rocket propulsion and he was one of the first men to conceive the space elevator.

two body dynamics, with the inclusion of the low thrust acceleration terms, in polar coordinates reads:

$$\begin{aligned}
 \dot{r} &= u & \dot{\theta} &= \frac{v}{r} \\
 \dot{u} &= \frac{v^2}{r} - \mu_{\odot}/r^2 + \underbrace{\frac{\tau T(P)}{m(t)} \cos \phi}_{a_r} & \dot{v} &= -\frac{u v}{r} + \underbrace{\frac{\tau T(P)}{m(t)} \sin \phi}_{a_{\theta}} \\
 \dot{m} &= -\tau \dot{m}_p(P)
 \end{aligned} \tag{4.16}$$

where a_r and a_{θ} are the radial and tangential components of the acceleration vector, τ the thruster switcher and μ_{\odot} is the Sun gravitational parameter. Both the thrust $T(P)$ and the propellant mass consumption $\dot{m}_p(P)$ are modeled by means of polynomial dependencies on the available power P .

The elements of the control vector $\vec{s} = [\phi, P, \tau]$ are the planar thrust angle ϕ , the input power P and the switching function $\tau \in \{0, 1\}$, to take into account the possibility of ballistic arcs.

The Lagrange multipliers $\vec{\lambda} = [\lambda_r, \lambda_{\theta}, \lambda_u, \lambda_v, \lambda_m]$ are included in the problem by considering the Hamiltonian:

$$H = \sum_i \vec{\lambda}_{x(i)} \dot{\vec{x}}(i) = \lambda_r u + \lambda_{\theta} \frac{v}{r} + \lambda_u \left(\frac{v^2}{r} - \frac{\mu_{\odot}}{r^2} + a_r \right) - \lambda_v \left(\frac{u v}{r} - a_{\theta} \right) - \lambda_m \tau \dot{m}_p(P) \tag{4.17}$$

The λ_i differential equations are obtained from $\dot{\lambda}_i = -H_{x(i)}$, Eq. (4.8), and read:

$$\begin{aligned}
 \dot{\lambda}_r &= \lambda_{\theta} \frac{v}{r^2} + \lambda_u \left(\frac{v^2}{r^2} - \frac{2\mu_{\odot}}{r^3} - \frac{\partial a_r}{\partial r} \right) - \lambda_v \left(\frac{u v}{r^2} + \frac{\partial a_{\theta}}{\partial \theta} \right) & \dot{\lambda}_{\theta} &= 0 \\
 \dot{\lambda}_u &= -\lambda_r + \lambda_v \frac{v}{r} & \dot{\lambda}_v &= -\frac{\lambda_{\theta}}{r} - 2\lambda_u \frac{v}{r} + \lambda_v \frac{u}{r} \\
 \dot{\lambda}_m &= \frac{1}{m} (\lambda_u a_r + \lambda_v a_{\theta})
 \end{aligned} \tag{4.18}$$

These Euler-Lagrange equations, Eq. (4.18), together with the dynamical equations, Eq. (4.16), constitute a system of ten nonlinear and coupled differential equations. These two systems have to be integrated simultaneously and the Pontryagin minimum principle, Eq. (4.10), gives at each integration step the control laws for the elements of the control vector \vec{s} .

It turns out that the optimal thrust direction has to be always aligned with the primer vector (cfr. Sec. 4.1.2), i.e. the optimal instantaneous value of ϕ , ϕ^* , is given by^[92]:

$$\frac{\partial H}{\partial \phi} = 0 \Rightarrow \cos \phi^* = \frac{-\lambda_u}{\sqrt{\lambda_u^2 + \lambda_v^2}}, \quad \sin \phi^* = \frac{-\lambda_v}{\sqrt{\lambda_u^2 + \lambda_v^2}} \tag{4.19}$$

It is worth nothing that as written Eq. (4.19) are intended to be used to minimize the performance index. In the case of maximization problems the signs, deriving from the Legendre-Clebsh conditions, must be inverted (cfr. Sec. 4.1.2) as well as the sign of the functional J .

The optimal value of the switcher, τ^* , follows the bang-bang strategy explained in Sec. 4.1.2, with the switch function f :

$$\tau^* = \begin{cases} 0, & \text{if } f \leq 0 \\ 1, & \text{if } f > 0 \end{cases} \quad \text{with } f = \frac{T(P)}{m}(\lambda_u \cos \phi + \lambda_v \sin \phi) - \lambda_m \dot{m}_p(P)$$

As one of the optimal control parameters is the input power of the thruster, the propellant mass consumption and the thrust of the device are expressed only as functions of this power P . In other words, the I_{sp} is not taken directly into account, but empirical polynomial expressions are considered to define $I_{sp}(P)$.

The optimal law for the input power P^* results from $\partial H / \partial P = 0$ and it depends on the specific polynomial expression of $T(P)$. Assuming a quadratic polynomial dependence from P both for the thrust ($T(P) = aP^2 + bP + c$) and for the propellant mass consumption ($\dot{m}_p(P) = dP^2 + eP + f$), the optimum law reads^[85]:

$$P^* = \begin{cases} \kappa, & \text{if } q_2 < 0 \cap \kappa \in [P_{\text{MIN}} \ P_{\text{MAX}}] \\ P_{\text{MIN}}, & \text{if } q_2 < 0 \cap \kappa < P_{\text{MIN}} \text{ or } q_2 > 0 \cap \kappa > (P_{\text{MIN}} + P_{\text{MAX}})/2 \\ P_{\text{MAX}}, & \text{if } q_2 < 0 \cap \kappa > P_{\text{MAX}} \text{ or } q_2 > 0 \cap \kappa < (P_{\text{MIN}} + P_{\text{MAX}})/2 \end{cases}$$

where $q_2 = a(\lambda_u \cos \phi + \lambda_v \sin \phi) / m - \lambda_m d$, $q_1 = b(\lambda_u \cos \phi + \lambda_v \sin \phi) / m - \lambda_m e$ and $\kappa = -q_1 / (2q_2)$.

Such polynomial expressions are available for instance for the PPS-1350 engine^[85]. This thruster is assumed to work in a bounded range of powers, so the input power is limited by $P_{\text{MIN}} = 460$ W and $P_{\text{MAX}} = 1500$ W. In this interval, these coefficients take the values:

$$\begin{aligned} T(P) &= \underbrace{4.68}_{c \text{ [mN]}} + \underbrace{60.94}_{b \text{ [mN/kW]}} P + \underbrace{(-5.1)}_{a \text{ [mN/kW}^2\text{]}} P^2 \\ \dot{m}_p(P) &= \underbrace{1.935}_{f \text{ [mg]}} + \underbrace{2.545}_{e \text{ [mg/kW]}} P + \underbrace{(-0.3716)}_{d \text{ [mg/kW}^2\text{]}} P^2 \end{aligned} \quad (4.20)$$

Within this framework, the indirect optimization method is applied twice. In a first step to minimize the mission transfer time, therefore $J = t_f$ is the index to minimize. In a second step also the propellant mass for a given transfer time is subject to minimization, i.e. the objective function is the propellant mass: $J = m_{prop}$.

The problem is completed by the physical boundary conditions on the states. The initial and final radii are the ones of Earth and Mars and the initial and final velocities are only tangential and equal to the circular velocities of the planets. The initial spacecraft mass is intended at the boundary of the Earth Sphere of Influence (SoI) ($r_{SoI}|_{\oplus} = r_{\oplus\odot}(m_{\oplus}/m_{\odot})^{2/5}$).

The final value of λ_m has to be 0 for minimum time problems and -1 for minimum mass problems (cfr. Sec. 4.1.2). The position along the heliocentric martian orbit where the encounter takes place is left free and this results in $\lambda_{\theta}(t = t_f) = 0$. Furthermore, for the time minimization several fixed time problems, with different transfer durations, are solved and among these the one satisfying also the transversality condition on the Hamiltonian is chosen.

It is worth nothing that the problem has polar symmetry and accordingly the departure angular position on the Earth orbit is not considered in the control vector. It has been assumed, without losing of generality, along the x -axis, i.e. $\theta_0 = 0$.

In equations, for the minimum time problem the final conditions the TP-BVP has to satisfy are:

$$r(t_f) = r_{Mars}, \quad u(t_f) = 0, \quad v(t_f) = \sqrt{\mu_{\odot}/r_{Mars}}, \quad \lambda_{\theta}(t_f) = 0, \quad \lambda_m = 0 \quad (4.21)$$

together with the transversality condition enforced on the Hamiltonian: $H(t_f) = -1$. While for the minimum mass in fix time problem these conditions are given by:

$$r(t_f) = r_{Mars}, \quad u(t_f) = 0, \quad v(t_f) = \sqrt{\mu_{\odot}/r_{Mars}}, \quad \lambda_{\theta}(t_f) = 0, \quad \lambda_m = -1 \quad (4.22)$$

The equations of motion are integrated in their non dimensional form with a tolerance of $1e-9$ and the TPBVP has been solved with similar accuracy. The final states result from the numerical integration and a numerical scheme varies the initial values of $\vec{\lambda}$ to satisfy Eq. (4.21) or (4.22).

As an example, two minimum time Earth-Mars transfers, different only because their initial masses, are presented in Fig. 4.2.

Since in this case minimum time transfers are sought, the variable τ is always 1, i.e. the thruster never switches off and the power is always at the maximum of the admissible interval. Accordingly, the mass consumption is linear in time. A summary of these parameters is presented in Fig. 4.3.

For an initial mass of 700 kg, the propellant mass fraction is the 31% and the minimum transfer time is 515 days. On the other had, for an heavier spacecraft with an initial mass of 1000 kg, the 32% of propellant is required and the transfer time is 751 days; results in perfect agreement with^[85].

This method shows fast convergence and limited computational time once a sufficiently accurate initial guess for the costate is supplied.

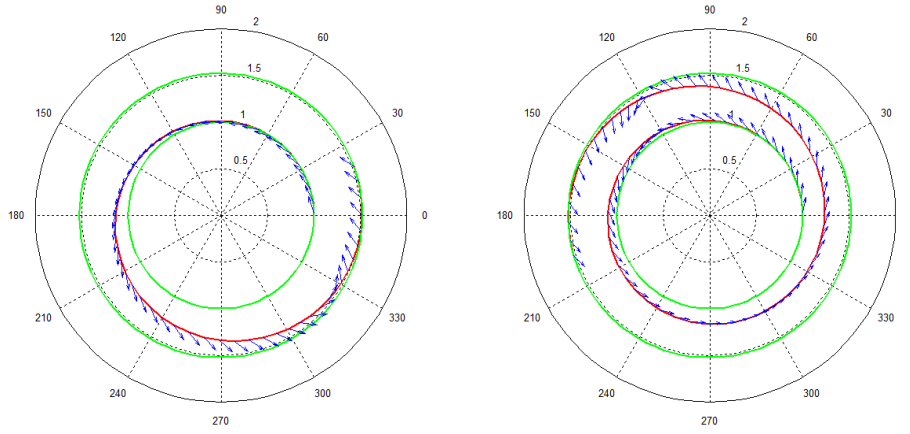


Figure 4.2: $M_0 = 700$ kg (left) and $M_0 = 1000$ kg (right) Earth-Mars minimum time transfers in the heliocentric polar reference frame.

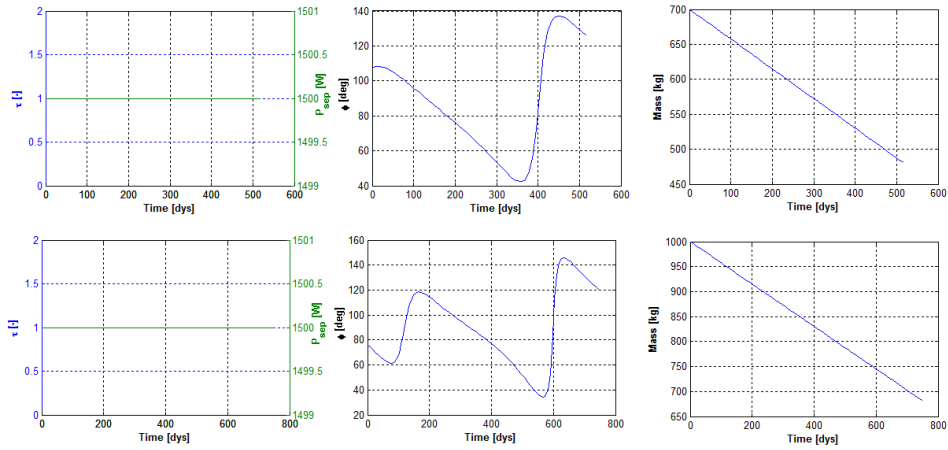


Figure 4.3: Power and τ , thrust angle and mass consumption evolutions for $M_0 = 700$ kg (first row) and $M_0 = 1000$ kg (second row) Earth-Mars transfers. Trajectories in Fig. 4.2.

Considering the same planar, polar, two body model, also minimum mass trajectories for fixed transfer times can be computed. To achieve this goal a mission time larger than the minimum one has been assumed. In this case the final condition on the Hamiltonian is not required (fix time problem) and the transversality condition on λ_m has to be satisfied (cfr. Eq. (4.22)).

The first case (Fig. 4.4, left) represents an Earth to Mars transfer with

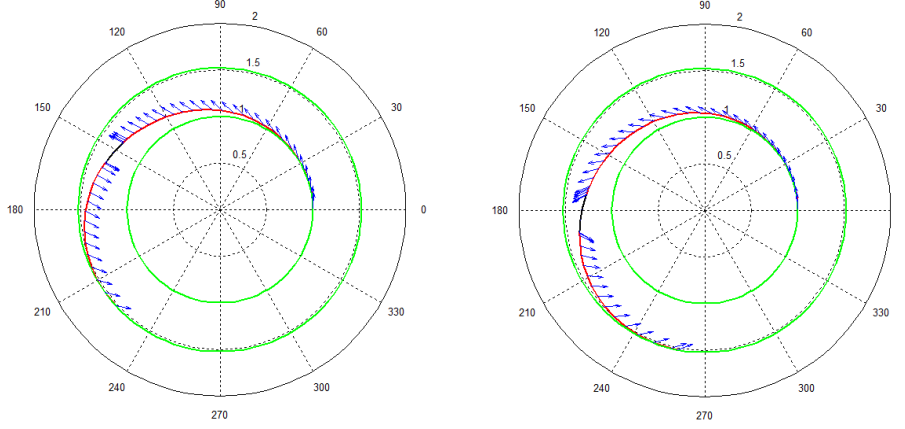


Figure 4.4: $M_0 = 300$ kg (left) and $M_0 = 350$ kg (right) Earth-Mars minimum mass transfers in the heliocentric polar reference frame. The two fixed times are respectively 300 days and 400 days.

an initial mass of 300 kg completed in 300 days. The optimal control strategy results in the classical thrust-coast-thrust strategy and the 40% of the initial mass (≈ 120 kg) is consumed.

The second case, on the right hand side of Fig. 4.4, shows a similar transfer where the initial mass is supposed to be 400 kg and the transfer time is fixed to 350 days. In this case the 35% of the initial mass has to be allocated for the propellant (≈ 140 kg) and again the thrust-coast-thrust strategy results from the optimization scheme. Also in this case the results are in agreement with^[85].

As before, also these minimum mass transfers examples are completed with the plots of the time behaviors. In 4.5 the thrust laws and the instantaneous mass are shown for both cases.

Let us conclude these examples by stressing that the planar two body dynamics and the exactly circular orbits for Earth and Mars are quite strong assumptions. Nevertheless the same approach works fine also in more complete settings considering a three dimensional two body model, ephemeris and power decreasing with the heliocentric distance^[86].

4.4 Three Body Application: Low Thrust Heteroclinic Transfers

Let us now sketch a similar approach considering the CR3BP dynamics.

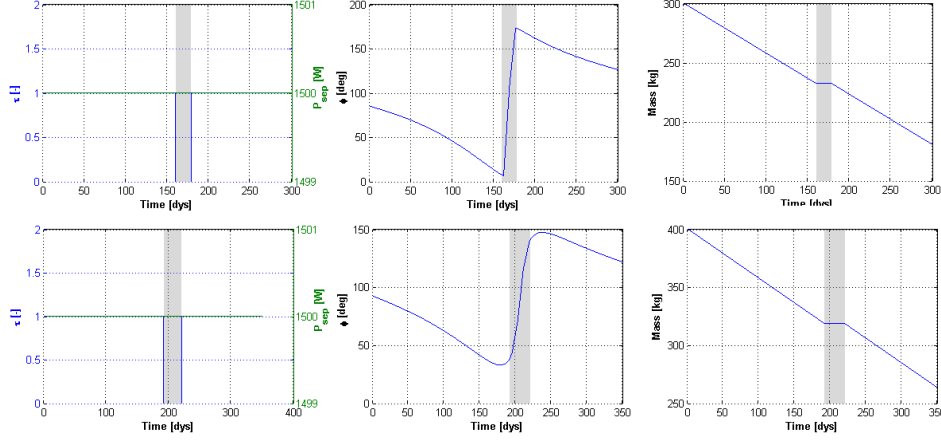


Figure 4.5: Power and τ , thrust angle and mass consumption evolutions for $M_0 = 300$ kg (first row) and $M_0 = 350$ kg (second row) Earth-Mars transfers. Trajectories in Fig. 4.4.

In Sec. 3.4 the possibility to obtain heteroclinic connections between two Lyapunov orbits without any thrust requirement has been explained. However, if in the relevant Poincaré section only the positions of two manifolds match, a chemical impulse must be applied in this point in order to obtain the matching also between the two velocities. In this way non-zero cost heteroclinic transfers are obtained. The chemical impulse to apply is simply given by the vectorial difference between the two velocities.^[40]

Let us consider now the coupling of two different three body systems. Such a kind of single burn heteroclinic connections can still be designed between two manifolds of two different periodic orbits of the two models. For instance, between the stable manifold of a Lyapunov around \mathcal{L}_2 in the Sun-Earth system and the unstable manifold of a \mathcal{L}_1 Lyapunov of the Earth-Moon system. It has been proven^[14] that in this situation free transfers does not exist, unlike from the \mathcal{L}_1 - \mathcal{L}_1 case.

Thus, the idea is to refine one of these non-zero cost transfers by replacing the chemical burn with a low thrust arc. It is like to spread the chemical impulse along a small trajectory segment. This is designed again by means of an indirect method and the electric powered arc is guessed straddle on the section plane. In the low thrust refined connections the orbits belonging to the Sun-Earth and Earth-Moon manifolds are kept fixed. So the *same* original trajectories on both manifolds are linked by a low thrust arc, computed in the Sun-Earth model.

In this case the elements of the control vector \vec{s} are:

- the initial departing time from the Sun-Earth manifold, i.e. when the thruster is switched on after a certain time spent on the manifold;
- the duration of the powered phase, computed in the Sun-Earth model;
- the arrival time, backward propagated from the target Earth-Moon Lyapunov that represents the time spent on the target manifold;
- the 5 Lagrange Multipliers $(\lambda_x, \lambda_y, \lambda_u, \lambda_v, \lambda_m)$ ruling the TPBVP.

The costate associated with the mass has been introduced as the thruster has, in general, the possibility to switch off. However, the initial guesses investigated are too near to the Poincaré section, so the thrusting time is not that long and the behavior is the thruster always on.

In this case, it is not possible to derive the optimal conditions for all the elements of the control vector, as it is not possible to compute the derivatives of the Hamiltonian with respect to some components of \vec{s} . For instance, no analytical relations exist between the time spent on a give manifold and H .

Thus, a direct minimization of the performance index is attempted and the adjoints are only used to compute the instantaneous optimum of the thrust direction. This results in a *hybrid method*^{[96][88]} that turns out to be extremely useful to include in the control vector also elements that do not admit any analytical expression of the optimal control laws^[33].

The powered version of the CR3BP equations of motion are required, specified for the Sun-Earth system ($\mu = 0.30404234e-5$). These are essentially the equations of motion, Eq. (2.27), with the usual additional acceleration term due to the thruster (in the same fashion of the two body powered equations, Eq. (4.16)). These read:

$$\begin{aligned}\ddot{x} - 2\dot{y} &= \Omega_x + a_x \\ \ddot{y} + 2\dot{x} &= \Omega_y + a_y \\ \ddot{z} &= \Omega_z + a_z \\ \dot{m} &= -\tau ||\vec{T}|| / (g_0 I_{sp})\end{aligned}\tag{4.23}$$

with $\vec{a} = \vec{T}/m$, $\vec{T} = [T_x, T_y, T_z]^T$ and where the last equation takes into account the mass decreasing (cfr. Eq. (4.14)). It is worth nothing that in this case the thrust does not have any explicit dependence, in particular it is not a function of the power like in Sec. 4.3.

Although the aim of the current section is to define a low thrust heteroclinic connection between two planar Lyapunov orbits, the complete three

dimensional case of the Hamiltonian is here presented for shake of completeness. It takes the form:

$$\begin{aligned}
 H = & \left[2v + x - \frac{(1-\mu)(x+\mu)}{r_1^3} - \frac{\mu(-1+x+\mu)}{r_2^3} + \frac{T_x}{m} \right] \lambda_u + \left[-\frac{y(1-\mu)}{r_1^3} + \right. \\
 & \left. - \frac{y\mu}{r_2^3} - 2u + y + \frac{T_y}{m} \right] \lambda_v + \left[-\frac{z(1-\mu)}{r_1^3} - \frac{z\mu}{r_2^3} + \frac{T_z}{m} \right] \lambda_w + u\lambda_x + v\lambda_y \\
 & + w\lambda_z + \frac{\tau T}{I_{sp} g_0} \lambda_m
 \end{aligned} \tag{4.24}$$

Again by means of the Euler-Lagrange equations, Eq. (4.8), the evolution of the adjoints in the CR3BP synodic frame is computed:

$$\begin{aligned}
 \dot{\lambda}_x &= \lambda_w \left[-\frac{3z\mu(-1+x+\mu)}{r_2^5} + \frac{3z(-1+\mu)(x+\mu)}{r_1^5} \right] + \\
 & \lambda_u \left[-1 + \frac{1-\mu}{r_1^3} + \frac{\mu}{r_2^3} - \frac{3\mu(-1+x+\mu)^2}{r_2^5} - \frac{3(1-\mu)(x+\mu)^2}{r_1^5} \right] + \\
 & \lambda_v \left[-\frac{3y\mu(-1+x+\mu)}{r_2^5} - \frac{3y(1-\mu)(x+\mu)}{r_1^5} \right] \\
 \dot{\lambda}_y &= \lambda_w \left[\frac{3yz(-1+\mu)}{r_1^5} - \frac{3yz\mu}{r_2^5} \right] + \\
 & \lambda_u \left[-\frac{3y\mu(-1+x+\mu)}{r_2^5} - \frac{3y(1-\mu)(x+\mu)}{r_1^5} \right] + \\
 & \lambda_v \left[-1 - \frac{3y^2(1-\mu)}{r_1^5} + \frac{1-\mu}{r_1^3} - \frac{3y^2\mu}{r_2^5} + \frac{\mu}{r_2^3} \right] \\
 \dot{\lambda}_z &= \lambda_w \left[\frac{3z^2(-1+\mu)}{r_1^5} - \frac{-1+\mu}{r_1^3} - \frac{3z^2\mu}{r_2^5} + \frac{\mu}{r_2^3} \right] + \\
 & \lambda_u \left[-\frac{3z\mu(-1+x+\mu)}{r_2^5} - \frac{3z(1-\mu)(x+\mu)}{r_1^5} \right] + \\
 & \lambda_v \left[-\frac{3yz(1-\mu)}{r_1^5} - \frac{3yz\mu}{r_2^5} \right] \\
 \dot{\lambda}_u &= 2\lambda_v - \lambda_x \\
 \dot{\lambda}_v &= -2\lambda_u - \lambda_y \\
 \dot{\lambda}_w &= -\lambda_z
 \end{aligned} \tag{4.25}$$

The optimal thrust direction is along the primer vector and the adjoint variables control also the value of τ by means of the bang-bang strategy; the specific dynamics do not change the general optimum laws derived in Sec. 4.1.2. The optimal value of all the other elements (i.e. durations) can not be determined by the minimum principle and these are simply iteratively changed in the solution of the TPBVP^{[87][97]}. The aim is to minimize the propellant mass consumption and satisfy the final physical non linear constraint that the error between the obtained final state at the end of the thrusting

phase and the target one^[33], that is the point determined by the arrival time on the Earth-Moon manifold, is zero.

The whole trajectory, as seen in the Sun-Earth frame (left) and in the Earth-Moon one (right), is shown in Fig. 4.6. Here the original trajectory is represented by the red curve, for the Sun-Earth trajectory on the manifold, and the blue curve, for the trajectory on the Earth-Moon manifold. The refined trajectory is represented by the magenta line (superimposed to the red path up to the thruster switching on), the cyan line (superimposed to the blue path up to the thruster switching off) and the brown line where the thruster is operating.

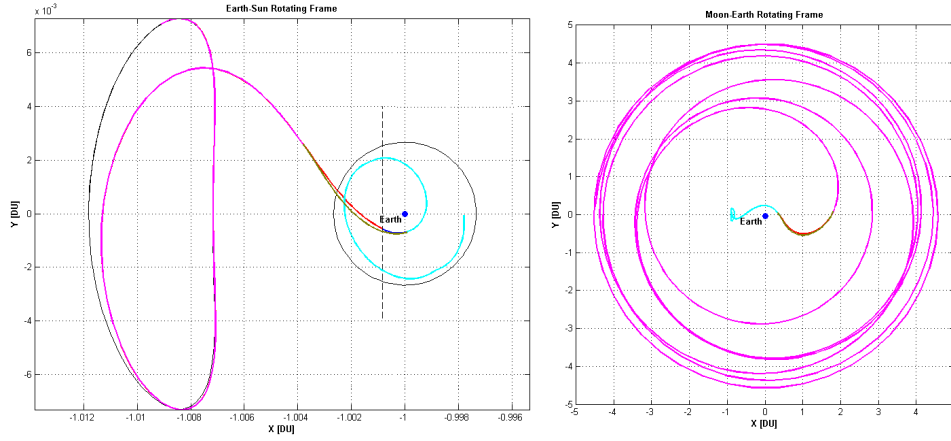


Figure 4.6: Low thrust heteroclinic connection between Sun-Earth \mathcal{L}_2 and Earth-Moon \mathcal{L}_1 ; in the Sun-Earth synodic frame (left) and in the Earth-Moon one (right).

All the computations have been done in the Sun-Earth rotating frame, moreover in this case the small primary of both system has been assumed located on the negative x -axis.

A test spacecraft with an initial mass of 1000 kg has been used together with $I_{sp} = 2000$ s and $T = 0.5$ N. With these data, the low thrust heteroclinic connection requires an electric $\Delta v \approx 351$ m/s, that corresponds to a $\Delta m \approx 17.7$ kg. Considering a chemical impulse of $I_{sp}|_{ch} = 320$ s, it is possible to compare these results with the chemical case, both in terms of mass consumption and Δv (given by the vectorial difference of manifolds velocity on the Poincaré section). As explained in Sec. 4.2, the low thrust refined trajectory presents a lower mass consumption and a higher Δv . Although the electric thruster requires approximately 30 m/s of additional Δv with respect to the chemical case (≈ 351 instead of ≈ 320 m/s), it saves approximately

80 kg of propellant mass (≈ 17.7 instead of ≈ 97 kg).

As the low thrust arc has been guessed very close to the discontinuity (the vertical dashed line in Fig. 4.6), this kind of transfers has to be considered only locally optimal. In the sense that a global search of the optimum region has been not performed and making the low thrust arc free to start/end on a different trajectory of the manifolds could result in shorter powered phases and consequently less expansive transfers realizing the same heteroclinic connection.

The time behaviors of the mass, thrust angles, heliocentric position and velocity are presented in Fig. 4.7 with the same color convention of Fig. 4.6.

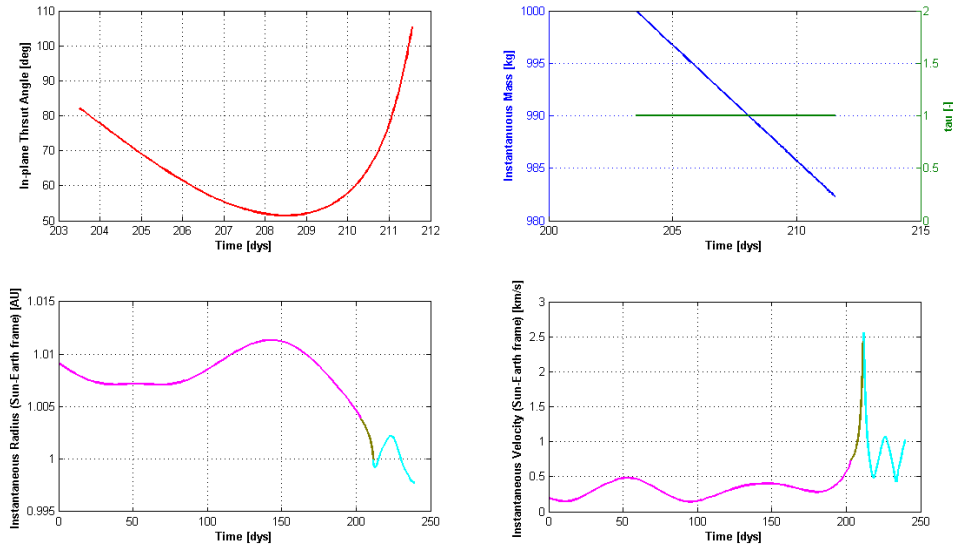


Figure 4.7: Thrust angle, mass, instantaneous radius and velocity for the low thrust heteroclinic connection between Sun-Earth \mathcal{L}_2 and Earth-Moon \mathcal{L}_1 .

It has to be stressed that the Earth-Moon manifold is not integrated in the Sun-Earth system, but just a coordinate transformation between the two systems is performed. This causes the trajectories composing this manifold to have different energies in the Sun-Earth system.

4.5 Considerations

Some considerations about the use of the hybrid algorithm are here appropriate. This approach allows maintaining a low number of variables if compared with direct methods and at the same time allows the inclusion of other ele-

ments in the control vector beside the initial values of the adjoint variables. In this scheme, instead of implementing a root finding procedure to satisfy the resulting TPBVP including all the optimality constraints, a numerical direct minimization of the performance index is sought.

Nevertheless, it has to be stressed that this approach might not satisfy the final transversality conditions deriving from indirect methods. These conditions are an integral part of the optimal control problem and consequently a hybrid approach does not have any analytical proof of the optimality of the solution obtained.

This method resembles a sort of single shooting approach where the thruster control laws are parameterized by the initial value of the Lagrange multipliers. The direct minimization of the performance index subject to physical constraints replaces the analytic optimal control law. This is required as in the control vector are included also elements for which it is not possible to derive analytic conditions for the stationarity of the Hamiltonian. Thus the minimization of the functional is given by iterative procedures and the optimal control laws are only used to parameterize the evolution of the adjoint ruling the thruster behavior.

In this sense the applications presented are only to be intended as feasible solutions presenting a numerical minimum of a given index into a neighborhood of other feasible solutions around them.

Chapter 5

Low Energy, Low Thrust Deep Space Missions

Real verifications of the CR3BP, like comets orbits or particular families of asteroids around Sun-planet equilibrium points, brought to change the solar system view. Instead of considering a set of independent, almost circular heliocentric orbits governed only by the Sun attraction, the solar system is better understandable looking it as a net of gravity forces balancing and dominating one each other depending on the regions. This approach is particularly useful also from a mission analysis point of view as the path of a probe can be designed by exploiting this net. Interplanetary low energy mission have been already proposed^[47] as well as operational phases designed within the three body model, like the tour of the Jupiter's moons^[40].

In this section, an example of one dimensional manifolds connected by electric propulsion is presented in order to design a small tour of the Uranus moons. This operational phase is supposed to be the last part of an interplanetary low power transfer^[98] designed in the CR3BP. Furthermore, also an application of a manifold to manifold transition is presented. This passage is intended to design an Earth-Mars transfer and the energy required to move away from the Sun-Earth manifold up to get into the Sun-Mars one is supposed to be provided by an electric thruster.

5.1 Low Thrust Transition between one dimensional Manifolds

The conjunction, by means of low thrust arcs, of one dimensional manifolds associated with different three body models is presented as first naive application of the combination of manifold and low thrust in the framework of

non Earth-Moon mission scenarios. This is carried out to perform a *moons tour* and the Uranus moon system is chosen as workbench. This is a novel space mission profile, already proposed in other contexts^{[40][14]}, that takes advantage both from multi-body regimes and from the low thrust characteristics. With this approach, the planetary moons can be explored for longer times if compared with the classical (multi) swing-by approach^[99]. Furthermore, the intricate net of their gravitational fields can be exploited to reduce the mission propellant mass requirement in combination with low thrust arcs enabling to move from a ballistic phase to another.

The Uranus system provides a very interesting dynamical environment because its five main moons are sufficiently massive, with almost circular and coplanar orbits and near enough to form several three body models with the planet acting as principal body.

The main purpose of this section is to define a methodology to design a tour within the Uranus system that visits each of its main moons including a temporary capture around each of them obtained by a ballistic arrival and departure arc.

The trajectory proposed starts with a ballistic approach arc towards the outer moon, Oberon, and ends with a stable orbit around Uranus with a radius smaller than the inner moon, Miranda, mean orbital distance. During the complete transfer, closed orbits around Oberon, Titania, Umbriel, Ariel and Miranda (the five main moons from the outmost to the closer one with respect to Uranus) are executed^[100]. This would enable scientific studies of these moons for a duration considerably longer if compared with single or multiple fly-bys^[99].

The tour is computed within several PCR3BPs, based on which the stable and unstable manifolds associated with the libration points (one dimensional) of each system are computed. The connection of two generic states, respectively on an unstable and on a stable manifold, enables the passage from one system to the other^[101]. This transition requires an energy change provided by the electric device. Here low thrust arcs (or alternatively ballistic arcs among multiple chemical impulses) are mandatory as there are no intersections in the position space among the manifolds of the various systems.

The problem is decoupled in several PCR3BP composed by Uranus and one moon at a time. The forbidden regions of each system have to be open to allow the transit from the exterior realm, through the moon realm to the inner realm where the stable manifold of the next PCR3BP is targeted.

The lowest energy value that permits the transit from the outer realm, traversing the moon region, into the inner realm is the one associated with \mathcal{L}_2 . Therefore, the manifolds used for this application, and thus the energy

level, are the ones associated with this point. These can be computed as explained in Sec. 3.2.1.

In Fig. 5.1 the Hill regions (left) and the one dimensional manifolds of each Uranus-moon system (right) are represented, each in the proper rotating frame. The energy level used to obtain the picture is $E_{\mathcal{L}_2}$ of the Uranus-Miranda system, the lowest one considered as this system has the lower value of the mass parameter (cfr. App. A).

Without losing generality, the Uranus-Oberon system is considered the reference one and for the tour computation everything is transformed into this system.

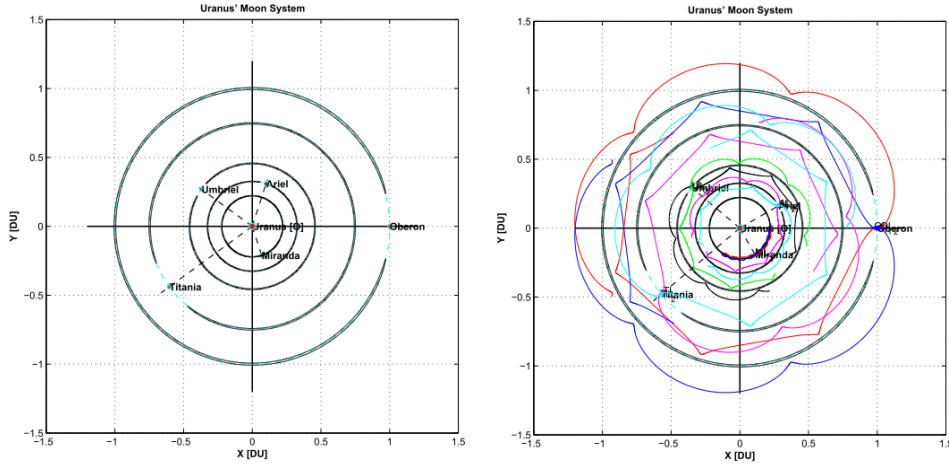


Figure 5.1: Uranus-Oberon/Titania/Umbriel/Ariel/Miranda Hill regions (left) and one dimensional manifolds (right) each as seen in the proper synodic barycentric frame.

The low thrust arcs are modeled by adding on the right hand side of the usual PCR3BP equations, Eq. (2.27), an additional perturbative term of the form: $\vec{a} = \|\vec{a}\| \cos \alpha \hat{\mathbf{T}} + \|\vec{a}\| \sin \alpha \hat{\mathbf{N}}$, Eq. (4.23), split into the tangential $\hat{\mathbf{T}}$ and normal $\hat{\mathbf{N}}$ directions. The modulus $\|\vec{a}\|$ includes a switch function τ ; this, together with the thrust angle α , are elements of the control vector.

The computation of the \mathcal{L}_2 stable manifold (the one leading from the exterior to the moon realm and then into the inner one) requires the propagation of the initial conditions for a time span beginning at the end of the powered phase of the previously considered transfer. The propagation is performed backward for a time that identifies the duration for which the spacecraft lies on the stable manifold. The duration of this time span (t_{mani}) and the initial

position of the relative moon (θ) are terms of the control vector.

Furthermore, the exit time from the previously considered, unstable manifold of \mathcal{L}_1 (t_0) is also considered as a term of the control vector together with the duration of the powered phase (t_{el}), not a-priori defined.

In this case the thrust laws (α, τ) are included in the control vector by a time discretization of the propulsion phase. It has been divided into n -mesh points and at each knot the thrust modulus and angle are con-

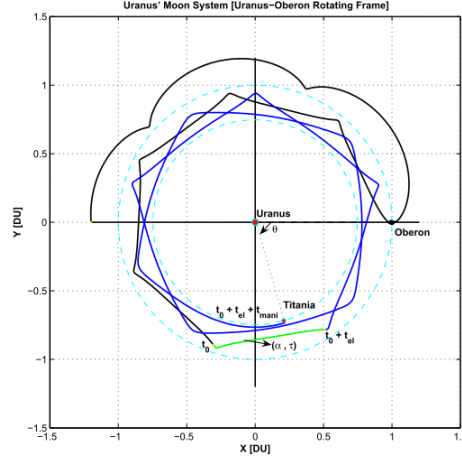


Figure 5.2: Control vector elements for the Oberon-Titania transfer.

sidered as elements of the control vector. The thrust law between two consecutive mesh points is then interpolated in a linear way. A fixed number of knots, $n = 10$, has been arbitrarily chosen for normal transfers where this is doubled for long propulsion phases (Titania-Umbriel and Ariel-Miranda) to limit the computational time.

Thus, the complete control vector is composed by the three durations, one angle representing the initial phase of the target moon and two n -dimensional arrays. So the control \vec{u} is a $(2n+4)$ -dimensional vector. The complete control vector is schematically presented, for the first Oberon-Titania transition, in Fig. 5.2

Each transit has to be accomplished by using the minimum propellant mass and with the constraint that the final state of the propulsion phase matches with the initial state of the \mathcal{L}_2 stable manifold of the target moon. This results in a NLP solved by means of a SQP approach^[102]. In order to constrain the computational time, a tolerance of 5% has been imposed on the phase distance of the conjunction states.

This kind of approach (a sort of direct shooting explained in Sec. 4.1.1) is quite dependent on the initial guess and a high computational load can result if the initial guess is very poor or if it lies on the boundary of the feasible region. It is worth nothing that the value of the small perturbation d , introduced in Sec. 3.2.1, has been subject of few numerical iterations in order to obtain a value corresponding with a minimum altitude not less

than 50 km above the surface of each moon (thus d changes depending on the specific PCR3BP). Moreover, this value affects also the number of closed orbits around each moon and the associated duration of the unstable ballistic capture.

5.1.1 The Moon Tour

Considering an initial mass of 500 kg, $I_{sp} = 3200$ s, $P|_{const} = 1000$ W and $\eta_T = 0.5$, the resulting tour is represented in Fig. 5.3, on the left in the Uranus-Oberon rotating frame and on the right in the Uranus centered system. This tour can be performed in approximately 957 days and it requires only 35 kg of propellant mass, corresponding to the 7% of the total spacecraft mass. With the considered thruster characteristics this means a total Δv of 2.26 km/s.

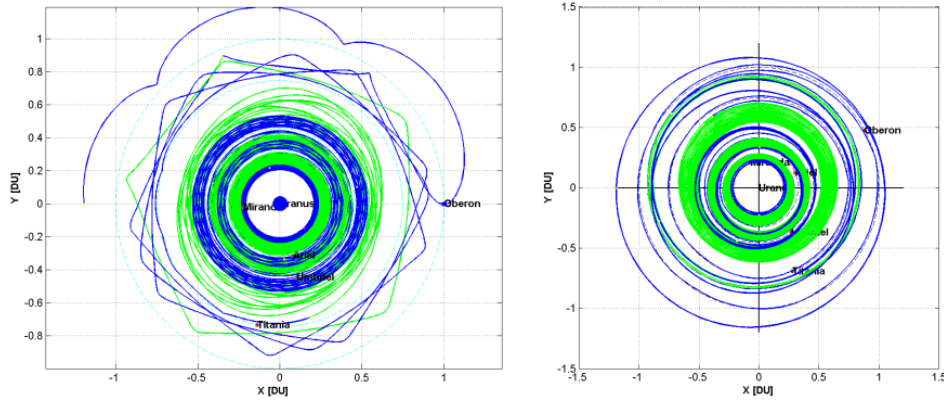


Figure 5.3: Uranus moons tour in the Uranus-Oberon frame (left) and in the Uranus inertial one (left). In blue the ballistic phases, in green the powered ones.

The transition from Oberon to Titania requires only a relatively short propulsion phase of approximately 56 days due to the close proximity of the two moons and their similar physical characteristics. On the other hand, the transition to Umbriel and Miranda requires approximately 150 and 128 days respectively, the longest ones. This is explained by the large radial and physical difference with respect to the previous system.

To complete the description, the trend of some relevant parameters, e.g. the instantaneous position and velocity referred to Uranus and the spacecraft mass, together with a detail of the Titania capture phase (the others are similar) are presented in Fig. 5.4.

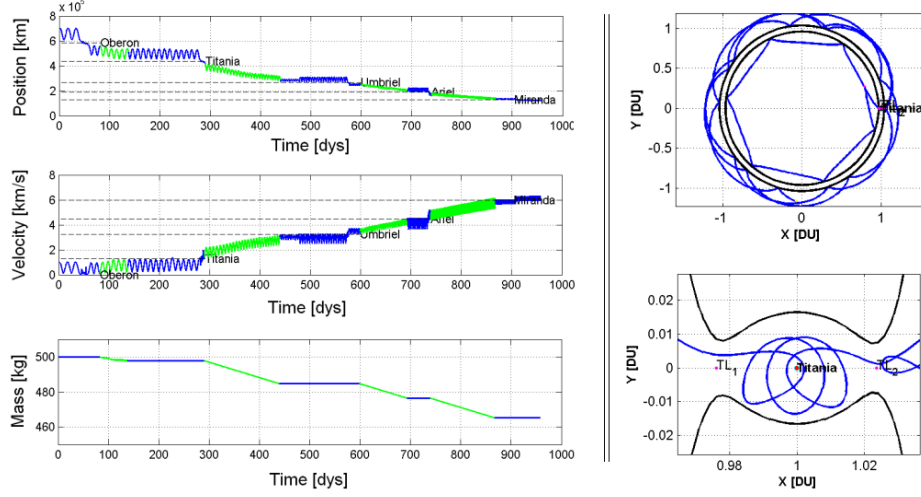


Figure 5.4: Left: time evolution of position, velocity and mass for the Uranus moon tour. Right: details of the Titania ballistic capture phase.

5.1.2 Earth-Uranus Transfer

This tour has been thought as the last part of an interplanetary mission of a small spacecraft equipped with Radioisotope Thermoelectric Generators (RTGs)^[103]. Since these modules work better and better as the heliocentric distance is increased, the target Uranus has been chosen after a trade off between the transfer time and the propellant mass consumption^[104]. The interplanetary transfer is assisted by a high energy launch, providing the spacecraft with a high departure velocity to maintain acceptable transfer times. Following the launch, the electric propulsion is used to decelerate the spacecraft up to the Uranus capture and subsequent tour beginning^{[98][105]}.

The departure angular phase along the circular heliocentric Earth orbit (i.e. the launch date) and the departure excess energy have a strong effect on the shape of the trajectory^{[106][107]}. An erroneous selection of the initial position or of the excess energy might render the transfer unfeasible or with an excessively long duration^[108]. Following launch, the electric propulsion must modify the velocity in all three dimensions in order to adhere the imposed final conditions. In particular, considering a heliocentric cartesian frame, it is worth nothing that the initial state is in the x - y plane, whereas the final state, which corresponds with the start of the Uranian tour, is in the x - z plane, due to the high inclination of the Uranus spin axis tilted of 97.77 deg with respect to the ecliptic plane (the moon orbits are approximately onto the Uranus equatorial plane). The Sun-Uranus CR3BP has been used ($\mu = 4.3528e-5$),

although this model has to be considered only as a heavy approximation since at least Jupiter/Saturn have to be taken into account for such long interplanetary transfers.

The iterative scheme computes both the in-plane and the out-of-plane thrust components, while minimizing the time required to reach the final state. Initially a gradient method is applied to generate a sufficiently accurate initial guess for a subsequent forward shooting method. The latter method requires an accurate guess at $t = t_0$, which is obtained by the former, more robust, optimization scheme^[91]. To maintain the mission duration into a reasonable range, the transfer time has been considered as functional to minimize and a limit on the final mass after the interplanetary transfer is imposed indirectly.

The whole interplanetary path, using the chemical escape and the electric capture, is presented in Fig. 5.5 with the in-plane and the out-of-plane motion.

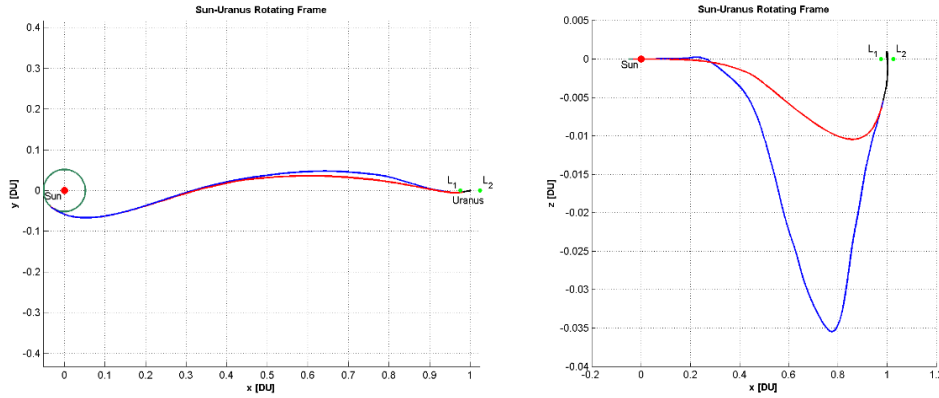


Figure 5.5: Interplanetary Earth-Uranus transfer; on the left in the x - y and on the right in the x - z , with exaggerate out-of-plane scale.

In Fig. 5.5 the gradient solution (blue) and the forward shooting one (red) are superimposed. The first one is slightly more expensive than the second one especially because it performs a larger out-of-plane excursion. The gradient sub-optimal path is used only as initial guess for the forward shooting that results in a lower propellant mass consumption with approximately the same transfer time. The out-of-plane thrust angle is extremely moderate, due to the fact that the velocity component along z at the final state is relatively small and the distance of 19.2 AU is available to achieve this starting from

planar conditions.

In Fig. 5.6 a detail of the electric capture phase (black line) is represented. It starts from the forward shooting solution when this reaches the Uranus Sphere of Influence. During this phase the energy of the spacecraft gradually decreases leading to a closure of the Hill regions with consequent capture of the probe. In addition, the spacecraft is aligning its position and velocity with the requirements imposed by the planetary tour.

Considering an initial mass of 900 kg^[109] launched with a $C_3 = 130 \text{ km}^2/\text{s}^2$ (data suitable, for instance, for an Atlas V launcher equipped with a Star 48V upper stage), this transfer takes approximately 9.14 years to reach the Uranus Sphere of Influence requiring 292.7 kg of propellant mass. Afterwards, ≈ 2.56 years, with 83 kg of mass consumption, are required to de-spiralling until a high elliptic uranian orbit is achieved^[103].

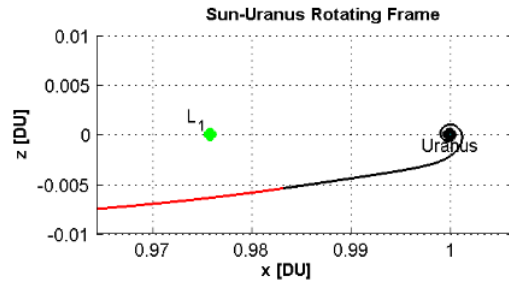


Figure 5.6: Electric capture (black line) detail in the Uranus realm, from its Sphere of Influence.

5.2 Low Thrust Halo to Halo Interplanetary Transfers

The core idea of this section is to investigate about the possibility to apply a low thrust propulsion strategy to interconnect ballistic trajectories on invariant manifolds associated with multiple circular restricted three body systems^[68]. Sun-planet three body models can be considered to compute arrival and departure ballistic trajectories^[5] and the electric propulsion used to interconnect these trajectories.

A remarkable advantage of this approach in terms of mission design is that it allows to detect connection trajectories also if a direct intersection of the ballistic arcs (i.e. manifolds) on a given Poincaré section does not exist.

Once two ballistic trajectories have been computed and propagated up to the surface of section, an intersection in the position space corresponds to initial conditions to propagate forward and backward to obtain the connection. The vectorial difference in velocity on the surface of section represents the chemical impulse to supply in that point (cfr. Sec. 3.3-3.5). This method has been used to design several transfer trajectories in the CR3BP framework^{[76][39]}, but it is not applicable if there are no intersections between the manifolds in the position space (cfr. Sec. 4.4). This lack of intersections is well known for the CR3BP formed by the Sun and all the inner planets, while

for the outer planets the manifolds intersect and this results in low energy paths that asteroids and small bodies can follow to move around the solar system^[69].

The ability of the electric thruster to provide the energy change required to transit the spacecraft between the manifolds of two systems appears suitable also in this context. Moreover, the inclusion of low thrust arcs provided by an electric propulsion system results in a further propellant mass saving if compared with the chemical alternative. Intrinsically associated with the low thrust propulsion, however, are the extended arcs between the manifolds during which the thrust must be continuously provided.

The considered approach, see Fig. 5.7, consists of a first ballistic escape phase along the departing planet unstable manifold followed by the powered phase which modifies the spacecraft energy so that upon thrust completion the spacecraft adheres the phase space conditions enabling the insertion on the destination stable manifold. Here a second ballistic phase follows, where the CR3BP dynamics of the target Sun-planet system guide the spacecraft onto a periodic orbit around the libration point of the target planet^[110].

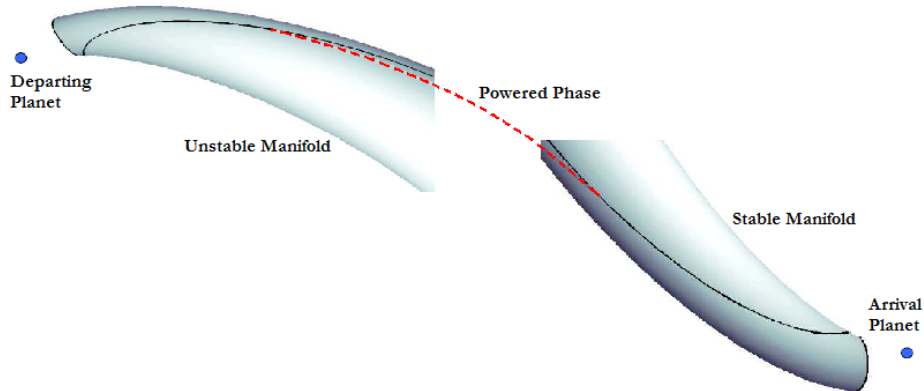


Figure 5.7: Low thrust Halo to Halo interplanetary transfer; a stable and an unstable manifolds of two different three body systems are linked by means of an electric powered arc.

To design the thrusting phase an active control of the thrust parameters is required, in order to obey the final conditions imposed by the manifold dynamics. The in-plane and the out-of-plane control angles have to be computed together with the behavior of the electric thruster where also the possibility of coasting phases can be taken into account.

It has to be stressed since now that such a kind of interplanetary trajectories can be used to transfer a spacecraft or a cargo from a near Earth

station (e.g. on a periodic orbit near \mathcal{L}_1) to a similar station near the target planet. These transfers seem especially useful for scientific exploration missions with major constraints on the propellant mass, in order to maximize the allocation of the on board resources to the scientific equipment, rather than on the transfer time^[5].

5.2.1 Design Strategy

The dynamics of the spacecraft are studied within different models depending on the distance from the main attractors. In particular, the approximate dynamics associated with the two primaries Sun-departing/arrival planet are considered during the ballistic escape and capture phases, while a more complete dynamics, by taking into account all the three attractors, is used during the interplanetary powered phase.

The basic dynamics employed is again the CR3BP outlined in Sec. 2.2, during the escape and capture phases, while, in order to define a more accurate and realistic dynamics, during the powered interplanetary phase the BCM scheme is considered (cfr. Sec. 2.3). In this case the additional perturber is one of the two planets, moving along a circular path around the center of mass of the other two primaries, i.e. the Sun and the other planet.

The perturbation of this additional body is not considered during the permanence on the Sun-planet manifold because the distance of the spacecraft with respect to the other small primary is very large and the other planet's gravity can be neglected. This allows the computation of libration points, periodic orbits and manifolds because the CR3BP model is considered.

With this idea, the CR3BP equations are used only in their ballistic version for the phases on the manifolds, while the BCM is used together with the low thrust terms. Accordingly on the right hand side of Eq. (2.44) an additional acceleration term appears:

$$\begin{aligned}\ddot{x} - 2\dot{y} &= \partial\Omega_4/\partial x + a_x \\ \ddot{y} + 2\dot{x} &= \partial\Omega_4/\partial y + a_y \\ \ddot{z} &= \partial\Omega_4/\partial z + a_z\end{aligned}\tag{5.1}$$

where the Ω_4 is the modified effective potential of Eq. (2.45). These accelerations have the form of Eq. (4.14), i.e. $a_i = \tau T/m \hat{\mathbf{a}}(i)$, where τ is the thruster switch variable and $\hat{\mathbf{a}}$ represents again the unit acceleration vector.

The power available for the electric thruster is supposed to be provided by a solar electric device, therefore a natural diminution of the power available with the heliocentric distance is considered. Considering an initial fix power in a heliocentric orbit of radius 1 AU, the inverse square law is considered for

the power decrease. Thus, the effective available power for the thruster (from which the mass consumption and the thrust are computed by means of Eq. (4.14)) scales as $P = P_{\text{in}}/r^2$. It is worth nothing that in this expression (as in the following equations) the units are already non dimensional and thus the heliocentric Earth distance is unitary.

The first step to perform in order to apply the outlined procedure, is to compute a specific periodic orbit around the proper libration point for a given energy value. The specific libration point depends on whether the transfer is sought toward an inner planet, where the periodic orbit has to be computed around \mathcal{L}_1 of the Sun-departing planet system, or toward an outer planet, where the interesting point is \mathcal{L}_2 . The energy value of this orbit, actually related to its amplitude, can be a given value that satisfies some of the mission requirements or can be an element of the control vector. Once this periodic orbit has been defined (cfr. Sec. 3.1.1), the relevant unstable manifold for the departing phase has to be propagated (cfr. Sec. 3.2). In a specular fashion also the arrival periodic orbit and the inherent stable manifold has to be computed.

In order to define a more realistic procedure, Halo orbits and relevant manifolds are considered, but the extension to the planar case with Lyapunov orbits is straightforward. Thus the specific orbits are chosen (a-priori or resulting from the numerical scheme) by selecting a specific value of their out-of-plane amplitude, A_z .

The combination low energy - low thrust better exploits its capabilities when a reduction of the propellant mass consumption is sought instead of the transfer time. Thus, in order to design the transfer, the objective is to minimize the propellant mass fraction consumed during the mission subject to the constraint that the final position of the thrusting phase matches the final conditions of the ballistic capture backward propagated from the final position on the target Halo orbit. It has to be stressed that, as also the possibility of a thruster switch off is considered, the minimization of the propellant mass is not equivalent to minimize the duration of the powered phase.

The hybrid approach (outlined in Sec. 4.4) results very useful for mixed optimal problems, like in this case, in which only a part of the elements of the control vector admits an explicit derivation of the optimal laws. Thus, the thrusting strategy applied during the interplanetary powered phase is computed by an indirect approach, using elements of the calculus of variations, although a direct minimization of the performance index is attempted to include also other elements in the control vector.

Optimal control theory is applied to derive the thrust angles and the

thruster on/off control laws (resulting in the primer direction and bang-bang strategy explained in Sec. 4.1.2), however also other search variables are included in the control vector and the resulting two point boundary value problem is solved by a sequential quadratic programming method^[83]. This means that the resulting trajectory is, first of all, a feasible solution of the given problem and it presents also a local minimum of the mass consumption if compared with close solutions.

To apply the calculus of variations and the minimum principle, the Hamiltonian of the problem is required in order to derive the Euler-Lagrange equations (cfr. Sec. 4.1.2) in the framework of the BCM. In similar fashion like Sec. 4.4, the Hamiltonian reads $H = \sum_i \vec{\lambda}_{\mathbf{x}(i)} \cdot \dot{\mathbf{x}}(i)$ with $i = [x, y, z, u, v, w, m]$ and from this the evolutions of the multipliers, Eq. (4.8), are ruled by:

$$\begin{aligned}
\dot{\lambda}_x = & \lambda_v \left[-\frac{3y\mu_E(-1+x+\mu_E)}{r_2^5} - \frac{2\sin\theta_M(x-\rho_M\cos\theta_M)\mu_M}{r_3^4} + \right. \\
& -\frac{3y(1-\mu_E)(x+\mu_E)}{r_1^5} - \frac{3(x-\rho_M\cos\theta_M)(y-\rho_M\sin\theta_M)\mu_M}{r_3^5} + \\
& \left. \frac{2\hat{a}_y T\tau(x+\mu_E)}{mr_1^4} \right] + \lambda_u \left[\frac{1-\mu_E}{r_1^3} - 1 + \frac{\mu_E}{r_2^3} - \frac{3\mu_E(-1+x+\mu_E)^2}{r_2^5} + \right. \\
& -\frac{3(1-\mu_E)(x+\mu_E)^2}{r_1^5} + \frac{\mu_M}{r_3^3} - \frac{2\cos\theta_M(x-R_M\cos\theta_M)\mu_M}{r_3^4} + \\
& -\frac{3(x-\rho_M\cos\theta_M)^2\mu_M}{r_3^5} + \left. \frac{2\hat{a}_x T\tau(x+\mu_E)}{mr_1^4} \right] + \\
& \lambda_w \left[-\frac{3z\mu_E(-1+x+\mu_E)}{r_2^5} + \frac{3z(-1+\mu_E)(x+\mu_E)}{r_1^5} + \right. \\
& -\frac{3z(x-\rho_M\cos\theta_M)\mu_M}{r_3^5} + \left. \frac{2\hat{a}_z T\tau(x+\mu_E)}{mr_1^4} \right] - \lambda_m \frac{2T\tau(x+\mu_E)}{I_{sp}g_0r_1^4} \\
\dot{\lambda}_y = & \lambda_w \left[\frac{3yz(-1+\mu_E)}{r_1^5} - \frac{3yz\mu_E}{r_2^5} - \frac{3z(y-\rho_M\sin\theta_M)\mu_M}{r_3^5} + \frac{2\hat{a}_z T\tau y}{mr_1^4} \right] + \\
& \lambda_u \left[-\frac{3y\mu_E(-1+x+\mu_E)}{r_2^5} - \frac{2\cos\theta_M(y-\rho_M\sin\theta_M)\mu_M}{r_3^4} - \right. \\
& \frac{3(x-\rho_M\cos\theta_M)(y-\rho_M\sin\theta_M)\mu_M}{r_3^5} - \frac{3y(1-\mu_E)(x+\mu_E)}{r_1^5} + \\
& \left. \frac{2\hat{a}_x T\tau y}{mr_1^4} \right] + \lambda_v \left[-1 - \frac{3y^2(1-\mu_E)}{r_1^5} + \frac{1-\mu_E}{r_1^3} - \frac{3y^2\mu_E}{r_2^5} + \frac{\mu_E}{r_2^3} + \right. \\
& \frac{\mu_M}{r_3^3} - \frac{2\sin\theta_M(y-\rho_M\sin\theta_M)\mu_M}{r_3^4} - \frac{3(y-\rho_M\sin\theta_M)^2\mu_M}{r_3^5} + \\
& \left. \frac{2\hat{a}_y T\tau y}{mr_1^4} \right] - \lambda_m \frac{2T\tau y}{I_{sp}g_0r_1^4}
\end{aligned}$$

$$\begin{aligned}
\dot{\lambda}_z &= \lambda_w \left[\frac{3z^2(-1 + \mu_E)}{r_1^5} - \frac{-1 + \mu_E}{r_1^3} - \frac{3z^2\mu_E}{r_2^5} + \frac{\mu_E}{r_2^3} - \frac{3z^2\mu_M}{r_3^5} + \frac{\mu_M}{r_3^3} + \right. \\
&\quad \left. \frac{2\hat{a}_z T \tau z}{mr_1^4} \right] + \lambda_u \left[-\frac{3z\mu_E(-1 + x + \mu_E)}{r_2^5} - \frac{3z(1 - \mu_E)(x + \mu_E)}{r_1^5} + \right. \\
&\quad \left. -\frac{2z\mu_M \cos \theta_M}{r_3^4} - \frac{3z(x - \rho_M \cos \theta_M)\mu_M}{r_3^5} + \frac{2\hat{a}_x T \tau z}{mr_1^4} \right] + \\
&\quad \lambda_v \left[-\frac{3yz\mu_E}{r_2^5} - \frac{2z\mu_M \sin \theta_M}{r_3^4} - \frac{3z(y - \rho_M \sin \theta_M)\mu_M}{r_3^5} + \right. \\
&\quad \left. -\frac{3yz(1 - \mu_E)}{r_1^5} + \frac{2\hat{a}_y T \tau z}{mr_1^4} \right] - \lambda_m \frac{2T \tau z}{I_{sp} g_0 r_1^4} \\
\dot{\lambda}_u &= 2\lambda_v - \lambda_x \\
\dot{\lambda}_v &= -2\lambda_u - \lambda_y \\
\dot{\lambda}_w &= -\lambda_z \\
\dot{\lambda}_m &= \frac{2\hat{a}_x T \tau \lambda_u}{m^2 r_1^2} + \frac{2\hat{a}_y T \tau \lambda_v}{m^2 r_1^2} + \frac{2\hat{a}_z T \tau \lambda_w}{m^2 r_1^2}
\end{aligned} \tag{5.2}$$

It is worth noting that the derivation of the adjoint equations takes into account also the decrease of the power with the heliocentric radius, this causes the presence of terms due to the thrust in the differential equations for the Lagrange multipliers associated with the positions. Moreover also the adjoint equation for the Lagrange multiplier associated with the mass has to be considered as this variable is required in the Hamiltonian for the derivation of the τ optimum law.

The permanence on the unstable departing manifold (t_1), the duration of the thrusting phase (t_2), the permanence on the stable arrival manifold (t_3), the initial position of the perturber in the synodic frame (θ_P), the z -amplitudes of the arrival (A_{z_a}) and departure (A_{z_d}) orbits and the angular positions on both orbits (ν_a, ν_d) are considered as variables. Thus, the complete control vector is composed by three times, one angle, two angle-like variables (identifying the departure and arrival positions), one seven dimensional vector (for the adjoint $\vec{\lambda}$) and two A_z amplitudes. These angle like variables are actually the elapsed times, within the period of the Halo orbits, identifying the specific trajectory on the manifold.

The problem is stated as a non-linear programming problem and solved again by means of a SQP method that updates the fourteen search variables trying to minimize the performance index and satisfying the constraints. The SQP approach, however, results in some local solutions close to the initial guess supplied; in order to overtake this limitation and correctly identify the region of the global minimum also a comparison with a genetic algorithm search is performed.

For the statement of the genetic algorithm approach the same structure of the local optimization can be used but the final constraints are imposed directly in the fitness function by means of two (one for the error on positions and one for the error on velocities) weights. This means that the function to be minimized is composed by the propellant mass and weighted errors on the final state at the end of the electric powered phase. These errors are in non dimensional units and the two weights are usually close to the unit with the one associated to the velocity error slightly larger (≈ 2).

Moreover, also side constraints on the elements of the control vector must be considered in order to “guide” the evolution of the initial population. This is chosen as uniformly distributed over the search space defined by boundaries on the various elements of the control vector, assuring in this way the feasibility of the solution.

5.2.2 Earth-Mars: A Study Case

The described procedure can be applied to a representative case where an interplanetary Halo to Halo low thrust transfer is addressed between Earth and Mars.

It has to be noted that, using the BCM as general dynamical model and simply tuning the mass parameters of the three bodies, also the Earth escape phase and the Mars capture one, can be studied like in the CR3BP where only the primaries, respectively Sun-Earth and Sun-Mars, are considered.

For the interplanetary BCM phase the principal system chosen is the Sun-Earth CR3BP where the Mars gravitational perturbation is added. In this case the approach requires three additional assumptions if compared with the classical CR3BP:

- the Sun-Earth system and the Sun-Mars system are coplanar. It is justified by the low inclination of the martian orbit which is inclined only 1.85 deg above the ecliptic plane;
- Mars moves on a closed orbit around the Sun-Earth center of mass. It is justified by the small value of $\mu_{Earth} = 0.30404234e-5$ that puts the origin of the rotating frame inside the Sun;
- the orbit of Mars is circular. This is the main assumption since the eccentricity of Mars is ≈ 0.09 and this can introduce some differences when trajectories computed in this BCM are exported into ephemeris models.

Considering the geometry of the problem under investigation, as it is a transfer toward an outer planet, it is obvious that the escape phase must be sought by exploiting the unstable manifold associated with a Sun-Earth \mathcal{L}_2

Halo orbit, while the capture phase must lie on the stable manifold associated with a \mathcal{L}_1 Sun-Mars Halo orbit ($\mu_{Mars} = 3.2257e-7$).

The first step is to compute the relevant Halos. Considering the amplitude as the independent variable (cfr. Sec. 3.1.1), the complete trends of the other two amplitudes and of the period required to complete one of these orbits are plotted in Fig. 5.8, for the Mars and the Earth case.

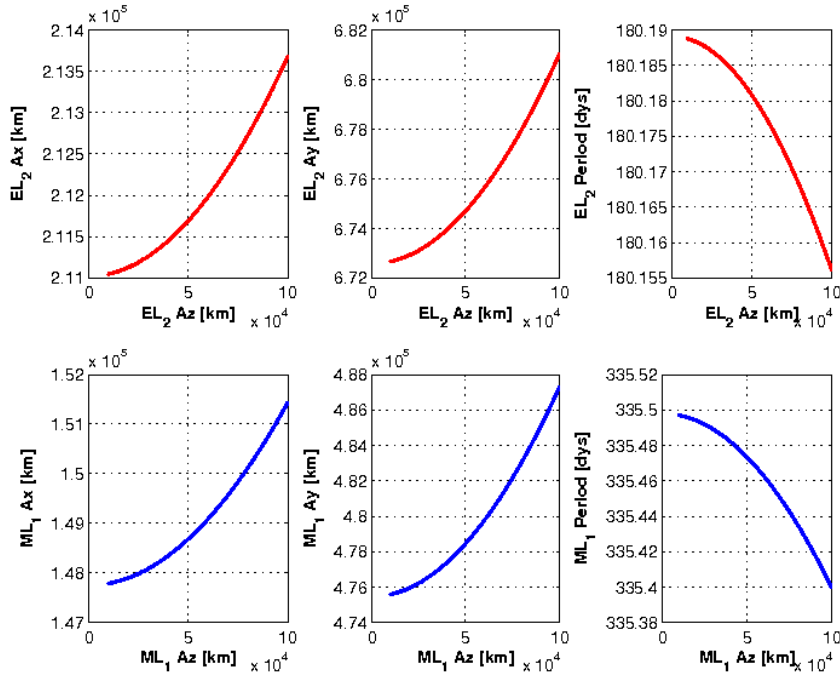


Figure 5.8: Trends of the planar amplitudes and period for Halo orbits around Sun-Earth \mathcal{L}_2 (upper row) and Sun-Mars \mathcal{L}_1 (lower row).

Once the two ranges of initial and final conditions are known, the inherent manifolds have to be generated in order to obtain all the dependencies of the performance index from the elements of the control vector.

The propellant mass is the performance index of the minimization problem and a preliminary GA (cfr. Sec. 4.1.3) optimization procedure is considered together with a local hybrid scheme (cfr. Sec. 4.4).

For the preliminary global optimization phase, boundaries are imposed on the durations of the three phases (respectively $[0.5, 2.5]$ years, $[0.5, 1.5]$ years, $[0.5, 2.5]$ years) and on the out-of-plane amplitudes of the initial and final Halo orbits ($[1e4, 1e5]$ km). The angle like variables can span the whole $[0, 2\pi]$

range and no side constraints on the values of the Lagrange multipliers have been fixed. A population of one hundred individuals has been arbitrarily chosen and ten stall generations are used as stop condition.

Along with the genetic algorithm optimization, also a comparative grid search has been performed. The elements of the control vector have been systematically varied, one at a time keeping everything else fixed. The corresponding value of the performance index augmented with the error between the obtained and the target final state has been computed. This augmented functional results to be linear only with respect to some elements of the control vector, see Fig. 5.9. In particular, it is minimized by a thrusting time of 0.5 years (the lower bound considered for this variable), a departure time of 2.5 years and an initial Mars angle of 120 deg. The trend with respect to the arrival time is quite smooth even though it is minimum for 2.5 years. The augmented functional is relatively independent of the initial and final positions and from the two A_z amplitudes that result just in some small local differences. This is obvious as the effects of these two parameters are only small variations in the final positions of the two phases to match. Thus, the optimal value resulting from the genetic algorithm approach is expected to be into this range, at least for a part of the control vector.

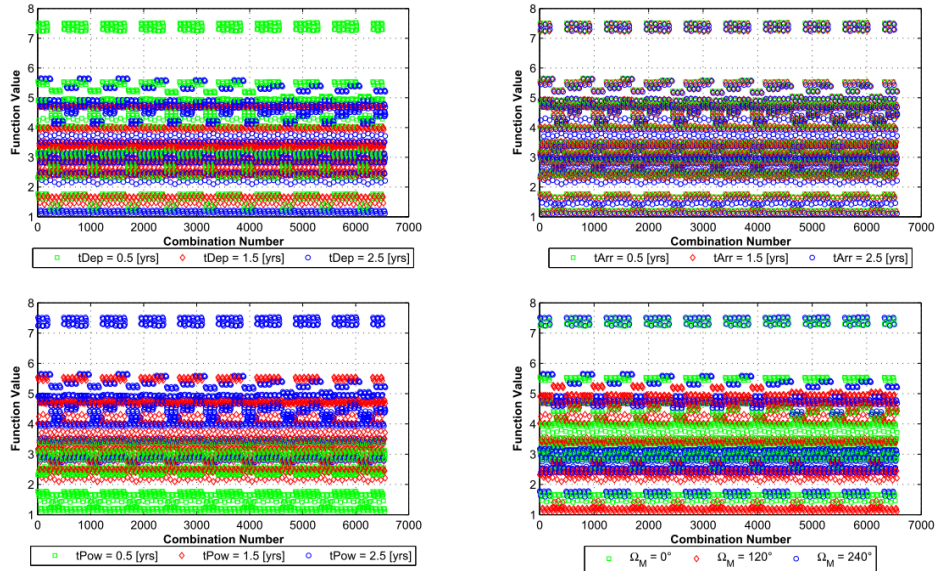


Figure 5.9: Values of the propellant mass plus the error in the final state for a grid search on the elements of the control vector. Form the top left corner the grid search is performed on the departure time, arrival time, thrusting time and Earth-Mars initial relative angle.

In the following both local results (*a*) and global ones (*b*) are derived; moreover, based on the results of the global approach some local results are computed by considering the output of the global approach as initial guesses for the local one (*c*).

Some parameters have been chosen for the spacecraft in the Earth Halo orbit (initial conditions): $I_{sp} = 3000$ s, $m_0 = 1000$ kg, $\eta_T = 0.55$ and $acc_{in} = 3.4e-4$ m/s². Based on these fixed values the control vector has been updated, from an initial guess, in order to minimize the functional and satisfy the final constraints (in the phase space) to end the powered arc on the Sun-Mars \mathcal{L}_1 stable manifold. The equations of motion have been numerically integrated in non dimensional units (with a variable step integrator with tolerance of $1e-9$) for variable time spans.

Two approaches are followed: a *Simple Approach* where the out-of-plane amplitudes of the two Halo orbits are considered constant and are removed from the control vector. This approach can be useful for particular missions with fixed initial and/or final conditions. On the other hand, in a *Complete Approach* the two amplitudes are re-included in the control vector and the optimization scheme is applied as described in Sec. 5.2.1.

Of course, changing the initial and final Halo amplitudes in the Simple Approach results in different transfers. A set of representative cases is summarized in Tab. 5.1, where solutions for an intermediate value of A_z , in the chosen range, are given.

Optimization Approach	A_z Halos Amplitudes [km]	Final Mass [kg]	Transfer Time [years]
<i>a</i>	5e4	767	2.82
<i>b</i>	5e4	774	3.69
<i>c</i>	5e4	771	2.66

Table 5.1: Comparison of results for $A_z = 5e4$ km in the Simple Approach methodology

It is important to underline that the solutions obtained by the genetic algorithm never exactly satisfy the conditions required for the manifold transition, so the subsequent local optimization is always needed. Thus, the results of the global method (*b*) for the propellant mass and the total transfer time must be intended as indicative results identifying only the region of the global minimum.

For the Complete Approach, the solutions obtained from a global (*b*) and a local-by-global (*c*) approach can be compared only with solutions obtained with a randomly guessed A_z (as in this case the departing orbits can not have the same z -amplitude). Some results of this Complete Approach are

summarized in Tab. 5.2.

Optimization Approach	A_z Halos Amplitudes [km]	Final Mass [kg]	Transfer Time [years]
<i>a</i>	4e4	791	3.93
<i>a</i>	6e4	786	4.53
<i>b</i>		772	4.59
<i>c</i>		795	4.16

Table 5.2: Comparison of results for the Complete Approach methodology

In the approaches involving a global search, *b* and *c*, also the guess for the Halo amplitudes is included as uniformly distributed, within the chosen range, in the initial GA population.

It is worth noting that solutions obtained by using the global (*b*), and the subsequent local (*c*), scheme are quite close to local solutions (*a*) both in the Simple and in the Complete Approach. In fact, the final masses are comparable and also the total transfer time range is quite narrow. This latter result is mainly dependent on the arrival time (permanence time on the stable Sun-Mars manifold) which is the parameter most varying in this analysis. The similarity in the mass propellant requirement confirms that the thrusting time is of the same order, approximately one year.

The general behavior of the thruster on/off variable results always in a thrust-coast-thrust strategy, usually considered as the optimal strategy (cfr. Sec. 4.3), although it has not been a-priori imposed.

In order to show a general Earth-Mars transfer between two Halo orbits, let us present a mission application of the described method. In particular the example refers to the solution of the Complete Approach with an initial guess of two A_z amplitudes of 4e4 km.

The trajectory, as seen in the Sun-Earth frame where these two bodies appear at rest, is represented in the left hand side of Fig. 5.10, while on the right side the trajectory in the Sun-Mars frame is plotted. It is worth noting that the manifold of the moving planet, in each frame, appears as a set of lines wrapping around the heliocentric circular orbit of the planet. The ballistic phases are represented by black lines and superimposed to the inherent manifold.

In Fig. 5.10, the electric powered phase is plotted with the golden line and the coast arc, resulting from the τ control law, in magenta. Details of the departure and arrival periodic orbits are presented in Fig. 5.11, where also the specific departing/arrival trajectory on the unstable/stable manifold is highlighted with the black bold line.

The solution, as it appears in the inertial heliocentric frame is plotted

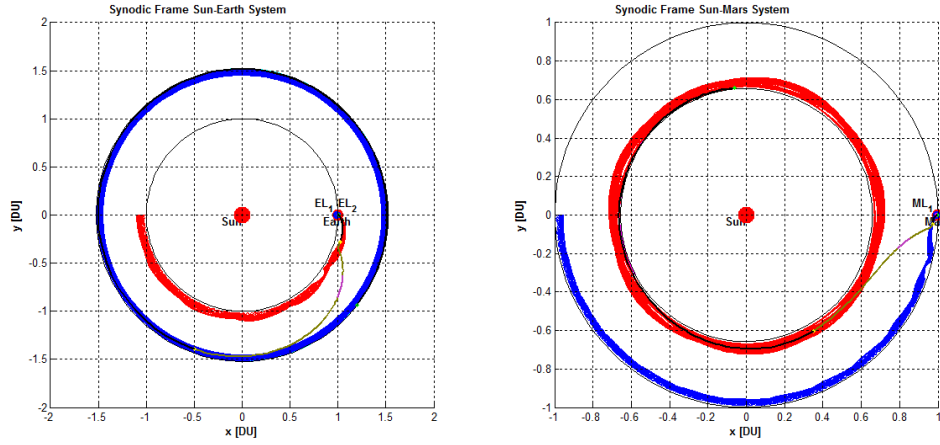


Figure 5.10: Earth-Mars Halo to Halo transfer in the Sun-Earth (left) and Sun-Mars (right) rotating frame.

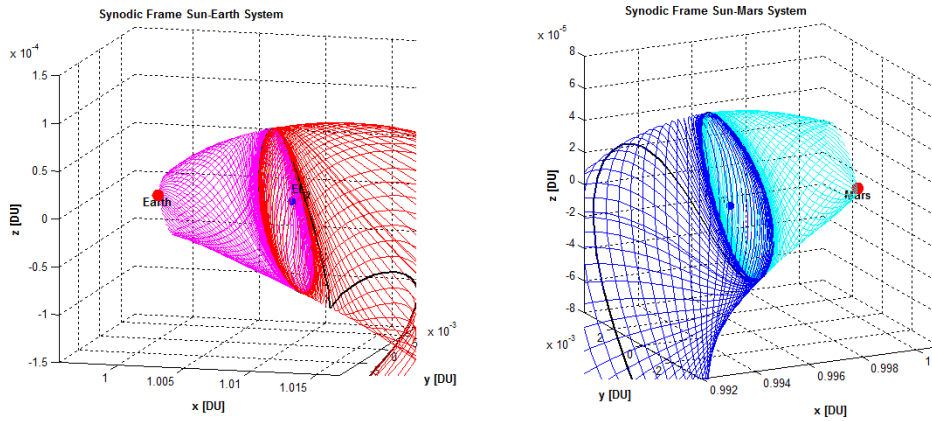


Figure 5.11: Earth escape (left) and Mars capture (right) details. The effective orbit is presented with the bold black line superimposed to the relevant manifold.

in Fig. 5.12. It is interesting to observe that, in this perspective, the two Halo orbits (as well as part of the departing/approaching trajectory) result in approximately circular heliocentric orbits with radii very similar to the one of the planet that, during the permanence on these orbits, is always visible. This can increase the scientific outcome of such missions, as this period can be usefully exploited for observations or to collect data.

In the right hand side of Fig. 5.12 also the out-of-plane motion is plotted in a false scale to make it visible.

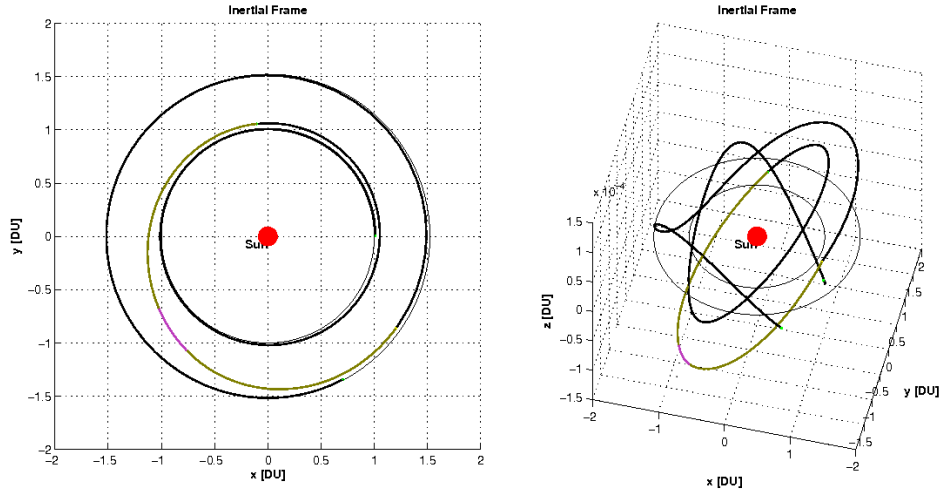


Figure 5.12: Planar and three dimensional (on the right with false out-of-plane scale) views of the Earth-Mars transfer in the heliocentric inertial frame.

To complete the description of this test case also the trends of some parameters of interest, like the thrust angles and the thruster switch on/off, are shown in Fig. 5.13. The overshadow zones are phases where the electric device is not operating; these are always in the middle of the powered arc, i.e. the optimal thrust profile includes an intermediate coasting arc.

It is worth noting that, although the out-of-plane thrust component is very small if compared with the in-plane components, this control is mandatory in order to match the two ballistic phases associated with the intrinsically three dimensional Halo orbits.

In the example presented, the solutions converges to an A_z amplitude for the Earth Halo of 12278.9 km and of 11955.1 km for the Mars Halo. The time on the departing manifold is 1.31 years, followed by 0.89 years of thruster operational phase and afterward by 1.73 years spent on the Mars manifold. The initial angular phase of Mars in the Sun-Earth frame is 264.9 deg. Overall, the Halo to Halo transfer is accomplished in 3.93 years after which approximately 791 kg are delivered into the target Halo.

Finally, also the time evolutions of the position and velocity with respect to the Sun-Earth and the Sun-Mars system are shown in Fig. 5.14.

It is interesting to observe the role of the Sun, the Sun-Earth and the Sun-

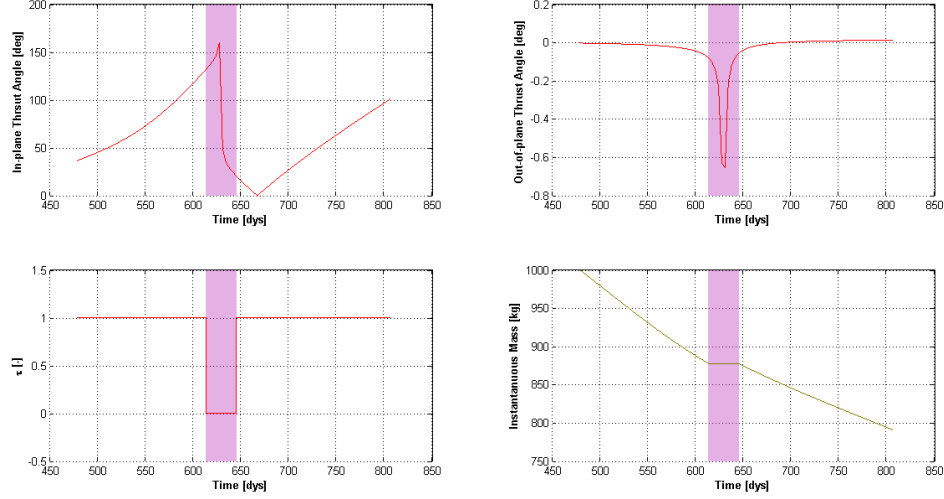


Figure 5.13: Control laws for the Earth-Mars transfer; the shaded zones are where the coasting phase takes place.

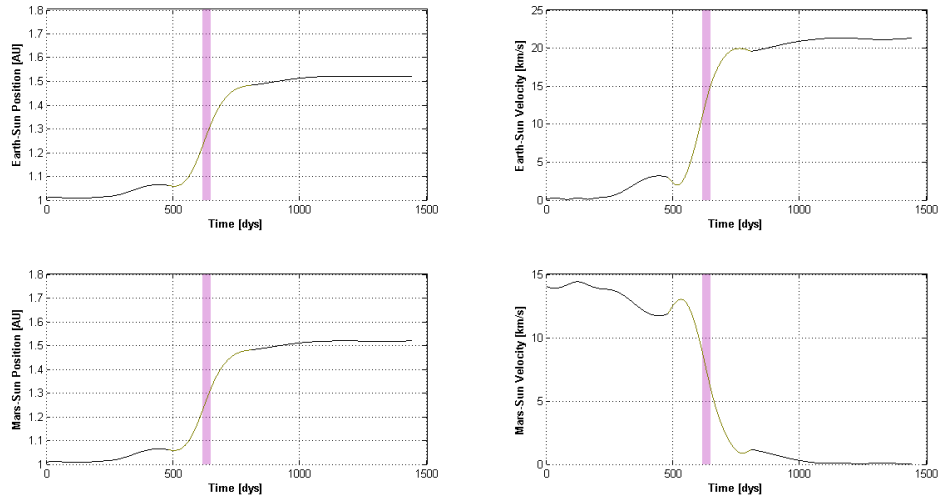


Figure 5.14: Instantaneous radius and velocity in the Sun-Earth (upper row) and Sun-Mars (lower row) system.

Earth-Mars gravity attractions acting along the thrusting phase; i.e. after the time spent onto the Earth unstable manifold up to the insertion into the Mars stable one.

In Fig. 5.15 the propellant mass required to complete the transfer is

plotted against the number of attractors considered. Some numerical experiments have been performed by considering both the Simple and the Complete version of the control vector.

The resulting trend is an increasing of the propellant mass with the number of the attractors. It is worth nothing that the guessed angular position of Mars is crucial not just for the full BCM model, but also for the other models as the final conditions to be satisfied strongly depend on this angle. The error in propellant mass resulting from a strong simplification of the dynamic environment (only the Sun) is ≈ 20 kg, which is $\approx 15\%$ of the total propellant mass requirements.

Furthermore, comparing these results with the same transfer computed considering a constant available electric power ($P = P_{in|const}$) and no control on the thruster on/off ($\tau|_{const} = 1$) there is a saving of the 10% of the propellant mass^[111]. Performing the preliminary global approach leads to a saving of 1.5 years on the maximum transfer time detected, also if this is not the function directly minimized.

The propellant mass fraction computed for the various transfers results always slightly larger than the 20% with a transfer time of the order of 3-4.5 years; these data appear suitable only for cargo-like missions, rather than for human Earth-Mars missions.

Finally, it is interesting to observe that the present strategy allows also the transfer between two orbits around two planets as it is sufficient to replace the conditions on the manifolds with conditions inside the two manifolds.

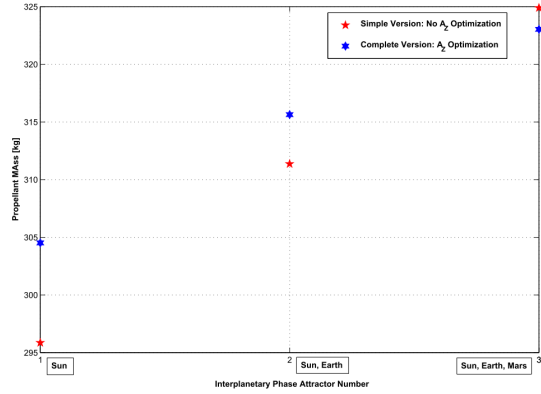


Figure 5.15: Propellant mass vs. attractor number for the Simple and Complete Approach.

Chapter 6

Novel Mission Scenarios in the Earth-Moon System

It has been already outlined that the inclusion of low thrust arcs leads to an improvement of the payload mass fraction although this approach usually requires longer transfer times with respect to high thrust cases. This is not a big deal for unmanned missions and it represents a valuable alternative especially in the Earth-Moon system^[45]. Moreover, in the framework of the CR3BP it is also possible to couple these low thrust phases with low energy ballistic transfers obtaining consequently further propellant mass reductions.

The Earth-Moon system represents one of the closest dynamical environments where the CR3BP can be applied. Its mass parameter is one of the largest μ for any physical system, although it is worth nothing that the dynamics in Earth neighborhoods are only roughly approximated by this model. In actual missions the Sun influence, the atmospheric drag and the Earth oblateness exert significant influences on the motion and the trajectories resulting from the CR3BP must be intended as first guesses to be refined in full force models.

The first real application of the three body concept to an actual transfer was, in the early nineties, the rescue of the Japanese mission HITEN¹ by means of a low energy, Sun perturbed trajectory^[4].

In this chapter some innovative mission scenarios in the Earth-Moon system are proposed. The first one exploits a combination of the low energy and

¹This mission was designed to serve as relay for another spacecraft sent to the Moon. Due to a communication loss, the moon mission failed and it was proposed to send the HITEN spacecraft to the Moon. However, the on board propellant was not sufficient to reach a lunar orbit by means of classical transfers. Accordingly the new trajectory was designed by exploiting the Sun perturbation and the Moon WSB.

low thrust concepts in order to design an electric escape from a geocentric orbit up to a ballistic trajectory flowing in the Moon neighborhoods. Afterwards, trajectories from geocentric to selenocentric orbits are addressed by exploiting low thrust escapes, capture phases and coasting arcs in the CR3BP. Finally, an application of an electric powered mission toward a periodic orbit enabled only by the CR3BP is explored by outlining the unique advantages resulting from this combination.

6.1 Low Thrust Transfer to a Manifold Chain

As outlined in Sec. 2.2.5-3.2, there exists a set of ballistic trajectories leading toward a collinear point. The aim of this example is to design a transfer from a geocentric orbit to the Moon neighborhoods with a naive exploitation of this kind of trajectories.

Bearing in mind the geometry of the problem, see Fig. 6.1, it is clear that, departing from Earth, the insertion into the stable manifold of a periodic orbit inherent to \mathcal{L}_1 is an advantageous way to move toward the Moon neighborhoods. The CR3BP characteristics can be exploited to design a low thrust escape from a departing geocentric orbit to reach a specific trajectory on the stable \mathcal{L}_1 manifold. This particular trajectory on the manifold can be chosen in order to obtain a specific lunar or cislunar exploration phase^[45].

In this section, an example of a possible selection of this path and the required thrusting phase to reach specific initial conditions for the ballistic continuation is shown.

The application employs a heteroclinic chain between two periodic Lyapunov orbits. It is derived by the intersection of the \mathcal{L}_1 unstable manifold and the \mathcal{L}_2 stable one in the Moon realm, in a similar fashion like Sec. 3.4. This sequence is exploited in order to permit to reach the target Lyapunov by means of its stable manifold, from this moving along the \mathcal{L}_1 Lyapunov and hereafter shifting to the heteroclinic connection toward the \mathcal{L}_2 planar Lyapunov. Thus the final target orbit is actually a periodic orbit around Earth-Moon \mathcal{L}_2 ^[112]. All of these transits are ballistic; therefore the Jacobi constant does not change along the whole chain. The planar version of the Earth-Moon CR3BP is considered. Of course, it is not obvious that the two manifolds of these orbits intersect in the section plane at the first cut (cfr. Sec. 3.4).

Thus, the first step to design such a kind of missions is to define two planar Lyapunov orbits around \mathcal{L}_1 and \mathcal{L}_2 with the same value of the Jacobi constant. Bearing in mind that these orbits are parameterized according to their planar amplitude (cfr. Sec. 3.1.1), once one of the two amplitudes, around \mathcal{L}_1 or \mathcal{L}_2 , is chosen, the corresponding Jacobi constant is fixed. With

this value, the A_x resulting in a Lyapunov orbit with the same value of Jacobi constant around the other equilibrium point, can be identified by a zero finding method (e.g. Newton procedure).

Choosing for \mathcal{L}_1 $A_x = 1e4$ km results in $J = 3.17135754$ that corresponds to an orbit with $A_x = 9260$ km around \mathcal{L}_2 . The selection of the first amplitude, and consequently of the value of J , is somehow arbitrary, but it can be selected according to specific mission requirements, such as communications, eclipses and so on.

As outlined in Sec. 3.4, between these two periodic orbits there exists a family of heteroclinic connections. What we are interested in are the ones departing from the \mathcal{L}_1 Lyapunov and going toward the \mathcal{L}_2 Lyapunov, as the scope is to reach \mathcal{L}_1 by means of the branch of its stable manifold flowing in the Earth realm.

Considering again (cfr. Sec. 3.4) the second cuts of both manifolds on the Poincaré section located in $x = 1 - \mu$, it is possible to define the initial condition of a heteroclinic connection between the two Lyapunov orbits. The selection of the second cut is mandatory as at the first one the manifolds images do not intersect. Furthermore it is sought as at least a single loop around the Moon is intended to be performed for demonstrative purposes. The initial condition selected corresponds to a symmetric solution, see Fig. 6.1.

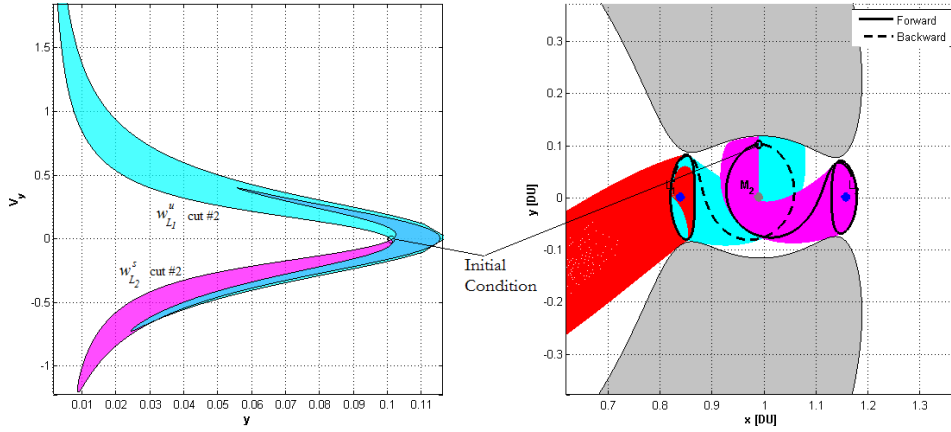


Figure 6.1: Initial condition on the intersection of the second cuts of the \mathcal{L}_1 unstable and \mathcal{L}_2 stable manifolds (left) and corresponding symmetric, one-Moon-loop Heteroclinic orbit (right).

The initial condition detected in this way assures only to reach the two Lyapunov orbits and, depending on the numerical accuracy, to perform at

least one revolution on these. However, the dynamics in this region of the phase space are extremely sensible with respect to a slight variation of the initial conditions and thus iteratively varying the decimal digits of the initial condition it is possible to obtain a trajectory that, backward in time, performs one revolution of the \mathcal{L}_1 Lyapunov before to escape along its stable manifold in the Earth realm. It has to be stressed, that the saddle component of the collinear points is several orders of magnitude larger than the others, so any escape from the Lyapunov follows these tube-like structures. Nevertheless only some peculiar trajectories arriving from these manifolds are able to perform the Lyapunov to Lyapunov heteroclinic transition.

Of course, in order to have a more realistic initial state, once the initial condition on the section plane has been correctly updated, it is possible to propagate it backward up to the first $y = 0$ intersection along the negative x -axis (the first one in the Earth realm) and consider this as initial state for a complete forward propagation. Considering an integration tolerance of $1e-12$ for a variable step integrator and performing the integration in non dimensional units, the initial condition corresponding to the required trajectory is: $\vec{x} = [-0.321737254242, 0, 0.824975718586, -1.632131399635]$. The resulting trajectory flows along the \mathcal{L}_1 stable manifold, performs a revolution on the \mathcal{L}_1 Lyapunov, moves along the heteroclinic connection toward \mathcal{L}_2 and performs also more than one revolution on this orbit. In Fig. 6.2 this “Manifold chain” is shown for a time span of 29 days (15 TU) together with the trends of the instantaneous radius and velocity referred to the usual CR3BP synodic barycentric frame.

6.1.1 GTO to Manifold Chain Transfer

Once the target trajectory has been selected, the aim is to define a low thrust strategy to reach this initial condition^[112]. This is the definition of a transfer toward specific final conditions, that could also have been the ones of a one dimensional manifold or any other specific target state fixed in advance.

A standard GTO (200x35768 km) has been assumed as departing orbit. It is supposed that 500 kg small scientific spacecraft has to be delivered at the beginning of the ballistic phase and at this point it is supposed to be equipped with an electric thruster able to provide $I_{sp} = 2000$ s and an initial acceleration of $7.13e-4$ m/s².

The whole powered phase, Eq. (4.23), is computed backward from the target state, this is due to the extreme sensitivity of this condition. Considering a forward computation, in fact, these conditions would result in an error hard to satisfy with the very high required accuracy.

The thrusting phase is defined by means of the thrust direction, governed by the initial (in a backward perspective) values of the Lagrange multipliers

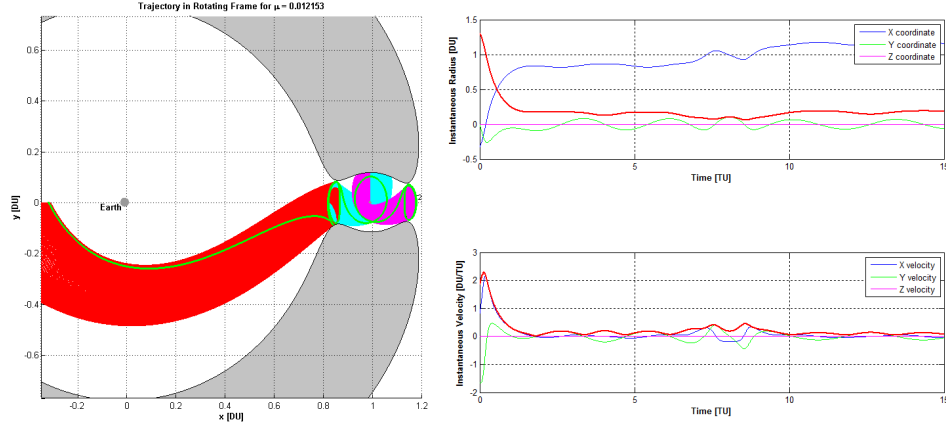


Figure 6.2: Trajectory (left) and radius and velocity evolution (right) for the Earth-Moon “Manifold chain” (\mathcal{L}_1 stable manifold- \mathcal{L}_1 Lyapunov- \mathcal{L}_1 unstable manifold- \mathcal{L}_2 stable manifold- \mathcal{L}_2 Lyapunov).

(cfr. Sec. 4.1.2), and its duration. Thus, the target point has been considered fixed and only the thrust direction and its duration are a-priori unknowns.

The resulting transfer and the ballistic chain of Fig. 6.2 are represented in Fig. 6.3 in a rotating frame (left) and geocentric inertial one (right).

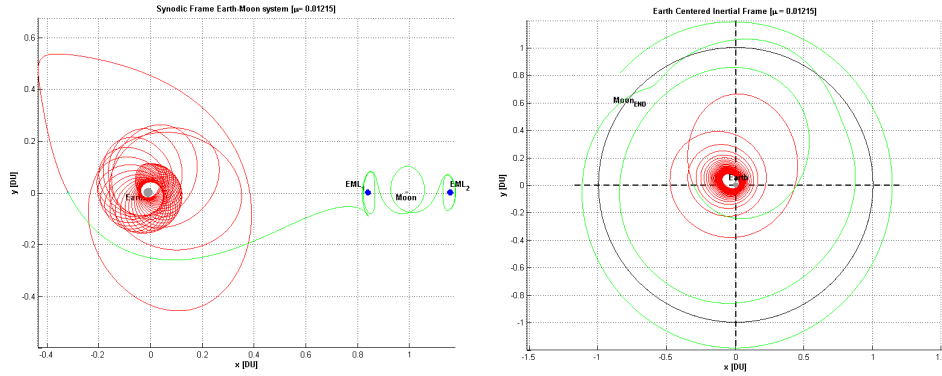


Figure 6.3: GTO to “Manifold chain” transfer and subsequent ballistic propagation. In the Earth-Moon barycentric frame (left) and in the geocentric inertial one (right).

The design of this solution aims to minimize the propellant mass consumption satisfying final non linear constraints. The final error to minimize

is the distance between the obtained geocentric osculating semi-major axis and eccentricity with respect to the target ones. These are the ones of the GTO, ie. $a_{\text{target}} = 24362 \text{ km}$ and $ecc_{\text{target}} = 0.73$.

The explanation of this application is completed by the trend of some parameters of interest. In Fig. 6.4, the time backward evolutions of the mass, of the position and velocity, of the geocentric eccentricity and semi-major axis are shown. In these last two graphs also the target values, extremely close to the last points of the plots, are represented. The error on the final semi-major axis and eccentricity is of the order of $1e-5$ on the norm of the two differences (distances in non dimensional units). This is the real advantage of the backward propagation as this final error can be easily satisfied with quite high accuracy (resulting only in a slightly different departing GTO) in regions where any small error on the flow is less critical.

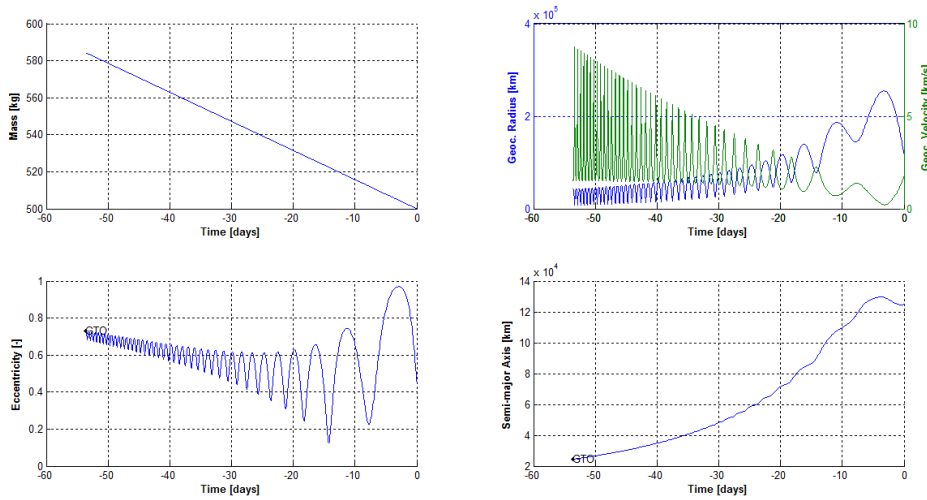


Figure 6.4: Backward evolution of mass, position and velocity, geocentric eccentricity and semi-major for the trajectory of Fig. 6.3.

The solution shown is a local minimum that requires less than two months of continuous thrusting and a mass consumption on 80 kg to reach the beginning of the ballistic phase. Of course, such a mission does not make any sense considering the two body dynamics and it would be much more expansive (representative comparisons in Sec. 6.2 and Sec. 6.3.1) if performed by chemical means.

6.2 Optimal Earth-Moon CR3BP Low Thrust Trajectories

The idea of this section is to design low thrust transfer trajectories from a given geocentric orbit to a selenocentric one, considering the three dimensional three body dynamics.

As general stated, the transfer analysis requires a continuous thrusting phase from a Low Earth Orbit (LEO) up to a Low Lunar Orbit (LLO). However, the first Earth spiraling out phase aims only at gaining energy so that the most efficient solution is the tangential thrust. This is also required in order to quickly transit through the Van-Allen belts, donuts of energetic charged particles (plasma) held in place by the Earth magnetic field, that cause significant damages to all electrical on board equipments, including the thruster and the power generation system.

Thus, the interesting part of the mission design is from a quite high altitude geocentric orbit up to the LLO insertion. A Geostationary Earth Orbit (GEO) has been chosen as starting orbit. It is worth nothing that this does not mean that it is actually required to reach a GEO before to start the LLO low thrust transfer (which wouldn't be a clever choice), but that a sort of constant offset to the propellant mass consumption and to the transfer time has to be added to the results of the present analysis.

In the early sixties Edelbaum^[113] assumed a constant acceleration magnitude (i.e. constant mass) to define the optimum low thrust transfer between two circular inclined orbits. Considering only the tangential and the normal acceleration components, these assumptions allow linearizing the Lagrange Planetary Equations^[11] around a circular orbit and compute a closed form solution of the optimal trajectory^[95]. Only the out-of-plane thrust angle is considered as control variable for the maximum inclination change and this results in a piecewise constant function switching signs at the nodal points. Moreover, it turns out to be equivalent to minimizing the transfer time for a given inclination and semi-major axis change.

This approach leads to the “Edelbaum equation” for constant acceleration, circle to circle, inclination change (Δi) transfer:

$$\Delta v = \sqrt{v_0^2 + v_f^2 - 2v_0v_f \cos \frac{\pi}{2} \Delta i} \quad (6.1)$$

where v_0 and v_f are respectively the circular velocities along the initial and final orbits. Since the acceleration (acc) is constant, also the transfer time (Δt) can be easily computed from the Δv : $\Delta t = \Delta v / acc$.

In this way, it is possible to avoid to propagate (and optimize) the first spirals from a LEO to GEO. The propellant mass fraction and the transfer

time required to reach a GEO-like orbit can be computed by means of this analytic approximation and the actual transfer design starts from this orbit.

To give an idea, let us compute the cost required to reach the GEO from an equatorial LEO, with 200 km altitude. A numerical propagation with tangential thrust, always on, ends with $ecc \approx 0.05$ (indeed, almost circular) and requires a $\Delta v_{LEO-GEO}^{num} = 4.88$ km/s, computed by using the Tsiolkovsky equation, Eq. (4.15), with $I_{sp} = 2500$ s. The Edelbaum approach, considering no inclination change, results in $\Delta v_{LEO-GEO}^{Edel} = 4.7$ km/s and thus not really different although the strong assumption of constant mass. Avoiding to compute these first tangentially powered spirals saves hours of computational time in an iterative scheme that evaluates hundreds of times the objective function.

So, in order to improve the convergence properties of the method and reduce the computational load, the minimum mass transfers are computed from the GEO to a LLO. To the results, a mass and a time offset, approximated by the Edelbaum approach, have to be added.

The trajectories are computed by using the classical CR3BP dynamical model, but using a polar rotating frame centered in one of the primaries depending on the specific mission segment. Those equations have been derived by replacing in the dynamical equations, Eq. (2.27), the usual cartesian-polar transformation and solving for the new set of variables: $[\rho, \theta, \psi, v_\rho, v_\theta, v_\psi]$. Where ρ is the radial distance from the center of the reference frame, θ and ψ are respectively the in-plane and out-of-plane angles measured counter-clockwise from the x -axis and from the equatorial plane, and v_ρ, v_θ, v_ψ are the associated velocities.

The equations of motion in a rotating spherical frame centered in one of the primary are summarized in Eq. (6.2). Here the upper signs, the first subscript of μ and $R = \sqrt{D^2 + \rho^2} - 2D\rho \cos \theta \cos \psi$ have to be considered for the Earth escape phase, while the lower signs, the second μ subscript and

$R = \sqrt{D^2 + \rho^2 + 2D\rho \cos \theta \cos \psi}$ for the Moon capture phase:

$$\begin{aligned}
\dot{\rho} &= v_\rho \\
\dot{\theta} &= \frac{v_\theta}{\rho} \sec \psi \\
\dot{\psi} &= \frac{v_\psi}{\rho} \\
\dot{v}_\rho &= \frac{v_\theta^2}{\rho} + \frac{v_\psi^2}{\rho} + \frac{\rho\omega^2}{2} + 2v_\theta\omega \cos \psi + \frac{1}{2}\rho\omega^2 \cos 2\psi - \frac{\rho\mu_{m/e}}{R^3} - \frac{\mu_{e/m}}{\rho^2} + \\
&\quad \frac{\mu_{m/e} \cos \psi \cos \theta}{D^2} \pm \frac{D\mu_{m/e} \cos \psi \cos \theta}{R^3} \\
\dot{v}_\theta &= -\frac{v_\rho v_\theta}{\rho} - 2v_\rho\omega \cos \psi + 2v_\psi\omega \sin \psi \mp \frac{\mu_{m/e} \sin \theta D}{R^3} - \\
&\quad \frac{\mu_{m/e} \sin \theta}{D^2} + \frac{v_\theta v_\psi \tan \psi}{\rho} \\
\dot{v}_\psi &= -\frac{v_\rho v_\psi}{\rho} - 2v_\theta\omega \sin \psi - \rho\omega^2 \cos \psi \sin \psi - \frac{\mu_{m/e} \sin \psi \cos \theta}{D^2} \mp \\
&\quad \frac{D\mu_{m/e} \sin \psi \cos \theta}{R^3} - \frac{v_\theta^2 \tan \psi}{\rho}
\end{aligned} \tag{6.2}$$

where $\mu_e = 1 - \mu$, $\mu_m = \mu$ and ω the angular velocity of the rotating frame, unitary in the usual non dimensional coordinates. This set of equations results in the CR3BP dynamics centered in one of the two primaries and consequently a further coordinate transformation is required to transit from one system to the other.

Earth centered coordinates are used to model the escape phase, while the Moon centered ones are used in the selenocentric capture phase for a better modeling the dynamics in this region^[114].

Eq. (6.2) are presented in their ballistic form, but during the thrusting arcs additional acceleration terms have to be added on the right side, these terms take the form: $\hat{\mathbf{k}}T/(m_0 - \dot{m}t)$, where $\hat{\mathbf{k}}$ is the unit vector along $[\rho, \theta, \phi]$.

6.2.1 Thrust-Coast-Thrust Approach

The whole transfer is divided a-priori into three phases. A first Earth spiralling out phase is followed by a ballistic translunar coasting phase ruled only by the CR3BP dynamics. After this phase the last de-spiralling phase is performed in order to acquire the target LLO that represents a mission specific requirement. Of course, the durations of these three phases, represented in the example of Fig. 6.5, are not known and thus these are included in the control vector.

The subdivision of the mission into these three phases is considered in order to “simulate” the classical bang-bang strategy and to keep the option to obtain also fast solutions, easily derivable from the elimination of the in-

intermediate ballistic phase. Furthermore in this way, depending on the initial guess provided for the duration of the coasting phase, it is possible to obtain “long” and “short” solutions spending respectively a long or a short time in coasting. “Long” solutions can easily explore also the geospace far from the Moon, which remains however the final target, without any additional propellant mass requirement.

The Earth escape phase and the ballistic (if present) phase are forward propagated by means of the Earth centered polar equations, Eq. (6.2), while the Moon capture phase is backward propagated from the target LLO by using the selenocentric equations (Eq. (6.2)). The two states have to match at a given point. This match point is chosen to be on the boundary of the Sphere of Influence of the Moon (in CR3BP

units: $r_{SoI}|_{\text{moon}} = (\mu/(1 - \mu))^{2/5}$). It is interesting observing that the Sphere of Influence is an intrinsically two body concept, also the Hill sphere ($r_h = (\mu/3)^{1/3}$) could have been used, leading to similar results.

Thus, the forward segment and the backward propagated one have to match at the boundary of the Moon SoI. This results in a vector ($\in \mathbb{R}^6$) of errors to be nullified representing the constraints of the minimization scheme^[114]. The initial and final geocentric and selenocentric orbits are inputs of the specific transfer, but the starting point (where the thruster is switched on/off) along these orbits is not a-priori imposed.

Again a hybrid method (cfr. Sec. 4.4) is used, where the optimal profile of the two powered phases is ruled by the evolution of the Lagrange multipliers, and a direct minimization of the performance index, i.e. the propellant mass fraction, is sought at each iteration step^[88].

In order to compute the control laws for the two electric phases by means of the primer vector (cfr. Sec. 4.1.2), the evolutions of the Lagrange multipliers $[\lambda_\rho, \lambda_\theta, \lambda_\psi, \lambda_{v_\rho}, \lambda_{v_\theta}, \lambda_{v_\psi}]$ are required. These can be computed by taking the partial derivatives with respect to the proper state variable (cfr. Eq. (4.8)) of the Hamiltonian of the problem.

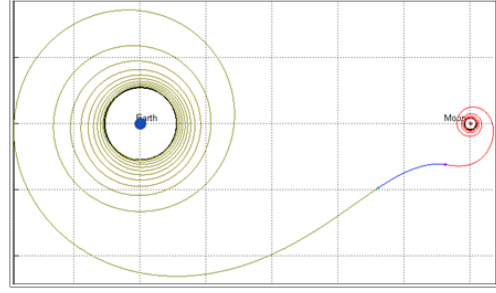


Figure 6.5: GEO-LLO CR3BP low thrust transfer. The three phases, thrust-coast-thrust, are presented with three different colors.

This procedure results in:

$$\begin{aligned}
\dot{\lambda}_\rho &= \lambda_\theta \frac{v_\theta}{\rho^2} \sec \psi + \lambda_\psi \frac{v_\psi}{\rho^2} + \lambda_{v_\rho} \left[\frac{v_\theta^2}{\rho^2} + \frac{v_\psi^2}{\rho^2} - \frac{\omega^2}{2} - \frac{1}{2} \omega^2 \cos 2\psi + \frac{\mu_{m/e}}{R^3} + \right. \\
&\quad \left. - \frac{3\mu_{m/e}}{R^5} (\rho \mp D \cos \theta \cos \psi)^2 - \frac{2\mu_{e/m}}{\rho^3} \right] + \\
&\quad \lambda_{v_\psi} \left[\omega^2 \cos \psi \sin \psi - \frac{v_\rho v_\psi}{\rho^2} \right. \\
&\quad \left. \mp \frac{3D\mu_{m/e} \sin \psi \cos \theta}{2R^5} (2\rho \mp 2D \cos \theta \cos \psi) - \frac{v_\theta^2 \tan \psi}{\rho^2} \right] + \\
&\quad \lambda_{v_\theta} \left[-\frac{v_\rho v_\theta}{\rho^2} \mp \frac{3D\mu_{m/e} \sin \theta}{2R^5} (2\rho \mp 2D \cos \theta \cos \psi) + \frac{v_\theta v_\psi \tan \psi}{\rho^2} \right] \\
\dot{\lambda}_\theta &= \lambda_{v_\rho} \left[\frac{\mu_{m/e} \cos \psi \sin \theta}{D^2} + \frac{3D\mu_{m/e} \rho \cos \psi \sin \theta}{R^5} (D \cos \theta \cos \psi) \right. \\
&\quad \left. \mp \rho \pm \frac{D\mu_{m/e} \cos \psi \sin \theta}{R^3} \right] + \\
&\quad \lambda_{v_\theta} \left[\frac{\mu_{m/e} \cos \theta}{D^2} \pm \frac{\mu_{m/e} D \cos \theta}{R^3} - \frac{3D^2 \mu_{m/e} \rho}{R^5} \cos \psi \sin^2 \theta \right] + \\
&\quad \lambda_{v_\psi} \left[-\frac{\mu_{m/e} \sin \theta \sin \psi}{D^2} - \frac{3D^2 \rho \mu_{m/e}}{R^5} \cos \theta \cos \psi \sin \theta \sin \psi \right. \\
&\quad \left. \mp \frac{D\mu_{m/e} \sin \theta \sin \psi}{R^3} \right] \\
\dot{\lambda}_\psi &= \lambda_{v_\rho} \left[\rho \omega^2 \sin 2\psi + \frac{\mu_{m/e} \cos \theta \sin \psi}{D^2} \pm \frac{D\mu_{m/e} \cos \theta \sin \psi}{R^3} + \right. \\
&\quad \left. 2v_\theta \omega \sin \psi + \frac{3D\mu_{m/e} \rho \cos \theta \sin \psi}{R^5} (D \cos \theta \cos \psi \mp \rho) \right] + \\
&\quad \lambda_{v_\theta} \left[-2v_\psi \omega \cos \psi - \frac{v_\theta v_\psi \sec^2 \psi}{\rho} - 2v_\rho \omega \sin \psi + \right. \\
&\quad \left. - \frac{3\mu_{m/e} D^2 \rho \cos \theta \sin \theta \sin \psi}{R^5} \right] - \lambda_\theta \frac{v_\theta \sec \psi \tan \psi}{\rho} + \\
&\quad \lambda_{v_\psi} \left[2v_\theta \omega \cos \psi + \rho \omega^2 \cos^2 \psi + \frac{v_\theta^2 \sec^2 \psi}{\rho} \pm \frac{D\mu_{m/e} \cos \theta \cos \psi}{R^3} + \right. \\
&\quad \left. \frac{\mu_{m/e} \cos \theta \cos \psi}{D^2} - \rho \omega^2 \sin^2 \psi - \frac{3\mu_{m/e} D^2 \rho \cos^2 \theta \sin^2 \psi}{R^5} \right] \\
\dot{\lambda}_{v_\rho} &= -\lambda_\rho + \lambda_{v_\theta} \left[\frac{v_\theta}{\rho} + 2\omega \cos \psi \right] + \lambda_{v_\psi} \frac{v_\psi}{\rho} \\
\dot{\lambda}_{v_\theta} &= \lambda_{v_\rho} \left[-\frac{2v_\theta}{\rho} - 2\omega \cos \psi \right] + \lambda_{v_\psi} \left[2\omega \sin \psi + \frac{2v_\theta \tan \psi}{\rho} \right] + \\
&\quad \lambda_{v_\theta} \left[\frac{v_\rho}{\rho} - \frac{v_\psi \tan \psi}{\rho} \right] - \lambda_\theta \frac{\sec \psi}{\rho} \\
\dot{\lambda}_{v_\psi} &= -\lambda_{v_\rho} \frac{2v_\psi}{\rho} + \lambda_{v_\theta} \frac{v_\rho}{\rho} - \frac{\lambda_\psi}{\rho} + \lambda_{v_\theta} \left[-2\omega \sin \psi - \frac{v_\theta \tan \psi}{\rho} \right]
\end{aligned} \tag{6.3}$$

As the thruster is considered always on during the two spiralling phases, the λ_m evolution is not required because it is involved only in the computation of the switch function τ , not considered in this case.

Thus, for each propulsion phase the equations of motion, Eq. (6.2), are propagated together with the adjoint equations, Eq. (6.3), and the instantaneous optimal thrust direction is given by: $\hat{\mathbf{a}} = -\bar{\lambda}_{\mathbf{v}}/||\bar{\lambda}_{\mathbf{v}}||$ with the velocity vector composed by $\vec{v} = [v_\rho, v_\theta, v_\psi]$.

The control vector is a vector $\in \mathbb{R}^{17}$ containing the two sets of initial conditions of the adjoints, three times (the durations of the three phases), and two angular variables characterizing the departing and arriving anomalies. The SQP^[102] method has been used to minimize the propellant mass and to satisfy the match constraints. The differential equations are integrated in non dimensional units by means of a variable step integrator with an absolute and relative tolerance of $1e-9$.

6.2.2 Earth-Moon Transfer Examples

A test spacecraft has been considered with an initial acceleration in GEO of $7.6453e-4 \text{ m/s}^2$, $m_0 = 1000 \text{ kg}$ and $I_{sp} = 2000 \text{ s}$. With these fix values various iterations have been performed with increasing inclination of the target LLO (one of the most critical parameters) and with different initial guesses on the length of the three phases and of the Lagrange multipliers.

The departing orbit is defined in terms of $[a_E, ecc_E, incl_E, \omega_E, \Omega_E]$, the departing true longitude ν_E is not fixed in advance. For the GEO case, it reduces to: $[a_E = 35768 \text{ km}, ecc_E = 0, incl_E = 0 \text{ deg}]$, ω_E and Ω_E are not defined neither required. The arrival LLO, in a similar fashion, is defined by means of $[a_M, ecc_M, incl_M, \omega_M, \Omega_M]$ that are inputs depending on the specific test case, while the arrival true anomaly ν_M (or the equivalent anomaly) is not a-priori fixed, but found by the numerical scheme.

Two typical results are presented in Fig. 6.6, where a “short” transfer towards a circular, 25 deg inclination selenocentric orbit is represented, and in Fig. 6.7 where a “long” solution to a circular, 45 deg inclined target orbit is shown. Both final lunar orbits have $a_M = 5000 \text{ km}$ but different Ω_M .

The “short” transfer of Fig. 6.6 takes 41 days and delivers in the target LLO 885 kg of mass. The Earth escape phase takes 27 days and consumes 92 kg of propellant mass, obviously the largest part. After, the coasting phase takes for approximately one week and finally 6 days and 22 kg are required to reach the 25 deg inclined target LLO.

The “long” transfer of Fig. 6.7 requires 59 days and delivers in the target LLO 872 kg of mass. Thus, in this case, the transfer is 13 kg more expansive than the “short” solution of Fig. 6.6 and its transfer time is 20 days longer. The Earth escape phase takes 29 days and consumes 98 kg of propellant mass, again the largest part for the whole trajectory. After, the coasting phase takes approximately 20 days and finally 9 days and 30 kg are required to reach the 45 deg inclined LLO.

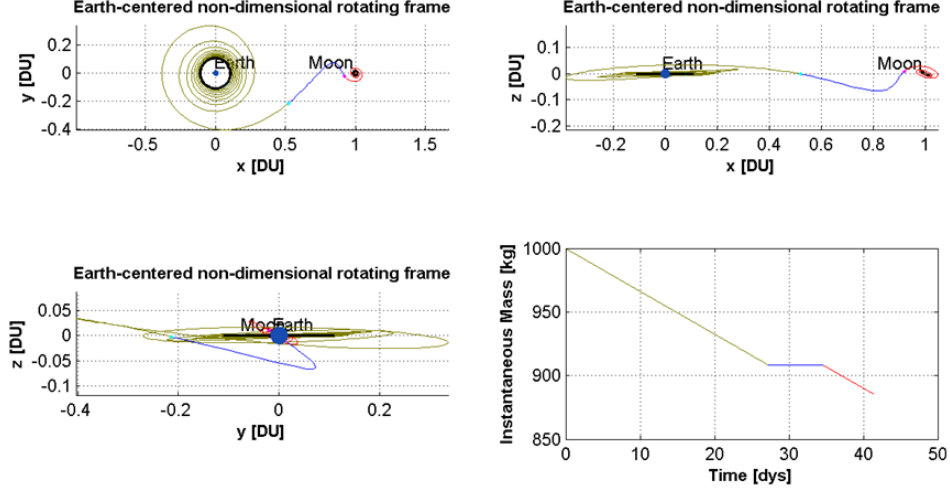


Figure 6.6: Three views and mass evolution of a GEO to LLO “short” solution ($a_M = 5000$ km, $ecc_M = 0$, $\Omega_M = 90$ deg, $incl_M = 25$ deg).

The main difference of the “short” and “long” solution lies in the length of the ballistic arc, related to the whole transfer time, while the propellant mass consumption is not significantly affected by this difference.

Moreover, if the transfer time is the mission driving factor, also solutions without any ballistic phase can be obtained. As the transfer has been divided a-priori into three phases, simply setting zero the duration of the ballistic phase and removing this from the iteration scheme results in a thrust-thrust solution. Here the first powered phase, still in Earth centered frame, is intended for the escape and the second one for the lunar capture. This kind of transfers are usually approximately 10% more expensive in terms of propellant mass fraction if compared with the thrust-coast-thrust strategy here presented.

The current analysis lacks of a global optimization and thus the resulting transfers have to be intended only as locally minimum propellant solutions; a complete different guess of the elements of the control vector can result (for converging simulations) in more/less expensive solutions. This is a classical issue of each local optimization scheme, in particular of the hybrid one. For the present analysis the initial guesses have been generated by means of a grid of initial conditions, in particular on the durations of the three phases that can vary from few weeks up to few months.

In Fig. 6.8 and Fig. 6.9 the evolutions of some interesting parameters are shown. The Lagrange multipliers vary quite a lot during the transfer and the

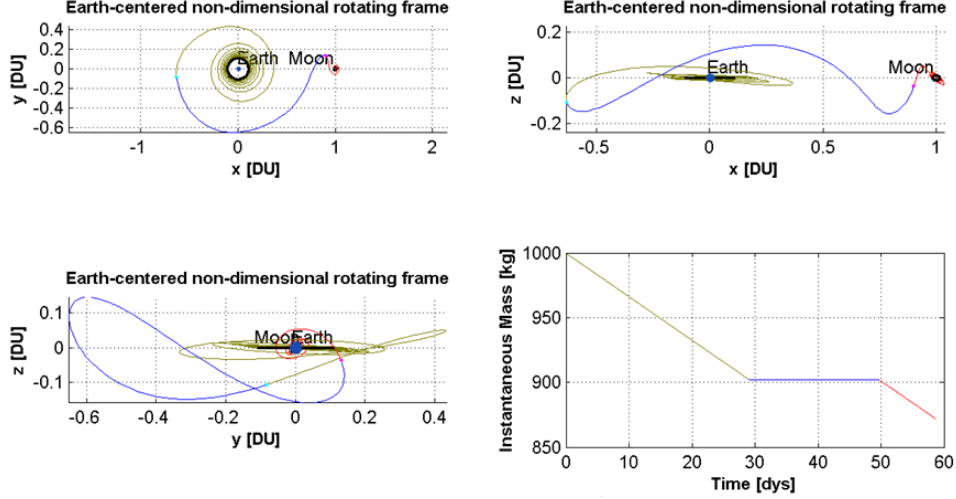


Figure 6.7: Three views and mass evolution of a GEO to LLO “long” solution ($a_M = 5000$ km, $ecc_M = 0$, $\Omega_M = 0$ deg, $incl_M = 45$ deg).

magnitude of the one associated with the radial direction is usually two or three orders of magnitude larger than the others, both for the Earth escape and the Moon capture phase. The geocentric position and velocity respect the same color convention of the trajectories in Fig. 6.6 and Fig. 6.7. Also the evolution of the in-plane and out-of-plane thrust angles is shown where they exhibit the typical evolution given by the spirals of low thrust arcs.

Solutions up to 80 deg of inclination of the LLO have been obtained, although the numerical sensitivity with respect to the initial guess (especially for the adjoints) increases for increasing inclinations. For increasing inclinations of the target LLO, the result of a previous transfer with lower $incl_M$ has been used as initial guess; this resemble a sort of continuation procedure. Its main limit is that in a chaotic system, like the CR3BP, the dynamics can change abruptly but still giving a converging solution with a completely different escape/ballistic/capture phase. This issue is present especially in the electric Moon capture phase and a very small step in $incl_M$ is required to drive the solution to converge with the same dynamics of the initial guess.

In Fig. 6.10 an application of such continuation procedure for a Earth-Moon low thrust transfer is shown. It presents a lunar swing-by during the capture phase. This swing-by can be the last part of the powered phase or it can take place during the electric de-spiralling. On the left, Fig.6.10(a), the first planar trajectory used as “initial seed” of the procedure is plotted and on the right, Fig. 6.10(b), the continuation carried out on the LLO inclination

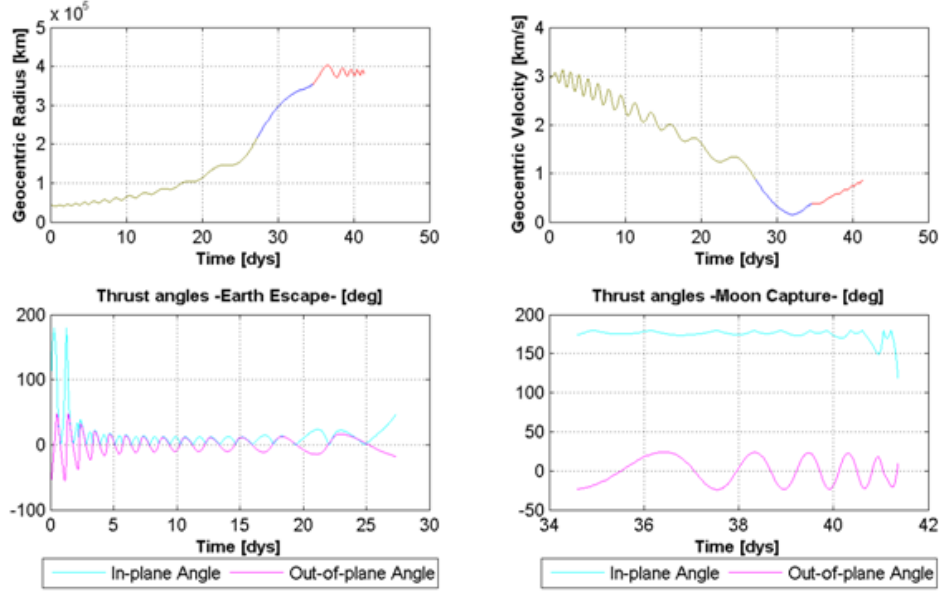


Figure 6.8: Time evolutions of geocentric radius, velocity and thrusting angles for the transfer of Fig. 6.6.

up to $incl_M = 50$ deg is shown. The continuation could still be carried on but a very small change in the target inclination (continuation step) is required as the Moon swing-by tends to disappear.

From Fig. 6.10(b)), it comes out that the role of the out-of-plane motion results in a slightly more expensive transfer, where only the 0.4% of additional propellant, if compared with the planar solution, is required to reach a 50 deg inclined LLO^[88]. In Fig. 6.10(b), moreover, it is shown also the transfer time required to reach the LLO for increasing inclinations. This does not change significantly at least until the dynamics used in the transfer (in this case a short ballistic phase and the lunar swing-by) remain the same.

For a planar case ($incl_M = 0$), it is possible to deliver more than the 92% of the initial mass in a 5000 km circular LLO. For the three dimensional case this value also depends on the orientation (actually Ω_M) of the target LLO besides from the initial guesses, for the adjoints and for the durations.

This method is very effective to design a generic preliminary geocentric-to-selenocentric transfer where the initial and/or the final orbits have to stick some specific mission requirements. Starting from a GEO (or GEO-like) orbit up to a circular lunar orbit, thousands of kilometers above its surface, requires a transfer time that can span a quite large range. It can vary from slightly

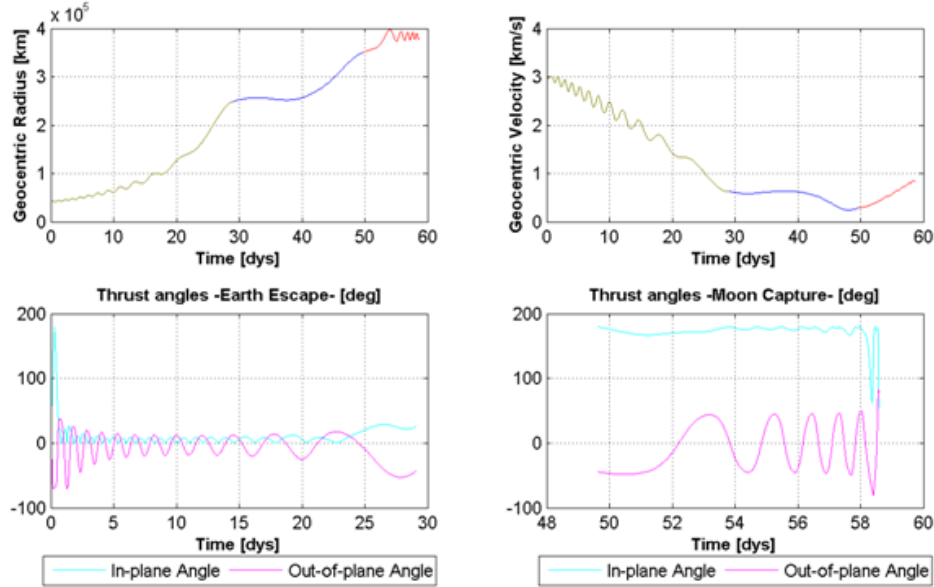


Figure 6.9: Time evolutions of geocentric radius, velocity and thrusting angles for the transfer of Fig. 6.7.

more than one month to more than three months and depends, in particular, on the duration of the coasting phase. A longer ballistic phase allows also exploring different regions of the geospace while shorter and slightly more expensive transfers are obtainable simply considering a thrusting-thrusting solution without any coasting phase. The Earth escape phase takes at least 25 days while the moon capture can be obtained in at least 5 days.

Finally, the same approach can also be used to design low thrust transfers between two geocentric/selenocentric orbits. However, in this context, the resulting control laws given by this approach are not very accurate, especially when the starting and the ending orbits differ for a high Δi and a large number of revolutions is required.

6.3 Low Thrust Transfer To Backflip Orbits

The scope of this last section is to design a low thrust transfer from a Low Earth Orbit to a “useful” periodic orbit in the Earth-Moon CR3BP. A useful periodic orbit is here intended as one that moves both in the Earth-Moon plane and out of this plane without any requirements of propellant mass. This is achieved by exploiting a particular class of periodic orbits (Sec. 3.1.2), the Backflip Orbits.

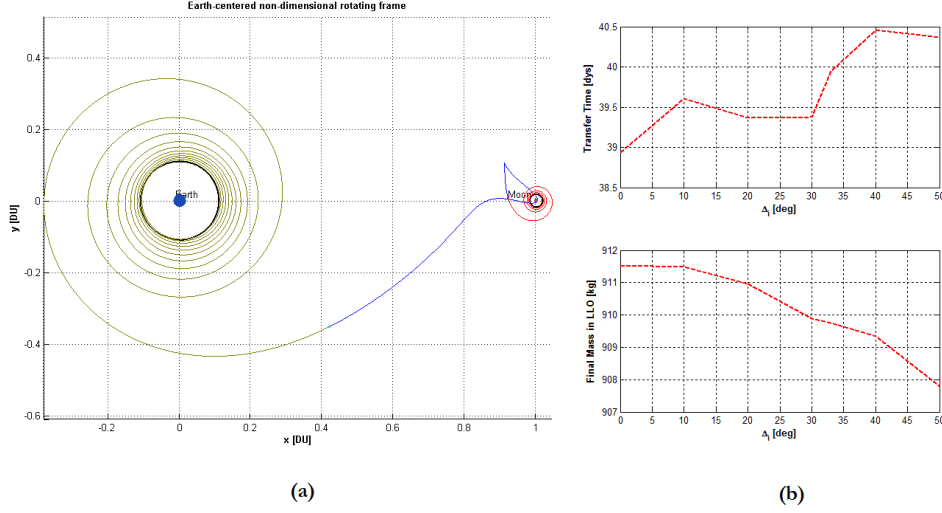


Figure 6.10: Left: GEO to LLO ($a_M = 5000$ km, $\Omega_M = 90$ deg, $incl_M = 0$ deg) transfer with a lunar swing-by in the capture. Right: continuation procedure carried out on the $incl_M$ showing the trend of the whole transfer time (up) and of the propellant mass consumption (below).

The unique characteristics of this class of periodic solutions allow the design of an almost planar transfer from a geocentric orbit and the use of the Backflip intrinsic characteristics to explore the geospace out of the Earth-Moon plane. The main advantage of this approach is that periodic plane changes can be obtained by performing an almost planar transfer. In order to save propellant mass, so as to increase the scientific payload of the mission, a low thrust transfer is considered. This foresees a thrusting phase to gain energy from a departing circular geocentric orbit and a second thrusting phase to match the state of the target Backflip orbit, separated by an intermediate ballistic phase^[115].

This results in a combined application of a low thrust manoeuvre and of a periodic solution in the CR3BP to design a new class of missions to explore the Earth-Moon neighborhoods in a quite inexpensive way. In addition, a low thrust transit between two different Backflip orbits is analyzed and considered as a possible extension of the mission proposed.

The plane change is one of the most expensive manoeuvres to perform during a space transfer and the idea to exploit some gravitational encounters to change the orbital plane has been already applied successfully in several missions, especially in an interplanetary framework (e.g. Ulysses, Cassini).

Despite that, what can be very useful is if such kinds of encounters are periodic and non powered. Moreover, an additional advantage is if the gravitational encounters move a small body alternatively from an in-plane arc to an out-of-plane one. This means that the powered transfer towards such a kind of trajectories can be obtained without any (or with a very small) plane change and the periodicity assures the repeatability of a closed trajectory with the advantage of the exploration of completely different regions (planar and inclined in the same path).

The CR3BP offers a suitable framework to model such a kind of scenario:

- the moving body is subjected to the gravitational influence of a primary and of a perturbing body that is used for the double plane change;
- the motion can be studied in a reference frame where the two bodies appear at rest and this means that the gravitational encounters take place always at the same position;
- in this model several periodic orbits, arising from bifurcations of some basic families, satisfy such kind of characteristics and can serve as the initial and final conditions for the transfer orbits considered here.

In the early eighties the concept of the *Double Lunar Swing-by* was proposed^[116]. It states that there exists a class of trajectories for which a first swing-by sends the spacecraft from the Earth-Moon orbit plane to an off-plane orbit, such that there will be a second Moon encounter. The latter, in turn, returns the spacecraft to the initial Earth-Moon orbit plane. The double lunar swing-by trajectories were used by the HITEN and GEOTAIL missions^{[116][117]} for geomagnetic tail exploration, which utilized direct (prograde) orbits and almost in-plane trajectories between lunar swing-bys.

The Backflip trajectories expand the idea of the double lunar swing-by^[117] as periodic orbits satisfying the concept of the double lunar swing-by. It was used, for the first time, ten years later during the WIND mission².

Again, a convenient choice to significantly reduce the propellant mass fraction required to reach this orbit is to consider a non conventional propulsion strategy. The electric thrust provides fuel efficient solutions to obtain high total impulse trajectories with more favorable mass ratios than for the

²The main goal of such a mission was the analysis of Earth's magnetic tail, plasma sheet, energetic particle composition and magnetic field in the geospace^[2]. To achieve this goal the mission, after its nominal operations phase in a Lissajous orbit around Sun-Earth \mathcal{L}_1 , was extended so as to further investigate as broadly as possible the space around Earth. The resulting trajectory predominantly explored the equatorial region, but the only data collected significantly out of the Earth-Moon plane were obtained by exploiting Backflip orbits.

chemical case. This motivates the idea to use the low thrust approach to reach this kind of trajectories in the Earth-Moon CR3BP.

Moreover, a subset of the Backflip orbits (Sec. 3.1.2) is here investigated. The presence of a part of the Backflip trajectories lying close to the Earth-Moon plane can be further advantageous as it means that the transfer can be obtained as an almost planar transfer. Thus, a further propellant mass saving is achievable.

The dynamical model considered is one more time the CR3BP in its ballistic version for the Backflip orbits and for the coasting transfer phases, Eq. (2.27). For the powered segments the usual inclusion of the thrust acceleration and the further equation to model the mass decrease are taken into account, Eq. (4.23).

Let us identify the Backflip branch extrapolating the set of periodic orbit emanating from \mathcal{L}_1 from the bifurcation diagram of Fig. 3.4.

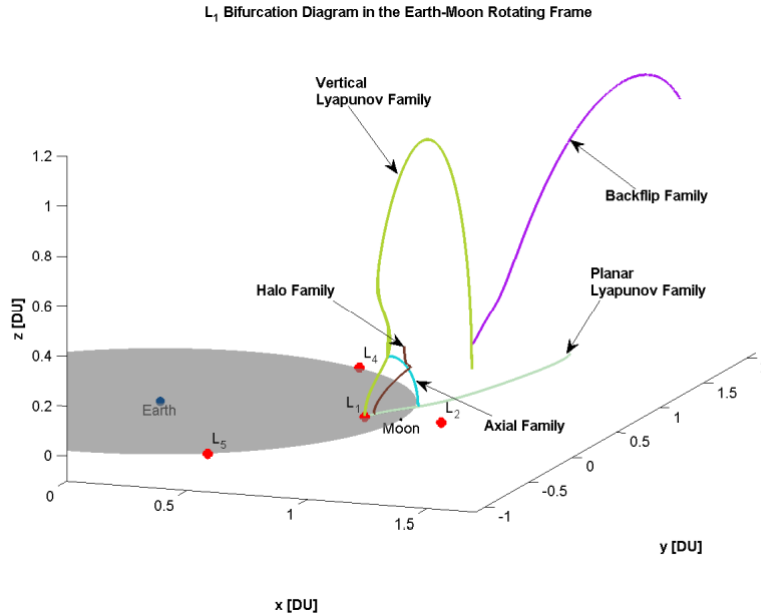


Figure 6.11: Earth-Moon \mathcal{L}_1 Bifurcation diagram.

Fig. 6.11 represents the continuation curves corresponding to the set of periodic orbits emanating from Earth-Moon \mathcal{L}_1 . In this bifurcation diagram each point of the curves represents the projection in the position space, of an initial condition resulting in a periodic orbit (cfr. Sec. 3.1.2). These periodic orbits are divided into families, each arising from successive bifurcation points

of the planar and vertical Lyapunov families. In Fig. 6.11, it is possible to identify the planar Lyapunov orbits (grey line), the vertical Lyapunov orbits (green line), the Halo orbits (brown line), the axial orbits (cyan line) and the Backflip orbits (violet line).

This last family is the one that is here used to design the application proposed. It arises from a bifurcation point of the vertical Lyapunov family associated to \mathcal{L}_1 and ends with Moon impacts. Each orbit of this kind is composed by two arcs connected by a lunar swing-by and, depending on the specific orbit of the family, one of these can be almost planar. For the symmetries of the CR3BP (cfr. Sec. 2.2.2) there exists a Northern family (where the maximum out-of-plane excursion is above the Earth-Moon plane) and a Southern one (below that plane).

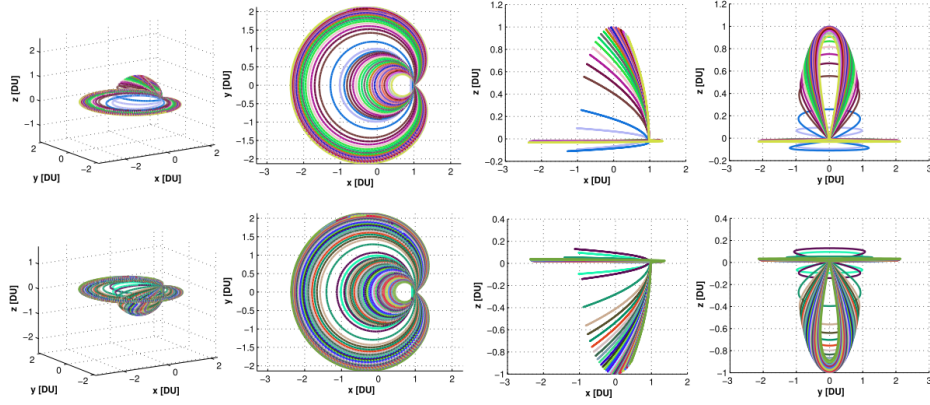


Figure 6.12: Earth-Moon Backflip family. Northern family (upper row) and Southern family (lower row).

Several orbits of the Northern and Southern family are shown in Fig. 6.12. These are parameterized with respect to their period in the range $[28, 49]$ days with a step size that is not constant but adapted along the continuation curve, according to the pseudo-arc length method (cfr. Sec. 3.1.2).

6.3.1 Transfer Design

The steering angles time history is derived by utilizing the necessary conditions from optimal control theory (cfr. Sec. 4.1.2). During the thruster working phases the equations of motion and the equation for the mass consumption are integrated forward together with the adjoint equation for the Lagrange multipliers (cfr. Sec. 4.1.2). These control the thrust direction by means of Eq. (4.25). No thruster switch on/off has been considered during a

specific thrusting phase and accordingly the Lagrange multipliers associated with the mass does not play any role (like in Sec. 6.2.1).

Moreover, in the control vectors also other elements that do not have any analytic expression of the control laws are embedded. These are typically the duration of the thrusting phase or angular positions along the initial/final orbit. The specific set of elements of the control vector depends on the specific trajectory segment.

This results again in the hybrid scheme where a direct minimization of the propellant mass is attempted at each iteration step, while the analytic optimal thrust direction is considered from optimal control theory.

Furthermore, some non linear constraints must be fulfilled by the solution: in particular the final state of the transfer must match a state (in the phase space) of the target Backflip.

Nelder-Mead^[79] and SQP approaches have been used to solve such problem, and both result in local solutions which are “near” the initial guess supplied. No global optimization has been performed on the following trajectories, but the initial guess for the elements of the control vector results from a grid search, in particular on the durations of the three phases^[115]. The first convergence criterion to be respected is that the error on the final constraints must be smaller than a given threshold (cfr. Sec. 6.3.2). The iterations have been stopped when the value of the objective function and/or the error on the final constraints reached hundreds of stall iterations without any improvement. Non-convergence phenomena present quite rarely for reasonable durations of the three phases, while they can be quite frequent for extremely long or short thrusting or ballistic phases. In this way the values of the boundaries (cfr. Sec. 6.3.2) within which define the grid of initial conditions have been defined.

The transfer design follows three steps: the identification of suitable initial and final conditions, a basic mission profile and a proposed possible extension. Thus, the whole application proposed is presented in two sections: a basic mission profile, describing the transfer from GEO to Backflip, and a possible mission extension, where the transfer between two Backflip orbits is addressed.

Initial and Final Conditions

Although the general aim is to design a low thrust transfer from a LEO to a Backflip orbit, the first part LEO-GEO is removed from the transfer design since it requires an almost tangential thrust because the main aim is to gain energy to move away from Earth. It does not need any specific optimization analysis and it can be also performed chemically or by the launcher. Again it can be considered as a sort of constant offset to add to results obtained

with the current approach (like in Sec. 6.2).

Some fixed characteristics are assumed for the spacecraft in the departing GEO; in particular, an initial mass of 1000 kg, an initial acceleration of $7.65e-4 \text{ m/s}^2$ and a constant specific impulse of 2000 s.

Again a preliminary Edelbaum analysis^[113], can be performed to get an idea, analytically approximated, of the cost required for this phase of the transfer, Eq. (6.1). Considering a 300-1000 km altitude LEO orbit, the Δv required to reach a GEO is in the range 4.71-4.32 km/s that can be performed chemically ($I_{sp}|_{ch} = 320 \text{ s}$) consuming a propellant mass of the order of the 70% of the initial mass. Assuming the same specific impulse of the test spacecraft here considered, to have 1000 kg in GEO the required mass in LEO is 1270-1254 kg, therefore the propellant mass consumption is of the order of the 20% of the initial mass.

It is worth noting that the selection of a GEO orbit is somewhat arbitrary; another circular orbit of smaller radius or, with slight modifications, an elliptic one (like a GTO) could be also considered as starting orbit.

To address the feasibility of the method, the target orbit is selected within the Northern Backflip family. The transfer design can easily extend to an orbit of the Southern family with minor changes. The target orbit has been a-priori imposed and not included in the iterative scheme. This has been done to avoid the convergence towards a completely useless orbit (from an operational point of view; for instance, one with an extremely large or small out-of-plane excursion or passing too close to the Moon surface) and to let the freedom to satisfy specific mission requirements about the maximum out-of-plane amplitude to explore.

The target Backflip is required to have an almost planar arc (in order to have the maximum exploitation of the characteristics of these orbits) and it has to reach a z -amplitude of the order of one half of the Earth-Moon distance ($\approx 1.9e5 \text{ km}$). This last requirement is a test case with a significant out-of-plane excursion (larger than the WIND mission case^[2]). Nevertheless, the same approach here outlined can be also used for other constraints on the out-of-plane amplitude. The candidate target Backflip orbit is shown in Fig. 6.13. It has approximately 32 days of period.

The main drawback of Backflip orbits satisfying these two requirements (and not impacting the Moon) is that they move in clockwise directions, namely these are retrograde orbits so, during the transfer the electric thruster must accomplish also the inversion of motion from a prograde GEO orbit.

The low thrust transfer here presented does not change significantly also considering target orbits nearby the chosen one. These have a range for the z -component of $[1.5-2.3]e5 \text{ km}$, the range of the Jacobi constant is ap-

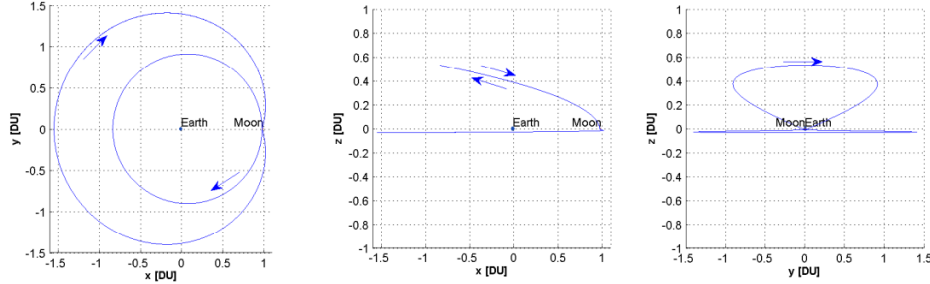


Figure 6.13: Three views of the target Backflip orbit with an out-of-plane excursion of 0.5 DU .

proximately $[-0.8, -0.4]$ and the range of periods is approximately $[29-35]$ days. Some of these orbits are represented in Fig. 6.14.

It is worth noting that choosing the target Backflip orbit does not mean that the inlet point is a-priori assigned, so it is included in the control vector by means of an angle-like variable that is actually the elapsed time on the ballistic solution. Thus the Backflip orbit is reintegrated, starting from an initial condition located on the x - z plane, for a variable time (represented by this variable) up to the electric powered phase. The zero of this angle-like variables has been assumed on the $y = 0$ intersection of the Backflip orbit along the negative x -axis, since here the out-of-plane component is very small and the point is far from the lunar swing-by, so the scheme is numerically more stable.

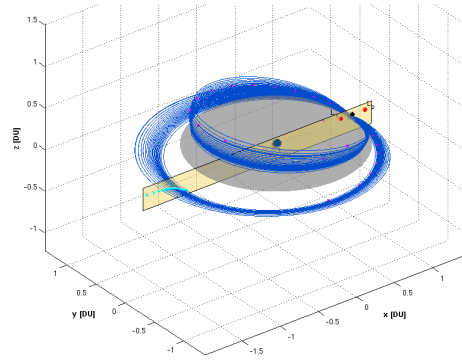


Figure 6.14: Range of Backflip orbits with characteristics similar to the target one chosen.

Transfer from GEO to Backflip

The whole GEO-Backflip transfer is composed by three phases. It has been a-priori divided into arcs representing a thrust-coast-thrust strategy, two powered phases (phases 1 and 3) separated by a ballistic phase (phase 2). Phase 1 is aimed to gain energy and spiral out from the GEO, Phase 2 is considered to save propellant mass, and Phase 3 is designed to perform the inversion. Each powered phase (subscript 1 and 3) has six unknown initial conditions for the Lagrange multipliers (identifying the thrust direction) and

unknown duration $(\vec{\lambda}, t)$. Moreover, also the departure true longitude (θ_0) is unknown as well as an angle-like variable (θ_f) identifying the target condition on the Backflip orbit. Finally, also the duration of the ballistic phase is unknown (t_2) . This means that the complete control vector is composed by: $\vec{u} = [\vec{\lambda}_1, t_1, t_2, \vec{\lambda}_3, t_3, \theta_0, \theta_f] \in \mathbb{R}^{17}$.

The elements of this control vector are updated in order to obtain the transfer (i.e. to satisfy the final non linear constraints that the final state of Phase 3 matches a point on the target Backflip) with the local minimum of mass consumption.

Transfer between Backflips

As proposed extension to the basic mission profile, a low-thrust transit between two Backflip orbits is considered next. A transfer between a Northern and Southern family has been selected as the mission goal, although the approach will work the same for transfers between Northern and Northern, Southern and Northern, or Southern and Southern families. Thus, this section presents, as possible mission extension, a low thrust transfer from a Northern Backflip to a Southern one; it is just a test case and the approach presented works also for other combinations of Backflip orbits.

The approach follows closely the previous one and also in this case the target orbit in the Southern family has been a-priori selected. The requirements are the same as before, but in this case an out-of-plane (below the Earth-Moon plane) amplitude required is of the order of 70% ($2.7e5$ km) of the Earth-Moon distance, to explore the generality of the methodology.

The main difference along the almost planar arc of the Northern and Southern Backflip is the different z -component which is slightly positive for the Southern family and slightly negative for the Northern family. This means that, in scale, the importance of the out-of-plane thrust angle is higher than in the GEO to Backflip transfer.

In this case only a single thrusting phase is required and the elements of the control vector are the initial conditions of the associated six Lagrange multipliers, the duration of this phase and the angle-like variables identifying the initial (θ_0) and final conditions (θ_f) along, respectively, the Northern and the Southern Backflip. Thus, the complete control vector is: $\vec{u} = [\vec{\lambda}, t, \theta_0, \theta_f] \in \mathbb{R}^9$.

It is important to observe that the angle-like variables are always guessed (here as before) along the almost planar arcs of the Backflip orbits in order to try to perform the transfer with the minimum plane change possible. As before, this control vector has been used in the hybrid optimization scheme to solve the minimum problem and satisfy the final constraints that the final state of this thrusting phase matches a state of the Southern Backflip.

6.3.2 Results

As no global optimization has been performed, several trajectories can be obtained from the described approach changing the initial conditions for the control vectors and allowing the convergence of the optimization scheme to settle to different outcomes. This has been done for a grid of few tens of uniformly spaced initial guesses, where the duration of the three phases has been changed respectively within the ranges: $[20, 40]$ - $[0, 30]$ - $[10, 30]$ days. On the other hand, the angle-like variables have been always guessed in a range around zero to obtain almost planar transfers.

The equations of motion have been forward propagated in non dimensional units with a variable step integrator with a relative and absolute tolerance of $1e-9$ and with similar accuracy also the final non linear constraints have been satisfied. This results in trajectories that exactly match the target Backflip, after the thruster is switched off, up to three Moon encounters. After the third one, indeed, a slight deviation of the two paths (the obtained Backflip and the target one), of the order of tens kilometers, takes place suggesting that for real applications some correction manoeuvres must be planned.

A couple of typical trajectories obtained are shown in Fig. 6.15 in planar and side views in the usual Earth-Moon barycentric synodic frame. The first row presents a very short ballistic phase and it is the best solution found, the minimum of the mass consumption. The lower row presents a completely different dynamics, in particular a significantly longer ballistic phase, and it represents the upper bound of the mass consumption found (worse case) in the range of the initial guesses tested to start the procedure.

For the best trajectory depicted in Fig. 6.15 (the upper one), the evolution of the instantaneous position and velocity are plotted in Fig. 6.16, while the in-plane and the out-of-plane thrust angles, together with the mass consumption are represented in Fig. 6.17.

It is worth noting that approximately 100 kg are required for the Earth spiralling out phase and around 70 kg for the inversion of the motion. The ballistic phase duration changes from 5 up to 28 days. The Earth escape phase takes, in both cases, approximately one month, while the inversion of motion spans from 19 up to 24 days.

For the mission extension the solutions found are in a very narrow range in terms of propellant mass and transfer time; in this case minimum time trajectories are also minimum mass trajectories. This happens because the transfer time is more or less the same (less than one day of difference) and guessing the two angle-like variables always along the almost planar arc of the Backflips, results just in a translation of similar powered arcs.

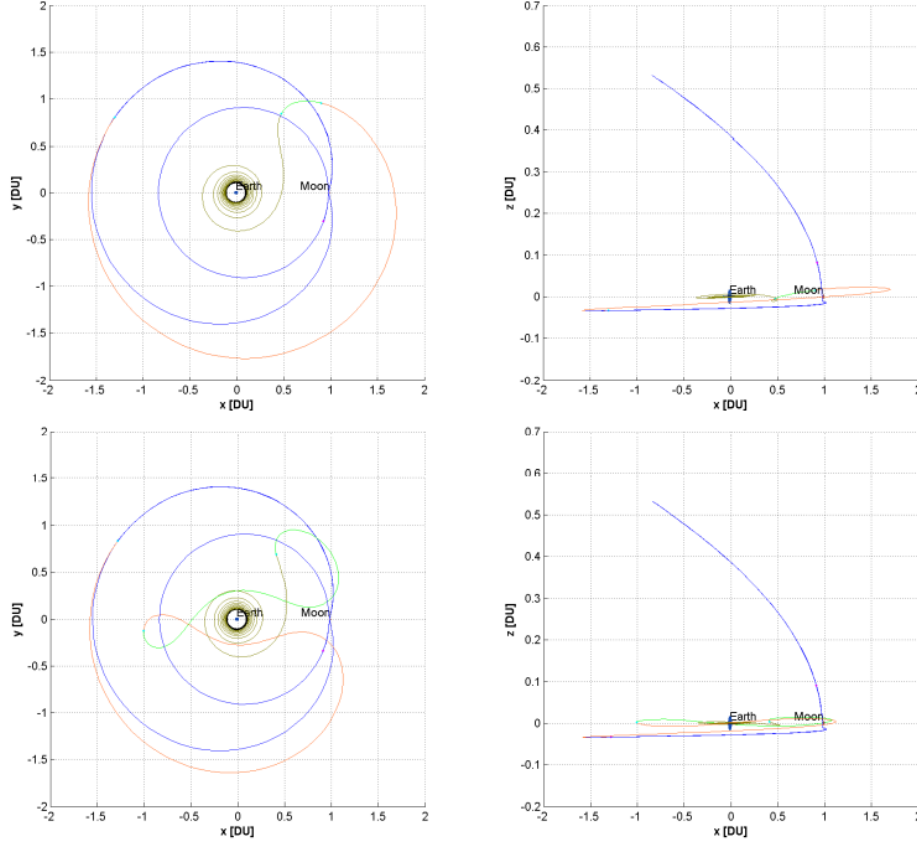


Figure 6.15: GEO to Backflip transfers. First row: smaller propellant mass transfer found in x-y and x-z views. Second row: costly transfer found in x-y and x-z views (rotating frame).

A typical transfer of this kind is shown in Fig. 6.18, as seen in a synodic barycentric frame (upper row) and in a geocentric inertial reference (lower row); also the trends of the instantaneous mass and of the thrust angles are presented in Fig. 6.19.

The GEO to Backflip transfer can be accomplished in 52-81 days with a mass consumption of 168-178 kg. It is worth noting that solutions of minimum mass are not, differently from the Backflip to Backflip transition, solutions of minimum time, in particular minimizing the mass requires the minimization of the two powered phases.

The initial mass guessed in the Northern Backflip (that determines the initial acceleration for the Backflip-Backflip transfer) is of 800 kg, namely slightly lower than the actual worst case obtained for the basic mission profile;

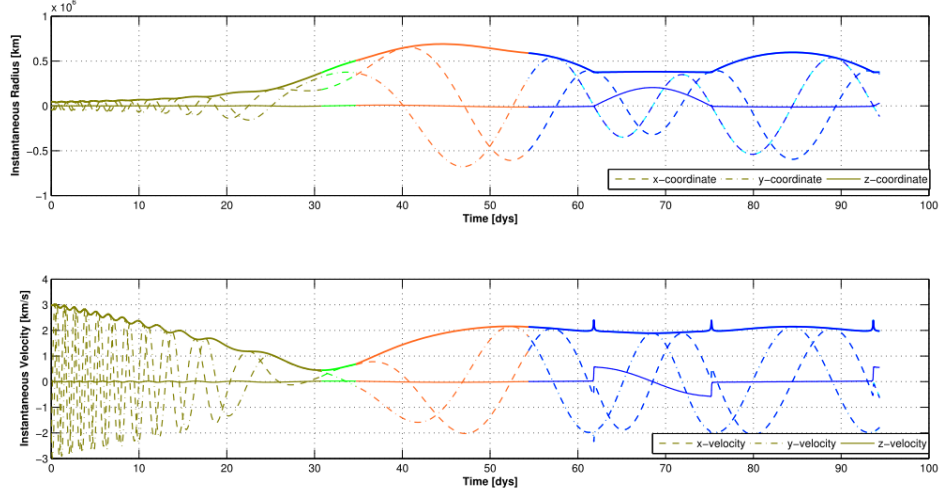


Figure 6.16: Position and velocity evolutions for the less expensive transfer (upper row of Fig. 6.15).

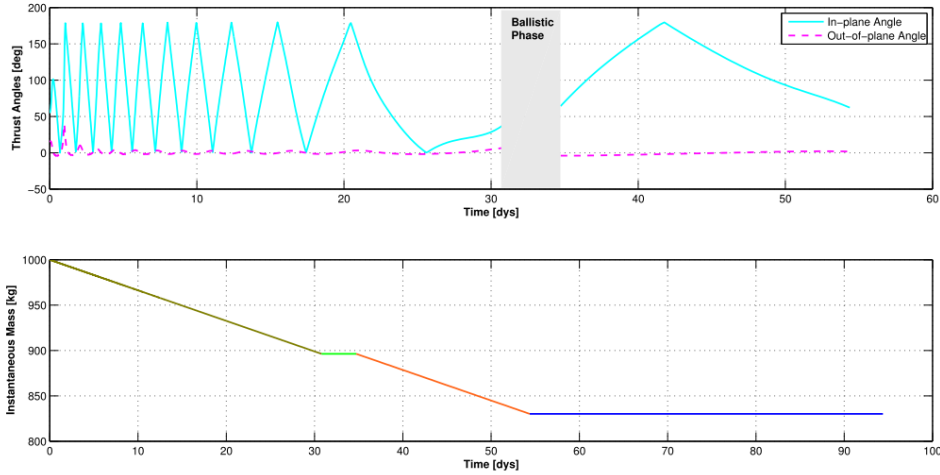


Figure 6.17: Thrust angles and instantaneous mass for the less expensive transfer (upper row of Fig. 6.15).

this has been done in order to let a mass clearance for correction manoeuvres during this operational phase.

For the Backflip-Backflip transitions the motion does not need any inversion as both the departure and the arrival orbits are retrograde. The proposed mission extension can be performed in 6.5-7.3 days and with 22.5-

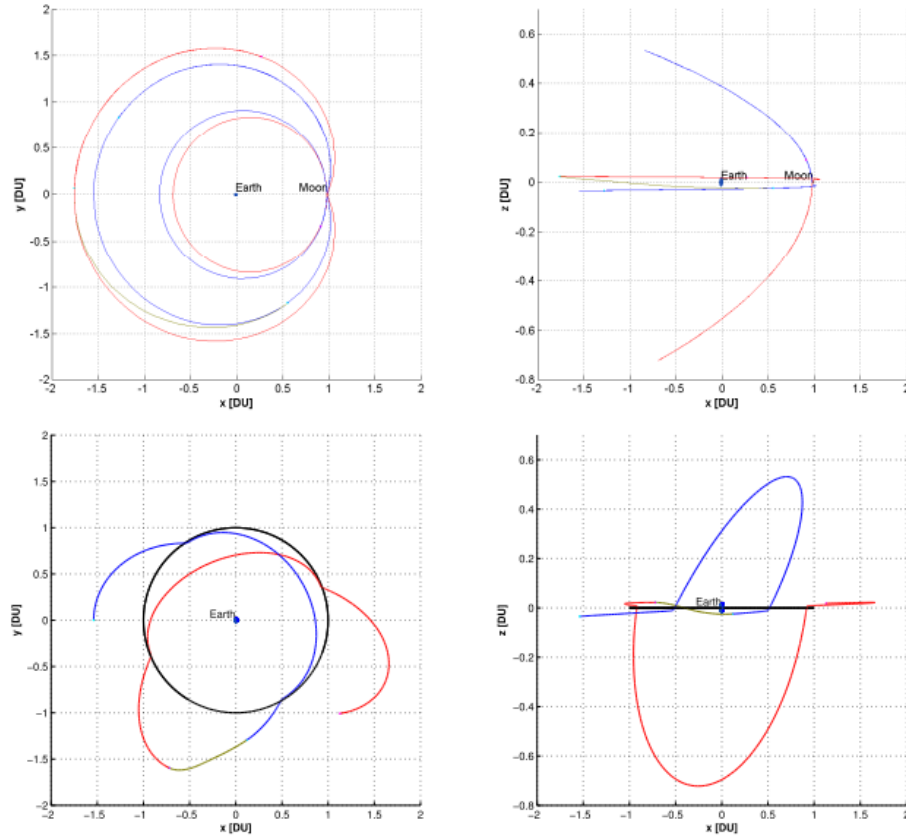


Figure 6.18: Backflip to Backflip transfer. First row: x-y and x-z views in the Earth-Moon rotating frame. Second row: x-y and x-z views in the geocentric inertial frame.

24 kg of propellant mass^[115].

Thus, a complete mission can be composed with low thrust, almost planar arcs from a GEO to a Backflip and, after an arbitrary time, also a Backflip to Backflip transfer can be designed again by means of an almost planar low thrust arc. In summary, less than 3 months and 180 kg are required for the worse transfer found by testing several initial guesses, especially for the duration of the three phases. To achieve the additional Backflip-Backflip transfer approximately one week and 25 kg of propellant are required. Transfers of this kind can be performed towards another Backflip orbit and/or more than once during the entire mission, as the propellant requirement is very small.

It is worth noting that there is also another family of periodic orbits

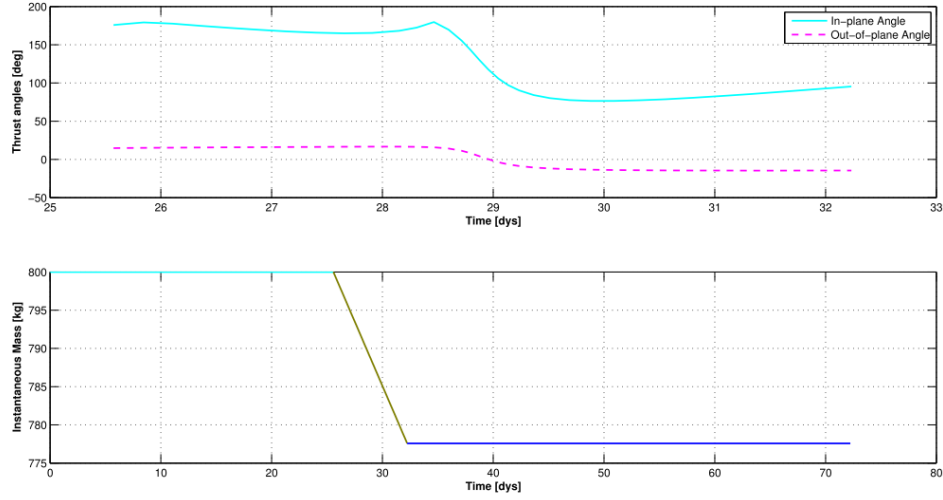


Figure 6.19: Thrust angles and instantaneous mass for the Backflip-Backflip transfer. Trajectory in Fig. 6.18.

with similar characteristics arising from a bifurcation of the planar family of Lyapunov orbit when their amplitude grows up to the order of the Earth-Moon distance^{[118][66]}.

Of course, the approach remains the same also if the bodies under investigation are different from Earth and Moon. Finally, it has to be stressed that the CR3BP is only a starting point to design such a kind of mission. For real applications, non deterministic manoeuvres are required to correct the trajectory in a full force model where the circular restricted three body assumptions represent only low order approximations.

Chapter 7

Conclusions

The main goal of this thesis was the investigation and the exploitation of capabilities enabled, already in the early mission analysis phase, by non-Keplerian models. Multi body regimes give rise to unique transfer options and operational orbits whose efficiency and flexibility can be further extended by considering the inclusion of low thrust propulsion strategies.

The direction followed in this work starts from the general N -body dynamics with special emphasis to the three body model and from this to the circular restricted one. Once this model has been defined, its theoretical analysis reveals the presence of equilibrium points, periodic orbits around them and ballistic solutions moving to/from these. All of these features have been numerically computed, starting from analytic initial guesses, and analyzed.

Dynamical system theory is a valuable help to identify these structures and it has been exploited also to investigate about global periodic orbits, their stability and normalization procedures. Moreover, the useful tool of the Poincaré section has been used to analyze homoclinic and heteroclinic orbits as well as resonance conditions and transitions with general understanding of this phenomenon in the Earth-Moon system.

Up to this point, purely ballistic solutions have been defined and exploited, however, in order to design a complete mission, thrusting phases are required. These arcs have been supposed to be powered by electric devices able to provide low thrust for extended duration. This methodology results in lower propellant mass fractions and higher transfer times if compared with chemical solutions. This has been tested both for interplanetary transfers and Earth-Moon trajectories.

As the inclusion of low thrust arcs is sought, optimal control theory becomes a valuable help. Indirect and hybrid methods are theoretically derived and presented in some test cases, in two and three body dynamics.

Thus, transfer solutions involving manifolds and low thrust phases are presented. In the beginning considering one dimensional manifolds among different three body systems in order to design a small tour of the Uranus main moons, and afterwards considering two dimensional manifolds associated with Halo orbits of the Sun-Earth and Sun-Mars systems. All of these ballistic trajectories are successfully exploited in order to design a sort of *patched manifold* transfers where the energy change required to move from a system to another is provided by the electric thruster.

Finally, also several applications in the Earth-Moon system are presented. The easiest one is a low thrust transfer from a GTO to a ballistic orbit leading towards the Moon neighborhoods and exploring its realm for free. Exemplificative Earth to Moon trajectories are presented with initial and final orbits that can be fixed by specific mission requirements. The whole transfers have been divided into the thrust-coast-thrust sequence and computed considering again the Earth-Moon three body dynamics. Finally, low thrust transfers towards doubly plane change periodic orbits are presented. These orbits, arising in the Earth-Moon three body system, offer unique possibilities of exploration of the geospace out from the Moon orbital plane and, beside to be less expansive if performed electrically, transfers of this kind are hardly conceivable by means of chemical thrusters.

The applications here presented tend to follow increasing complexity and to motivate comparisons with the classical chemical-Keplerian model. Advantages of these innovative solutions, measured in terms of propellant mass and mission feasibility, are highlighted through the whole work. The last application, in particular, represents a mission completely beyond the limits of the classical mission analysis approach.

All in all, the theoretical background and the applications presented outline methodologies to preliminary design and analyze non-Keplerian missions, stressing their advantages both in terms of on board requirements and flexibility.

Appendix A

Parameter Values

The location of the three collinear points can be found by computing the three real roots of the quintic equation, Eq. (2.2.4), in the intervals $x < -\mu$, $-\mu < x < (1 - \mu)$ and $x > (1 - \mu)$ that correspond respectively to \mathcal{L}_3 , \mathcal{L}_1 and \mathcal{L}_2 .

However, the location, with respect to the small primary, of the first two collinear points can be approximated by the series expansions^[13]:

$$\delta_1 = r_h \left(1 - \frac{1}{3}r_h - \frac{1}{9}r_h^2 + \dots \right), \quad \delta_2 = r_h \left(1 + \frac{1}{3}r_h - \frac{1}{9}r_h^2 + \dots \right) \quad (\text{A.1})$$

where δ_1 holds for \mathcal{L}_1 , δ_2 for \mathcal{L}_2 and $r_h = \left(\frac{\mu}{3}\right)^{\frac{1}{3}}$ is the *Hill radius*. Thus, the location of the first two collinear points in the usual synodic barycentric frame is given by: $x_{\mathcal{L}_1} = 1 - \mu - \delta_1$ and $x_{\mathcal{L}_2} = 1 - \mu + \delta_2$.

This holds as \mathcal{L}_1 and \mathcal{L}_2 are, at the first order, located where the m_1 and m_2 gravity accelerations balance the centrifugal force. The Hill's work on the lunar motion^[31] brought to a first order approximation of the CR3BP model in the neighborhoods of the small primary. The main assumptions are that $\mu \ll 1$ and the terms of order $O(\mu^2)$ can be neglected. This results in a re-writing of the CR3BP equations, Eq. (2.27), where the effective potential, Eq. (2.20), is replaced by:

$$\Omega_H = \frac{3}{2}\bar{x}^2 - \frac{\mu}{\Delta}$$

being the origin of the frame m_2 . This means that $x = 1 + \bar{x}$ and $y = \bar{y}$, where $r_2^2 = \Delta = \bar{x}^2 + \bar{y}^2$ and $r_1^2 = 2\bar{x} + 1$ are the approximate distances from the two primaries. When $\partial U_H / \partial \bar{x} = 0$, a first order approximation of the location of \mathcal{L}_1 and \mathcal{L}_2 can be obtained. This happens when $3\Delta^3 = \mu$, that leads to the definition of the Hill radius $\Delta = r_h$. Thus at the first order \mathcal{L}_1

and \mathcal{L}_2 are located at the same distance, given by the Hill radius, from m_2 . From the same linearized approach also a first order approximation of the Jacobi constant is available. It results, for \mathcal{L}_1 and \mathcal{L}_2 in $J_{\mathcal{L}_1-\mathcal{L}_2} = 3^{4/3}\mu^{2/3}$.

In a similar fashion, also δ_3 , the distance between \mathcal{L}_3 and the larger primary ($x_{\mathcal{L}_3} = -\mu - \delta_3$), can be approximated by the series expansion^[13]:

$$\delta_3 = 1 - \nu \left(1 + \frac{23}{84}\nu^2 + \dots \right), \quad \nu = \frac{7}{12}\mu \quad (\text{A.2})$$

In general, the accuracy of these series is quite high already at low orders, moreover the smaller μ is, the closer the analytical value to the numerical solution of the quintic equation is.

The values of the mass parameters, distance units [DU] and time units [TU] for some three body systems of interest is summarized in Tab. A.1 with the numerically computed locations of their collinear equilibria.

System	μ	DU [km]	TU [sec]	\mathcal{L}_1 [DU]	\mathcal{L}_2 [DU]	\mathcal{L}_3 [DU]
Sun-Jupiter	9.537e-4	7.784e8	5.9563e7	0.93238	1.06881	-1.00040
Sun-Earth/Moon	3.04042e-6	1.49598e8	5.0759e6	0.98999	1.01007	-1.00000
Earth-Moon	0.12151e-1	3.844e5	3.9716e5	0.83737	1.15527	-1.00506
Sun-Mars	3.2257e-7	2.27937e8	9.4395e6	0.99525	1.00476	-1.00000
Sun-Venus	2.4476e-6	1.08209e8	3.0898e6	0.99067	1.00938	-1.00000
Jupiter-Io	4.6869e-5	421700	2.4339e4	0.97513	1.02519	-1.00002
Jupiter-Europa	2.5278e-5	671034	1.7876e5	0.97976	1.02046	-1.00001
Jupiter-Ganymede	7.7938e-5	1070410	9.8320e4	0.97059	1.02984	-1.00003
Jupiter-Callisto	5.6874e-5	1882710	2.3322e5	0.97355	1.02681	-1.00002
Uranus-Oberon	3.4792e-5	583519	1.8539e5	0.97750	1.02277	-1.00002
Uranus-Titania	4.0703e-5	435910	1.1970e5	0.97630	1.02400	-1.00002
Uranus-Umbriel	1.3853e-5	266300	5.7157e4	0.98343	1.01673	-1.00001
Uranus-Ariel	1.5584e-5	190020	3.4452e4	0.98277	1.01740	-1.00001
Uranus-Miranda	7.6075e-7	129390	1.9358e4	0.97084	1.02959	-1.00003

Table A.1: Physical constants and collinear libration point locations for some three bodies systems

The transformation from dimensional to non dimensional units can be easily performed by dividing the distances with DU and the times with TU; the opposite way works the inverse transformation.

Bibliography

- [1] Bernelli-Zazzera, F., Topputo, F., and Massari, M., “Assessment of Mission design Including Utilization of Libration Points and Weak Stability Boundaries,” *Ariadna Study id: 03/4103*..
- [2] Sharer, P. J., Dunham, D. W., Jen, S., Roberts, C. E., Seacord, A. W., and Folta, D. C., “Double lunar swingby and Lissajous trajectory design for the WIND mission,” *IAF Int. Astronautical Congress, 43rd, WA*, 1992.
- [3] Canalias, E., Gomez, G., Marcote, M., and Masdemont, J. J., “Assessment of Mission design Including Utilization of Libration Points and Weak Stability Boundaries,” *Ariadna Study id: 03/4103*.
- [4] Belbruno, E. and Miller, J., “Sun-Perturbed Earth-to-Moon Transfers with Ballistic Capture,” *Journal of Guidance, Control and Dynamics*, Vol. 16, No. 4, 1993, pp. 770–775.
- [5] Lo, M. W. and Ross, S. D., “Low Energy Interplanetary Transfers Using Lagrangian Points,” *Nasa Tech Brief, from JPL new technology report, NPO-20377*, Vol. 23, No. 11, 1999.
- [6] Koon, W. S., Lo, M. W., Marsden, J. E., and Ross, S. D., “The Genesis trajectory and heteroclinic connections,” *AAS 99-451, AAS/AIAA Astrodynamics Specialist Conf., Girdwood, AK*, 1999, pp. 2327–2343.
- [7] Anderson, D. J., Pencil, E., Larry, L., Dankanich, J., Munk, M. M., and Kremic, T., “NASA’s In-Space Propulsion Technology Project Overview, Near-term Products and Mission Applicability,” *IEEE/AIAA Aerospace Conference, Big Sky, MT*, 2009.

- [8] Saccoccia, G. and Gonzalez, J., "European activities in Electric Propulsion," *AIAA-2003-5271, 39th Joint Propulsion Conf., Huntsville, AL*, 2003.
- [9] Bolt, E. M. and Meiss, J. D., "Targeting Chaotic Orbits to the Moon Through Recurrence," *Physics Letters*, Vol. 204, 1995, pp. 374–378.
- [10] Schroer, C. G. and Ott, E., "Targeting in Hamiltonian Systems that have a Mixed Regular/Chaotic Phase Space," *Chaos*, Vol. 7, No. 4, 1997, pp. 512–519.
- [11] Battin, R. H., *An Introduction to the Mathematics and Methods of Astrodynamics*, AIAA Inc., New York, 1st ed., 1987.
- [12] Meyer, K. R., *Periodic Solutions of the N-body Problem*, World Scientific Monograph Series in Mathematics, Springer-Verlag Berlin And Heidelberg GmbH & Co, 1999.
- [13] Szebehely, V., *Theory of Orbits - The Restricted Problem of Three Bodies*, Academic Press Inc., Harcourt Brace Jovanovich Publishers, Orlando, Florida, 1967.
- [14] Koon, W. S., Lo, M. W., Marsden, J. E., and Ross, S. D., *Dynamical Systems, the Three-Body Problem and Space Mission Design*, World Scientific, Pasadena, 2000.
- [15] Gómez, G., Jorba, A., Masdemont, J. J., and Simó, C., *Dynamics and Mission Design Near Libration Points, Vols 1-4*, World Scientific Monograph Series in Mathematics, Singapore, 2001.
- [16] Arnol'd, V. I., *Mathematical Aspects of Classical and Celestial Mechanics, Dynamical Systems III. Series: Encyclopaedia of Mathematical Sciences*, Springer-Verlag, 2006.
- [17] Whittaker, E. T., *A Treatise on the Analytical Dynamics of Particles and Rigid Bodies*, Cambridge University Press, 1989.
- [18] Wiggins, S., *Introduction to Applied Nonlinear Dynamical Systems and Chaos*, Springer-Verlag, Berlin, vol. 2 of texts in applied mathematics science ed., 1990.
- [19] Butikov, E., "Regular Keplerian Motions in Classical Many-Body Systems," *European Journal of Physics*, Vol. 21, 2000, pp. 465–482.
- [20] Moeckel, R., "On Central Configurations," *Mathematische Zeitschrift*, Vol. 205, 1990, pp. 499–517.

- [21] Chenciner, A. and Montgomery, R., “A remarkable periodic solution of the three-body problem in the case of equal masses,” *Annals of Mathematics*, Vol. 152, 2000, pp. 881–901.
- [22] Lagrange, J. L., *Essai sur le problème des trois corps*, Prix de l’Académie Royale des Sciences de Paris, 1772.
- [23] Euler, L., “De Motu Rectilineo Trium Corporum se Mutuo Attrahentium,” *Novi Commentarii Academiae Scientiarum Petropolitanae*, Vol. 11, 1765, pp. 144–151.
- [24] Montgomery, R., “The N-body problem, the braid group, and action-minimizing periodic solutions,” *Nonlinearity*, Vol. 11, 1998, pp. 363–376.
- [25] Arnol’d, V. I., *Encyclopedia of Mathematical Sciences, Dynamical Systems III*, Springer-Verlag, 1988.
- [26] Celletti, A. and Chierchia, L., “KAM Stability and Celestial Mechanics,” *Memoirs of the American Mathematical Society*, Vol. 878, 2007.
- [27] Poincaré, H., “Sur le Problème des Trois Corps et les Équations de la Dynamique,” *Acta Mathematica*, Vol. 13, 1890, pp. 1–271.
- [28] Lehti, R., “Karl Frithiof Sundman’s investigations in celestial mechanics I/II,” *Nordisk Matematisk Tidskrift*, Vol. 49, No. 1, 2001, pp. 7–20.
- [29] Llibre, J., Martinez, R., and Simó, C., “Transversality of the invariant manifolds associated to the Lyapunov family of periodic orbits near L2 in the restricted three-body problem,” *Journal of Differential Equations*, Vol. 58, 1985, pp. 104–156.
- [30] Poincaré, H., *Les Methodes Nouvelles de la Mécanique Céleste*, Gautiers-Villars et fils, Paris, 1892-1899. Reprinted by Dover, New York, 1957.
- [31] Hill, G. W., “Researches in Lunar Theory,” *Americal Journal of Mathematics*, Vol. 1, 1878, pp. 5–54.
- [32] Meyer, K. R. and Schmidt, D. S., “The Stability of the Lagrange Triangular Point and a Theorem of Arnol’d,” *Journal of Differential Equations*, Vol. 62, 1986, pp. 222–236.
- [33] Tantardini, M., Fantino, E., Ren, Y., Pergola, P., Gomez, G., and Masdemont, J. J., “Spacecraft trajectories to the L3 point of the Sun-Earth

- three-body problem,” *Journal of Celestial Mechanics and Dynamical Astronomy*, Vol. 108, No. 3, 2010, pp. 215–232.
- [34] McGehee, R., *Some homoclinic orbits for the restricted three-body problem*, Ph.D. thesis, University of Wisconsin, Madison, 1969.
- [35] Conley, C. C., “On the ultimate behavior of orbits with respect to an unstable critical point. Oscillating, asymptotic, and capture orbits,” *Journal of Differential Equations*, Vol. 5, 1969, pp. 136–158.
- [36] Lyapunov, A. M., *The general problem of the stability of motion*, Taylor & Francis, London, 1992.
- [37] Farquhar, R. W., *The control and use of Libration-Point satellites*, Ph.D. thesis, Stanford University, California, 1968.
- [38] Conley, C. C., “Low energy transit orbits in the restricted three-body problem,” *SIAM Journal of Applied Mathematics*, Vol. 16, 1968, pp. 732–746.
- [39] Gómez, G., Koon, W. S., Lo, M. W., Marsden, J. E., Masdemont, J. J., and Ross, S., “Invariant manifolds, the Spatial Three-Body Problem and Space Mission Design,” *Advances in the Astronautical Sciences*, Vol. 109 part 1, 2001, pp. 3–22.
- [40] Ross, S. D., Koon, W. S., Lo, M. W., and Marsden, J. E., “Constructing a Low Energy Transfer Between Jovian Moons,” *Contemporary Mathematics*, Vol. 292, 2002, pp. 129–145.
- [41] Lichtenberg, A. J. and Lieberman, M. A., *Regular and Chaotic Dynamics*, New York, Springer, 1992.
- [42] Masdemont, J. J. and Mondelo, J., “Notes for the Numerical and Analytical Techniques Lectures,” *Notes of the Summer Workshop on Advanced Topics in Astrodynamics*, Barcelona, 2004.
- [43] Kolmogorov, A. N., “The General Theory of Dynamical Systems and Classical Mechanics,” *Int. Congress of Mathematicians, Amsterdam, 1954, English translation in “Foundations of Mechanics” J. E. Marsden*, Vol. 1, 1954, pp. 315–333.
- [44] Howell, K. C., Barden, B. T., Wilson, R. S., and Lo, M. W., “Trajectory Design Using a Dynamical Systems Approach with Application to GENESIS,” *AAS Paper 97-709, AAS/AIAA Astrodynamics Specialist Conf., Sun Valley, ID*, 1997, pp. 1665–1684.

- [45] Howell, K. C., Barden, B. T., and Lo, M. W., "Application of dynamical systems theory to trajectory design for a libration point mission," *Astronautical Sciences*, Vol. 45, No. 2, 1997, pp. 161–178.
- [46] Campbell, E. T., *Bifurcations from Families of Periodic Solutions in the Circular Restricted Three Body Problem with Application to Trajectory Design*, Ph.D. thesis, Purdue University, Indiana, 1999.
- [47] Topputo, F., *Low-Thrust Non-Keplerian Orbits: Analysis, Design and Control*, Ph.D. thesis, Politecnico di Milano, Italy, 2007.
- [48] Belbruno, E. A., *Capture Dynamics and Chaotic Motions in Celestial Mechanics: With Applications to the Construction of Low Energy Transfers*, Princeton University Press, 2004.
- [49] Roy, A. E. and Ovenden, M. W., "On the Occurrence of Commensurable Mean Motion in the Solar System. The Mirror Theorem," *Monthly Notes of the Royal Astronomical Society*, Vol. II, 1955.
- [50] Jorba, A. and Masdemont, J. J., "Dynamics in the centre manifold of the collinear points of the Restricted Three Body Problem," *Phisica D*, Vol. 132, 1999, pp. 189–213.
- [51] Richardson, D. L., "Analytic Construction of Periodic Orbits about Collinear Points," *Celestial Mechanics*, Vol. 22, 1980, pp. 241–253.
- [52] Logan, J. D., *Applied Mathematics*, John Wiley & Sons, Washington, second edition ed., 1997.
- [53] Richardson, D. L., "A Note on a Lagrangian Formulation for Motion about the Collinear Points," *Celestial Mechanics*, Vol. 22, 1980, pp. 231–236.
- [54] Thurman, R. and Worfolk, P. A., *The geometry of Halo orbits in the Circular Restricted Three-Body problem*, Ph.D. thesis, Geometry Center Research report, University of Minnesota, 1995.
- [55] Multon, F. R., *Periodic Orbits*, Carnegie Institution of Washington Publications, Washington, 1920.
- [56] Doedel, E. J., Keller, H. B., and Kernévez, J. P., "Numerical Analysis and Control in Bifurcation Problems," *Int. Journal of Bifurcation and Chaos*, Vol. 1, No. 3, 1991, pp. 493–520.

- [57] Dichmann, D. J., Doedel, E. J., and Paffenroth, R. C., “The computation of periodic solutions of the 3-Body problem using the numerical continuation software AUTO,” in: “*Libration Point Orbits and Applications*”, eds. World Scientific, 2003.
- [58] Keller, H. B., *Numerical Solutions of Bifurcation and Nonlinear Eigenvalue Problems, Application of Bifurcation Theory*, Academic Press, Washington, 2nd ed., 1977.
- [59] Doedel, E. J., Romanov, V., Paffenroth, R. C., Keller, H. B., Dichmann, D. J., Galan-Vioque, J., and Vanderbauwhede, A., “Elemental periodic orbits associated with the libration points in the Circular Restricted 3-Body Problem,” *Int. Journal of Bifurcation and Chaos*, Vol. 17, 2007.
- [60] Muñoz-Almaraz, F. J., *Continuación de órbitas periódicas en sistemas Hamiltonianos con simetría*, Ph.D. thesis, Matemática Aplicada II, Universidad de Sevilla, Spain, 2003.
- [61] Doedel, E. J., “AUTO, a program for the automatic bifurcation analysis of autonomous Systems,” *Congressus Numerantium*, 30, Vol. 1981, pp. 265–284.
- [62] Floquet, G., “Sur les équations différentielles linéaires á coefficients périodiques,” *Ann De Lécole Normale Supérieure*, Vol. 12, 1883, pp. 47–88.
- [63] Hénon, M. and Guyot, M., *Stability of Periodic Orbits in the Restricted Problem; in Periodic Orbits, Stability and Resonances*, D. Reidel Publishing Company, Dordrecht-Holland, 1970.
- [64] Leiva, A. M. and Biozzo, C. B., “The Earth-Moon CR3BP: a full Atlas of low-energy fast periodic transfer orbits,” *Actual Problems in Celestial Mechanics and Dynamical Astronomy*, Cluj-Napoca, Romania, 2006.
- [65] Howell, K. C., “Families of Orbits in the Vicinity of the Collinear Libration Points,” *Journal of the Astronautical Sciences*, Vol. 49, 2001, pp. 107–125.
- [66] Gómez, G., Koon, W. S., Lo, M. W., Marsden, J. E., Masdemont, J. J., and Ross, S. D., “Connecting orbits and invariant manifolds in the spatial restricted three-body problem,” *Nonlinearity, Institute of Physics Publishing*, Vol. 17, 2004, pp. 1571–1606.
- [67] Koon, W. S., Lo, M. W., Marsden, J. E., and Ross, S. D., “Resonance and capture of Jupiter comets,” *Celestial Mechanics and Dynamical Astronomy*, Vol. 81, 2001, pp. 27–38.

- [68] Dellnitz, M., Junge, O., Post, M., and Thiere, B., "On target for Venus - set oriented computation of energy efficient low thrust trajectories," *Celestial Mechanics and Dynamical Astronomy*, Vol. 95, 2006, pp. 770–775.
- [69] Dellnitz, M., Junge, O., Lo, M. W., Marsden, J. E., Padberg, K., Preis, R., Ross, S. D., and Thiere, B., "Transport of Mars-Crossing Asteroids from the Quasi-Hilda Region," *Physical review letters*, Vol. 94, 2005.
- [70] Meyer, K. R., "Normal forms for Hamiltonian systems," *Celestial Mechanics*, Vol. 9, 1974, pp. 517–522.
- [71] Gregorio, L. D. and Pergola, P., "Normal Forms for the PCR3BP to Detect Invariant Manifolds Close and Far from Equilibria," *SIAM Conf. on Applications of Dynamical Systems, Snowbird, UT*, 2009, (and preprint 2009).
- [72] Gustavson, F. G., "On constructing formal integrals of a Hamiltonian system near anequilibrium point," *Astronomical Journal*, Vol. 71, No. 8, 1966, pp. 670–686.
- [73] Jorba, A. and Villanueva, J., "Numerical Computation of Normal Forms around some Periodic Orbits of the Restricted Three Body Problem," *Phisica D*, Vol. 114, 1998, pp. 197–229.
- [74] Dragt, A. J. and Finn, J. M., "Lie series and invariant functions for analytic symplectic maps," *Journal of Mathematical Physics*, Vol. 17, 1976, pp. 2215–2227.
- [75] Deprit, A., "Canonical transformations depending on a small parameter," *Celestial Mechanics*, Vol. 1, 1969, pp. 12–30.
- [76] Koon, W. S., Lo, M. W., Marsden, J. E., and Ross, S. D., "Heteroclinic connections between periodic orbits and resonance transitions in celestial mechanics," *Chaos*, Vol. 10, No. 2, 2000, pp. 427–469.
- [77] Belbruno, E. A. and Carrico, J. P., "Calculation of Weak Stability Boundary Ballistic Lunar Transfer Trajectories," *AIAA-2000-4142, AIAA/AAS Astrodynamics Specialist Conf., Denver, CO*, 2000.
- [78] García, F. and Gómez, G., "A note on Weak Stability Boundaries," *Celestial Mechanics and Dynamical Astronomy*, Vol. 97, No. 2, 2006, pp. 87–100.

- [79] Luersen, M. A. and Riche, R. L., "Globalized Nelder-Mead method for engineering optimization," *3rd Int. Conf. on Engineering Computational Technology*, 2002, pp. 156–166.
- [80] Froeschlé, C., Lohinger, E., and Lega, E., "On the Relationship Between Local Lyapunov Characteristic Numbers, Largest Eigenvalues and Maximum Stretching Parameters," in *"The Dynamics of Small Bodies in the Solar System"*, B. A. Steves and A. E. Roy, Kluwer Academic Publishers, The Netherlands, 1999.
- [81] Anderson, R. L., Lo, M. W., and Born, G. H., "Application of Local Lyapunov Exponents to Maneuver Design and Navigation in the Three-Body Problem," *AAS 03-569, AAS/AIAA Astrodynamics Specialist Conf., Big Sky, MT*, 2003.
- [82] Betts, J. T., "Practical Methods for Optimal Control Using Nonlinear Programming," *Advances in Design and Control, Society for Industrial and Applied Mathematics*, 2001.
- [83] Bryson, A. E. and Ho, Y.-C., *Applied Optimal Control*, Hemisphere Publishing Corporation, 1975.
- [84] Jahn, R. G., *Physics of Electric Propulsion*, Dover, 2006.
- [85] Mengali, G. and Quarta, A. A., "Optimal Trade Studies of Interplanetary Electric Propulsion Missions," *Acta Astronautica*, Vol. 62, No. 12, 2008, pp. 657–667.
- [86] Mengali, G. and Quarta, A. A., "Fuel-Optimal, Power Limited Rendezvous with Variable Thruster Efficiency," *Journal of Guidance, Control and Dynamics*, Vol. 28, No. 6, 2005, pp. 1194–1199.
- [87] Ozimek, M. T. and Howell, K. C., "Low-Thrust Transfers in the Earth-Moon System with Applications to Libration Point Orbits," *Journal of Guidance, Control and Dynamics*, Vol. 33, No. 2, 2010, pp. 533–549.
- [88] Kluever, C. A. and Pierson, B. L., "Optimal Low-Thrust Three-Dimensional Earth-Moon Trajectories," *Journal of Guidance and Control*, Vol. 18, No. 4, 1995, pp. 830–837.
- [89] Betts, J. T., "Survey of Numerical Methods for Trajectory Optimization," *Journal of Guidance, Control, and Dynamics*, Vol. 21, No. 2, 1998, pp. 193–207.

- [90] Lewis, F. L. and Syrmos, V. L., *Optimal Control*, John Wiley and Sons, 605 Third avenue, New York, 2nd ed., 1995.
- [91] Bryson, A. E., *Dynamic Optimization*, Addison-Wesley, California, 1999.
- [92] Pontryagin, L. S., Boltyanskii, V. G., Gamkrelidze, R. V., and Mishchenko, E., *The Mathematical Theory of Optimal Processes*, Wiley-Interscience, 1st ed., 1962.
- [93] Lawden, D., *Optimal Trajectories for Space Navigation*, Butterworths Publishers, London, 1963.
- [94] Bäck, T., *Evolutionary algorithms in theory and practice: evolution strategies, evolutionary programming, genetic algorithms*, Oxford University Press, 1996.
- [95] Chobotov, V. A., *Orbital Mechanics*, AIAA Inc., Reston, Virginia, 2nd ed., 1996.
- [96] Gao, Y. and Kluever, C. A., “Low-Thrust Interplanetary Orbit Transfers Using Hybrid Trajectory Optimization Method with Multiple Shooting,” *AIAA 2004-4088, AIAA/AAS Astrodynamics Specialist Conference and Exhibit, Providence, RI*, 2004.
- [97] Pierson, B. and Kluever, C., “Three-Stage Approach to Optimal Low-Thrust Earth-Moon Trajectories,” *Journal of Guidance, Control and Dynamics*, Vol. 17, No. 6, 1994, pp. 1275–1282.
- [98] Noble, R. J., “Radioisotope Electric Propulsion of Small Payloads for Regular Access to Deep Space,” *AIAA 93-1897, 29th Joint Propulsion Conf., Monterey, CA*, 1993.
- [99] Alessi, E. M. and Pergola, P., “Strategy to Achieve Gravitational Capture at Callisto,” *IAF Int. Astronautical Congress, 61st, Prague, Czech Republic*, 2010.
- [100] Pergola, P., Casaregola, C., Geurts, K., and Andrenucci, M., “Three Body Invariant Manifold Transition with Electric Propulsion,” in *Space Manifold Dynamics, Springer US, Space Technology Library series*, 2010.
- [101] Pergola, P., Casaregola, C., Geurts, K., and Andrenucci, M., “Exploitation of Three-Body Dynamics by Electric Propulsion for Outer Planetary Missions,” *AIAA-2007-5234, 43rd Joint Propulsion Conf., Cincinnati, OH*, 2007.

- [102] Pierson, B. L., *Sequential Quadratic Programming and its use in Optimal Control Model Comparisons, Optimal Control Theory and Economic Analysis 3*, North-Holland, Amsterdam, 1998.
- [103] Pergola, P., Casaregola, C., Geurts, K., and Andrenucci, M., "Power Constrained Uranus Transfer and Moons Tour by Three Body Invariant Manifolds and Electric Propulsion," *AAS-08196, 18th Space Flight Mechanics Meeting, Galveston, TX*, 2008.
- [104] Geurts, K., Casaregola, C., Pergola, P., and Andrenucci, M., "Power Constrained Electric Propulsion Missions to the Outer Planets," *IEPC-2007-304, 30th Int. Electric Propulsion Conf., Florence, Italy*, 2007.
- [105] Oleson, S. R., Benson, S., Gefert, L., Patterson, M., and Schreiber, J., "Radioisotope Electric Propulsion for Fast Outer Planetary Orbiters," *AIAA-2002-3967, 38th Joint Propulsion Conf., Indianapolis, IN*, 2002.
- [106] Noble, R. J., "Radioisotope Electric Propulsion for Small Robotic Space Probes," *Journal of the British Interplanetary Society*, Vol. 49, 1996, pp. 445–468.
- [107] Oleson, S. R., Gefert, L., Patterson, M., Schreiber, J., and Benson, S., "Outer Planet Exploration with Advanced Radioisotope Electric Propulsion," *IEPC-2001-0179, 27th Int. Electric Propulsion Conf., Pasadena, CA*, 2001.
- [108] Geurts, K., Pergola, P., Casaregola, C., and Andrenucci, M., "Radioisotope Low-Power Electric Propulsion Missions to the Outer Planets," *AIAA-2007-5234, 43rd Joint Propulsion Conf., Cincinnati, OH*, 2007.
- [109] Fiehler, D. I. and Oleson, S. R., "Radioisotope Electric Propulsion Missions Utilizing a Common Spacecraft Design," *Int. Astronautical Congress, Vancouver, Canada*, 2004.
- [110] Pergola, P., Geurts, K., Casaregola, C., and Andrenucci, M., "Earth-Mars Halo to Halo Low Thrust Manifold Transfers," *Celestial Mechanics and Dynamical Astronomy*, Vol. 105, No. 1-3, 2009, pp. 19–32.
- [111] Pergola, P., Geurts, K., Casaregola, C., and Andrenucci, M., "Electric Propulsion in a Three Body Model for Interplanetary Transfers," *5th Space Propulsion Conf., Heraklion, Crete*, 2008.
- [112] Starchville, T. F. and Melton, R. G., "Optimal Low-Thrust Trajectories to Earth-Moon L2 Halo Orbits (Circular Problem)," *AAS 97-714, AAS/AIAA Astrodynamics Specialists Conf., Sun Valley, ID*, 1997.

- [113] Edelbaum, T. N., "Propulsion Requirements for Controllable Satellites," *American Rocket Society Journal*, Vol. 31, 1961, pp. 1079–1089.
- [114] Kluever, C. A., "Optimal Earth-Moon Trajectories Using Combined Chemical-Electric Propulsion," *Journal of Guidance, Control and Dynamics*, Vol. 20, No. 2, 1997, pp. 252–245.
- [115] Pergola, P., "Low Thrust Transfer to Backflip Orbits," *Advances in Space Research*, Vol. 46, No. 10, 2010, pp. 1280–1291.
- [116] Farquhar, R. W. and Dunham, D. W., "A New Trajectory Concept for Exploring the Earth's Geomagnetic Tail," *Journal of Guidance and Control*, Vol. 4, No. 2, 1981, pp. 192–196.
- [117] Uphoff, C., "The Art and Science of Lunar Gravity Assist," *AAS 89-170, AAS/GSFC Int. Symposium on Orbital Mechanics and Mission Design, Advances in the Astronautical Sciences*, Vol. 69, 1989, pp. 333–436.
- [118] Gómez, G. and Masdemont, J. J., "Some Zero Cost Transfers Between Libration Point Orbits," *AAS 00-177, AAS/AIAA Space Flight Mechanics Meeting, Clearwater, FL*, 2000.

List of Figures

2.1	Inertial and synodic barycentric frames.	17
2.2	CR3BP synodic barycentric reference frame.	19
2.3	Effective Potential for the Earth-Moon system.	21
2.4	Zero velocity curves for increasing energy values for the Earth-Moon system.	24
2.5	Earth-Moon libration point positions in the synodic frame with the zero velocity curves associated to their energy values. . .	26
2.6	Dependence on μ of the x coordinate of the libration points (left) and their energy (right).	27
2.7	Regions allowed for the motion (white) for increasing energy values (from the upper left corner) for the Earth-Moon system. . .	28
2.8	Intersection points between the centrifugal (red) and gravitational (blue) force to locate the collinear equilibria.	29
2.9	$y = 0$ section of the Effective Potential, it shows the concavity of this function in the three collinear equilibrium points. . .	30
2.10	<i>center x center x saddle</i> behavior of the flow in the neighborhood of a collinear equilibrium point.	34
2.11	Schematic representation of the flow in the Equilibrium Region. . .	37
2.12	Left: the BCM reference frame. Right: Modified Effective Potential slices for a representative system where $\mu = 1e-2$, $\mu_p = 5e-3$ placed at 135 deg and $\rho_p = 1.2$ DU.	39
2.13	Stable and Unstable manifolds emanating from a hyperbolic equilibrium point.	41
2.14	Phase portraits of the Standard Map for $h = 0.5, 1.0, 1.5, 2.0$ from the upper left corner.	42
2.15	Left: schematic representation of the homoclinic tangle. Right: homoclinic tangle of the saddle point of the Standard Map after few (up) and 15 iterations (down).	44

3.1	Analytical seed (green) and numerical differential correction (blue) of southern Halos (left) and planar Lyapunov orbits (right) around \mathcal{L}_1 in the Sun-Earth system.	51
3.2	Northern \mathcal{L}_1 /Southern \mathcal{L}_2 Halo (left) and $\mathcal{L}_1/\mathcal{L}_2$ Lyapunov families (right) in the Earth-Moon system.	52
3.3	Schematic ideas of the Natural Continuation procedure (left) and of the Pseudo Arc-length one (right).	54
3.4	Real (left) and schematic (right) bifurcation diagram for the Earth-Moon CR3BP. Each curve is a continuation curve of periodic orbits emanating from one of the five equilibria. . . .	55
3.5	Family of \mathcal{L}_3 Halo orbits in the Earth-Moon system.	56
3.6	Family of \mathcal{L}_4 - \mathcal{L}_5 vertical orbits in the Earth-Moon system. . . .	57
3.7	From left to right schematic representation of: Tangent, Period Doubling and Secondary Hopf Bifurcation.	60
3.8	Views of a P-symmetric, 1-linearly unstable periodic orbit in the Earth-Moon system.	60
3.9	Form the seed of Fig. 3.8: in the upper left corner the motion of the characteristic multipliers for different energies; in the upper right corner the evolution of the stability indexes and in the lower row three views of the continued branch of the periodic family.	61
3.10	Views of a P-symmetric, 2-linearly unstable periodic orbit in the Earth-Moon system.	62
3.11	Form the seed of Fig. 3.10: in the upper left corner the motion of the characteristic multipliers for different energies; in the upper right corner the evolution of the stability indexes and in the lower row three views of the continued branch of the periodic family.	63
3.12	One dimensional manifolds of \mathcal{L}_1 in the Sun-Jupiter system. . . .	64
3.13	One dimensional manifolds of \mathcal{L}_2 in the Sun-Jupiter system. . . .	65
3.14	Two dimensional manifolds of \mathcal{L}_1 with $J = 3.0331$, for the Sun-Jupiter system in the inner and in the Jupiter realm. . . .	66
3.15	Two dimensional manifolds of \mathcal{L}_2 with $J = 3.0331$, for the Sun-Jupiter system in the outer and in the Jupiter realm. . . .	67
3.16	\mathcal{L}_1 Homoclinic connection for the Sun-Jupiter system in the inner realm; on the left on the Poincaré section plane and on the right in the position space.	77
3.17	\mathcal{L}_1 Homoclinic connections for the Sun-Jupiter system in the Jupiter realm; on the left on the Poincaré section plane and on the right in the position space.	78

3.18	\mathcal{L}_1 - \mathcal{L}_2 Heteroclinic connection for the Sun-Jupiter system in the Jupiter realm; on the left on the Poincaré section plane and on the right in the position space.	79
3.19	\mathcal{L}_1 - \mathcal{L}_2 transit orbit and Heteroclinic connection for the Sun-Jupiter system in the Jupiter realm; on the left on the Poincaré section plane and on the right in the position space.	81
3.20	Energy evolution of the $y = 0$ Poincaré sections domain. In a three dimensional view and with slices for four energy values.	83
3.21	Earth-Moon Poincaré section on the $y = 0$ plane with $J = 3.160$	84
3.22	Semi-major axis vs longitude of periapsis map of the Poincaré section presented in Fig. 3.21. Also the nominal resonant semi-major axes are overlapped.	86
3.23	Minimum Moon distance and Jacobi constant for varying eccentricity for the $2:1$ resonance in the Earth-Moon system.	87
3.24	$2:1$ resonance hopping with temporary Moon capture for $e = 0.1762$ in the Earth-Moon system.	88
3.25	$2:1$ resonance hopping to external resonances for $e = 0.505$ in the Earth-Moon system.	89
3.26	$5:2$ Exact Resonance in the synodic (first column) and in the inertial (second column) frame for the Earth-Moon system. Also the trends of the semi-major axis (upper right corner) and of the energy (lower right corner) is shown.	90
3.27	Local Lyapunov Exponent for an Earth-Moon \mathcal{L}_2 Halo orbit; on the left the magnitude of the LLE along the orbit and on the right its time behavior.	92
3.28	Local Lyapunov Exponent for an Earth-Moon \mathcal{L}_1 Halo orbit; on the left the magnitude of the LLE along the orbit and on the right its time behavior.	93
3.29	Moon realm characterization by means of the LLE for $e = 0$	94
3.30	Moon realm characterization by means of the LLE for $e = 0.70$	95
4.1	Schematic view of the single shooting method (right) and of the direct collocation method (left) for a system with a single state and a single control.	99
4.2	$M_0 = 700$ kg (left) and $M_0 = 1000$ kg (right) Earth-Mars minimum time transfers in the heliocentric polar reference frame.	112
4.3	Power and τ , thrust angle and mass consumption evolutions for $M_0 = 700$ kg (first row) and $M_0 = 1000$ kg (second row) Earth-Mars transfers. Trajectories in Fig. 4.2.	112

4.4	$M_0 = 300$ kg (left) and $M_0 = 350$ kg (right) Earth-Mars minimum mass transfers in the heliocentric polar reference frame. The two fixed times are respectively 300 days and 400 days.	113
4.5	Power and τ , thrust angle and mass consumption evolutions for $M_0 = 300$ kg (first row) and $M_0 = 350$ kg (second row) Earth-Mars transfers. Trajectories in Fig. 4.4.	114
4.6	Low thrust heteroclinic connection between Sun-Earth \mathcal{L}_2 and Earth-Moon \mathcal{L}_1 ; in the Sun-Earth synodic frame (left) and in the Earth-Moon one (right).	117
4.7	Thrust angle, mass, instantaneous radius and velocity for the low thrust heteroclinic connection between Sun-Earth \mathcal{L}_2 and Earth-Moon \mathcal{L}_1	118
5.1	Uranus-Oberon/Titania/Umbriel/Ariel/Miranda Hill regions (left) and one dimensional manifolds (right) each as seen in the proper synodic barycentric frame.	122
5.2	Control vector elements for the Oberon-Titania transfer.	123
5.3	Uranus moons tour in the Uranus-Oberon frame (left) and in the Uranus inertial one (left). In blue the ballistic phases, in green the powered ones.	124
5.4	Left: time evolution of position, velocity and mass for the Uranus moon tour. Right: details of the Titania ballistic capture phase.	125
5.5	Interplanetary Earth-Uranus transfer; on the left in the $x-y$ and on the right in the $x-z$, with exaggerate out-of-plane scale.	126
5.6	Electric capture (black line) detail in the Uranus realm, from its Sphere of Influence.	127
5.7	Low thrust Halo to Halo interplanetary transfer; a stable and an unstable manifolds of two different three body systems are linked by means of an electric powered arc.	128
5.8	Trends of the planar amplitudes and period for Halo orbits around Sun-Earth \mathcal{L}_2 (upper row) and Sun-Mars \mathcal{L}_1 (lower row).	134
5.9	Values of the propellant mass plus the error in the final state for a grid search on the elements of the control vector. Form the top left corner the grid search is performed on the departure time, arrival time, thrusting time and Earth-Mars initial relative angle.	135
5.10	Earth-Mars Halo to Halo transfer in the Sun-Earth (left) and Sun-Mars (right) rotating frame.	138

5.11	Earth escape (left) and Mars capture (right) details. The effective orbit is presented with the bold black line superimposed to the relevant manifold.	138
5.12	Planar and three dimensional (on the right with false out-of-plane scale) views of the Earth-Mars transfer in the heliocentric inertial frame.	139
5.13	Control laws for the Earth-Mars transfer; the shaded zones are where the coasting phase takes place.	140
5.14	Instantaneous radius and velocity in the Sun-Earth (upper row) and Sun-Mars (lower row) system.	140
5.15	Propellant mass vs. attractor number for the Simple and Complete Approach.	141
6.1	Initial condition on the intersection of the second cuts of the \mathcal{L}_1 unstable and \mathcal{L}_2 stable manifolds (left) and corresponding symmetric, one-Moon-loop Heteroclinic orbit (right).	144
6.2	Trajectory (left) and radius and velocity evolution (right) for the Earth-Moon “Manifold chain” (\mathcal{L}_1 stable manifold- \mathcal{L}_1 Lyapunov- \mathcal{L}_1 unstable manifold- \mathcal{L}_2 stable manifold- \mathcal{L}_2 Lyapunov).	146
6.3	GTO to “Manifold chain” transfer and subsequent ballistic propagation. In the Earth-Moon barycentric frame (left) and in the geocentric inertial one (right).	146
6.4	Backward evolution of mass, position and velocity, geocentric eccentricity and semi-major for the trajectory of Fig. 6.3.	147
6.5	GEO-LLO CR3BP low thrust transfer. The three phases, thrust-coast-thrust, are presented with three different colors.	151
6.6	Three views and mass evolution of a GEO to LLO “short” solution ($a_M = 5000$ km, $ecc_M = 0$, $\Omega_M = 90$ deg, $incl_M = 25$ deg).	154
6.7	Three views and mass evolution of a GEO to LLO “long” solution ($a_M = 5000$ km, $ecc_M = 0$, $\Omega_M = 0$ deg, $incl_M = 45$ deg).	155
6.8	Time evolutions of geocentric radius, velocity and thrusting angles for the transfer of Fig. 6.6.	156
6.9	Time evolutions of geocentric radius, velocity and thrusting angles for the transfer of Fig. 6.7.	157
6.10	Left: GEO to LLO ($a_M = 5000$ km, $\Omega_M = 90$ deg, $incl_M = 0$ deg) transfer with a lunar swing-by in the capture. Right: continuation procedure carried out on the $incl_M$ showing the trend of the whole transfer time (up) and of the propellant mass consumption (below).	158
6.11	Earth-Moon \mathcal{L}_1 Bifurcation diagram.	160

6.12	Earth-Moon Backflip family. Northern family (upper row) and Southern family (lower row).	161
6.13	Three views of the target Backflip orbit with an out-of-plane excursion of 0.5 DU	164
6.14	Range of Backflip orbits with characteristics similar to the target one chosen.	164
6.15	GEO to Backflip transfers. First row: smaller propellant mass transfer found in x - y and x - z views. Second row: costly transfer found in x - y and x - z views (rotating frame).	167
6.16	Position and velocity evolutions for the less expensive transfer (upper row of Fig. 6.15).	168
6.17	Thrust angles and instantaneous mass for the less expensive transfer (upper row of Fig. 6.15).	168
6.18	Backflip to Backflip transfer. First row: x - y and x - z views in the Earth-Moon rotating frame. Second row: x - y and x - z views in the geocentric inertial frame.	169
6.19	Thrust angles and instantaneous mass for the Backflip-Backflip transfer. Trajectory in Fig. 6.18.	170

List of Tables

5.1	Comparison of results for $A_z = 5e4 \text{ km}$ in the Simple Approach methodology	136
5.2	Comparison of results for the Complete Approach methodology	137
A.1	Physical constants and collinear libration point locations for some three bodies systems	174